



Polymer-Based Volume Holographic Grating Couplers for Optical Interconnects


A Thesis
Presented to
The Academic Faculty
By
Shun-Der Wu

in Partial Fulfillment
of the Requirements for the Degree
Doctor of Philosophy in Electrical and Computer Engineering

Georgia Institute of Technology
March 2004
Copyright © 2004 by Shun-Der Wu

Polymer-Based Volume Holographic Grating Couplers for Optical Interconnects

Approved:


Dr. Elias N. Glytsis, Chair


Dr. Thomas K. Gaylord


Dr. Ali Adibi

Date Approved: Mar. 17, 2004

To my parents,
Ping-Ho Wu and Hsiu-Tuan Wu-Cheng,
and to my wife,
Hui-Chun Hsu

ACKNOWLEDGEMENTS

This thesis could not have been completed without the support and assistance of many people. First and foremost, I would like to thank my advisor Dr. Elias N. Glytsis for all patience, confidence, encouragement, and support he gave me in the past four and a half years. What I learned from him is not only the knowledge but also the attitude for doing research. He is an excellent teacher, an ideal advisor, as well as a good friend. Without his intelligent insights, his profound discussions, and his professional guidance, this thesis could not have been completed. In addition, I would like to thank Dr. Thomas K. Gaylord for his assistance and his generosity especially in Dr. Glytsis' absence in Greece. He has provided me all resources in his laboratories and treated me as one of his own student. I also want to thank Dr. Ali Adibi, Dr. Emmanouil M. Tentzeris, and Dr. Phillip N. First for serving on my thesis proposal and thesis defense committees.

I have been very blessed to work with remarkable colleagues and friends including Mr. Ricardo Villalaz, Ms. Carole Montarou, Mr. Brent Bachim, Mr. Mohammad Braiwish, Mr. Greg Gilby, Mr. Yu-Ming (Arthur) Wu, and Mr. Hung-Fei Kuo. Particular thanks to Ricardo Villalaz for his patient explanations for the fabrications of volume holographic grating couplers and to Yu-Ming Wu and Hung-Fei Kuo for some interesting discussions in the analysis of gratings and thin-film multiple quantum well lasers integrated with waveguides.

I greatly appreciate the financial support provided by the Rotary Club (District 3470) at Tainan area in my first academic year (Aug. 1999–June 2000). Special thanks to Dr. Chun-Ta Tzeng and Ms. Chia-Hua Tsai for their time and efforts in helping me to apply the Rotary Ambassadorial Scholarship in 1998.

Studying in the Department of Engineering Science at National Cheng-Kung Univer-

sity (Tainan, Taiwan) was an important phase in my whole life because I met Dr. Jung-Hua Chou. I really appreciate for his love, listening, encouragement, companionship, and support in the past twelve years from the bottom of my heart. For me, Dr. Chou is like my second father in my life. I cannot thank enough for what he has done for me. I am also grateful to my good friends in Taiwan including Ms. Yao-Yu Wang (Ant), Mr. Chia-Hsin Cheng, and Dr. Chia-Lun Tsai, for their friendship.

On a personal note, I think it is impossible to adequately put into words what my family has contributed to my life because I owe much of what I am today to my loving family. To my father Mr. Ping-Ho Wu, I always remember how hard and intensive he has worked to provide me the best growing and learning environment. To my mother Ms. Hsiu-Tuan Wu-Cheng, she have always encouraged me, loved me, and desired the best for me. Many thanks to my sister, Su-Lin, and brothers, Ming-Tong and Long-Chi, for their support, encouragement, sacrifices, and what they have done for this family in my absence in the United States for pursuing my PhD degree. Most of all, I would like to thank my wife, Hui-Chun. Her love , companionship, encouragement, and good humor, have made the most difficult times bearable and the good times enjoyable. Additionally, I would like to thank my new born baby, who is expected to be a pretty girl on April 30, 2004, for everything which she will bring into my life.

Finally, I want to thank myself for my diligence and insistence to pursue my PhD degree in the United States. I always remember how hard I studied for various disciplines and how hard I worked for part-time jobs to accumulate my energy for my dream as I was an undergraduate student. It is not easy, but I make it and cherish it.

SHUN-DER WU

Georgia Institute of Technology

March 2004

TABLE OF CONTENTS

ACKNOWLEDGEMENTS	iv
TABLE OF CONTENTS	vi
LIST OF TABLES	xi
LIST OF FIGURES	xiii
SUMMARY	xviii
CHAPTER 1 INTRODUCTION	1
1.1 Research Objectives	5
1.2 Literature Review	5
1.2.1 Finite-Number-of-Periods Gratings	5
1.2.2 Dynamics of Holographic Grating Formations in Photopolymers	6
1.2.3 Output Grating Couplers	10
1.2.4 Input Grating Couplers	11
1.3 Thesis Overview	13
CHAPTER 2 FINITE-DIFFERENCE FREQUENCY-DOMAIN METHOD	15
2.1 Configurations of Finite-Number-of-Periods Holographic Gratings	16
2.2 Formulation of the Finite-Difference Frequency-Domain Method	18
2.3 Numerical Considerations and Absorbing Boundary Conditions	20
2.3.1 Performance of the Uniaxial Perfectly Matched Layer	20
2.3.2 Numerical Consideration of the Mesh Size	23

2.4	Calculations of Diffraction Efficiencies	25
2.5	Summary and Discussion	28
CHAPTER 3 FINITE-NUMBER-OF-PERIODS HOLOGRAPHIC GRAT-		
	INGS	29
3.1	Unslanted Finite-Number-of-Periods Holographic Gratings	30
3.1.1	Forward Diffraction Efficiencies	30
3.1.2	Electric Field Intensity	31
3.2	Slanted Finite-Number-of-Periods Holographic Transmission Gratings . . .	33
3.2.1	Forward Diffraction Efficiencies	33
3.2.2	Electric Field Intensity	35
3.3	Slanted Finite-Number-of-Periods Holographic Reflection Gratings	36
3.3.1	Backward Diffraction Efficiencies	36
3.3.2	Electric Field Intensity	37
3.4	Comparison of Finite-Number-of-Periods Holographic to Finite-Number-of- Periods Surface-Relief Gratings	38
3.5	Summary and Discussion	41
CHAPTER 4 DYNAMICS OF HOLOGRAPHIC GRATING FORMATIONS		
	IN PHOTOPOLYMERS	43
4.1	Theoretical Model of Holographic Grating Formations in Photopolymers . .	45
4.1.1	Nonlocal Diffusion Model	45
4.1.2	Finite-Difference Time-Domain Method	47
4.2	Theoretical Results of Holographic Grating Formations in Photopolymers .	49
4.2.1	Effects of Dimensionless Variables on Holographic Grating Formations	49
4.2.2	Comparison of the Finite-Difference Time-Domain Method and the Low-Harmonic-Component Approximation	54
4.3	Unslanted Holographic Gratings	56

4.3.1	Real-Time Diffraction-Efficiency Measurement	56
4.3.2	Effects of Exposure Irradiance on the Unslanted Holographic Grating Recording	58
4.3.3	Effects of Post-Baking Processing	62
4.3.4	Characteristic Parameters of Holographic Photopolymers	64
4.4	Slanted Holographic Gratings	68
4.4.1	Real-Time Diffraction-Efficiency Measurement	68
4.4.2	Experimental Setup of Angular Selectivity	73
4.4.3	Optimization of Rigorous Coupled-Wave Analysis Fittings to Angular- Dependent Transmission Efficiencies	74
4.4.4	Recording Shrinkage of DuPont OmniDex613 Photopolymers	76
4.4.5	Effects of Post-Baking Processing	80
4.4.6	Characteristic Parameters of Holographic Photopolymers	87
4.5	Summary and Discussion	90

CHAPTER 5 OUTPUT VOLUME HOLOGRAPHIC GRATING COUPLERS 94

5.1	Output Volume Holographic Grating Coupler Configurations	97
5.2	Output Volume Holographic Grating Couplers in the Waveguide Film Region	99
5.2.1	Output Coupling Efficiencies	100
5.2.2	Electric and Magnetic Fields	104
5.2.3	Near and Far Fields	108
5.3	Output Volume Holographic Grating Couplers in the Waveguide Cover Region	111
5.3.1	Output Coupling Efficiencies	111
5.3.2	Electric and Magnetic Fields	114
5.3.3	Near and Far Fields	118
5.3.4	Beat Lengths	120
5.4	Summary and Discussion	123

CHAPTER 6 INPUT VOLUME HOLOGRAPHIC GRATING COUPLERS 125

6.1	Input Volume Holographic Grating Coupler Configurations	126
6.2	Input Volume Holographic Grating Couplers in the Waveguide Film Region	129
6.2.1	Electric Fields	130
6.2.2	Optimization of Input Coupling Efficiencies	132
6.3	Input Volume Holographic Grating Couplers in the Waveguide Cover Region	135
6.3.1	Electric Fields	136
6.3.2	Optimization of Input Coupling Efficiencies	138
6.4	Summary and Discussion	142

CHAPTER 7 DESIGN, FABRICATION, AND PERFORMANCE OF A VOLUME HOLOGRAPHIC GRATING COUPLER 144

7.1	Design of a Volume Holographic Grating Coupler	145
7.2	Design of a Holographic Recording Configuration	146
7.2.1	Arrangement of Interferometric Recording	146
7.2.2	Interference Pattern	148
7.3	Fabrication of a Volume Holographic Grating Coupler	151
7.3.1	Sample Preparation	151
7.3.2	Grating Recording	153
7.4	Performance of a Volume Holographic Grating Coupler	154
7.5	Summary and Discussion	157

CHAPTER 8 CONCLUSIONS 159

8.1	Summary of Results	160
8.1.1	Finite-Difference Frequency-Domain Method	160
8.1.2	Finite-Number-of-Periods Holographic Gratings	160
8.1.3	Dynamics of Holographic Grating Formations in Photopolymers . .	162
8.1.4	Output Volume Holographic Grating Couplers	164

8.1.5	Input Volume Holographic Grating Couplers	165
8.1.6	Design, Fabrication, and Performance of a Volume Holographic Grating Coupler	166
8.2	Future Research	166
APPENDIX A THE CONJUGATE GRADIENT METHOD		169
APPENDIX B CALCULATION OF REFRACTIVE -INDEX MODULATIONS FROM MEASURED DIFFRACTION EFFICIENCIES		171
APPENDIX C DIFFRACTION INTEGRALS FOR FAR-FIELD CALCULATIONS		174
APPENDIX D MODAL DECOMPOSITION FOR THE POWER CALCULATIONS OF WAVEGUIDE MODES		176
BIBLIOGRAPHY		179
VITA		191

LIST OF TABLES

Table 3.1	Comparison of the accuracy of the RCWA of 2-level FNP surface-relief gratings and unslanted FNP holographic gratings.	39
Table 3.2	Comparison of the accuracy of the RCWA for 8-level FNP surface-relief gratings and slanted FNP holographic transmission gratings.	40
Table 4.1	Characteristic parameters of unslanted holographic grating formations Based on the DuPont OmniDex613 photopolymers for exposure to $\lambda_{0,w} = 363.8$ nm UV light.	68
Table 4.2	Optimum baking conditions for slanted holographic gratings based on DuPont OmniDex613 photopolymers for exposure to $\lambda_{0,w} = 363.8$ nm UV light.	80
Table 4.3	Characteristic parameters of slanted holographic grating formations based on the DuPont OmniDex613 photopolymers for exposure to $\lambda_{0,w} = 363.8$ nm UV light.	89
Table 5.1	Design parameters of output volume holographic grating couplers.	100
Table 5.2	Performance of an output volume holographic grating coupler in the waveguide film region.	103
Table 5.3	Performance of an output volume holographic grating coupler in the waveguide cover region.	113
Table 6.1	Optimization of a finite input VHGC in a waveguide film region illuminated by various incident-beam profiles.	135
Table 6.2	Optimization of a finite input VHGC in a waveguide cover region illuminated by various incident-beam profiles.	141
Table 7.1	Experimental measurements of the performance of a VHGC in the waveguide cover region.	156

Table B.1	Saturation refractive-index modulations calculated from experimental data using the RCWA or Kogelnik's theory with corrections for Fresnel losses.	173
-----------	---	-----

LIST OF FIGURES

Figure 1.1	Schematic for a general free-space optical interconnect.	2
Figure 1.2	Schematic for a guided-wave optical interconnects.	3
Figure 1.3	The mechanisms of holographic grating formations during exposure. . . .	8
Figure 2.1	Geometric configuration of the two-dimensional diffraction problem of a finite-number-of-periods holographic grating illuminated by a finite-size beam.	17
Figure 2.2	Artificial reflection errors of the UPML with varying conductivity.	23
Figure 2.3	Optimal values of maximum conductivities for UPMLs.	24
Figure 2.4	Effect of mesh sizes on the numerical accuracy of the FDFD method. . . .	25
Figure 2.5	TE-polarized and normally incident wave on a planar interface problem. .	26
Figure 2.6	TM-polarized and normally incident wave on a planar interface problem.	27
Figure 3.1	Forward diffraction efficiencies of unslanted FNP holographic gratings. .	31
Figure 3.2	Two-dimensional diffracted field intensity patterns of unslanted FNP ho- lographic gratings.	32
Figure 3.3	Forward diffraction efficiencies of slanted FNP holographic transmission gratings.	34
Figure 3.4	Two-dimensional diffracted field intensity patterns of slanted FNP holo- graphic transmission gratings.	35
Figure 3.5	Backward diffraction efficiencies of slanted FNP holographic reflection gratings.	37
Figure 3.6	Two-dimensional diffracted field intensity patterns of slanted FNP holo- graphic reflection gratings.	38

Figure 4.1	Temporary profiles of the monomer concentration and the polymer concentration within one grating period.	50
Figure 4.2	Harmonic components of polymer concentrations.	51
Figure 4.3	Polymer-concentration profiles at the steady state for various dimensionless reaction rates.	52
Figure 4.4	Saturation values of the first three harmonics of polymer concentrations.	53
Figure 4.5	Nonlinearities of holographic grating formations.	54
Figure 4.6	Error of the low-harmonic-component approximation for the analysis of the nonlocal diffusion model.	55
Figure 4.7	Experimental setup of the real-time diffraction-monitoring technique to study the dynamics of unslanted holographic grating formations.	57
Figure 4.8	Experimentally monitored diffraction efficiencies for unslanted transmission gratings recorded on DuPont OmniDex613 photopolymers.	59
Figure 4.9	Experimentally monitored refractive-index modulations for unslanted transmission gratings recorded on DuPont OmniDex613 photopolymers.	61
Figure 4.10	Errors of refractive-index modulations estimated by use of Kogelnik's theory.	62
Figure 4.11	Effects of post-baking conditions on the refractive-index modulations. ...	64
Figure 4.12	Theoretical model fitting to the experimentally growth curves of refractive-index modulations for unslanted gratings.	67
Figure 4.13	Experimental setup of the real-time diffraction-monitoring technique to study the dynamics of small slant-angle holographic grating formations. .	69
Figure 4.14	Experimental setup of the real-time diffraction-monitoring technique to study the dynamics of large slant-angle holographic grating formations. .	71
Figure 4.15	Experimental setup for the angular-selectivity measurements of a recorded sample to determine the shrinkage factor, the refractive-index modulation, and the shift of the Bragg angle.	74

Figure 4.16 Angular selectivity of small slant-angle gratings with $\Lambda = 0.5 \mu\text{m}$ and $\phi = 13.71^\circ$	78
Figure 4.17 Angular selectivity of large slant-angle gratings with $\Lambda = 0.5 \mu\text{m}$ and $\phi = 45.0^\circ$	79
Figure 4.18 Effects of post-baking processing for small slant-angle gratings with $\Lambda = 0.5 \mu\text{m}$ and $\phi = 13.71^\circ$	81
Figure 4.19 Angular-dependent transmission efficiencies of small slant-angle grating ($\Lambda = 0.5 \mu\text{m}$ and $\phi = 13.71^\circ$) recorded by $I_0 = 0.240 \text{ mW/cm}^2$ before and after baking at three various temperatures ($T_b=90, 120$, and 150° C) for $t_b = 1.5 \text{ h}$	83
Figure 4.20 Effects of post-baking processing for large slant-angle gratings with $\Lambda = 0.5 \mu\text{m}$ and $\phi = 45.0^\circ$	85
Figure 4.21 Angular-dependent transmission efficiencies of large slant-angle grating ($\Lambda = 0.5 \mu\text{m}$ and $\phi = 45.0^\circ$) recorded by $I_0 = 0.240 \text{ mW/cm}^2$ before and after baking at three various temperatures ($T_b=90, 120$, and 150° C) for $t_b = 1.5 \text{ h}$	86
Figure 4.22 Theoretical model fittings to the experimentally growth curves of refractive-index modulations for slanted holographic gratings.	88
Figure 5.1 Two configurations of output VHGCs.	98
Figure 5.2 Transverse field profiles of an output VHGC in the waveguide film region.	101
Figure 5.3 Filed-amplitude and filed-phase patterns of an output VHGC with $L_g = 100 \mu\text{m}$ and $t_g = t_w = 1.8 \mu\text{m}$ in the waveguide film region.	105
Figure 5.4 Corresponding intensities of Fourier spectrums of the upward field profiles of an output VHGC in the waveguide film region.	107
Figure 5.5 Normalized field intensity at the top surface of the waveguide film layer of an output VHGC in the waveguide film region.	108

Figure 5.6	Normalized intensity of far-field distribution of an output VHGC in the waveguide film region.	110
Figure 5.7	Transverse field profiles of an output VHGC in the waveguide cover region.	112
Figure 5.8	Filed-amplitude and filed-phase patterns of an output VHGC with $L_g = 100 \mu\text{m}$ and $t_g = 6.0 \mu\text{m}$ in the waveguide cover region.	115
Figure 5.9	Filed-amplitude and filed-phase patterns of an output VHGC with $L_g = 100 \mu\text{m}$ and $t_g = 1.8 \mu\text{m}$ in the waveguide cover region.	116
Figure 5.10	Corresponding intensities of Fourier spectrums of the upward field profiles of an output VHGC in the waveguide cover region.	117
Figure 5.11	Normalized field intensity at the top surface of the waveguide film layer of an output VHGC in the waveguide cover region.	119
Figure 5.12	Normalized intensity of far-field distribution of an output VHGC in the waveguide cover region.	121
Figure 5.13	Beat length for the configuration of an output VHGC in the waveguide cover region.	122
Figure 6.1	Two configurations of input VHGCs.	126
Figure 6.2	Three profiles of finite-width incident beams for input VHGCs.	128
Figure 6.3	Two dimensional field-amplitude patterns of a finite input VHGC in the waveguide film region illuminated by a TE-polarized Gaussian beam. . .	130
Figure 6.4	Field profiles of the transmitted field and the waveguide-coupled field corresponding to Fig. 6.3.	131
Figure 6.5	Input coupling efficiencies of TE_0 mode for a finite input VHGC in the waveguide film region illuminated by various beam profiles.	133
Figure 6.6	Two dimensional field-amplitude patterns of a finite input VHGC in the waveguide cover region illuminated by a TE-polarized Gaussian beam. .	130

Figure 6.7	Field profiles of the transmitted field and the waveguide-coupled field corresponding to Fig. 6.6.	137
Figure 6.8	Input coupling efficiencies of TE_0 mode for a finite input VHGC in the waveguide cover region illuminated by various beam profiles.	139
Figure 6.9	Input coupling efficiencies of TE_1 mode for a finite input VHGC in the waveguide cover region illuminated by various beam profiles.	140
Figure 7.1	Corresponding wavevector diagram for the design of a VHGC in the waveguide cover region with output coupling angle θ_c	145
Figure 7.2	Configuration of volume holographic grating recording.	147
Figure 7.3	Configuration of a prism system for the fabrication of volume holographic gratings.	148
Figure 7.4	Effects of material shrinkage on a photopolymer after recording.	150
Figure 7.5	Design of a VHGC in the waveguide cover region based on the prism system for holographic recording.	152
Figure 7.6	The normalized transmitted power as a function of incident angle θ_{inc} for the fabrication of VHGC.	155
Figure 7.7	The normalized transmitted power as a function of the corresponding refractive index, n_{eff} , for the fabrication of VHGC.	157
Figure B.1	Configuration for determining correction factors of the Fresnel reflection loss.	172
Figure D.1	Configuration of a multilayer slab waveguide.	176

SUMMARY

Volume holographic grating couplers (VHGCs) are becoming increasingly attractive devices for the application of optical interconnects because of their higher preferential coupling, dry fabrication processing, and low cost. Moreover, for many practical cases for high-data rate interconnects, the needed gratings have limited spatial apertures and are usually illuminated by finite-width beams, such as Gaussian beams.

In order to design and characterize the performance of finite-size volume holographic gratings, a rigorous method of analysis is needed. In this work, the finite-difference frequency-domain (FDFD) method is applied to analyze rigorously both unslanted and slanted finite-number-of-periods gratings and is compared to the rigorous coupled-wave analysis (RCWA). Furthermore, the FDFD method is adapted for the analysis of VHGCs and is compared to the RCWA/leak-mode approach. Both output and input grating couplers, which are placed either in the waveguide film region or in the waveguide cover region, are investigated in this research. On the other hand, the DuPont OmniDex613 photopolymers are used to fabricate VHGCs in the experiment. In order to obtain a holographic grating with higher refractive-index modulation and thus higher diffraction efficiency, both the theoretical analysis of a nonlocal diffusion model solved rigorously by use of the finite-difference time-domain (FDTD) method and the experimental techniques of real-time diffraction-monitoring and angular-selectivity measurements are applied to study the optimization of holographic recording process. Finally, a VHGC in the waveguide cover region is designed, fabricated, and tested.

CHAPTER 1

INTRODUCTION

Over the last several decades, improvements in circuit designs, materials, and microelectronics fabrication technologies have continued to exponentially reduce the minimum feature sizes of integrated circuits on electronic chips. This is known as Moore’s law, which states that the number of transistors on a silicon chip increases by a factor of 2 every 18 months. However, as the number of transistors increases, the performance of a system is dominated by interconnection medium rather than the devices. Unfortunately, the conventional electrical interconnects used in electronic devices have not advanced as rapidly as the performance of devices. From this perspective, to improve the performance of future systems new architectures and emerging technologies need to be developed.

In recent years, optical interconnects have been considered as a promising technology capable of supporting future packaging system interconnection requirements. Since the fundamental physics of optical interconnections is completely different from the conventional electrical interconnections [1], optical interconnections have the potential to solve some of the physical problems existing in electrical interconnections, such as electromagnetic interference, crosstalk, voltage isolation, “aspect ratio” limit, impedance matching, and timing skew in signals [1–3].

Based on the different routing methods, the optical interconnects can be classified into free-space and guided-wave. Free-space optics [4–11] utilizes diffractive optical elements (DOEs) and/or microlenses arrays to guide an optical signal in free-space or in a bulk medium. The general structure for a free-space optical interconnect implemented with

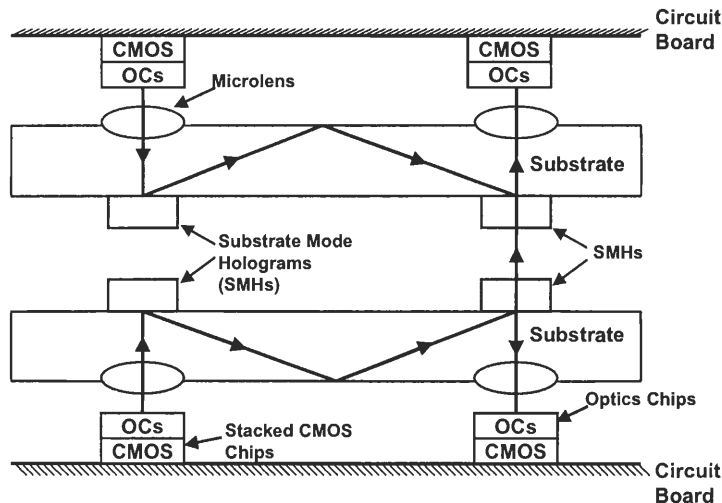


Figure 1.1: Schematic for a general free-space optical interconnect. The substrate-mode holograms (SMHs) are designed to couple incident beams in and out of a substrate, and signal propagates with total internal reflection within the substrate. The microlenses are used for beam collimating and focusing.

substrate-mode holograms (SMHs) is shown in Fig. 1.1. In this system, the SMHs are designed to couple optical signals in and out of a substrate to provide required interconnect functions such as chip-to-chip connections, bidirectional connections, fan-in, and fan-out [5], and the microlenses are designed for beam collimating and beam focusing. On the other hand, guided-wave optics [12–16] uses waveguides to contain the optical signals within a board, a multiple-chip-module, or on a chip. Figure 1.2 shows an example of guided-wave optical interconnect. In this system, the optical signal emitting from the laser is coupled into the slab waveguide by use of a grating coupler, and then is guided to the output grating-coupler, which diffracts the optical signal up to a photodetector. In general, the SMHs, microlenses, and grating couplers can be implemented by surface-relief gratings fabricated by using microelectronics fabrication technologies including thin-film deposition and etching methods, or by holographic gratings fabricated using interferometric recording processes.

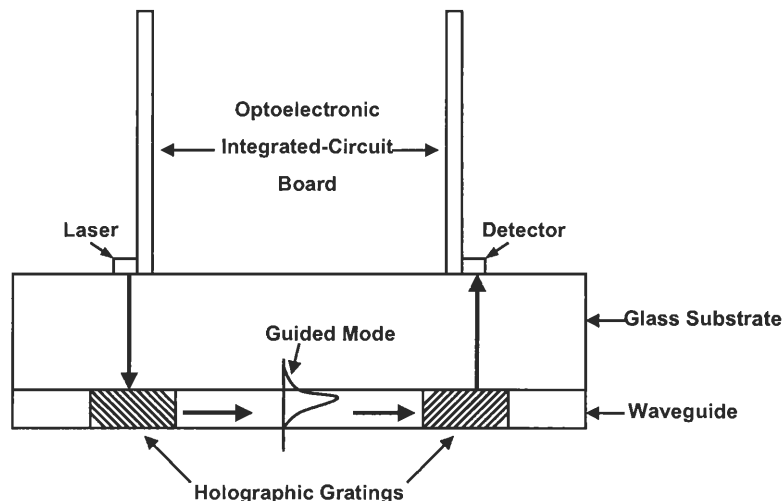


Figure 1.2: Schematic for a guided-wave optical interconnect system. The holographic grating couplers are designed to couple beams in and out of a waveguide structure.

For both routing methods, diffractive optics is an important technology to make optical interconnections feasible. For example, diffractive optical elements (DOEs), such as diffractive lenses, diffractive mirrors, surface-relief gratings, and volume holographic gratings, can be applied to free-space optics as focusing diffractive lenses [17–19] and to guided-wave optics as waveguide couplers [15, 20–22]. In addition to optical interconnects, DOEs have various other applications including beam focusing [23, 24], optical pick-up heads [25–27], filters [28, 29], wavelength-selective coupling [30, 31], wavelength-division multiplexing [32], optical sensors [33–36], distributed-feedback lasers [37–39], and multiple quantum well infrared photodetectors [40, 41].

In practical applications, preferential-order coupling is usually necessary for efficient and cross-talk-free optical interconnects. In order to achieve preferential-order coupling, researchers have applied a variety of methods such as gratings with reflective layers embedded in the substrate [25, 26, 42–45], gratings with double surface corrugations [46], blazed grat-

ings [47, 48], and gratings comprised of parallelogramic surface profiles [49, 50]. However, these methods add complexity to the fabrication process because of complicated deposition, very precise electron-beam lithography, or chemically assisted ion-beam etching process. In addition, the fabrication errors resulting from the grating etching process and inconsistencies of the refractive indices of deposited materials may change the performance characteristics of surface-relief gratings [51].

On the other hand, Schultz *et al.* [20–22] recently used a photopolymer holographic recording material to fabricate volume holographic grating couplers (VHGCs), first proposed by Kogelnik and Sosnowski [52], to obtain extremely high ($> 98\%$) preferential-order coupling [20]. The use of photopolymers eliminates all of the chemical and etching steps, therefore reducing the fabrication complexity. Moreover, for many practical cases for high-data rate interconnections, the needed gratings could have limited spatial apertures and are usually illuminated by finite-width beams.

Because the finite-size gratings illuminated by the finite-width beams are required for practical applications, the traditional assumptions, such as the infinite gratings and the infinite-incident beams, used in analyzing the grating diffraction problems may no longer be valid. These requirements have motivated research to develop a rigorous numerical method for grating diffraction problems. For optical interconnects, VHGCs can be used to couple an incident guided mode out of a waveguide or an incident beam into a waveguide with high coupling efficiencies. Moreover, VHGCs provide more advantages including higher preferential-order coupling, dry processing, and lower cost than surface-relief gratings do. Therefore, the analysis and fabrication of VHGCs as well as the study of the dynamics of holographic grating formations in photopolymers are important issues in research.

1.1 Research Objectives

Given the above motivations, the objectives of this research are to analyze accurately the interaction of finite-width beams with finite-size holographic gratings, to study theoretically and experimentally the dynamic behaviors of holographic grating formations in photopolymers, and to analyze, design, fabricate, and test VHGCs for optical interconnect applications for both input and output coupling configurations. First, the finite-difference frequency-domain (FDFD) method [53–55] is developed and applied to solve rigorously the finite gratings illuminated by finite-incident beams and is compared with the rigorous coupled-wave analysis (RCWA) [56]. Then, the FDFD method is adapted for the analysis of both output and input VHGCs, which could be used in optical interconnect systems. The numerical results of the FDFD method for the analysis of output VHGCs are compared to those of the RCWA in conjunction with the leaky-mode approach. Furthermore, the dynamics of holographic grating formations in DuPont OmniDex613 photopolymers are studied both theoretically and experimentally for both unslanted and slanted gratings. Finally, a VHGC in the waveguide cover region is designed, fabricated, and tested providing also a comparison between the developed theory and the experiment.

1.2 Literature Review

1.2.1 Finite-Number-of-Periods Gratings

In typical grating diffraction analysis, the rigorous coupled-wave analysis (RCWA) [56] is the most common method applied to analyze an infinite-number-of-periods (INP) grating (of perfect periodicity) illuminated by a plane wave (an infinite-width beam). However, for many practical applications, the gratings could have finite sizes and are usually illuminated by finite-width beams, such as Gaussian beams.

In order to analyze finite-size (or infinite-size) gratings illuminated by finite-size

beams, Kriezis *et al.* [57] applied a plane-wave spectrum decomposition of a Gaussian beam in conjunction with the method of moments to study the effect of finite beams in periodic metallic planar screens. Bendickson *et al.* [58] used a finite-beam RCWA to model finite beams on infinitely periodic gratings. On the other hand, Kok [59] used a mode-matching method and Mata-Mendez and Sumaya-Martinez [60] used a modal theory to determine the electromagnetic scattering of a plane wave by a finite number of rectangular grooves on a metallic plane. Pelosi *et al.* [61] used a heuristic diffraction coefficient to analyze the scattering of a plane wave from a metallic strip grating with finite dimension. In addition, Hirayama *et al.* [62, 63] used the boundary element method (BEM) to study the characteristics of finite-size diffractive lenses and finite-number-of-periods (FNP) dielectric/metallic lamellar surface-relief gratings. Recently, few researchers have started to consider the effects of FNP gratings and finite beams on the DOEs simultaneously. Mata-Mendez and Chavez-Rivas [64, 65] used the Rayleigh-Sommerfeld theory to study the diffraction of Gaussian and Hermite-Gaussian beams by a lamellar finite grating at the scalar diffraction regime. Finally, Bendickson *et al.* [58] developed a multiple-layer BEM to analyze the effect of finite-number-of-periods gratings and finite-width beams on the guided-mode resonant sub-wavelength surface-relief gratings.

However, there has been no rigorous analysis to determine the effects of FNP gratings and finite-width beams simultaneously on volume holographic gratings. Therefore, a more rigorous numerical method needs to be developed to study the effects of FNP gratings as well as finite-width beams on the diffraction efficiencies of volume holographic gratings.

1.2.2 Dynamics of Holographic Grating Formations in Photopolymers

In recent years, photopolymers such as HRF DuPont's series have become attractive optical recording materials for a variety of applications including grating couplers [22, 66], focusing gratings [20, 21], optical interconnects [67], optical storage disks [68], and holographic filters [69] because they have large refractive-index modulation ($\Delta n \sim 10^{-2}$) while the stan-

dard inorganic optical materials, such as lithium niobate, have much smaller refractive-index modulation ($\Delta n \sim 10^{-4}$). In addition, photopolymers also exhibit several attractive advantages including dry processing, long lifetime, good photospeed, wide spectral sensitivity, and relative low cost [70].

The fundamental mechanisms for holographic grating formations in the photopolymers consist of three steps [71–73]: (a) initiation, (b) propagation, and (c) termination (as shown in Fig. 1.3). First, when a photopolymer is exposed to an interference pattern, the dye is excited and photoinitiates free radicals. The free radicals *initiate* the spatially nonuniform polymerization of free monomers, which is defined by the interference pattern, and result in the decrease of the free-monomer concentration in bright regions. Because of the monomer concentration gradient, the free monomers will *propagate* from dark regions (with higher monomer concentration) to bright regions (with lower monomer concentration). This process *terminates* when no free monomer is available or thermal fixing occurs [74]. Thermal fixing is accomplished by flashing the hologram with a uniform-intensity UV light. The combination of polymerization and diffusion of free monomers creates a spatial modulation of refractive index and consequently yields a phase grating.

The characteristics of holographic grating formations in photopolymers have been studied by several researchers. Rhee *et al.* [70,75] applied the real-time diffraction-monitoring technique to study experimentally the temporal properties of holographic formations in DuPont photopolymers with respect to exposure irradiance, exposure time, processing situations, shrinkage effects, and storage effects. Kostuk [76] exploited the same measurement technique to study hologram formations in DuPont photopolymers at different stages of exposure and at different spatial frequencies (grating periods). On the other hand, Zhao and Mouroulis [77] proposed a one-dimensional local-response diffusion model with the assumption that the polymerization rate is proportional to the exposure irradiance to study the dynamic behavior of holographic grating formations in DuPont photopolymers. Later, Zhao and Mouroulis [78] modified the local diffusion model by using a more general instead

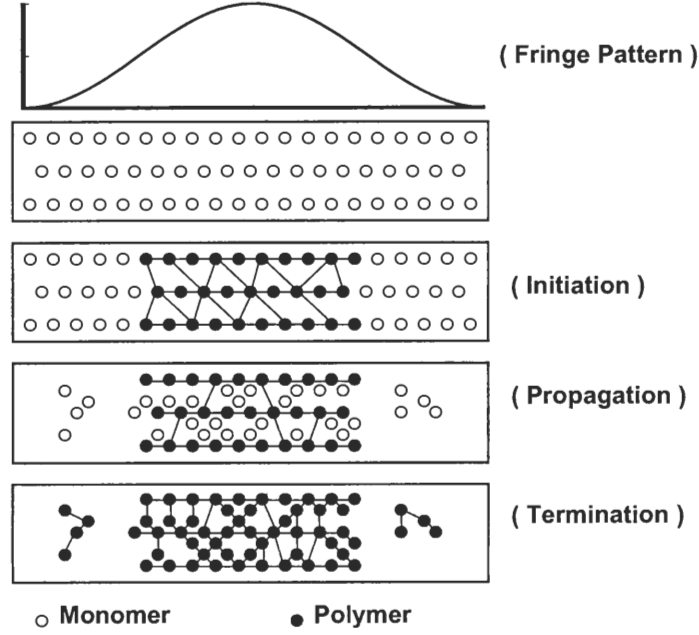


Figure 1.3: The mechanisms of holographic grating formations during exposure. There are three basic steps for developing holographic gratings in photopolymers: initiation, propagation, and termination.

of a linear relationship between the polymerization rate and the recording irradiance. This relationship was necessary in order to describe the nonzero-second-harmonic component of the refractive-index modulation. The latter component does not decrease to zero with decreasing recording irradiance (as a linear relationship between polymerization rate and recording irradiance assumes), effect that has been observed experimentally [79]. In addition, Colvin *et al.* [80] used the local diffusion model proposed by Zhao and Mouroulis in conjunction with cure dependence of both the photoreaction kinetics and the monomer diffusivity to study the hologram formations in photopolymers. However, this local diffusion model [72, 77, 78, 80] only provides a good explanation of low-spatial-frequency grating formations in photopolymers. Recently, Sheridan *et al.* [81–85] proposed a nonlocal-response

diffusion model by introducing a nonlocal variance parameter, σ , into the local-response diffusion model [77, 78] to model the effect of the formations of polymer chains growing away from their initiation locations. This nonlocal diffusion model can predict the existence of a high-frequency cutoff in the spatial-frequency response, while the local diffusion model cannot predict it correctly.

In order to solve the nonlocal diffusion equation numerically, Sheridan *et al.* [81–85] used a low-harmonic-component expansion on the monomer concentration and the diffusion coefficient, and they assumed that the refractive-index modulation is linearly proportional to the polymer concentration. Moreover, Sheridan *et al.* [81–84] applied Kogelnik’s first-order two-wave coupled-wave theory [86] with a correction factor for the Fresnel reflection loss to convert the diffraction efficiencies from the real-time measurement to the corresponding refractive-index modulation values. Then, they fitted the theoretical model to the experimental data to determine the various material properties, including monomer diffusion coefficient and nonlocal variance parameter.

Although the low-harmonic-component approximation has been applied to solve the nonlocal diffusion equation, it does not precisely predict the polymer concentration for the smaller dimensionless reaction rate. By comparing the two-harmonic-component approximation to the four-harmonic-component approximation, the accuracy of the first harmonic of the polymer concentration decreases as the dimensionless reaction rate decreases [82, 84]. The maximum error of the first harmonic component of the polymer concentration predicted by the two-harmonic-component approximation, with the assumption that the polymerization rate is proportional to the square root of the exposure irradiance, is $\sim 50\%$ [84]. Therefore, a more accurate modeling of the polymer concentration is needed.

In summary, photopolymers can be critically important materials for the realization of practical and efficient grating-based optical interconnects or devices in general. Therefore, there is an increasing need for the accurate modeling of holographic grating formations in photopolymers as well as for the optimization of the recording process parameters. In

addition, experimental measurements are needed for the validation of any new model and the determination of the physical parameters of the photopolymers especially at UV recording wavelengths.

1.2.3 Output Grating Couplers

Because of diverse applications of output grating couplers for coupling guided modes out of a thin film optical waveguide, many researchers have proposed various numerical methods to study their characteristics. Peng *et al.* [87, 88] first used modal analysis in conjunction with the leaky-wave approach to analyze rigorously the surface-relief grating coupler for output coupling for both TE and TM polarizations. Moreover, Tamir and Peng [89] studied the leakage parameters (relating to coupling efficiencies) of surface-relief gratings with respect to grating duty cycle, grating refractive indices, grating height, grating period, and grating profile on the basis of perturbation theory. Izhaky and Hardy [90, 91] proposed the unified coupled-mode formalism to study the problems of parallel waveguides with or without surface-relief gratings. Specifically, they studied the effects of grating parameters including groove depths, duty cycles, operation wavelengths, and refractive indices on the grating coupling performance. Viewing the surface-relief grating as a sequence of two alternating types of waveguide sections connected by means of step discontinuities, Borsboom and Frankena [92, 93] used the modal representation of the fields in the waveguide sections with scattering matrices of step discontinuities to study the two-dimensional uniform and focusing (chirped) surface-relief grating couplers with finite lengths for output coupling. In addition, Dinesen and Hesthaven [94, 95] proposed a boundary variation method (BVM) for the analysis of both infinite periodic and finite aperiodic (chirped) surface-relief grating couplers in two- and three-dimensional structures for output coupling. Recently, Lalanne *et al.* [96–98] applied the Fourier-modal method (also known as the RCWA) to analyze the waveguide and the surface-relief grating diffraction problems with the introduction of a virtual periodicity along the transverse direction in conjunction with artificial absorbers at

the boundaries of the elementary cells of the periodic structure.

For the analysis of output VHGCs, Harris *et al.* [99] applied the modified Born approximation, the WKB approach, and the reciprocity theory, to analyze output VHGCs without solving rigorously Maxwell's equations in the grating region. Peng *et al.* [88] applied modal analysis in conjunction with the leaky-mode approach to analyze an output VHGC with a sinusoidal permittivity variation. Wang and Dilauro [100] applied the thin grating decomposition method in conjunction with conventional waveguide analysis to analyze a VHGC embedded in a waveguide. Jones *et al.* [101] also analyzed an output VHGC embedded in a waveguide using the modal theory and Svidzinskii's theory. Finally, Schultz *et al.* [20] exploited the RCWA in conjunction with the leaky-wave approach to analyze and design an output VHGC for line focusing. However, the leaky-wave approach does not take into account the effects of reflection and the additional mode excitation resulting from the discontinuity between the waveguide and the VHGC and generally is not an accurate representation of the radiated (diffracted) field. For this reason, a more rigorous numerical method needs to be developed in order to analyze accurately and design output VHGCs.

1.2.4 Input Grating Couplers

In contrast to the output grating coupler, the input grating coupler is used to couple an incident beam into a thin film optical waveguide. In order to analyze the surface-relief grating for input coupling, Ogawa *et al.* [102] applied the perturbation theory in conjunction with the coupled transmission line analysis to study the input coupling efficiency of an infinite surface-relief grating coupler illuminated by a plane wave with respect to the grating periodicity, the grating depth, and the excitation condition. Neviere *et al.* [103–105] proposed a rigorous electromagnetic formalism deduced from Maxwell's equations to study the coupling resonances of an infinite surface-relief grating illuminated by a plane wave as well as by a limited incident beam. Dalgoutte and Wilkinson [106] applied modified Born approximation and reciprocity theory to study the characteristics of a Gaussian beam launched

into a single mode waveguide and a multimode waveguide by use of surface-relief grating couplers. Woldarczyk and Seshadri [107, 108] used the perturbation theory to analyze an infinite surface-relief grating with a plane wave incidence for both input and output coupling. Recently, different researchers [109–112] have applied the rigorous electromagnetic formalism proposed by Neviere *et al.* [103–105] to study the input coupling efficiency of an infinite surface-relief grating coupler illuminated by a Gaussian beam. Furthermore, Brazas and Li [113] also investigated the effects of the size of Gaussian beam and the length of a finite surface-relief grating on the input coupling efficiency. Finally, Waldhäusl *et al.* [114] used the first order perturbation theory and Kwan and Taylor [115] developed a three-layer waveguide model to study the characteristics of input grating couplers with blazed profiles. On the other hand, Ogawa and Chang [116] used the perturbation theory to analyze both unslanted and slanted input VHGCs with infinite lengths illuminated by a plane wave with TE polarization.

Although a variety of numerical methods have been developed to analyze the input grating couplers, especially for the surface-relief gratings, little study has been done for the input VHGC. For practical applications, the input VHGC could have finite length, and the incident beam is a Gaussian beam. Therefore, the grating length and the beam size could significantly affect the input coupling efficiency for an input VHGC. In addition, as the incident beam is coupled into a guided mode by a grating coupler, this guided mode will propagate in the waveguide and will be coupled out of the waveguide by the same grating. As a result, the input coupling efficiency will also depend on the incident-beam position on the grating coupler. For these reasons, the effects of the grating length, the beam size, and the incident-beam position on the input coupling efficiencies of input VHGCs will be investigated in this research to determine the optimum coupling conditions.

1.3 Thesis Overview

This thesis deals with the analysis, design, and fabrication of polymer-based VHGCs for optical interconnects. In Chapter 2, the FDFD method in conjunction with the UPML as an absorbing boundary used in this research is presented and discussed in some detail.

In Chapter 3, the FDFD method is applied to study the characteristics of a FNP holographic grating illuminated by a finite-width incident beam. Both unslanted and slanted gratings are investigated in transmission as well as in reflection configurations. The diffraction efficiency of a FNP holographic grating as a function of the grating size and the incident-beam size calculated by the FDFD method are also compared with the efficiencies determined by the RCWA. Furthermore, the effects of FNP holographic gratings on their diffraction performance are compared with their counterparts of the FNP surface-relief gratings.

In Chapter 4, the dynamic characteristics of holographic grating formations in photopolymers based on the theoretical analysis as well as the experimental measurement are presented. Both unslanted and slanted gratings are treated in this research. For the theoretical analysis, the nonlocal diffusion model is rewritten in a dimensionless form and is rigorously solved by using the finite-difference time-domain (FDTD) method and compared with the low-harmonic-component approximation. On the other hand, the real-time diffraction-monitoring technique in conjunction with the RCWA is applied to study the dynamic hologram recording characteristics of DuPont photopolymers. Furthermore, the angular-selectivity experiment is used to determine the angular-dependent transmission efficiency of a slanted grating, and therefore, to estimate the shrinkage factor of the recording material. The theoretical results are also fitted to the experimental data to determine the characteristic parameters of the DuPont photopolymer. Moreover, the effects of post-baking conditions on the enhancement of refractive-index modulations and the compensation of recording shrinkage are presented.

In Chapter 5, the FDFD method is applied to analyze rigorously the output VHGCs for both TE and TM polarizations and for zero- or 45-degree output coupling. Two configurations of output VHGCs in integrated optics are investigated. These two configurations depend on the position of the VHGC that can be placed either in the waveguide film region or in the waveguide cover region. The FDFD results are compared with their counterparts obtained by the RCWA in conjunction with the leaky-mode approach. The discontinuity effects as well as multimode excitation and interference are also presented.

On the other hand, the numerical results of the input VHGCs analyzed by use of the FDFD method are presented in Chapter 6. Similarly, an input VHGC placed either in the waveguide film region or in the waveguide cover region is analyzed. The effects of the grating length, the beam size, and the incident-beam position on the input coupling efficiencies of input VHGCs will be investigated in this research to determine the optimum coupling conditions.

In Chapter 7, the design, fabrication, and testing of a VHGC in the waveguide cover region are presented. Finally, in Chapter 8, the results of the thesis are summarized, and the possible directions for future research are presented.

CHAPTER 2

FINITE-DIFFERENCE FREQUENCY-DOMAIN METHOD

Although various numerical methods, such as the finite-beam RCWA [58], the mode-matching method [59], the modal theory [60], the boundary element method [58, 62, 63], and the Rayleigh-Sommerfeld theory [64, 65] have been applied to study the effects of finite beams and/or finite gratings (especially for the surface-relief gratings), there has been no rigorous analysis to determine the effects of finite-size gratings and finite beams simultaneously for volume holographic gratings. However, finite-size volume holographic gratings could be essential components of optical interconnects. Therefore, there is a need in developing analytical tools for the design and optimization of these gratings. In this chapter, the finite-difference frequency-domain (FDFD) method in conjunction with the uniaxial perfectly matched layers (UPMLs) [54, 55] (for studying the diffraction characteristics of finite-size gratings illuminated by finite beams in the case of volume holographic gratings) will be presented. In Section 2.3, the performance of the UPML and the numerical consideration of mesh size will be discussed. Moreover, to quantify the diffraction performance of various gratings, some power-related performance metrics such as the diffraction efficiency, the coupling efficiency, and the branching ratio have to be determined from the diffracted fields calculated by the FDFD method. Therefore, in Section 2.4, the fast Fourier transform (FFT) will be presented for the calculation of diffracted power.

2.1 Configurations of Finite-Number-of-Periods Holographic Gratings

The geometric configuration of the two-dimensional diffraction problem of a holographic grating of width L and thickness d is shown in Fig. 2.1(a). The grating consists of a variation in the permittivity throughout the volume of the grating with a period Λ and a slant angle ϕ . The grating vector \mathbf{K} is defined as $\mathbf{K} = |\mathbf{K}|(\hat{x} \cos \phi + \hat{y} \sin \phi)$ where $|\mathbf{K}| = 2\pi/\Lambda$ and \hat{x} , \hat{y} are the unit vectors along the x and y directions respectively. The permittivity in the grating region can be written as

$$\epsilon = \epsilon_0 \epsilon(x, y) = \epsilon_0 [\epsilon_0 + \sum_{p=1}^{\infty} \epsilon_p^c \cos(p\mathbf{K} \cdot \mathbf{r}) + \sum_{p=1}^{\infty} \epsilon_p^s \sin(p\mathbf{K} \cdot \mathbf{r})], \quad (2.1)$$

where ϵ_0 is the permittivity of free space, $\epsilon(x, y)$ is the dielectric constant, ϵ_0 is the average dielectric constant, and ϵ_p^c and ϵ_p^s are the p -th harmonics of the dielectric constant, and \mathbf{r} is the position vector ($\mathbf{r} = x\hat{x} + y\hat{y}$). Since regions 1 and 3 are unbounded, an absorbing boundary layer of width δ [see Fig. 2.1(a)] is included in order to truncate the computational domain. This is necessary since the FDFD method will be utilized for the solution of the diffraction problem. In this research the uniaxial perfectly matched layer [117–119] (UPML) is used as the absorbing boundary layer. After the insertion of the UPML the computational domain has dimensions L_x and L_y along the x and y directions respectively [Fig. 2.1(a)].

In order to model a finite-width incident beam a flat cosine-squared window function $g(y')$ is introduced to describe the profile of the beam. The function $g(y')$ is given by

$$g(y') = \begin{cases} 1 & 0 \leq |y'| \leq \frac{W}{2} \\ \cos^2 \left[\frac{|y'| - \frac{W}{2}}{2(D - \frac{W}{2})} \pi \right] & \frac{W}{2} \leq |y'| \leq D - \frac{W}{2}, \\ 0 & D - \frac{W}{2} \leq |y'| \leq \infty \end{cases} \quad (2.2)$$

where W is the flat width, $(2D - W)$ is the total width of the beam, $y' = y \cos \theta_{inc}$, and θ_{inc} is the incident angle. The beam profile is shown in Fig. 2.1(b). The resulting incident

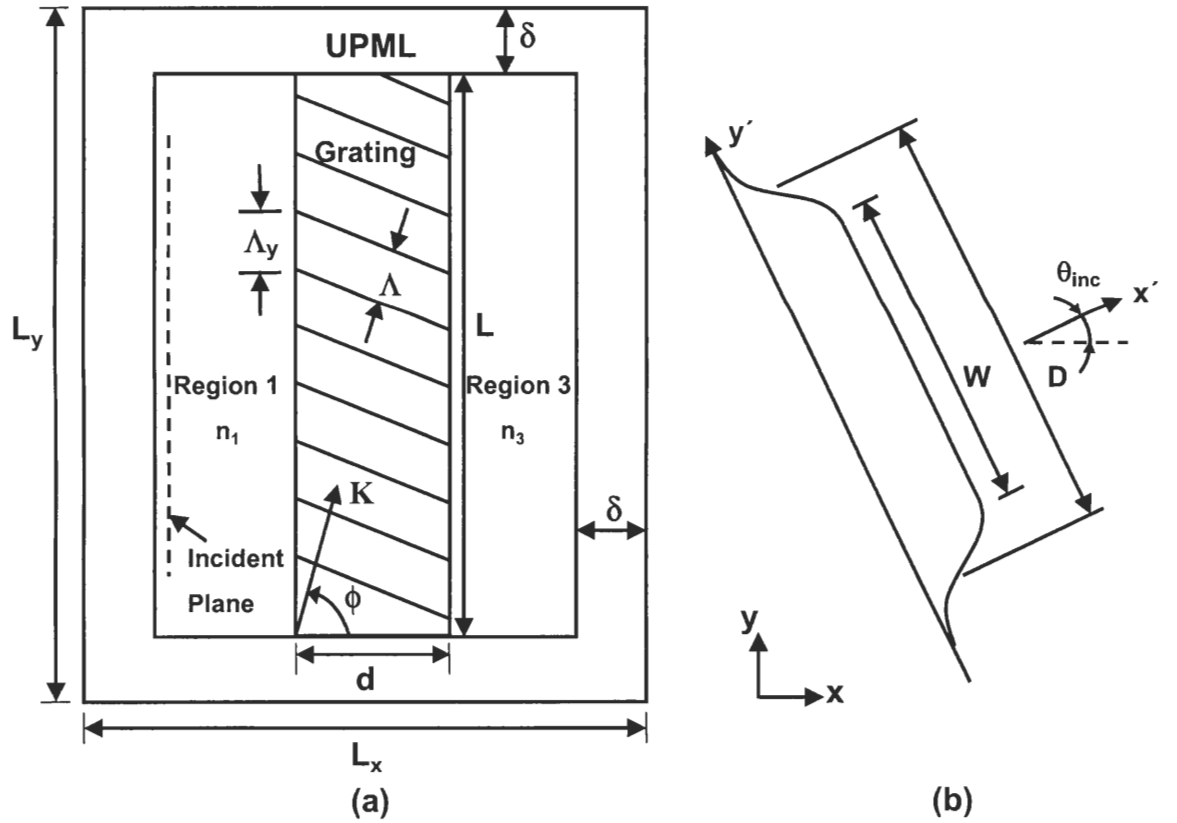


Figure 2.1: (a) Geometry used to model the diffraction of a finite-width beam from a finite-number-of-periods holographic grating. The holographic grating has a period Λ , a slant angle ϕ , a width L , and a thickness d . The thickness of the absorbing uniaxial perfectly matching layer (UPML) is δ . (b) The beam profile of the finite incident beam is shown with flat width W , total width $(2D - W)$, and incident angle θ_{inc} .

beam for TE/TM polarization can be presented by an electric/magnetic field as follows

$$\mathbf{E}_{inc}/\mathbf{H}_{inc} = g(y')\exp(-j\mathbf{k}\cdot\mathbf{r})\hat{z}, \quad (2.3)$$

where $\mathbf{k} = k_0 n_1 (\hat{x} \cos \theta_{inc} + \hat{y} \sin \theta_{inc})$, $k_0 = 2\pi/\lambda_0$, and λ_0 is the freespace wavelength. The finite-width beam is incident from region 1 with refractive index n_1 on the FNP grating, and then diffracts into region 3 with refractive index n_3 . In general, the profile of the incident beam can represent any type of finite-width beam, such as Gaussian, Hermite-Gaussian, etc., by appropriate selection of $g(y')$ function. In this research the flat cosine-squared profile function has been selected to represent the finite-width beam since this resembles more a plane wave if W is large compared to the wavelength. Therefore, comparisons with plane wave diffraction by gratings can be performed when the incident beam and the grating are large ($D \gg \lambda_0$).

2.2 Formulation of the Finite-Difference Frequency-Domain Method

The basic idea of the FDFD method is to apply the central difference approximation on the Helmholtz equation. For TE polarization, that is $\mathbf{E} = E_z \hat{z}$, the Helmholtz equation can be written as [55]

$$\nabla^2 E_z + \omega^2 \mu \epsilon_s E_z = 0. \quad (2.4)$$

Similarly, for TM polarization, that is $\mathbf{H} = H_z \hat{z}$, the Helmholtz equation can be written as [55]

$$\nabla^2 H_z + \omega^2 \mu \epsilon_s H_z - \frac{\nabla_2(j\omega\epsilon + \sigma)}{j\omega\epsilon + \sigma} \cdot \nabla_2 H_z = 0, \quad (2.5)$$

where $s = 1 - j\frac{\sigma}{\omega\epsilon}$, σ is the conductivity, ω is the angular frequency, and $\nabla_2 = \frac{\partial}{\partial x} \hat{x} + \frac{\partial}{\partial y} \hat{y}$.

To apply the central difference approximation on the Helmholtz equation, the mesh size should be determined first. Therefore, the number of grid points per wavelength in the

x direction, N_x , and in the y direction, N_y , of the FDFD method are determined by

$$N_x = \frac{\lambda_0/n_{max}}{\Delta x}, \quad (2.6)$$

$$N_y = \frac{\lambda_0/n_{max}}{\Delta y}, \quad (2.7)$$

where n_{max} is the maximum refractive index in the computational domain, Δx is the mesh size in the x direction, and Δy is the mesh size in the y direction. Therefore, the number of grid points in the x direction is $N_{x,max} = [L_x/\Delta x] + 1$ and in the y direction is $N_{y,max} = [L_y/\Delta y] + 1$ where $[A]$ represents the integer part of A .

After discretizing the Helmholtz equation by using the central difference approximation, the end result of the FDFD formulation is a set of linear algebraic equations that can be written compactly as

$$\bar{\bar{\mathbf{A}}}\mathbf{U} = \mathbf{b}, \quad (2.8)$$

where $\bar{\bar{\mathbf{A}}}$ is an $N_{x,max}N_{y,max} \times N_{x,max}N_{y,max}$ coefficient matrix depending on the material properties and the geometry of the problem, \mathbf{U} represents an $N_{x,max}N_{y,max} \times 1$ vector that contains the field values (\mathbf{E}_z or \mathbf{H}_z components for TE or TM polarization respectively), and \mathbf{b} is an $N_{x,max}N_{y,max} \times 1$ vector that represents the incident wave.

To analyze the diffraction characteristics of gratings, the grating problem should be decomposed into the incident field geometry and the scattered field geometry. For the incident field geometry, the grating and region 3 are removed from the computational domain and their space is filled by region 1. The finite-width incident beam is assigned on the incident plane as shown in Fig. 2.1(a). Therefore, Eq. (2.8) can be written as

$$\bar{\bar{\mathbf{A}}}_{\text{inc}}\mathbf{U}_{\text{inc}} = \mathbf{b}_s, \quad (2.9)$$

where $\bar{\bar{\mathbf{A}}}_{\text{inc}}$ is the coefficient matrix relating to the material properties without the grating and region 3 in the computational domain, \mathbf{U}_{inc} is the unknown incident field, and \mathbf{b}_s is the source term corresponding to the finite-width incident beam. On the other hand, for the scattered field geometry, the grating and region 3 are included in the computational

domain. In the latter case, Eq. (2.8) can be written as

$$\bar{\bar{\mathbf{A}}}_{\text{sca}} \mathbf{U}_{\text{sca}} = (\bar{\bar{\mathbf{A}}}_{\text{inc}} - \bar{\bar{\mathbf{A}}}_{\text{sca}}) \mathbf{U}_{\text{inc}}, \quad (2.10)$$

where $\bar{\bar{\mathbf{A}}}_{\text{sca}}$ is the coefficient matrix relating to the material properties with the grating and region 3 included in the computational domain, \mathbf{U}_{sca} is the unknown vector of the scattered field values, and \mathbf{U}_{inc} is the incident field vector obtained from Eq. (2.9). Finally, the total field in the computational domain is $\mathbf{U}_{\text{tot}} = \mathbf{U}_{\text{inc}} + \mathbf{U}_{\text{sca}}$.

To solve the large sparse linear systems for the incident and scattered fields as shown in Eqs. (2.9) and (2.10), the conjugate gradient method (CGM) [120] in its sparse formulation is utilized. CGM is the most popular iterative method because its residual error decreases monotonically at each iteration. The algorithm of the sparse-CGM is presented in Appendix A.

Finally, it is worth mentioning that, in principle, the presented methodology of solving the Helmholtz equation using the FDFD method can be applied in more general diffraction problems. For example instead of FNP holographic gratings, just as easily, surface-relief FNP gratings of any shape could be analyzed (while the boundary element method cannot be applied to holographic gratings). Even multiplexed FNP holographic gratings for applications in optical memories and optical computing can be similarly studied. A similar approach can also be used in integrated optics configurations to analyze a broad range of grating couplers.

2.3 Numerical Considerations and Absorbing Boundary Conditions

2.3.1 Performance of the Uniaxial Perfectly Matched Layer

To solve the Helmholtz equation using the FDFD method in an unbounded domain [as it is needed for the diffraction problem shown in Fig. 2.1(a)], it is necessary to apply absorbing

boundary conditions to truncate the computational domain to be able to absorb outgoing propagating waves from the structure and prevent them from reflecting back. In addition, the absorbing boundary conditions should provide good performance on the artificial reflection error. Generally speaking, the artificial reflection error should be decreased down to at least -80 dB [119].

In this research, the uniaxial perfectly matched layers (UPMLs) [117–119] are applied as absorbing layers to truncate the computational domain. Although the performance of UPMLs has been discussed in the finite-difference time-domain (FDTD) method [118], it is also necessary to understand their performance in the FDFD method because the FDFD and FDTD methods use different grid positions for the electromagnetic fields assignment.

The Maxwell's equations in the UPML formulation can be written as [117]

$$\nabla \times \mathbf{E} = -j\omega\mu\tilde{s}\mathbf{H}, \quad (2.11)$$

$$\nabla \times \mathbf{H} = j\omega\epsilon\tilde{s}\mathbf{E}, \quad (2.12)$$

$$\nabla \cdot (\epsilon\tilde{s}\mathbf{E}) = 0, \quad (2.13)$$

$$\nabla \cdot (\mu\tilde{s}\mathbf{H}) = 0, \quad (2.14)$$

where \tilde{s} is a complex diagonal tensor of the form

$$\tilde{s} = \begin{bmatrix} s_x^{-1}s_y s_z & 0 & 0 \\ 0 & s_x s_y^{-1}s_z & 0 \\ 0 & 0 & s_x s_y s_z^{-1} \end{bmatrix}, \quad (2.15)$$

and $s_i = 1 - j\frac{\sigma_i}{\omega\epsilon}$ for $i = x, y, z$. It is noted that s_i and σ_i are spatially variant only along the i direction.

For two-dimensional problems [such as in Fig. 2.1(a)], with the elimination of the magnetic field, the Helmholtz equation for TE polarization in the UPML region can be written as

$$\frac{1}{s_x} \frac{\partial}{\partial x} \left(\frac{1}{s_x} \frac{\partial E_z}{\partial x} \right) + \frac{1}{s_y} \frac{\partial}{\partial y} \left(\frac{1}{s_y} \frac{\partial E_z}{\partial y} \right) + \omega^2 \mu \epsilon E_z = 0. \quad (2.16)$$

Similarly, the Helmholtz equation for TM polarization in the UPML region can be written as

$$\frac{1}{s_x} \frac{\partial}{\partial x} \left(\frac{1}{s_x} \frac{\partial H_z}{\partial x} \right) + \frac{1}{s_y} \frac{\partial}{\partial y} \left(\frac{1}{s_y} \frac{\partial H_z}{\partial y} \right) + \omega^2 \mu \epsilon H_z = 0. \quad (2.17)$$

Several profiles, such as polynomial grading [118, 121] and geometric grading [122], have been suggested for σ_i . To simplify the implementation of UPML in the FDFD method, a polynomial grading is applied in this research. The polynomial grading dependence of σ_i is simply of the form

$$\sigma_i(r_i) = \sigma_{i,max} \left(\frac{r_i}{\delta} \right)^m, \quad \text{for } i = x, y, z, \quad (2.18)$$

where $\sigma_{i,max}$ is the maximum conductivity in the i direction of the UPML, r_i is the distance measured from the interface between the real computational domain and the UPML in the i direction, δ is the thickness of the UPML, and m is the polynomial order. In order to understand the performance of the UPML, the artificial reflection errors from the UPML should be investigated and the optimal values of $\sigma_{i,max}$ and m should be determined to minimize the reflection errors to less than -80 dB.

In order to determine the artificial reflection errors from the UPML, the behavior of an incident beam propagating in a homogeneous medium with dielectric constant ϵ is investigated by using the FDFD method and the diffraction integral method [17]. Since the diffraction integral method combines Huygen's principle with the appropriate Green's functions to study the electromagnetic fields propagating in an unbounded domain, the artificial reflection errors from the UPML can be defined as $20\log|\mathbf{U}_{\text{FDFD}} - \mathbf{U}_{\text{DIM}}|$ where \mathbf{U}_{FDFD} and \mathbf{U}_{DIM} are the fields calculated by the FDFD method and the diffraction integral method respectively. As shown in Fig. 2.2, the reflection errors are plotted as a function of $\sigma_{i,max}$ for various polynomial orders ($m = 2, 3, 4, 5$) for $\delta = 2.0 \mu\text{m}$ and $\epsilon = 3$. In general, for a given m , the reflection error decreases as $\sigma_{i,max}$ increases. However, as $\sigma_{i,max}$ increases further, the reflection error reaches a saturation value. Therefore, for a set of ϵ , δ , and m , the optimal values of $\sigma_{i,max}$ can be determined to minimize the reflection

error down to -90 dB from this diagram.

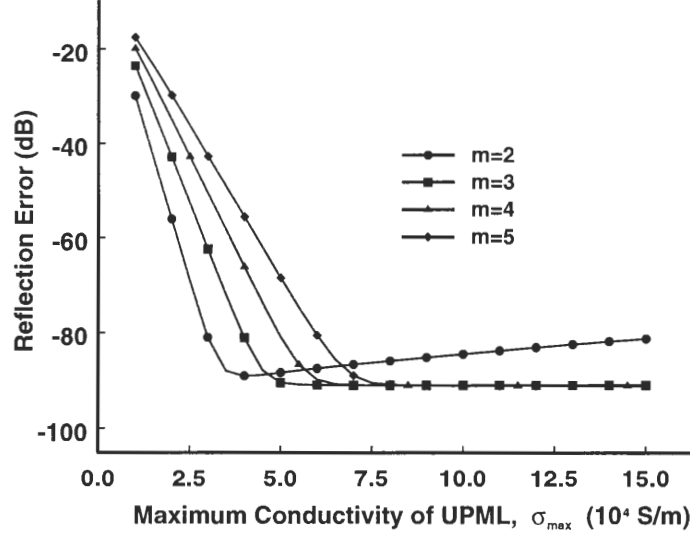


Figure 2.2: Artificial reflection errors from the UPML as functions of the maximum conductivity σ_{max} and the polynomial order m as the dielectric constant of the truncated medium is $\epsilon = 3$ and the thickness of the UPML is $\delta = 2.0\ \mu m$.

Figure 2.3 shows the optimal $\sigma_{i,max}$ as a function of ϵ for different polynomial orders ($m = 2, 3, 4, 5$) for $\delta = 2.0\ \mu m$. According to Fig. 2.3 the optimum parameters of the UPML can be selected in order to minimize the computational domain and to insure that the effect of the reflection error is down to at least -90 dB . For example, to truncate a grating with $\epsilon = \epsilon_0 = 2.25$, the optimal $\sigma_{i,max}$ is about $6.5 \times 10^4\text{ S/meter}$ for $m = 3$.

2.3.2 Numerical Consideration of the Mesh Size

In order to determine the effect of the mesh size on the numerical error, the planar interface problems for TE and TM polarizations are treated. Namely, there are two regions separated by a planar boundary in the computational domain. In this test case, the refractive indices in region 1 and region 2 are $n_1 = 1.0$ and $n_2 = 1.5$ respectively. To truncate regions 1 and 2, the maximum conductivities used in UPMLs are selected to be $\sigma_{1,max} = 3.7 \times 10^4\text{ S/meter}$

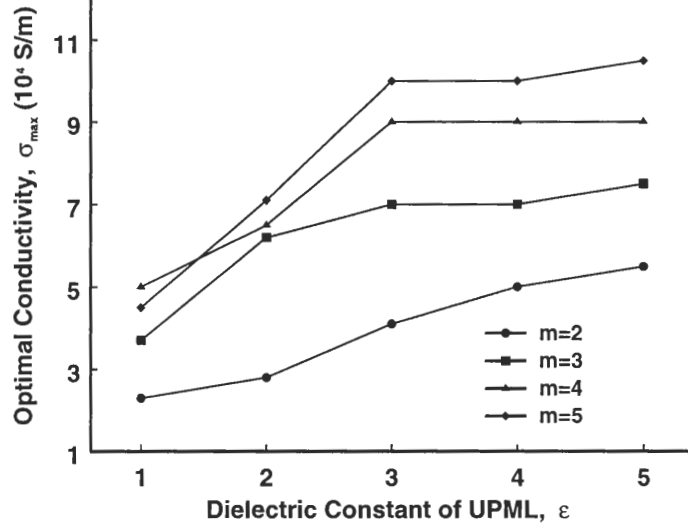


Figure 2.3: Optimal values of maximum conductivities as functions of the dielectric constant ϵ and the polynomial order m as the thickness of the UPML is $\delta = 2.0 \mu m$.

and $\sigma_{2,max} = 6.5 \times 10^4 S/meter$ for $m = 3$ (from the results of Fig. 2.3). Moreover, a normally incident beam with $W = 20 \mu m$ and $D = 25 \mu m$ propagates from region 1 to region 2.

According to Fresnel equations, the percent reflected and transmitted powers that are due to a normally incident plane wave (TE- or TM-polarized) are 4% and 96% respectively. Figure 2.4 shows the normalized transmitted and reflected powers as a function of the number of grid points per wavelength. As expected, the numerical error becomes smaller as the number of grid points per wavelength increases. However, a rather non-physical phenomenon is that the normalized transmitted power can be larger than 1.0 for $N_x = N_y = 5$ as it can be observed in Fig. 2.4. The reason of this non-physical effect is that the artificial wave reflects back to the real computational domain from the absorption layers. Therefore, the overall electromagnetic power can be overestimated. In addition, the convergence of the TM polarization is slower than that of the TE polarization. In order to

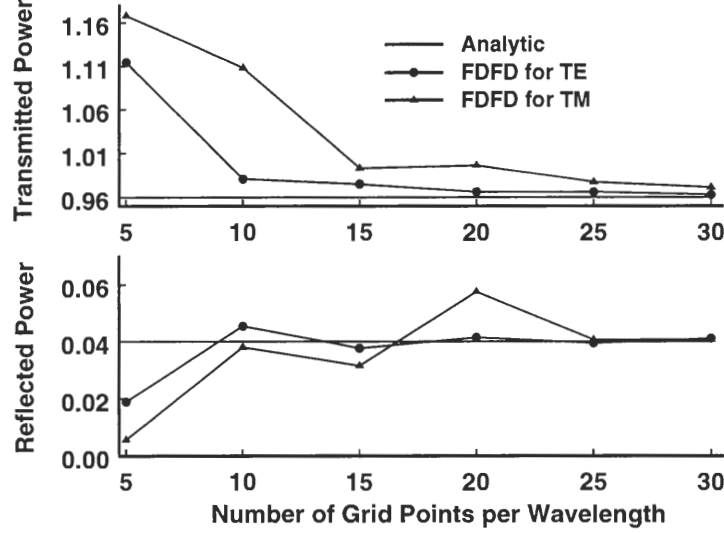


Figure 2.4: Normalized transmitted and reflected powers as a function of the number of grid points per wavelength ($N_x = N_y$) for the cases of a TE/TM-polarized normally incident plane wave on a planar interface between two regions of refractive indices $n_1 = 1.0$ and $n_2 = 1.5$.

avoid these non-physical effects $N_x, N_y \geq 20$ for the TE polarization and $N_x, N_y \geq 25$ for the TM polarization.

Furthermore, the accuracy of the FDFD method is assessed by comparison of the FDFD results with the ones obtained analytically for the magnitude of the electric field or the magnetic field. The results are summarized in Fig. 2.5 for TE polarization with $N_x = N_y = 20$ and in Fig. 2.6 for TM polarization with $N_x = N_y = 25$. The accuracy of the FDFD method is apparent both in region 1 and in region 2, including perfect continuity at the dielectric interface located at $x = 1.0 \mu m$.

2.4 Calculations of Diffraction Efficiencies

Applying the FDFD method, the scattered electromagnetic field by the FNP holographic grating can be determined. However, to quantify the performance of DOEs, it is useful

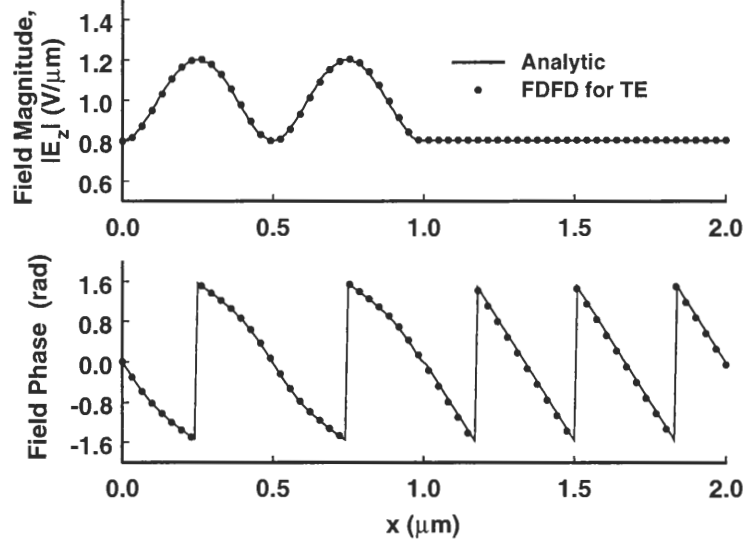


Figure 2.5: Magnitude and phase of the total electric field, E_z , as a function of x in the case of a TE-polarized normally incident plane wave on a planar interface between two regions of refractive indices $n_1 = 1.0$ and $n_2 = 1.5$. The planar interface is located at $x = 1.0 \mu\text{m}$.

to calculate some power-related performance metrics. Some metrics that are commonly used in the diffraction of light by gratings are the percentage of the power transmitted, the percentage of the power reflected, and the diffraction efficiency (DE) of a specified diffraction order. In order to determine these quantities, the fast Fourier transform (FFT) can be used. The angular spectrum, F_i , of the scattered field in region i ($i = 1$ or 3) can be expressed as

$$F_i(k_{ym}) = \sum_{q=0}^{M-1} U(x_i, q\Delta y) \exp[jk_{ym}(q\Delta y)], \quad (2.19)$$

where M is the number of sampling points of the scattered field, $k_{ym} = 2m\pi/(M\Delta y)$, U is the scattered field values obtained from Eqs. (2.9) and (2.10), and x_i is the plane on which the fields are used ($i = 1$ or 3). Once $F_i(k_{ym})$'s have been determined, the transmitted (P_3) and reflected (P_1) powers for TE incident polarization are given by [62, 63]

$$P_i^{TE} = \frac{\Delta y}{2M} \sum_{m=0}^{M-1} |F_i(k_{ym})|^2 \text{Re}\left\{\frac{k_{i,xm}^*}{\eta_i^* k_i^*}\right\} \quad (i = 1, 3). \quad (2.20)$$

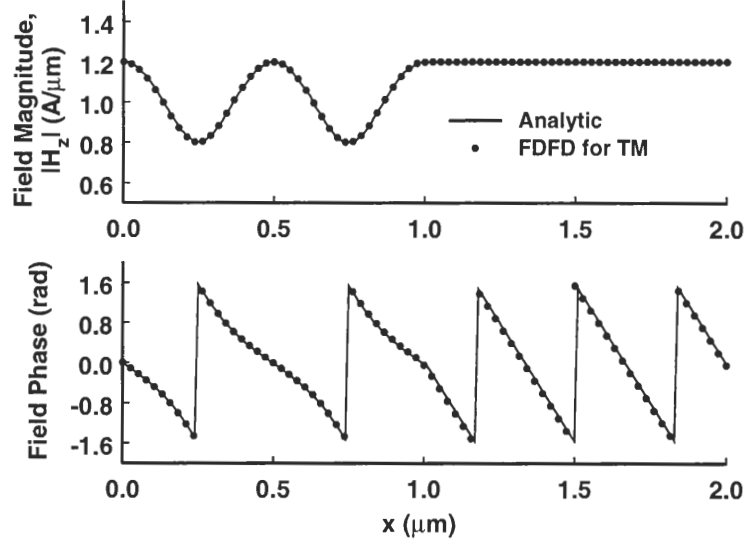


Figure 2.6: Magnitude and phase of the total magnetic field, H_z , as a function of x in the case of a TM-polarized normally incident plane wave on a planar interface between two regions of refractive indices $n_1 = 1.0$ and $n_2 = 1.5$. The planar interface is located at $x = 1.0 \mu\text{m}$.

Similarly, the transmitted (P_3) and reflected (P_1) powers of TM polarization can be determined by

$$P_i^{TM} = \frac{\Delta y}{2M} \sum_{m=0}^{M-1} |F_i(k_{ym})|^2 \text{Re}\left\{\frac{k_{i,xm}\eta_i}{k_i}\right\} \quad (i = 1, 3), \quad (2.21)$$

where $k_i = (2\pi/\lambda_0)n_i$ is the magnitude of wavevector in region i , $k_{i,xm} = (k_i^2 - k_{ym}^2)^{1/2}$, $\eta_i = \sqrt{\mu_i/\epsilon_i}$, and $\text{Re}\{\}$ denotes the real part of a complex number. Therefore, the percentages of the transmitted and reflected powers can be defined as $P_3^{TE/TM}/P_{inc}$ and $P_1^{TE/TM}/P_{inc}$ where P_{inc} is the power of the finite-width incident beam. In addition, the diffracted power of a specific diffracted order p in region i ($i = 1$ for backward and $i = 3$ for forward) for TE polarization is given by

$$P_{i,p}^{TE} = \frac{\Delta y}{2M} \sum_{m=k_{1,y}-(p-1/2)K_y}^{k_{1,y}-(p+1/2)K_y} |F_i(k_{ym})|^2 \text{Re}\left\{\frac{k_{i,xm}^*}{\eta_i^* k_i^*}\right\} \quad (i = 1, 3). \quad (2.22)$$

Similarly, the diffracted power of a specific diffracted order p in region i for TM polarization is given by

$$P_{i,p}^{TM} = \frac{\Delta y}{2M} \sum_{m=k_{1,y}-(p+1/2)K_y}^{k_{1,y}-(p-1/2)K_y} |F_i(k_{ym})|^2 \text{Re}\left\{\frac{k_{i,xm}\eta_i}{k_i}\right\} \quad (i = 1, 3), \quad (2.23)$$

where $k_{1,y} = k_0 n_1 \sin \theta_{inc}$, and $K_y = |\mathbf{K}| \sin \phi$. Therefore, the diffraction efficiencies of the p -th forward-diffracted order (DE_p^f) and p -th backward-diffracted order (DE_p^b) can be defined as $DE_p^f = P_{3,p}^{TE/TM} / P_{inc}$ and $DE_p^b = P_{1,p}^{TE/TM} / P_{inc}$ respectively.

2.5 Summary and Discussion

In this chapter, the finite-difference frequency-domain (FDFD) method in conjunction with uniaxial perfectly matched layers (UPMLs) for the analysis of a finite grating illuminated by a finite beam has been described. In addition, the numerical considerations of the UPML and the mesh size for the FDFD method have been studied. For the performance of the UPML, the artificial reflection error from the UPML decreases as the conductivity of the UPML increases and finally reaches a saturation value with -90 dB . On the other hand, the numerical error decreases as the number of grid per wavelength increases (i.e. the mesh size decreases). The convergence of the TM polarization is slower than that of TE polarization because the Helmholtz equation of TM polarization contains one more derivative term (as seen in Eq. 2.5). In general, the numbers of grid per wavelength for both TE and TM polarization are $N_x, N_y \geq 20$ and $N_x, N_y \geq 25$ respectively. Finally, the Fast Fourier transform (FFT) is also applied to determine the diffracted power, and therefore, the diffraction efficiency.

CHAPTER 3

FINITE-NUMBER-OF-PERIODS

HOLOGRAPHIC GRATINGS

In many practical applications for high-data rate interconnections, the needed gratings could have finite sizes and are usually illuminated by finite-width beams. Therefore, in this chapter, the effects of finite-number-periods (FNP) gratings and finite-width beam simultaneously on the diffraction efficiencies of volume holographic gratings will be studied. For all the cases that are treated in this research normally incident beams of TE or TM polarization are considered [$\theta_{inc} = 0^\circ$ in Fig. 2.1 (b)]. The flat widths of incident beams [W , in Fig. 2.1(b)] are varied between $1\Lambda_y$ to $12\Lambda_y$ ($1\Lambda_y, 2\Lambda_y, 4\Lambda_y, 6\Lambda_y, 8\Lambda_y, 10\Lambda_y$, and $12\Lambda_y$) where $\Lambda_y = \Lambda/\sin\phi$ is the grating period along the y direction (see Fig. 2.1). The freespace wavelength of the incident beam is assumed to be $\lambda_0 = 1.0\ \mu m$. The refractive indices of the regions surrounding the grating are $n_1 = n_3 = 1.0$. In the grating region, the average dielectric constant is $\epsilon_0 = 2.25$ and the modulation is $\epsilon_1^c = 0.06$ [one cosine harmonic is assumed in Eq. (2.1)]. These grating parameters correspond to the DuPont OmniDex613 photopolymer [134]. FNP gratings with widths L of $20\Lambda_y, 15\Lambda_y, 10\Lambda_y, 5\Lambda_y$, and $3\Lambda_y$ are investigated in this chapter. In order to obtain the transmitted/reflected power, the total/scattered field on a specified x_i plane in region i ($i = 3, 1$) is calculated by using the FDFD method. Once the total/scattered field is determined, the transmission/reflection efficiency of a specific diffraction order can be calculated using the FFT (as shown in Section 2.4).

3.1 Unslanted Finite-Number-of-Periods Holographic Gratings

3.1.1 Forward Diffraction Efficiencies

For the case of unslanted FNP holographic gratings, the grating period is $\Lambda = 2.5 \mu m$ and the grating thickness is $d = 8.0 \mu m$. The period and slant angle of this grating are selected such that the diffraction efficiencies of the ± 1 diffracted orders are reasonable. Based on these parameters, five diffracted orders are expected and the forward diffraction efficiencies of the ± 1 diffracted orders are $DE_{\pm 1}^{TE} = 10.98\%$ and $DE_{\pm 1}^{TM} = 10.37\%$ for TE and TM polarizations respectively in the INP gratings. In Fig. 3.1, the diffraction efficiency of the ± 1 forward diffracted orders, $DE_{\pm 1}^f$, is plotted as a function of normalized beam width for different grating widths L ($L = 20\Lambda, 15\Lambda, 10\Lambda, 5\Lambda, 3\Lambda$) for both TE and TM polarizations (for the unslanted grating, $\Lambda_y = \Lambda$).

As shown in Fig. 3.1, for the grating with $L = 20\Lambda$, the $DE_{\pm 1}^f$ is close to the RCWA calculated efficiency and remains constant when the incident-beam width increases. In this case, the width of the incident beam is always smaller than the grating width and the resulting diffraction resembles the diffraction by an infinite-width grating. For this reason, the resulting diffraction efficiencies $DE_{\pm 1}^f$ are close to the values predicted by the RCWA. For the grating with width $L = 10\Lambda$, as the incident-beam width increases but remains smaller than the grating width, the $DE_{\pm 1}^f$ is the same as for the grating of $L = 20\Lambda$ case. However, as the incident-beam width becomes comparable or exceeds the grating width ($W > 6\Lambda$), the $DE_{\pm 1}^f$ starts to decrease, because more of the incident light initially falls outside the grating region. For the smaller grating with width $L = 3\Lambda$, the $DE_{\pm 1}^f$ decreases monotonically as the incident-beam width increases. Also the maximum value of the $DE_{\pm 1}^f$ for the FNP gratings never exceeds that of the corresponding INP gratings.

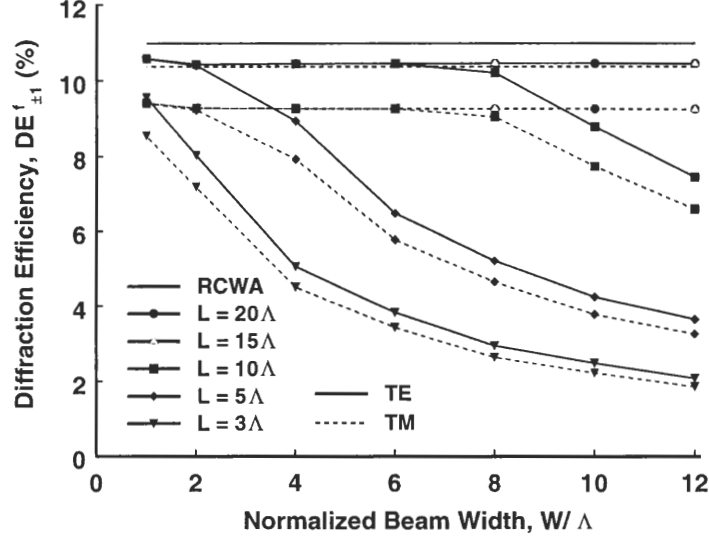


Figure 3.1: Forward diffraction efficiencies of the ± 1 diffracted orders as functions of W/Λ and L/Λ for an unslanted FNP holographic grating with $\Lambda = 2.5 \mu m$ and $d = 8 \mu m$. The solid lines and dash lines represent the results for TE polarization and TM polarization respectively. The RCWA results correspond to an infinite-number-of-periods grating illuminated by a plane wave (an infinite-width beam).

3.1.2 Electric Field Intensity

In order to gain a better physical understanding of the behavior of FNP gratings illuminated by finite-width beams, the resulting total electric or magnetic field intensity (calculated by the FDFD method) can be shown. For example, in Fig. 3.2, the electric field intensity is shown for an unslanted grating with $L = 10\Lambda$ illuminated by a TE-polarized beam with various widths ($W = 1\Lambda, 6\Lambda, 12\Lambda$). Dark areas indicate regions of small field intensity while lighter areas indicate regions of higher field intensity.

As seen in Fig. 3.2, most of the light is transmitted and the zero diffracted order is the primary order. By comparing Figs. 3.2(a), 3.2(b), and 3.2(c), it can be observed that there is more power diffracted in the directions of $+1$ and -1 diffracted orders for the smaller-width incident beam. The $+1$ and -1 diffracted orders are equal because

of the symmetry of the unslanted grating and the normal incidence. However, for the wider incident beam, as shown in Fig. 3.2(c), most of the power remains in the zero-order diffraction direction. Therefore, the $DE_{\pm 1}^f$ increases as the incident-beam width decreases in agreement with Fig. 3.1. This is not unexpected since the smaller-width beam contains a broader spectrum of spatial frequencies (wavevectors) than the wider beam does. Thus, more spatial frequencies in the narrow beam case are close to the Bragg condition resulting in more efficient diffraction along the ± 1 -order directions. On the other hand, the wider beam contains a much smaller range of spatial frequencies further from the Bragg condition, thus resulting in smaller $DE_{\pm 1}^f$ diffraction efficiencies.

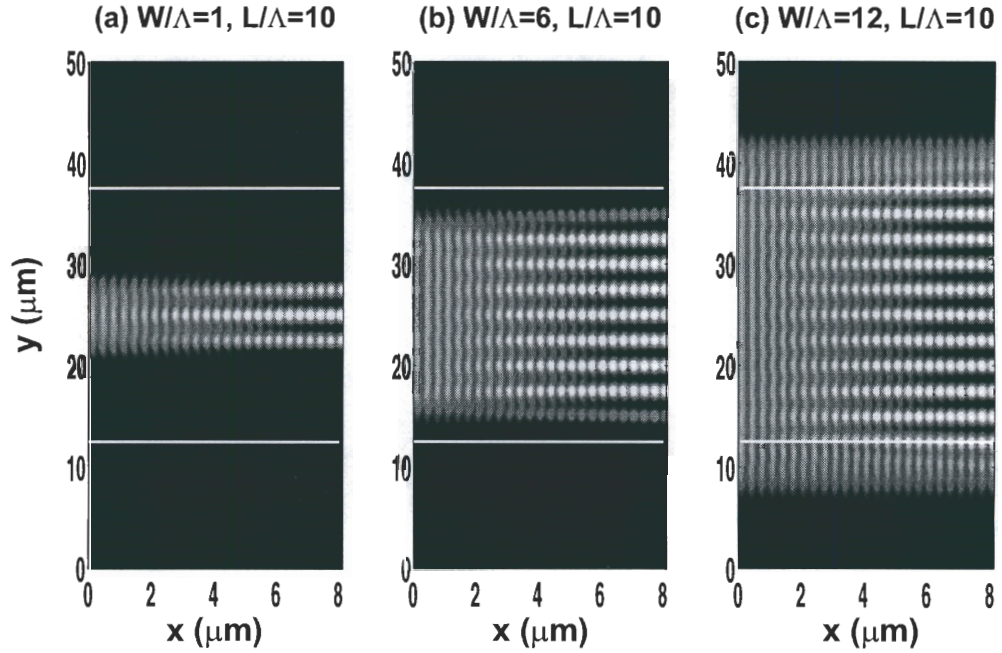


Figure 3.2: Two-dimensional diffracted field intensity patterns of unslanted FNP holographic gratings with $\Lambda = 2.5 \mu\text{m}$, $d = 8 \mu\text{m}$, and $L = 10\Lambda$ illuminated by a TE-polarized beam with (a) $W = \Lambda$, (b) $W = 6\Lambda$, and (c) $W = 12\Lambda$.

3.2 Slanted Finite-Number-of-Periods Holographic Transmission Gratings

3.2.1 Forward Diffraction Efficiencies

For the case of slanted FNP holographic transmission gratings, the grating period is assumed $\Lambda = 1.92 \mu m$, the slant angle is $\phi = 100^\circ$, and the thickness is $d = 20 \mu m$. Note that the period and the slant angle of this grating are designed such that the incident beam (if a plane wave) satisfies the first-order (for $i = -1$) Bragg condition. Based on this grating design, most of the power is transmitted into region 3.

In Fig. 3.3, the diffraction efficiency of the -1 forward diffracted order, DE_{-1}^f , is plotted as a function of the normalized beam width for various grating widths L ($L = 20\Lambda_y, 15\Lambda_y, 10\Lambda_y, 5\Lambda_y, 3\Lambda_y$). As shown in Fig. 3.3, for the wider (larger number of periods) grating with $L = 20\Lambda_y$, the DE_{-1}^f increases and approaches the RCWA calculated value as the incident-beam width increases. This trend is expected, because the wider the incident beam is the more resembles a plane wave behavior that satisfies the first-order Bragg condition. Narrower beams are more spread in wavevector space resulting in significant deviations from the Bragg condition and consequently less diffraction efficiency. For incident-beam widths greater than 10 grating periods ($W > 10\Lambda_y$), the diffraction efficiencies slowly converge to the values predicted by the RCWA.

For the grating with $L = 10\Lambda_y$, as the incident-beam width increases but remains smaller than the grating width, the DE_{-1}^f is almost the same as the one of the $L = 20\Lambda_y$ case. However, as the incident-beam width exceeds the grating width ($W > 6\Lambda_y$), the DE_{-1}^f starts to decrease, since more of the incident light initially falls outside the grating region and is not getting diffracted. Therefore, there exists a maximum diffraction efficiency in this case. The maximum values of DE_{-1}^f are 74.57% and 70.60% for TE and TM polarizations, respectively, for $W = 6\Lambda_y$. Similarly, a maximum diffraction efficiency can also be observed

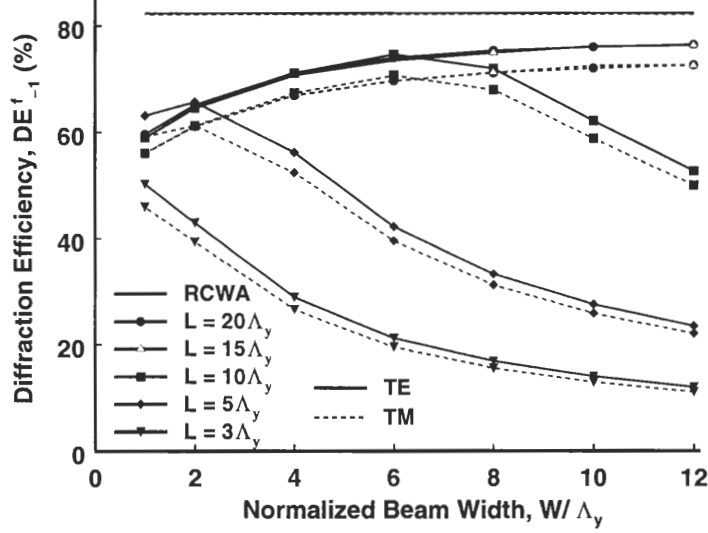


Figure 3.3: Forward diffraction efficiencies of the -1 diffracted order as functions of W/Λ_y and L/Λ_y for a slanted FNP holographic transmission grating with $\Lambda = 1.92 \mu m$, $\phi = 100^\circ$ and $d = 20 \mu m$. The solid lines and dash lines represent the results of TE polarization and TM polarization respectively. The RCWA results correspond to an infinite-number-of-periods grating illuminated by a plane wave (an infinite-width beam).

for the grating with $L = 5\Lambda_y$. By comparing with the $L = 10\Lambda_y$ case, the position of the maximum diffraction efficiency of the $L = 5\Lambda_y$ case is shifted towards the smaller incident beam, since for the smaller-width grating a smaller-width incident beam is needed to fill the grating region. In this case, the maximum values of DE_{-1}^f drop to 65.65% and 61.29% for TE and TM polarizations respectively. For the smaller grating width of $L = 3\Lambda_y$, the DE_{-1}^f is much smaller than the RCWA predicted value and decreases monotonically as the incident-beam width increases.

A rather interesting observation is the effect of the FNP grating as it is separated from the effect of the beam size. One might expect that for a given incident-beam width, the diffraction efficiency would always increase as the grating width increases. However, this is only correct for wide incident beams ($W > 8\Lambda_y$). In contrast, for narrow incident beams, the wider grating may have less diffraction efficiency than that of a less wide grating.

For example, as $W = \Lambda_y$, the diffraction efficiency of the $L = 20\Lambda_y$ case is less than that of $L = 5\Lambda_y$ case by $\sim 3.5\%$.

3.2.2 Electric Field Intensity

The electric field intensity for a slanted FNP holographic transmission grating with $L = 10\Lambda_y$ illuminated by a TE-polarized beam with various widths ($W = 1\Lambda_y, 6\Lambda_y, 12\Lambda_y$) is shown in Fig. 3.4. Dark areas indicate regions of small field intensity, and lighter areas indicate regions of higher field intensity. For the case of the slanted transmission grating, the -1 diffracted order is the primary order according to the Bragg condition.

As observed in Fig. 3.4(b), the incident beam fills almost completely the grating region. As a result the maximum DE_{-1}^f can be achieved. However, the narrower incident beam [shown in Fig. 3.4(a)] is more spread in wavevector space resulting in significant

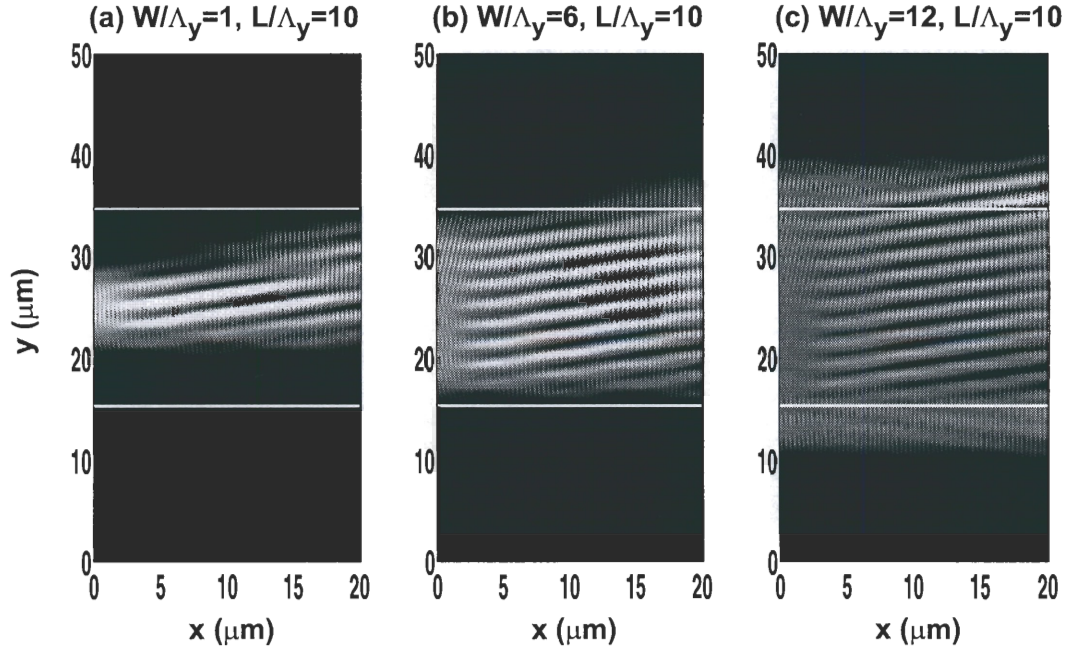


Figure 3.4: Two-dimensional diffracted field intensity patterns of slanted FNP holographic transmission gratings with $\Lambda = 1.92 \mu m$, $\phi = 100^\circ$, $d = 20 \mu m$, and $L = 10\Lambda_y$ illuminated by a TE-polarized beam with (a) $W = \Lambda_y$, (b) $W = 6\Lambda_y$, and (c) $W = 12\Lambda_y$.

deviations from the Bragg condition and consequently less diffraction efficiency. Therefore, the corresponding DE_{-1}^f decreases. On the other hand, for the wider incident beam [as shown in Fig. 3.4(c)], part of the incident light can not interact with the grating completely, thus the corresponding DE_{-1}^f decreases.

3.3 Slanted Finite-Number-of-Periods Holographic Reflection Gratings

3.3.1 Backward Diffraction Efficiencies

For the case of slanted FNP holographic reflection gratings, the grating period is $\Lambda = 0.34 \mu m$, the slant angle is $\phi = 170^\circ$, and the thickness is $d = 20 \mu m$. Note that the period and the slant angle of this grating are designed such that the incident beam satisfies the first-order (for $i = -1$) Bragg condition. Based on this grating design, the diffraction is primarily in the backward direction from the grating (reflection grating). In Fig. 3.5, the backward diffraction efficiency of the -1 diffracted order, DE_{-1}^b , is plotted as a function of the normalized beam width for various grating widths.

As shown in Fig. 3.5, for the wider grating with width $L = 20\Lambda_y$, the DE_{-1}^b increases and approaches the RCWA predicted value as the incident-beam width increases. The trend is expected and is similar to the case of transmission gratings. For the grating with $L = 10\Lambda_y$, as the incident-beam width increases but remains smaller than the grating width, the DE_{-1}^b increases slowly approaching the RCWA efficiency. However, as the incident-beam width exceeds the grating width ($W > 6\Lambda_y$), the DE_{-1}^b starts to decrease. Therefore, there exists a maximum backward diffraction efficiency in this case. The maximum values of DE_{-1}^b are 61.28% and 55.02% for TE and TM polarizations, respectively, for $W = 6\Lambda_y$. For the smaller grating of width $L = 3\Lambda_y$, the DE_{-1}^b is much smaller than the RCWA efficiency and decreases monotonically as the incident-beam width increases.

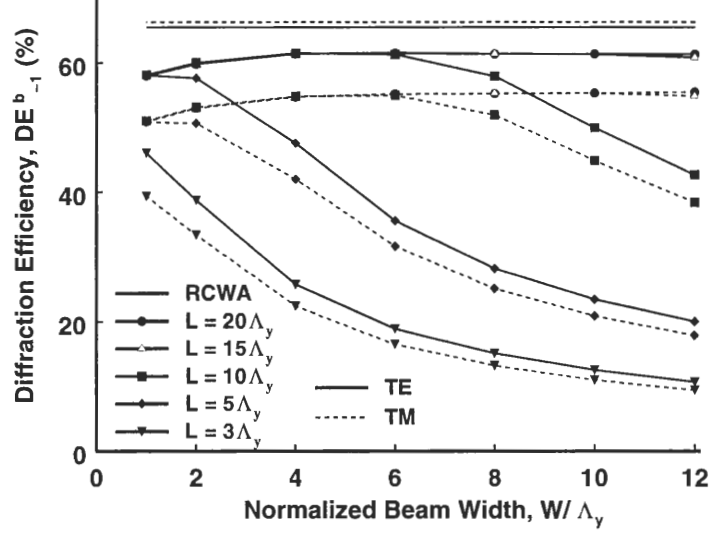


Figure 3.5: Backward diffraction efficiencies of the -1 diffracted order as functions of W/Λ_y and L/Λ_y for a slanted FNP holographic reflection grating with $\Lambda = 0.34 \mu m$, $\phi = 170^\circ$ and $d = 20 \mu m$. The solid lines and dash lines represent the results of TE polarization and TM polarization respectively. The RCWA results correspond to an infinite-number-of-periods grating illuminated by a plane wave (an infinite-width beam).

3.3.2 Electric Field Intensity

The electric field intensity for a slanted FNP holographic reflection grating with $L = 10\Lambda_y$ illuminated by a TE-polarized beam with various widths ($W = 1\Lambda_y, 6\Lambda_y, 12\Lambda_y$) is shown in Fig. 3.6. Dark areas indicate regions of small field intensity, and lighter areas indicate regions of higher field intensity.

As seen in Fig. 3.6(b), the incident beam fills almost completely the grating region resulting in the maximum DE_{-1}^b . However, the smaller incident beam [as shown in Fig. 3.6(a)] is more spread in wavevector space resulting in significant deviations from the Bragg condition and consequently less diffraction efficiency. Therefore, the DE_{-1}^b decreases. On the other hand, for the wider incident beam [as shown in Fig. 3.6(c)], some of the incident light initially falls outside the grating region resulting in less interaction with the

grating, thus the corresponding DE_{-1}^b decreases.

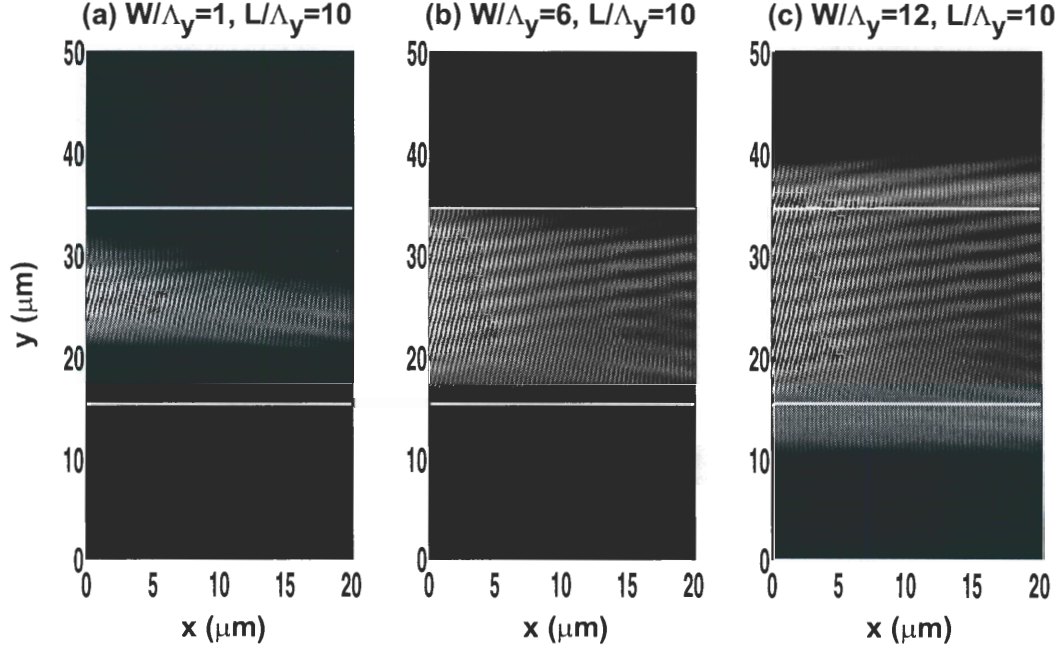


Figure 3.6: Two-dimensional diffracted field intensity patterns of slanted FNP holographic reflection gratings with $\Lambda = 0.34 \mu\text{m}$, $\phi = 170^\circ$, $d = 20 \mu\text{m}$, and $L = 10\Lambda_y$ illuminated by a TE-polarized beam with (a) $W = \Lambda_y$, (b) $W = 6\Lambda_y$, and (c) $W = 12\Lambda_y$.

3.4 Comparison of Finite-Number-of-Periods Holographic to Finite-Number-of-Periods Surface-Relief Gratings

In this section the effects of the FNP holographic gratings on their diffraction performance are compared to those of FNP surface-relief gratings. In order to accomplish this comparison the accuracy of the RCWA (which is valid for INP gratings) was examined in the cases of FNP holographic and FNP surface-relief gratings. The error of the RCWA for FNP gratings in the i -th forward- or backward-diffracted order efficiency can be defined (in percent) as

$$\text{Error} = \frac{DE_i^{u,RCWA} - DE_i^{u,FNP}}{DE_i^{u,FNP}} \times 100, \quad (3.1)$$

where $DE_i^{u,RCWA}$ and $DE_i^{u,FNP}$ are the diffraction efficiencies of INP gratings (calculated by the RCWA) and FNP gratings, respectively, for the i -th forward- or backward-diffracted order ($u = f$ for forward- and $u = b$ for backward-diffracted orders). The diffraction efficiencies of FNP surface-relief gratings and FNP holographic gratings are determined by using the boundary element method [63] and the FDFD method respectively. The results are summarized in Tables 3.1 and 3.2. For all cases, the freespace wavelength of the incident beam is $\lambda_0 = 1.0 \mu m$ and the widths of FNP gratings (L) are equal to the incident-beam parameter D . The groove depth of the surface-relief gratings and the thickness of the holographic gratings are designed to obtain the maximum diffraction efficiency. Furthermore, the average dielectric constant of the FNP holographic gratings and the dielectric constant of the substrate and ridges of FNP surface-relief gratings are equal to 2.25.

For unslanted gratings, the comparison of the accuracy of the RCWA for 2-level (rectangular-groove) FNP surface-relief gratings [63] and FNP holographic gratings [55] is shown in Table 3.1. For the case of TE polarization, the error of the RCWA for FNP

Table 3.1: Comparison of the accuracy of the RCWA for 2-level FNP surface-relief gratings and unslanted FNP holographic gratings

TE Polarization						
2-level FNP Surface-Relief Grating [63]				Unslanted FNP Holographic Grating [55]		
$\Lambda = 0.94 \mu m, d = 0.63 \mu m$				$\Lambda = 2.5 \mu m, d = 8.0 \mu m$		
$L(= D)$	$DE_{\pm 1}^{J,FNP}$	$DE_{\pm 1}^{J,RCWA}$	Error (%)	$DE_{\pm 1}^{J,FNP}$	$DE_{\pm 1}^{J,RCWA}$	Error (%)
5Λ	0.25750	0.37033	43.82	0.09669	0.10983	13.60
10Λ	0.30012	0.37033	23.39	0.10212	0.10983	7.55
15Λ	0.33022	0.37033	12.15	0.10430	0.10983	5.30
TM Polarization						
2-level FNP Surface-Relief Grating [63]				Unslanted FNP Holographic Grating [55]		
$\Lambda = 0.94 \mu m, d = 1.09 \mu m$				$\Lambda = 2.5 \mu m, d = 8.0 \mu m$		
$L(= D)$	$DE_{\pm 1}^{J,FNP}$	$DE_{\pm 1}^{J,RCWA}$	Error (%)	$DE_{\pm 1}^{J,FNP}$	$DE_{\pm 1}^{J,RCWA}$	Error (%)
5Λ	0.13736	0.16538	20.40	0.08578	0.10370	20.89
10Λ	0.14945	0.16538	10.66	0.09051	0.10370	14.58
15Λ	0.15714	0.16538	5.24	0.09255	0.10370	12.04

Table 3.2: Comparison of the accuracy of the RCWA for 8-level FNP surface-relief gratings and slanted FNP holographic transmission gratings

TE Polarization						
8-level FNP Surface-Relief Grating [63]			Slanted FNP Holographic Grating [55]			
$\Lambda_y = 0.94 \mu m, d = 1.1 \mu m$			$\Lambda_y = 1.95 \mu m, d = 20.0 \mu m$			
$L(= D)$	$DE_{-1}^{J,FNP}$	$DE_{-1}^{J,RCWA}$	Error (%)	$DE_{-1}^{J,FNP}$	$DE_{-1}^{J,RCWA}$	Error (%)
$5\Lambda_y$	0.46150	0.61540	33.35	0.63777	0.82310	29.06
$10\Lambda_y$	0.54949	0.61540	11.99	0.72707	0.82310	13.21
$15\Lambda_y$	0.57140	0.61540	7.70	0.76244	0.82310	7.96
TM Polarization						
8-level FNP Surface-Relief Grating [63]			Slanted FNP Holographic Grating [55]			
$\Lambda_y = 0.94 \mu m, d = 1.43 \mu m$			$\Lambda_y = 1.95 \mu m, d = 20.0 \mu m$			
$L(= D)$	$DE_{-1}^{J,FNP}$	$DE_{-1}^{J,RCWA}$	Error (%)	$DE_{-1}^{J,FNP}$	$DE_{-1}^{J,RCWA}$	Error (%)
$5\Lambda_y$	0.27692	0.30769	11.11	0.59534	0.82176	38.03
$10\Lambda_y$	0.28681	0.30769	7.28	0.68738	0.82176	19.55
$15\Lambda_y$	0.29670	0.30769	3.70	0.72549	0.82176	13.27

surface-relief gratings is larger than that for FNP holographic gratings. However, for the case of TM polarization, the error of the RCWA for FNP holographic gratings is larger than that for FNP surface-relief gratings. On the other hand, for slanted gratings, the comparison of the accuracy of the RCWA for 8-level (stair-step approximation of a blazed grating) FNP surface-relief gratings [63] and FNP holographic transmission gratings [55] is shown in Table 3.2. For the case of TE polarization, the error of the RCWA for FNP surface-relief gratings is almost the same as that for FNP holographic gratings. However, for the case of TM polarization, the error of the RCWA for FNP holographic gratings is larger than that for FNP surface-relief gratings. In general, the errors of the RCWA decrease as the grating width and the incident-beam width increase. Therefore, it can be concluded that the effects of the FNP on the diffraction efficiencies are important for both surface-relief and holographic gratings and which one is more severe depends on the actual gratings and the incident polarizations.

3.5 Summary and Discussion

In this chapter, the effects of the finite number of periods and the finite width of the incident beam on the diffraction performance of holographic gratings have been investigated for TE and TM incident polarizations by using the FDFD rigorous electromagnetic method. Both unslanted and slanted gratings in transmission and reflection configurations are examined. The diffraction efficiencies of various diffracted orders are used as the metric of each grating performance. These diffraction efficiencies are also compared to the ones predicted by the RCWA that is applicable to infinite-number-of-periods (INP) gratings and infinite-width incident beams (plane waves). The preceding numerical analysis of holographic gratings has shown that the finite number of periods and the finite-width beam can play an important role in the characteristics of diffraction efficiencies. For all the holographic grating cases treated, the maximum diffraction efficiencies for the FNP gratings never exceeds that of the corresponding INP gratings.

For unslanted gratings with at least 20 grating periods, the diffraction efficiencies are close to the ones predicted by the RCWA and remain constant as the incident-beam width increases (as far as its width remains within the grating $W \leq L$). However, as the number of periods decreases, the diffraction efficiency also decreases for a constant beam width. On the other hand, for slanted transmission/reflection gratings with at least 20 grating periods, the diffraction efficiencies approach the efficiencies predicted by the RCWA as the incident-beam width increases. However, as the incident-beam widths increase greater than ~ 10 grating periods ($W > 10\Lambda_y$), the diffraction efficiencies slowly converge to the values predicted by the RCWA. In general, as the number of periods decreases, the diffraction efficiency also decreases for a constant beam width.

On the comparison of the accuracy of the RCWA for FNP surface-relief gratings and FNP holographic gratings, the errors of the RCWA decrease as the grating width and the incident-beam width increase. In general, the errors of the RCWA for FNP holographic

gratings and FNP surface-relief gratings are of the same order revealing that the effects of the FNP on the diffraction performance are equally important but are also case and polarization dependent.

Finally, it is worth mentioning that in principle the presented methodology of solving the Helmholtz equation using the FDFD method can be used in more general diffraction problems. For example instead of FNP holographic gratings, just as easily, surface-relief FNP gratings of any shape could be analyzed (while the boundary element method cannot be applied to holographic gratings). Even multiplexed FNP holographic gratings for applications in optical memories and optical computing can be similarly studied. The same approach can also be used in integrated optics configurations to analyze a broad range of grating couplers. A study of finite-size holographic grating couplers for applications in integrated optics and optical interconnects will be presented in the following chapters. In addition, even if only a flat-cosine incident beam profile has been used in this work any profile that can be described by the function $g(y')$ of Eq. (2.3) could be as easily analyzed. In the case of a guided wave application, $g(y')$ represents the incident guide mode on the grating coupler.

CHAPTER 4

DYNAMICS OF HOLOGRAPHIC GRATING FORMATIONS IN PHOTOPOLYMERS

In order to study the dynamic characteristics of holographic grating formation in photopolymers, the real-time diffraction-monitoring technique [70, 75, 76] in conjunction with Kogelnik's first-order two-wave coupled-wave theory [86] has been applied to study experimentally the temporal properties such as diffraction efficiencies and refractive-index modulations of unslanted holographic grating formations in DuPont photopolymers with respect to exposure irradiance, exposure time, and processing situations. However, Kogelnik's theory [86] does not provide an accurate estimation of refractive-index modulation in this diffraction case because the average refractive index in the grating is not equal to those in the input and output regions. On the other hand, a one-dimensional local-response diffusion model [77, 78] was proposed by Zhao and Mouroulis in 1994 to study theoretically the dynamic properties of unslanted holographic grating formations in photopolymers. However, this local diffusion model [77, 78, 80] only provides a good explanation of low-spatial-frequency grating formations in photopolymers. Recently, a nonlocal-response diffusion model was proposed by Sheridan *et al.* [81–85] by introducing a nonlocal variance parameter, σ , into the local-response diffusion model [77, 78] to model the effect of the formation of polymer chains growing away from their initiation locations and was solved by use of low-harmonic-component approximation. This nonlocal diffusion model can predict the existence of a high-frequency cutoff in the spatial-frequency response, while the local diffusion model cannot predict it

correctly. Although the low-harmonic-component approximation has been applied to solve the nonlocal diffusion equation, it does not precisely predict the polymer concentration for the smaller dimensionless reaction rate [84]. Moreover, both the local and nonlocal diffusion models were only used for the theoretical study of the dynamics of unslanted holographic gratings during recording. However, for practical applications, such as grating couplers for optical interconnects [22, 66], the gratings are slanted. Therefore, both the experimental measurement and the theoretical analysis for studying the dynamics of unslanted or slanted gratings during holographic recording are needed.

Furthermore, in order to enhance the refractive-index modulation and thus the diffraction efficiency, the post-baking processing [67, 123] was also applied in the grating fabrication to improve the diffraction efficiency. However, both holographic recording [70, 75, 124–129] and post-baking processing [123, 130–132] introduce a shrinkage or expansion and a change of refractive index of the recording material. According to Kogelnik’s first-order two-wave coupled-wave theory [86], both effects can change the angular selectivity of a volume holographic grating (i.e. the shift of Bragg angle), especially for a slanted holographic grating. However, there has been no complete discussion for the effects of various baking conditions on diffraction efficiencies as well as on photopolymer shrinkage (or expansions) for both unslanted and slanted holographic gratings.

For these reasons, the real-time diffraction-monitoring technique in conjunction with the RCWA [133, 134] instead of Kogelnik’s theory is applied to study experimentally the dynamic behaviors of both unslanted and slanted grating formations based on DuPont OmniDex613 photopolymers (recorded by UV light with free-space wavelength 363.8 nm). On the other hand, the finite-difference time-domain (FDTD) method [133, 134] is applied to solve rigorously the nonlocal diffusion equation for both unslanted and slanted gratings. Furthermore, in order to estimate the shrinkage of a photopolymer after recording, the angular-dependent diffraction efficiency of a slanted grating is measured, and the corresponding angular-selective-curve is fitted by the RCWA in conjunction with Fresnel reflec-

tion losses instead of Bragg condition. Moreover, the effects of postprocessing including the baking time and the baking temperature on the refractive-index modulations and the shifts of Bragg angles of slanted holographic gratings (recorded by different exposure intensities) are also investigated systematically in this research.

4.1 Theoretical Model of Holographic Grating Formations in Photopolymers

4.1.1 Nonlocal Diffusion Model

The one-dimensional nonlocal diffusion equation describing the free-monomer diffusion and the free-monomer depletion during exposure can be written as [81–85]

$$\frac{\partial \Phi_m(x, t)}{\partial t} = \frac{\partial}{\partial x} \left\{ D(x, t) \frac{\partial \Phi_m(x, t)}{\partial x} \right\} - \int_{-\infty}^{\infty} G(x, x') F(x') \Phi_m(x', t) dx', \quad (4.1)$$

where $\Phi_m(x, t)$ is the free-monomer concentration, $D(x, t)$ is the diffusion coefficient, $F(x)$ is the polymerization rate, and $G(x, x')$ is the nonlocal response function representing the effect of the monomer concentration at location x' on the amount of monomer being polymerized at location x . The general relationship between the polymerization rate and the recording irradiance [78] and the diffusion coefficient exponential decrease with polymerization rate [77, 78] are expressed as follows,

$$F(x) = \kappa I_0^\nu [1 + V \cos(Kx)]^\nu, \quad (4.2)$$

and

$$D(x, t) = D_0 \exp[-\alpha F(x)t], \quad (4.3)$$

where κ is a proportionality coefficient, ν is the exponent of the relation between the polymerization rate and the exposure irradiance, I_0 is the mean irradiance on the photopolymer film, V is the fringe visibility, $K = 2\pi/\Lambda$ is the grating vector (Λ is the grating period), D_0 represents the initial diffusion coefficient, and α is the diffusion coefficient decay parameter.

In addition, a Gaussian probability distribution function is chosen as the nonlocal response function; thus, $G(x, x')$ can be expressed as [81–85]

$$G(x, x') = \frac{1}{\sqrt{2\pi}\sigma} \exp \left[-\frac{(x - x')^2}{2\sigma} \right], \quad (4.4)$$

where $\sqrt{\sigma}$ represents the nonlocal response length. After exposure time t (in seconds), the concentration $\Phi_p(x, t)$ of the polymerized monomer (polymer) at location x is given by [81]

$$\Phi_p(x, t) = \int_0^t \int_{-\infty}^{\infty} G(x, x') F(x') \Phi_m(x', t') dx' dt'. \quad (4.5)$$

In order to convert the nonlocal diffusion equation to its dimensionless form, four dimensionless variables (a reaction rate R_D , a nonlocal variance parameter σ_D , a time variable t_D , and a space variable x_D) are defined as [133, 134]

$$R_D = D_0 K^2 / \kappa I_0^\nu, \quad (4.6)$$

$$\sigma_D = \sigma K^2, \quad (4.7)$$

$$t_D = \kappa I_0^\nu t, \quad (4.8)$$

$$x_D = Kx. \quad (4.9)$$

Substituting these four dimensionless variables into Eqs. (4.1) and (4.5), the governing equations for the concentration of free monomer and polymer can be written in the dimensionless forms as

$$\begin{aligned} \frac{\partial \Phi_m(x_D, t_D)}{\partial t_D} &= R_D \frac{\partial}{\partial x_D} \left\{ D_D(x_D, t_D) \frac{\partial \Phi_m(x_D, t_D)}{\partial x_D} \right\} \\ &\quad - \int_{-\infty}^{\infty} G_D(x_D, x'_D) F_D(x'_D) \Phi_m(x'_D, t_D) dx'_D, \end{aligned} \quad (4.10)$$

and

$$\Phi_p(x_D, t_D) = \int_0^{t_D} \int_{-\infty}^{\infty} G_D(x_D, x'_D) F_D(x'_D) \Phi_m(x'_D, t'_D) dx'_D dt'_D, \quad (4.11)$$

where

$$F_D(x_D) = [1 + V \cos(x_D)]^\nu, \quad (4.12)$$

$$D_D(x_D, t_D) = \exp[-\alpha F_D(x_D) t_D], \quad (4.13)$$

$$G_D(x_D, x'_D) = \frac{1}{\sqrt{2\pi\sigma_D}} \exp \left[-\frac{(x_D - x'_D)^2}{2\sigma_D} \right]. \quad (4.14)$$

In general, the induced-during-the-recording-process refractive index depends not only on the polymer concentration (corresponding to saturation characteristics of the measured diffraction efficiencies) but also on the monomer concentration (corresponding to initial fast-rising peak of the measured diffraction efficiencies) [73, 75]. Therefore, the induced refractive index, $n(x_D, t_D)$, during exposure process can be expressed as [73]

$$n(x_D, t_D) = C_p \Phi_p(x_D, t_D) + C_m \Phi_m(x_D, t_D) \cos \phi', \quad (4.15)$$

where C_p and C_m are proportionality constants, and ϕ' is the relative phase difference between the monomer phase grating and the polymer phase grating.

4.1.2 Finite-Difference Time-Domain Method

In order to solve rigorously the free-monomer concentration and the polymer concentration [as shown in Eqs. (4.10) and (4.11)] during hologram recording, the finite-difference approximations are applied on the dimensionless-space domain and on the dimensionless-time domain to discretize the diffusion equation. First, assuming the increments in the dimensionless-space domain and in the dimensionless-time domain are Δx_D and Δt_D respectively, and then substituting them into Eq. (4.10), the free-monomer concentration at the i -th dimensionless-space point and at the j -th dimensionless-time step can be written as

$$\begin{aligned} \Phi_m(i, j) \cong & \left\{ 1 - 2C_2(i, j-1) \frac{\Delta t_D}{\Delta x_D^2} \right\} \Phi_m(i, j-1) \\ & + \left\{ C_2(i, j-1) \frac{\Delta t_D}{\Delta x_D^2} + C_1(i, j-1) \frac{\Delta t_D}{2\Delta x_D} \right\} \Phi_m(i+1, j-1) \\ & + \left\{ C_2(i, j-1) \frac{\Delta t_D}{\Delta x_D^2} - C_1(i, j-1) \frac{\Delta t_D}{2\Delta x_D} \right\} \Phi_m(i-1, j-1) \\ & - \Delta t_D C_3(i, j-1), \end{aligned} \quad (4.16)$$

where

$$C_1(i, j-1) = R_D \frac{\partial D_D(x_{D,i}, t_{D,j-1})}{\partial x_D}, \quad (4.17)$$

$$C_2(i, j-1) = R_D D_D(x_{D,i}, t_{D,j-1}), \quad (4.18)$$

$$C_3(i, j-1) \cong \frac{\Delta x_D}{2} \left\{ f_D(1, j-1) + 2 \sum_{k=2}^{N-1} f_D(k, j-1) + f_D(N, j-1) \right\}, \quad (4.19)$$

$$f_D(k, j-1) = G_D(x_{D,i}, x_{D,k}) F(x_{D,k}) \Phi_m(x_{D,k}, t_{D,j-1}), \quad (4.20)$$

N is number of sampling points in the dimensionless-space domain, $\Delta x_D = \frac{2\pi}{N-1}$, $x_{D,i} = -\pi + (i-1)\Delta x_D$, and $t_{D,j} = j\Delta t_D$. Similarly, the polymer concentration at the i -th dimensionless-space point and at the j -th dimensionless-time step can be represented as

$$\Phi_p(i, j) \cong \frac{\Delta t_D}{2} \left\{ C_3(i, 0) + 2 \sum_{k=1}^{j-1} C_3(i, k) + C_3(i, j) \right\}. \quad (4.21)$$

In this research, the number of sampling points in the dimensionless-space domain is chosen as $N = 200$. It is worth mentioning that the effect of the number of sampling points on the numerical accuracy of the FDTD method has been tested by using four different values of N ($N = 50, 100, 200$, and 300) to solve Eqs. (4.10) and (4.11) for $R_D = 1.0$, $\sigma_D = 0$, $\nu = 0.5$, and $\alpha = 0.0$. With respect to the case of $N = 300$ the differences of the saturation values of the first harmonic of the polymer concentrations are 0.24%, 0.05%, and 0.03% for $N = 50, 100$, and 200 respectively. Furthermore, as is well known for the numerical stability of the FDTD method, the increment in the dimensionless-time domain, Δt_D , must satisfy the stability criterion [135]

$$\Delta t_D \leq \frac{1}{2} \frac{\Delta x_D^2}{R_D}. \quad (4.22)$$

In this paper, $\Delta t_D = 0.4 \frac{\Delta x_D^2}{R_D}$ is used for all calculations.

Using the above procedure, the spatially nonuniform profile of the molecule concentration Φ_u ($u = m$ for the monomer concentration and $u = p$ for the polymer concentration) can be determined at any dimensionless-time t_D . However, to fit the theoretical results to the experimental data, it is useful to calculate the spatial-harmonic components of monomer/polymer concentrations. By applying the Discrete Fourier transform, the q -th

spatial-harmonic component of the monomer/polymer concentration at any dimensionless-time t_D , $\Phi_{u,q}(t_D)$, can be expressed as

$$\Phi_{u,q}(t_D) = \frac{1}{N-1} \sum_{i=1}^{N-1} \Phi_u(x_{D,i}, t_D) \cos(q x_{D,i}) \quad (u = m, p). \quad (4.23)$$

4.2 Theoretical Results of Holographic Grating Formations in Photopolymers

To illustrate the dynamics of holographic grating formation and compare the present method to the low-harmonic-component approximation model, Eqs. (4.10) and (4.11) are solved by the FDTD method with the initial condition $\Phi_m(x_D, 0) = 100 \text{ mole/cm}^3$, which is selected to be consistent with Sheridan and Lawrence's assumption [81]. The fringe visibility is assumed to be $V = 1.0$. Following the derivation done by Kown *et al.* [73] the polymerization rate is proportional to the square root of the exposure irradiance, so $\nu = 0.5$ is applied for all cases in this research. In addition, since changing α is equivalent to varying R_D [77, 78, 84], $\alpha = 0.0$ (which is equivalent of assuming that the diffusion coefficient is a constant $D = D_0$ during exposure) is used for all calculations.

4.2.1 Effects of Dimensionless Variables on Holographic Grating Formations

Figure 4.1 shows the monomer-concentration and the polymer-concentration profiles (within one grating period) at various dimensionless times with $R_D = 1.0$ for three different dimensionless-nonlocal variance parameters σ_D ($\sigma_D = 0.0, 0.62, 1.23$) [81]. As shown in Fig. 4.1(a), with continuous exposure, free monomers are depleted in the bright region resulting in a minimum concentration at $x/\Lambda = 0.0$. As free monomers are completely consumed for $t_D \geq 10$, the holographic grating formation reaches steady state because no free monomer remains in the system. With the diffusion and the polymerization of free monomers, the spatially nonuniform profiles of polymer concentrations [as shown in

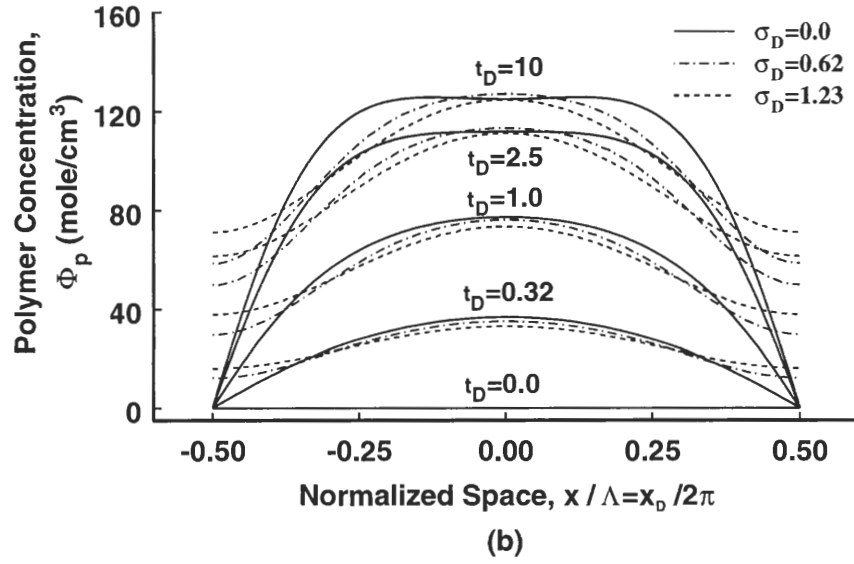
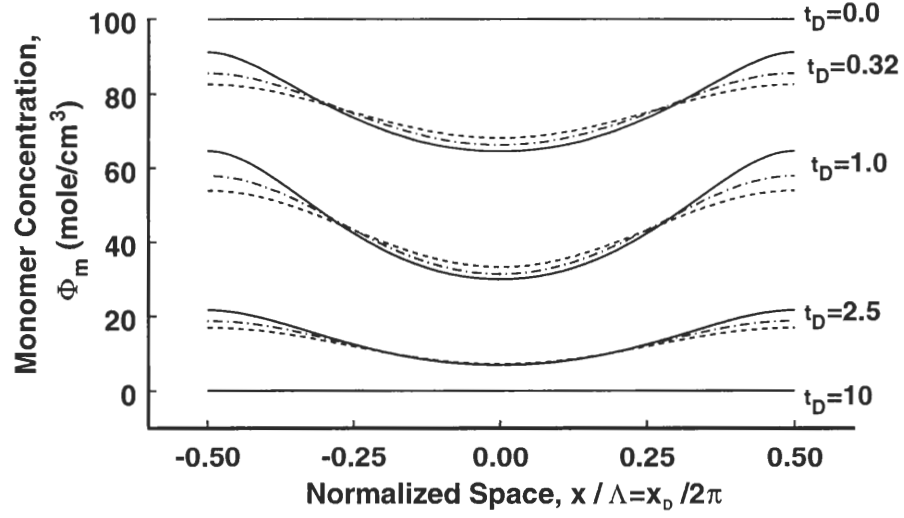


Figure 4.1: Profiles of (a) the monomer concentration Φ_m , and (b) the polymer concentration Φ_p within one grating period at various dimensionless times t_D for different dimensionless nonlocal variance parameters σ_D ($\sigma_D = 0.0, 0.62, 1.23$) with $R_D = 1.0$, $\alpha = 0.0$, and $\nu = 0.5$.

Fig. 4.1(b)] are developed. As seen in Fig. 4.1(b), for larger σ_D the polymer-concentration profiles resemble sinusoidal variations but have lower profile visibility.

By applying the Discrete Fourier transform the corresponding harmonics of the polymer concentration at various t_D [Fig. 4.1(b)] are plotted in Fig. 4.2. As shown in Fig. 4.2, as t_D increases, the amplitudes of harmonic components of the polymer concentration increase and finally reach the saturation values. Moreover, increasing σ_D (more nonlocal effect) the saturation value of the first harmonic and the amplitudes of higher harmonics of the polymer concentration decrease. Since the decreasing rate of the amplitude of higher harmonic is larger than that of the first harmonic, the larger σ_D is, the more the polymer profile resembles a sinusoidal polymer profile [that is in agreement with Fig. 4.1(b)]. In the other words, the error of the low-harmonic-component approximation decreases as σ_D increases.

In order to study the effect of dimensionless reaction rates R_D on the hologram

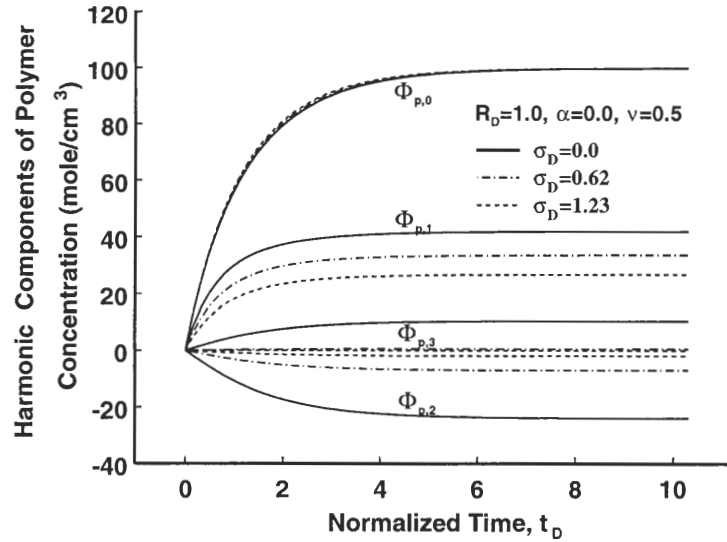


Figure 4.2: Harmonic components of polymer concentrations corresponding to Fig. 4.1(b) at various dimensionless times t_D for differing dimensionless nonlocal variance parameters σ_D ($\sigma_D = 0.0, 0.62, 1.23$) with $R_D = 1.0$, $\alpha = 0.0$, and $\nu = 0.5$. $\Phi_{p,q}$ represents the q -th harmonic of the polymer-concentration profile.

recording, the profiles of polymer concentrations at $t_D = 10$ (at the steady state) with various R_D ($R_D = 0.05, 0.1, 1.0, 10.0, 50.0$) are summarized in Fig. 4.3. For the higher dimensionless reaction rate ($R_D > 1.0$), the diffusion coefficient is higher than the polymerization rate, so the free monomer has enough time to diffuse from the dark region to the bright region before the polymerized reaction occurs. Thus, the maximum value of the polymer concentration occurs at $x/\Lambda = 0.0$. In contrast, for the smaller dimensionless reaction rate ($R_D < 1.0$), the polymerization occurs faster than diffusion and, consequently, results in two peaks of the polymer concentration near the dark regions. As seen in Fig. 4.3, the higher R_D corresponds to a more sinusoidal polymer profile. Therefore, higher R_D also implies more accuracy for the low-harmonic-component approximation.

Figure 4.4 shows the saturation values of harmonic components of polymer concentrations as a function of R_D (in log scale) for various σ_D ($\sigma_D = 0.0, 0.62, 1.23, 1.85$). As

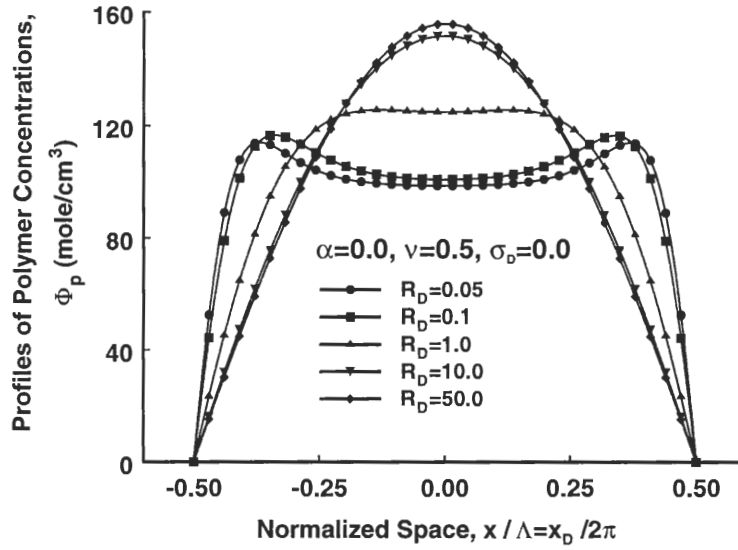


Figure 4.3: Polymer-concentration profiles Φ_p at the steady state for various values of R_D ($R_D = 0.05, 0.1, 1.0, 10.0, 50.0$) with $\alpha = 0.0$, $\nu = 0.5$, and $\sigma_D = 0.0$. The higher value of R_D corresponds to smaller grating period, higher diffusion coefficient, or lower exposure irradiance (lower polymerization rate).

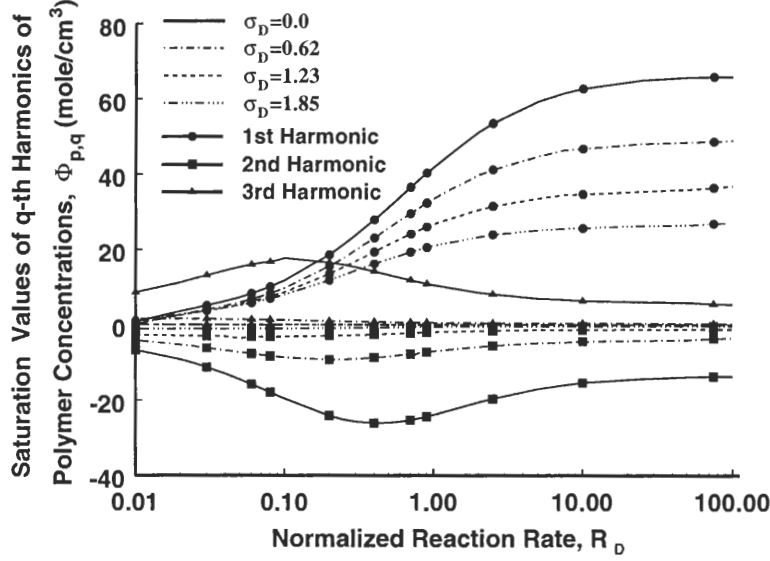


Figure 4.4: Saturation values of the first three harmonics of polymer concentrations as a function of R_D (in log scale) for various values of σ_D ($\sigma_D = 0.0, 0.62, 1.23, 1.85$).

seen in Fig. 4.4, for higher R_D ($R_D > 10.0$), the harmonic-component saturation values are independent of R_D . In this region, the amplitudes of the first-harmonic-component saturation values are much larger than those of higher-harmonic-component saturation values, so the recording profiles resemble sinusoidal ones. Therefore, the low-harmonic-component approximation provides an accurate analysis for larger R_D ($R_D > 10.0$). However, for smaller R_D ($R_D < 1.0$), the amplitudes of higher-harmonic-component saturation values become comparable to those of first-harmonic-component saturation values, so the more non-sinusoidal profiles are developed in this region. As a result, the low-harmonic-component approximation is not a very precise method to analyze the hologram recording for small R_D ($R_D < 1.0$).

To determine how good a sinusoidal profile is developed after exposure, the nonlinearity parameter of the q -th harmonic of the polymer concentration at the steady state $\chi_{p,q}^s$

($q > 1$) can be defined as

$$\chi_{p,q}^s = \frac{|\Phi_{p,q}^s|}{|\Phi_{p,1}^s|} \quad (q > 1), \quad (4.24)$$

where $|\Phi_{p,q}^s|$ and $|\Phi_{p,1}^s|$ are the amplitudes of the q -th ($q > 1$) harmonic and the first harmonic of the polymer concentration (at the steady state) respectively. As shown in Fig. 4.5, for larger R_D ($R_D > 10.0$), both $\chi_{p,2}^s$ and $\chi_{p,3}^s$ are less than 1.0 for all range of σ_D ; thus, the polymer-concentration profile resembles a sinusoidal one. However, for smaller R_D ($R_D < 0.1$), the polymer-concentration profile has larger nonlinearity resulting in a profile differing more from a sinusoidal one.

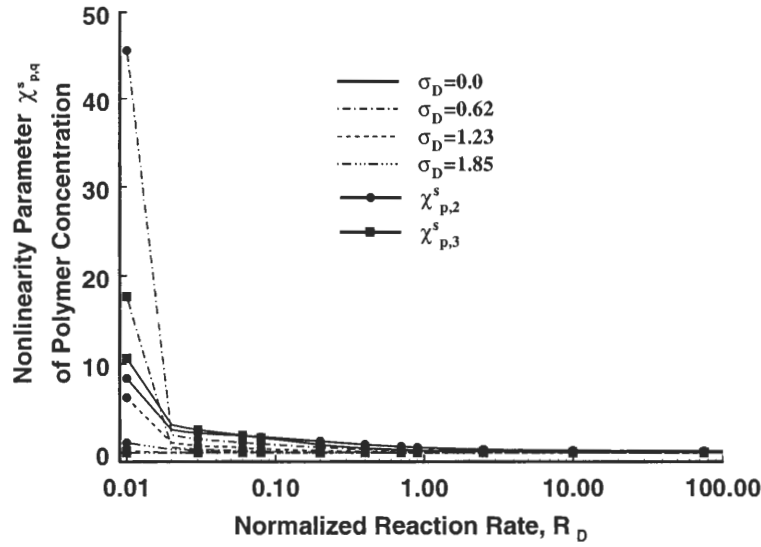


Figure 4.5: Nonlinearity of polymer concentration at the steady state as a function of R_D (in log scale) for various values of σ_D ($\sigma_D = 0.0, 0.62, 1.23, 1.85$). $\chi_{p,q}^s$ represents the nonlinearity of the q -th harmonic of the polymer concentration at steady state.

4.2.2 Comparison of the Finite-Difference Time-Domain Method and the Low-Harmonic-Component Approximation

As described in the previous section, the accuracy of the low-harmonic-component approximation has been studied qualitatively with respect to the dimensionless reaction rates R_D ,

dimensionless-nonlocal variance parameters σ_D , and nonlinearities of polymer-concentration profiles. In order to quantify the accuracy of the low-harmonic-component approximation, the error of the first-harmonic saturation value of the polymer concentration calculated using the low-harmonic-component approximation can be defined (in percent) as

$$\text{Error} = \frac{|\Phi_{p,1}^{s,FDTD} - \Phi_{p,1}^{s,LHC}|}{\Phi_{p,1}^{s,FDTD}} \times 100, \quad (4.25)$$

where $\Phi_{p,1}^{s,FDTD}$ and $\Phi_{p,1}^{s,LHC}$ are the first-harmonic-component saturation values of polymer concentrations calculated by the FDTD method and by the four-harmonic-component approximation [84], respectively. In Fig. 4.6, the error of the first-harmonic components calculated by the four-harmonic-component approximation [84] is plotted as a function of R_D (in log scale) for different σ_D values ($\sigma_D = 0.00, 1.62, 1.23, 1.85$).

As shown in Fig. 4.6, the error of four-harmonic-component approximation decreases as σ_D and R_D increase because the polymer-concentration profile for larger σ_D

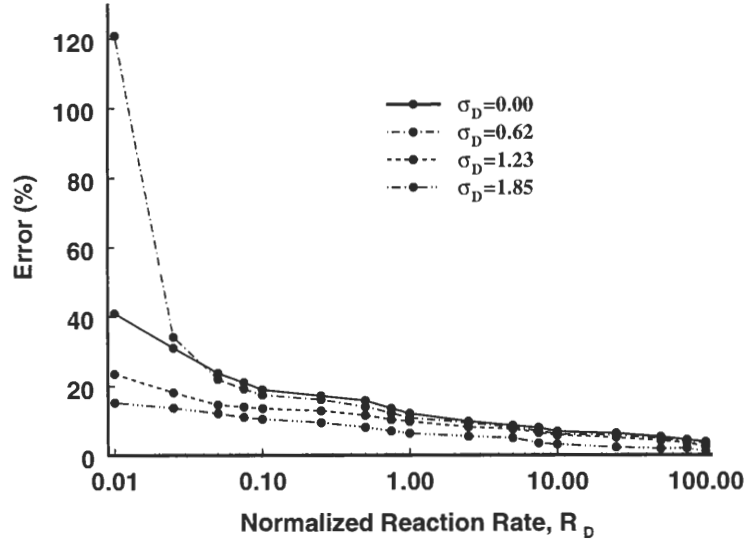


Figure 4.6: Errors of the first harmonic of polymer concentrations due to the four-harmonic-component approximation with respect to the finite-difference time-domain method as a function of R_D (in log scale) for various values of σ_D ($\sigma_D = 0.0, 0.62, 1.23, 1.85$).

and R_D resembles more a sinusoidal variation [as shown in Figs. 4.1(b) and 4.3]. The error of the four-harmonic-component approximation is less than 6% as $R_D > 10.0$ for all values of σ_D . However, as $R_D < 0.1$ for all values of σ_D , the error of four-harmonic-component approximation is larger than 10%. The presented results of the accuracy of the low-harmonic-component approximation by comparing the FDTD method to the four-harmonic-component approximation are in agreement with the literature results obtained by comparing the two-harmonic-component and the four-harmonic-component approximations [84]. Moreover, it is not unexpected that the trend of the error is similar to that of the nonlinearity because the more nonlinear response causes larger error of the low-harmonic-component approximation.

4.3 Unslanted Holographic Gratings

4.3.1 Real-Time Diffraction-Efficiency Measurement

The holographic recording material used in this research is the DuPont OmniDex613 photopolymer. This holographic photopolymer consists of a $6.0\mu m$ -thick photopolymer film coated onto the substrate of polyethylene terephthalate (Mylar layer). The refractive indices of the DuPont OmniDex613 photopolymer are $n_{g,w} = 1.535$ and $n_{g,r} = 1.50$ for free-space wavelength $\lambda_{0,w} = 363.8 nm$ (recording wavelength) and for free-space wavelength $\lambda_{0,r} = 632.8 nm$ (reading wavelength) respectively. A removable cover sheet is added to protect the photopolymer film. A sample is prepared by removing the cover sheet and laminating the photopolymer film onto a glass (fused silica) as a substrate. The thickness of this glass is $\sim 1.0 mm$, and its refractive index is 1.4567.

The experimental setup applied to study the dynamics of unslanted holographic grating formations is shown in Fig. 4.7 [70, 75, 76, 134] The holographic grating is created by use of a commercial argon-ion laser (Spectra-Physics BeamLok 2065-S) beam with diameter $1 cm$ and maximum available power $0.5 mW$ that is split into two incident beams,

referred to as the reference beam and the objective beam. The free-space wavelength of the argon-ion laser is $\lambda_{0,w} = 363.8 \text{ nm}$. In order to obtain a high contrast interference pattern, the intensity of two incident beams is adjusted to be equal (fringe visibility $V = 1.0$). The incident angle between the objective beam and the reference beam outside the sample is 60° (i.e. $\theta_o = \theta_r = 30^\circ$), and thus the period of this unslanted grating is $\Lambda = 363.8 \text{ nm}$. The dynamics of the holographic grating formation are studied by monitoring the diffraction efficiency during exposure by use of a He-Ne TE-polarized laser as a reading beam with free-space wavelength $\lambda_{0,r} = 632.8 \text{ nm}$ because the recording photopolymer (DuPont Om-

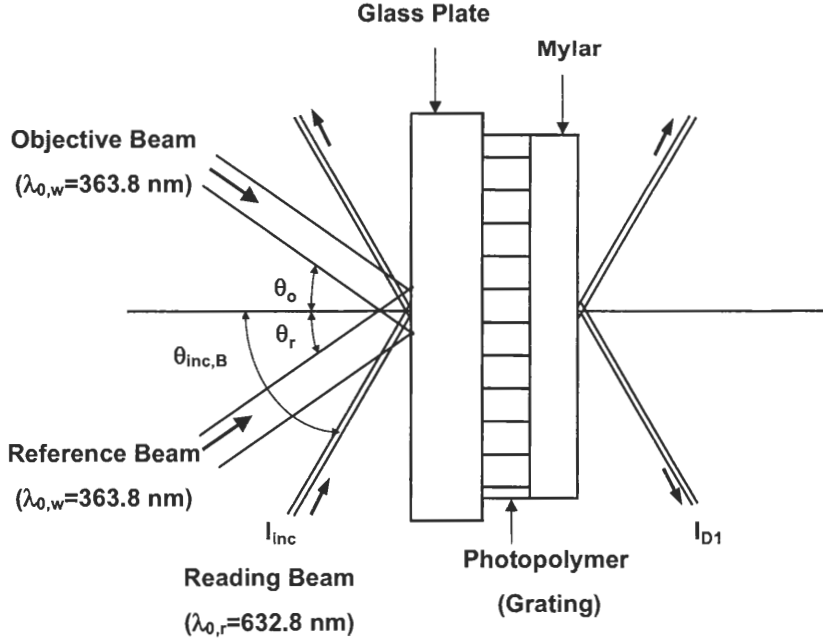


Figure 4.7: Schematic diagram of real-time diffraction-monitoring experiment for DuPont OmniDex613 photopolymer. A argon-ion laser with free-space wavelength $\lambda_{0,w} = 363.8 \text{ nm}$ is used as a writing beam to create the fringe interference, and a He-Ne laser with free-space wavelength $\lambda_{0,r} = 632.8 \text{ nm}$ is used to monitor the temporal behavior of hologram recording. The incident angle of writing beam is $\theta_o = \theta_r = 30^\circ$, resulting in a unslanted grating with a period $\Lambda = 363.8 \text{ nm}$. The incident angle of the reading beam is $\theta_{inc,B} = 60.42^\circ$, which satisfies the first-order Bragg condition.

niDex613) is not sensitive to red light. The incident angle of the reading beam outside the sample is $\theta_{inc,B} = 60.42^\circ$, which is selected such that the incident beam satisfies the first-order Bragg condition. Then, the power of the first-order diffracted-beam is measured by a photodetector, and the diffraction efficiency of the first-diffracted order DE_1 (in percent) can be defined as

$$DE_1 = \frac{I_{D1}}{I_{inc}} \times 100, \quad (4.26)$$

where I_{D1} is the diffracted intensity, and I_{inc} is the incident intensity.

After the holographic recording is completed, the sample is cured by a uniform UV light with wavelength $\lambda_0 = 365.0\text{ nm}$ and exposure irradiance $I_0 = 5.0\text{ mW/cm}^2$ for 20 seconds to polymerize the residual free-monomer. Then, a post-baking process is applied on the sample to improve the refractive-index modulation of the photopolymer. In order to investigate the effects of postprocessing on the refractive-index modulation of photopolymers, samples (after a uniform UV curing) are treated at different baking temperatures T_b ($T_b = 90^\circ\text{C}, 120^\circ\text{C}, 150^\circ\text{C}$) for various baking time periods t_b ($t_b = 1\text{ h}, 1.5\text{ h}, 2\text{ h}$) in this research.

4.3.2 Effects of Exposure Irradiance on the Unslanted Holographic Grating Recording

Figure 4.8 shows the dynamic diffraction efficiency of the first-diffracted order during hologram recording with respect to various exposure intensities I_0 ($I_0 = 0.043, 0.110, 0.240, 0.368\text{ mW/cm}^2$). As shown in Fig. 4.8, for the lower exposure irradiance ($I_0 = 0.043\text{ mW/cm}^2$), the DE_1 rises monotonically with a slow speed because the lower exposure irradiance corresponds to the lower polymerization rate; thus, the grating is developed slowly. As the exposure irradiance increases, for example $I_0 = 0.110$ or 0.240 mW/cm^2 , the polymerization rate also increases and is comparable to the diffusion coefficient of the free monomer. In these cases, the free monomers in the bright regions are depleted and polymerized quickly,

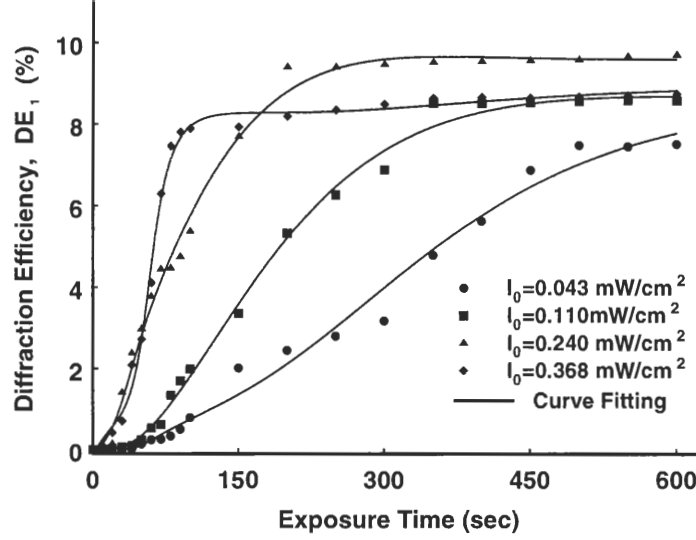


Figure 4.8: Experimentally monitored diffraction efficiencies as a function of exposure time for unslanted transmission gratings recorded on DuPont OmniDex613 photopolymer by use of various exposure irradiances I_0 ($I_0 = 0.043, 0.110, 0.240, 0.368 \text{ mW/cm}^2$). The solid lines represent the curve fitting for the experimental data.

and the free monomers have enough time to propagate from the dark regions to the bright regions to develop a phase grating resembling more of a sinusoidal variation. This phenomenon is similar to the numerical results of polymer concentrations for larger R_D (as shown in Fig. 4.3). Thus, increasing the exposure irradiance, the DE_1 increases faster and reaches a higher saturation value. If the exposure irradiance increases further, for example $I_0 = 0.368 \text{ mW/cm}^2$, the polymerization rate increases further and is larger than the diffusion rate (resulting in a smaller R_D). In this case, the holographic grating is developed immediately after exposure, and, consequently, the DE_1 rises faster because of the higher polymerization rate. However, since the diffusion coefficient is smaller than the polymerization rate in this case, the free monomers in the dark regions do not have enough time to diffuse to the bright regions before the polymerized reaction occurs. Thus, the polymer-concentration profile developed by use of a higher exposure irradiance does not represent

well a sinusoidal variation, which is similar to the numerical result of polymer concentrations for smaller R_D (shown in Fig. 4.3), resulting in a smaller saturation level of the first harmonic of the refractive index.

Since the diffusion equation illustrates the dynamics of holographic formations in terms of the monomer-concentration profile and the polymer-concentration profile, which correspond to the refractive index directly, it is necessary to convert the experimentally obtained data of diffraction efficiencies to the corresponding refractive-index modulations. Although Kogelnik's theory [86] with a correction factor for the Fresnel reflection loss has been applied by many researchers [73, 76, 77, 79–85] to accomplish this conversion, it does not provide an accurate estimation of refractive-index modulation in this diffraction case because the average refractive index in the grating is not equal to those in the input and output regions. Furthermore, multiple interference effects between the various layers could also affect the estimated refractive-index modulations. In this research, both Kogelnik's theory (corrected for Fresnel reflection losses) and the RCWA [56] are applied to estimate the refractive-index modulations. The number of diffracted orders retained in the RCWA was seven. Larger number of diffracted orders did not make any difference in the calculated diffraction efficiencies or refractive-index modulations. The detail description for converting experimental diffraction efficiencies to the corresponding refractive-index modulations by use of Kogelnik's theory and the RCWA can be found in Appendix B.

After applying the RCWA on the real-time measurement of diffraction efficiencies (as shown in Fig. 4.8 the first-order harmonics of refractive-index modulations, Δn_1 , are presented in Fig. 4.9 for various exposure intensities ($I_0 = 0.043, 0.110, 0.240, 0.368 \text{ mW/cm}^2$). As seen in Fig. 4.9, the growth curves of refractive-index modulations are similar to those of the monitored diffraction efficiencies (shown in Fig. 4.8). According to the experimental results the optimal exposure irradiance is $I_0 = 0.240 \text{ mW/cm}^2$, and the corresponding saturation value of refractive-index modulation is $\Delta n_1 = 0.011$.

To quantify the accuracy of Kogelnik's theory (corrected for Fresnel reflection losses),

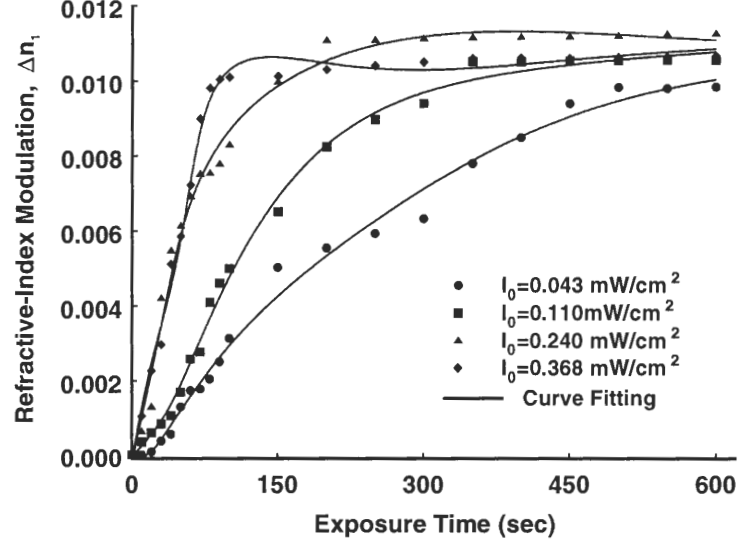


Figure 4.9: Experimental refractive-index modulations that are converted from monitored diffraction efficiencies (as shown in Fig. 4.8) by use of the RCWA, as a function of exposure time for unslanted transmission gratings recorded on DuPont OmniDex613 photopolymer by use of various exposure irradiances I_0 ($I_0 = 0.043, 0.110, 0.240, 0.368 \text{ mW/cm}^2$). The solid lines represent the curve fitting for the experimental data.

the error of refractive-index modulations (determined by Kogelnik's theory) is defined (in percent) as

$$\text{Error} = \frac{\Delta n_{1,RCWA} - \Delta n_{1,Kog}}{\Delta n_{1,RCWA}} \times 100, \quad (4.27)$$

where $\Delta n_{1,RCWA}$ and $\Delta n_{1,Kog}$ are refractive-index modulations estimated by the RCWA and Kogelnik's theory (corrected for Fresnel reflection losses) respectively. As shown in Fig. 4.10, after the holographic recording is finished (diffraction efficiencies reach saturation values), the errors of Kogelnik's theory are $\sim 30\%$ for all exposure intensities. In summary, Kogelnik's theory may not be a very precise method for the estimation of refractive-index modulation.

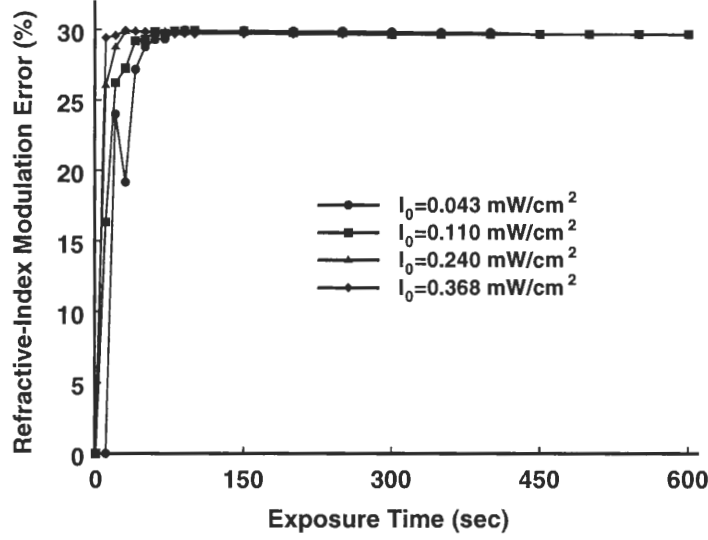


Figure 4.10: Errors of refractive-index modulations estimated by use of Kogelnik's theory with respect to RCWA for various exposure irradiances I_0 ($I_0 = 0.043, 0.110, 0.240, 0.368 \text{ mW/cm}^2$).

4.3.3 Effects of Post-Baking Processing

In order to enhance the refractive-index modulation and thus the diffraction efficiency, researchers have applied various exposure processing to fabricate holographic gratings. For example, Piazzolla and Jenkins [72] used the alternate illumination to fabricate a holographic grating, which was based on the DuPont HRF-150-38 photopolymer, and the diffraction efficiency increases by 10% in the experiment. Using the same DuPont photopolymer, Rhee *et al.* [75] exploited different combinations of postexposures on the grating fabrication, and the maximum increase of the diffraction efficiency is $\sim 5\%$. Moreover, Weitzel [136] studied the effect of the preillumination on the diffraction efficiency of a grating, which was fabricated by use of pulse exposure on the DuPont HRF-800X071-20 photopolymer film. The maximum diffraction efficiency increases from $\sim 7.5\%$ (without preillumination) to 40% and 75% by use of the pulse preillumination and the continuous incoherent preillumination respectively. However, the preillumination does not improve the performance of the grating,

which is fabricated by use of the CW exposure.

In addition to exposure conditions, the post-baking processing [67, 136, 137] was also mentioned in the grating fabrication to improve the diffraction efficiency. However, there has been no complete discussion for the effects of various baking temperatures and baking times on diffraction efficiencies of holographic gratings fabricated using photopolymers. In this research, to investigate the effects of the post-baking on diffraction efficiencies the grating samples are baked at various temperatures and baking times after the holographic recording and the uniform UV curing

Figure 4.11 shows the experimental results of refractive-index modulations as a function of the baking time for various baking temperatures ($T_b = 90^\circ C, 120^\circ C, 150^\circ C$) and different exposure intensities ($I_0 = 0.043, 0.110, 0.240, 0.368 \text{ mW/cm}^2$). As shown in Fig. 4.11, the post-baking processing does not enhance the refractive-index modulation a lot for the lower exposure irradiance ($I_0 = 0.043 \text{ mW/cm}^2$). However, as the exposure irradiance increases, the post-baking condition enhances the refractive-index modulation dramatically. For the exposure irradiance with $I_0 = 0.110 \text{ mW/cm}^2$, the optimum baking temperature and baking time are $T_b = 120^\circ C$ and time $t_b = 1.5 \text{ h}$ respectively. Based on this optimum baking condition, the refractive-index modulation increases from $\Delta n_1 = 1.056 \times 10^{-2}$, corresponding to $DE_1 = 8.58\%$ (without post-baking), to $\Delta n_1 = 2.404 \times 10^{-2}$ (corresponding to $DE_1 = 37.08\%$). Similarly, the optimum post-baking conditions for the exposure irradiance with $I_0 = 0.240 \text{ mW/cm}^2$ are $T_b = 120^\circ C$ and $t_b = 2 \text{ h}$, and, as a result, the refractive-index modulation rises from $\Delta n_1 = 1.126 \times 10^{-2}$, corresponding to $DE_1 = 9.71\%$ (without post-baking) to $\Delta n_1 = 2.750 \times 10^{-2}$ (corresponding to $DE_1 = 44.92\%$). Furthermore, increasing the exposure irradiance up to $I_0 = 0.368 \text{ mW/cm}^2$, the maximum increase of the refractive-index modulation occurs at $T_b = 120^\circ C$ and $t_b = 1.5 \text{ h}$. In this case, the refractive-index modulation rises from $\Delta n_1 = 1.066 \times 10^{-2}$, corresponding to $DE_1 = 8.75\%$ (without post-baking) to $\Delta n_1 = 2.422 \times 10^{-2}$ (corresponding to $DE_1 = 37.50\%$). Generally speaking, the optimum post-baking condition is $T_b = 120^\circ C$ and $t_b = 1.5 \text{ h}$. In addition,

comparing the experimental data for different exposure intensities for the grating fabrication (as shown in Fig. 4.11), the higher the refractive-index modulation is before baking the more the refractive-index modulation increases after baking (based on the optimum baking conditions).

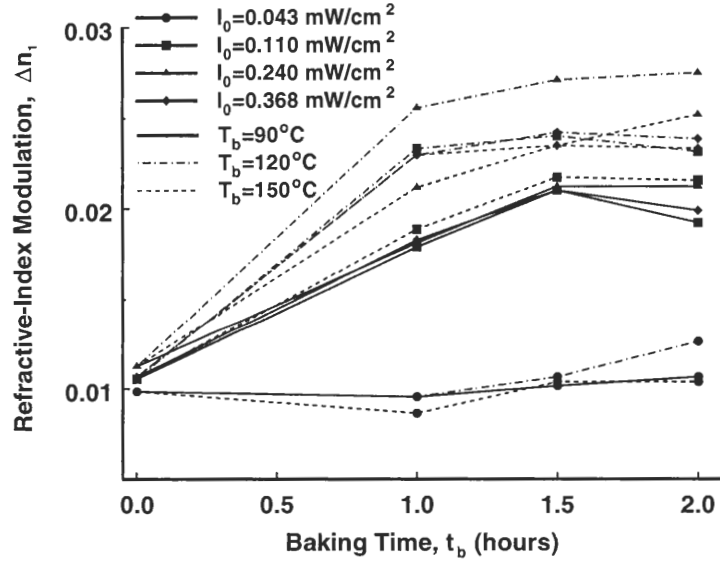


Figure 4.11: Effects of post-baking conditions on the refractive-index modulations for various exposure irradiances I_0 ($I_0 = 0.043, 0.110, 0.240, 0.368 \text{ mW/cm}^2$). The holographic-grating samples are baked at three different temperatures $T_b = 90^\circ\text{C}, 120^\circ\text{C}, 150^\circ\text{C}$ for three different time periods $t_b = 1 \text{ h}, 1.5 \text{ h}, 2 \text{ h}$.

4.3.4 Characteristic Parameters of Holographic Photopolymers

In this section the characteristic parameters of unslanted holographic gratings based on DuPont OmniDex613 photopolymers including diffusion coefficient D_0 , nonlocal response length $\sqrt{\sigma}$, and the value of κ are determined by fitting the theoretical model to the experimentally obtained growth-curves of the refractive-index modulations. In order to optimize the fittings of the theoretical results to the experimental data of the refractive-index modulations, an error function is defined and minimized. In this research, the error function

f_{error} is defined as

$$f_{error}(R_D, \sigma_D, \kappa, \phi', C_p, C_m) = \sum_{t_i} [\Delta n_{1,model}(R_D, \sigma_D, \kappa, \phi', C_p, C_m, t_i) - \Delta n_{1,exp}(t_i)]^2, \quad (4.28)$$

where $\Delta n_{1,model}(R_D, \sigma_D, \kappa, \phi', C_p, C_m, t_i)$ and $\Delta n_{1,exp}(t_i)$ are the refractive-index modulations obtained from the theoretical analysis and the real-time measurements, respectively, at exposure time t_i (where $i = 1, 2, \dots, M$ and M is the total number of measurements).

In order to minimize the error function [shown in Eq. (4.28)], i.e. to minimize the difference between the theoretical model and the experimental data, a quasi-Newton method [138] is applied in this research. Since the quasi-Newton method is used to solve minimization problems subject to simple bounds on the variables, the expected ranges of the variables have to be determined. Furthermore, some of the variables (κ and ϕ') can be estimated from the saturation data and therefore the number of variables that minimize f_{error} is reduced to the R_D, σ_D, C_p , and C_m . First let us assume the monomer phase grating and the polymer phase grating are in phase (i.e. $\phi' = 0$) because there is no zero-crossing point of growth curves of refractive-index modulations [73] (as shown in Fig. 4.9). Since the holographic formation reaches the steady state at $t_D = 10$, the values of κ can be estimated from the experimentally growth curves of refractive-index modulations at the steady state. Thus, κ can be determined by:

$$\kappa = \frac{10}{\sqrt{(1 - R_f)I_0 t_{sat}}}, \quad (4.29)$$

where R_f is a correction factor for the Fresnel loss of the glass (as described in Appendix B), and t_{sat} is the exposure time when the holographic formation reaches the steady state (i.e. the experimentally monitored diffraction efficiencies reach saturation values). As shown in Fig. 4.8, the steady-state exposure-times are $t_{sat} = 180, 320, 550$, and 1320 sec corresponding to the values of $\kappa = 0.10, 0.07, 0.06$, and $0.04 \text{ cm}/\sqrt{mW} \text{ sec}$ for $I_0 = 0.368, 0.240, 0.110$, and $0.043 \text{ mW}/\text{cm}^2$ respectively.

Since the free monomers are completely consumed at steady state, i.e. $\Phi_m(x_D, t_{D,sat}) =$

0, C_p can be estimated from Eq. (4.15) as follows,

$$C_p = \frac{\Delta n_1^s}{\Phi_{p,1}^s}, \quad (4.30)$$

where Δn_1^s is the experimentally obtained refractive-index modulation at steady state, and $\Phi_{p,1}^s$ is the theoretical saturation-value of the first harmonic of polymer concentration. According to Fig. 4.4, the saturation value of the first harmonic of the polymer concentration, $\Phi_{p,1}^s$, varies from $\sim 0.1 \text{ mole/cm}^3$ to $\sim 65 \text{ mole/cm}^3$. In addition, the experimentally obtained refractive-index modulation at steady state is $\Delta n_1^s \sim 0.01$ (as shown in Fig. 4.9). Therefore, the range of C_p is $10^{-1} \text{ cm}^3/\text{mole} \leq C_p \leq 1.5 \times 10^{-4} \text{ cm}^3/\text{mole}$. Next, it is assumed that the value of C_m is of the same order as C_p . Thus, the range of C_m is chosen as $10^{-1} \text{ cm}^3/\text{mole} \leq C_m \leq 1.5 \times 10^{-4} \text{ cm}^3/\text{mole}$. Furthermore, the ranges of R_D and σ_D are assigned as $10^{-2} \leq R_D \leq 10^2$ and $0 \leq \sigma_D \leq 10$ respectively in this research which are equivalent to the corresponding ranges used for non-normalized variables in literature [83]. It is worth mentioning that $\sigma_D = 0$ corresponds to the local diffusion model [81].

By using a quasi-Newton method with a finite-difference gradient [138] in conjunction with the expected ranges of R_D , σ_D , C_p , and C_m the error function f_{error} of Eq. (4.28) was minimized and the optimum values R_D , σ_D , C_p , and C_m were obtained. Figure 4.12 shows the theoretical fits (using the RCWA) to the experimentally growth curves of refractive-index modulations. As shown in Fig. 4.12, the theoretical predictions are very good. Table 4.1 summarizes the optimum values of R_D , σ_D , C_p , and C_m , which are used for the theoretical calculations in Fig. 4.12. The corresponding diffusion coefficients D_0 and nonlocal response length $\sqrt{\sigma}$ shown in Table 4.1 are estimated by:

$$D_0 = \kappa \Lambda^2 R_D \frac{\sqrt{(1-R_f)I_0}}{4\pi^2}, \quad (4.31)$$

and

$$\sqrt{\sigma} = \frac{\Lambda \sqrt{\sigma_D}}{2\pi}. \quad (4.32)$$

As shown in Table 4.1, D_0 remains almost constant, which is in agreement with the assumption of $\alpha = 0.0$ in this research. The average of diffusion coefficient is $D_0 =$

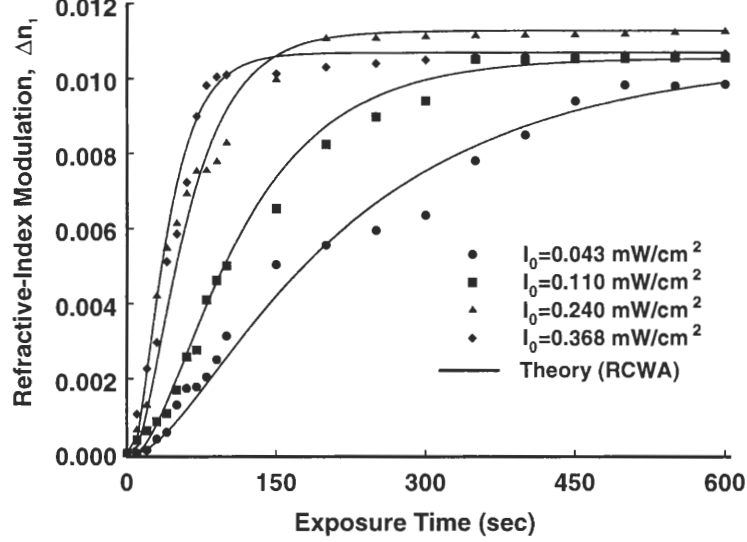


Figure 4.12: Comparison between theoretical models and experimentally obtained refractive-index modulations of unslanted holographic gratings for various exposure irradiances I_0 ($I_0 = 0.043, 0.110, 0.240, 0.368 \text{ mW/cm}^2$). The solid lines represent the theoretical results based on the RCWA and on characteristic parameters listed in Table 4.1.

$1.005 \times 10^{-12} \text{ cm}^2/\text{sec}$. However, Moreau *et al.* [127] experimentally predicted the diffusion coefficient of DuPont HRF600 photopolymer (similar to the DuPont OmniDex613) to be $D_0 = 6.52 \times 10^{-11} \text{ cm}^2/\text{sec}$. The main reason for the smaller value of the diffusion coefficient that we estimated is that we used much lower exposure irradiance and shorter wavelength ($I_0 = 0.043 \sim 0.368 \text{ mW/cm}^2$ at $\lambda_{0,w} = 363.8 \text{ nm}$) than Moreau *et al.* [127] used ($I_0 = 10 \text{ mW/cm}^2$ at $\lambda_{0,w} = 514.5 \text{ nm}$) to record the holographic gratings. Moreover, the nonlocal response length $\sqrt{\sigma}$ increases as the exposure irradiance decreases (i.e. R_D increases). The average nonlocal response length is $\sqrt{\sigma} = 59.27 \text{ nm}$. Since the exact composition of the DuPont OmniDex613 photopolymer is proprietary, the predicted value of the nonlocal length of DuPont OmniDex613 photopolymer is compared to those of other materials. For an acrylamide based photopolymer, the nonlocal length estimated by Lawrence *et al.* is $\sqrt{\sigma} = 75.9 \pm 25 \text{ nm}$ [84]. On the other hand, the values of $\sqrt{\sigma}$ of DuPont

photopolymers (the product number is not given) found in literature varies from 47.6 nm to 84.6 nm [83]. Therefore, the nonlocal length of DuPont OmniDex613 photopolymer predicted in this paper ($\sqrt{\sigma} = 59.27\text{ nm}$) seems very reasonable.

Table 4.1: Characteristic parameters of unslanted holographic grating formations based on the DuPont OmniDex613 photopolymers for exposure to $\lambda_{0,w} = 363.8\text{ nm}$ UV light

Exposure Irradiance $I_0(mW/cm^2)$	κ $cm/\sqrt{mW}sec$	R_D	σ_D	C_p $cm^3/mole$	C_m $cm^3/mole$	D_0 cm^2/sec	$\sqrt{\sigma}$ nm
0.043	0.04	3.89	1.30	3.3×10^{-4}	3.7×10^{-4}	0.988×10^{-12}	66.01
0.110	0.06	1.57	1.25	3.6×10^{-4}	4.0×10^{-4}	0.957×10^{-12}	64.74
0.240	0.07	0.96	0.92	3.8×10^{-4}	4.3×10^{-4}	1.009×10^{-12}	55.54
0.368	0.10	0.58	0.77	4.1×10^{-4}	4.6×10^{-4}	1.066×10^{-12}	50.81
Average	0.0675		1.06	3.7×10^{-4}	4.15×10^{-4}	1.005×10^{-12}	59.27

4.4 Slanted Holographic Gratings

4.4.1 Real-Time Diffraction-Efficiency Measurement

Similar to the recording configuration for unslanted-grating fabrication (as shown in Fig. 4.7), the basic interferometer for studying the dynamics of small slant-angle holographic grating formations in photopolymers is shown in Fig. 4.13 [70, 75, 76]. The holographic grating is recorded by use of a commercial argon-ion laser beam with diameter 1 cm and maximum available power 0.5 mW that is split into two incident beams, referred to as the reference beam and the objective beam. The free-space wavelength of the argon-ion laser is $\lambda_{0,w} = 363.8\text{ nm}$. As seen in Fig. 4.13, the incident angles of the objective beam and the reference beam (measured from the normal of the glass plate) are θ_o and θ_r . Thus, the grating period Λ and the slant angle ϕ (measured from the interface of the grating) without considering the shrinkage effect are

$$\Lambda = \frac{\lambda_{0,w}}{2n_{g,w} \sin[\frac{1}{2}(\theta'_o + \theta'_r)]}, \quad (4.33)$$

$$\phi = \frac{\theta'_o - \theta'_r}{2}, \quad (4.34)$$

where $\theta'_o = \sin^{-1}(\sin \theta_o/n_{g,w})$ and $\theta'_r = \sin^{-1}(\sin \theta_r/n_{g,w})$ are the angles of the objective beam and the reference beam respectively inside the photopolymer. In this research, the incident angles of the objective beam and the reference beam for fabricating a small slant-angle grating are selected as $\theta_o = 45.0^\circ$ and $\theta_r = 0.0^\circ$ respectively. As a result, without considering the shrinkage effect during holographic recording, the grating period is $\Lambda = 0.5 \mu m$, and the slant angle is $\phi = 13.71^\circ$. Furthermore, considering the Fresnel reflection losses and different projection areas of the objective beam and the reference beam, the power ratio between the objective beam and the reference beam for the small slant-angle

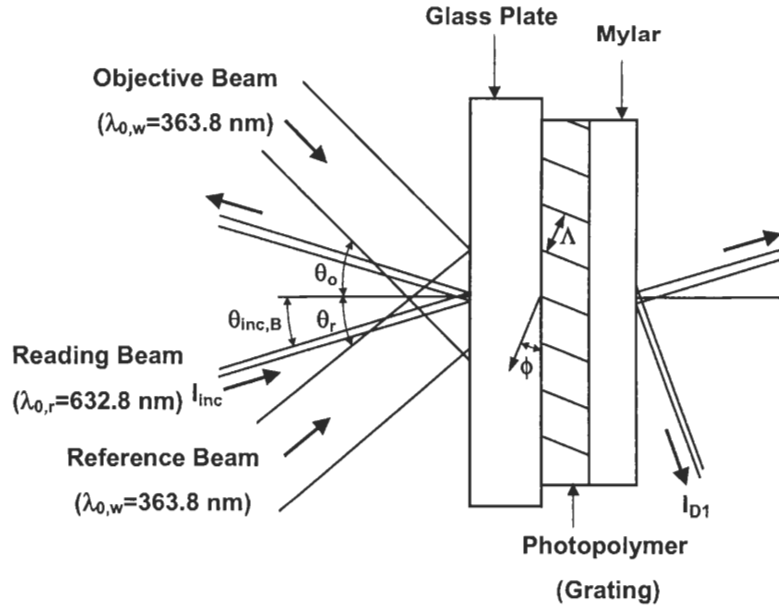


Figure 4.13: Schematic diagram of real-time diffraction-monitoring experiment for a small slant-angle grating based on DuPont OmniDex613 photopolymer. An argon-ion laser with free-space wavelength $\lambda_{0,w} = 363.8 \text{ nm}$ is used as a writing beam to create the fringe interference, and a He-Ne laser with free-space wavelength $\lambda_{0,r} = 632.8 \text{ nm}$ is used to monitor the temporal behavior of hologram recording. The incident angles of the objective beam and the reference beam are $\theta_o = 45.0^\circ$ and $\theta_r = 0.0^\circ$ respectively, and results in a slanted grating with a period $\Lambda = 0.5 \mu m$ and a slant angle $\phi = 13.71^\circ$. The incident angle of the reading beam is $\theta_{inc,B} = 17.01^\circ$, which satisfies the first-order Bragg condition.

grating is set at $P_o/P_r = 1.49$ to obtain equal intensities of these two beams (i.e. fringe visibility $V = 1.0$ inside the photopolymer).

Furthermore, the dynamics of the holographic grating formation are studied by monitoring the diffraction efficiency during exposure by use of a He-Ne TE-polarized laser as a reading beam with free-space wavelength $\lambda_{0,r} = 632.8 \text{ nm}$ because the recording photopolymer (DuPont OmniDex613) is not sensitive to red light. The incident angle of the reading beam outside the sample is $\theta_{inc,B} = 17.01^\circ$, which is selected such that the incident beam satisfies the first-order Bragg condition. Then, the power of the first-order diffracted-beam is measured by a photodetector, and therefore the diffraction efficiency of the first-diffracted order (DE_1), defined as a ratio of the intensity of the first-order diffracted-beam (I_{D1}) to the intensity of the incident beam (I_{inc}), can be obtained. Applying the RCWA with a correction factor for the Fresnel reflection loss (resulting from the interface between the glass plate and air) to the measured diffraction efficiency of the first-diffracted order [134], the corresponding refractive-index modulation of a small slant-angle grating formation during holographic recording can be estimated.

Although a slanted grating can be fabricated by use of the basic interferometric recording (as shown in Fig. 4.13), the maximum slant angle obtained from this recording configuration is $\phi = 26.94^\circ$ for a grating with period $\Lambda = 0.5 \mu\text{m}$ as the incident angles of the objective beam and the reference beam are $\theta_o = 90.0^\circ$ and $\theta_r = -20.56^\circ$ respectively. However, for practical applications, especially for input and output grating couplers, the slant angles of holographic gratings are about 45 degrees [22,66]. Thus, in order to fabricate a large slant-angle grating, especially for $\phi > 20.32^\circ$, a prism is needed [22,66]. The experimental setup for developing a large slant-angle grating is shown in Fig. 4.14. As seen in Fig. 4.14, a fused silica $45^\circ - 45^\circ - 90^\circ$ prism with refractive index $n_p = 1.47$ is inserted between the prepared sample and air. The outside surfaces of the prism are AR coated to reduce reflections.

Similarly, the free-space wavelength of recording beam is $\lambda_{0,w} = 363.8 \text{ nm}$, and the

incident angles of the objective beam and the reference beam (measured from the normal of the prism) are θ_o and θ_r . As a result, the grating period and the slant angle (measured from the interface of the grating) without considering the shrinkage effect can be represented as

$$\Lambda = \frac{\lambda_{0,w}}{2n_{g,w} \sin[\frac{1}{2}(\theta'_o - \theta'_r)]}, \quad (4.35)$$

$$\phi = \frac{\theta'_o + \theta'_r}{2}, \quad (4.36)$$

where $\theta'_o = \sin^{-1}\{\frac{n_{p,w} \sin[45 + \sin^{-1}(\sin \theta_o / n_{p,w})]}{n_{g,w}}\}$ and $\theta'_r = \sin^{-1}\{\frac{n_{p,w} \sin[45 + \sin^{-1}(\sin \theta_r / n_{p,w})]}{n_{g,w}}\}$.

Following the selected grating period of the small slant-angle grating ($\Lambda = 0.5 \mu m$) and

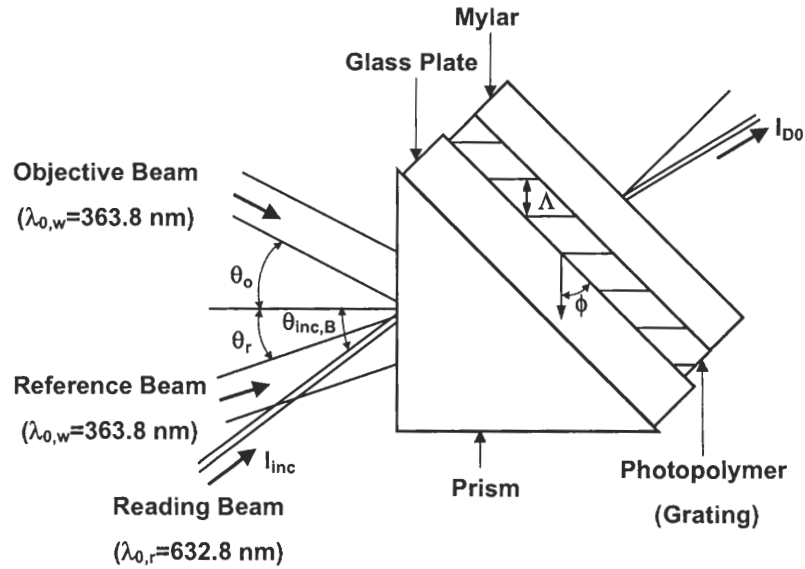


Figure 4.14: Schematic diagram of real-time diffraction-monitoring experiment for a large slant-angle grating based on DuPont OmniDex613 photopolymer. An argon-ion laser with free-space wavelength $\lambda_{0,w} = 363.8 \text{ nm}$ is used as a writing beam to create the fringe interference, and a He-Ne laser with free-space wavelength $\lambda_{0,r} = 632.8 \text{ nm}$ is used to monitor the temporal behavior of hologram recording. The incident angles of the objective beam and the reference beam are $\theta_o = 27.29^\circ$ and $\theta_r = 18.04^\circ$ respectively, and results in a slanted grating with a period $\Lambda = 0.5 \mu m$ and a slant angle $\phi = 45.0^\circ$. The incident angle of the reading beam is $\theta_{inc,B} = 37.62^\circ$, which satisfies the first-order Bragg condition.

designing the slant angle of the large slant-angle grating with $\phi = 45.0^\circ$, the incident angles of the objective beam and reference beam for fabricating a large slant-angle grating ($\Lambda = 0.5 \mu m, \phi = 45.0^\circ$) are $\theta_o = 27.29^\circ$ and $\theta_r = 18.04^\circ$ respectively. Similarly, in order to obtain equal intensities of these two beams, and thus $V = 1.0$ inside the photopolymer, the power ratio between the objective beam and the reference beam for the large slant-angle grating is set at $P_o/P_r = 1.96$.

Moreover, a He-Ne TE-polarized laser as a reading beam with free-space wavelength $\lambda_{0,r} = 632.8 nm$ is used to monitor the diffraction efficiency during exposure to study the dynamic characteristics of large slant-angle grating formations in photopolymers. The incident angle of the reading beam outside the sample is $\theta_{inc,B} = 37.62^\circ$, which is selected such that the incident beam satisfies the first-order Bragg condition. However, based on the grating with period $\Lambda = 0.5 \mu m$ and slant angle $\phi = 45.0^\circ$ fabricated by the prism system (as seen in Fig. 4.13), the diffracted angle of the first-order diffracted beam in the grating is 69.96° (measured from the normal of the grating interface) and results in the total internal reflection at the interface between the Mylar and air, so the first-order diffracted-beam cannot be detected. Therefore, instead of measuring the power of the first-order diffracted-beam, the power of the zero-order diffracted-beam (I_{D0}) is measured, and therefore the diffraction efficiency of the zero-diffracted order (DE_0) is determined. Then, the refractive-index modulation of a large slant-angle grating formation during exposure can be estimated by use of the RCWA with the correction factors of Fresnel reflections to the measured diffraction efficiency of the zero-diffracted order.

After the holographic recordings for both small and large slant-angle gratings are completed, the samples are cured by a uniform UV light with wavelength $\lambda_0 = 365.0 nm$ and exposure irradiance $I_0 = 2.0 mW/cm^2$ for 50 seconds to polymerize the residual free-monomer. Then, the samples are mounted on a rotational stage to study the deviations of Bragg angle caused by recording shrinkage (described in Section 4.4.2). Furthermore, in order to study systematically the effects of post-baking processing on the shift of Bragg

angle and the increment of refractive-index modulation, the samples for both small and large slant-angle gratings after exposure are treated at different baking temperatures T_b ($T_b = 90, 120, 150^\circ\text{C}$) for various baking time periods t_b ($t_b = 1, 1.5, 2\text{ h}$). When the heat processing is done, the samples are cooled down to room temperature. Then, the samples after post-baking processing are mounted on a rotational stage for angular-selectivity experiments to study the deviation of Bragg angle resulting from the post-baking processing.

4.4.2 Experimental Setup of Angular Selectivity

As has been mentioned in the previous section, the shift of Bragg angle resulting from both the holographic recording and the post-baking processing is an important parameter of a photopolymer, especially for a slanted holographic grating. In order to determine the shift of Bragg angle and estimate the shrinkage factor of the DuPont OmniDex613 photopolymer (recorded by UV with free-space wavelength $\lambda_{0,w} = 363.8\text{ nm}$), an angular-selectivity testing configuration shown in Fig. 4.15 is used. A recorded sample is mounted on a rotational stage and is illuminated by a He-Ne TE-polarized laser with free-space wavelength $\lambda_{0,r} = 632.8\text{ nm}$. In order to find the new Bragg angle ($\theta_{new,B}$) resulting from the shrinkage effect, light transmitted through the sample (not diffracted) is measured for a range of incident angles (θ_{inc}) around the designed Bragg angle θ_B . For example, for the small slant-angle grating with period $\Lambda = 0.5\text{ }\mu\text{m}$ and slant angle $\phi = 13.71^\circ$, the designed Bragg angle is $\theta_B = 17.01^\circ$. On the other hand, the corresponding designed Bragg angle of the large slant-angle grating with period $\Lambda = 0.5\text{ }\mu\text{m}$ and slant angle $\phi = 45.0^\circ$ is $\theta_B = -30.93^\circ$. The transmission efficiency of a slanted grating (i.e. the zero-order diffraction efficiency, DE_0) is defined as a ratio of the intensity of the transmitted beam (I_{D0}) to the intensity of the incident beam (I_{inc}). Then, the curve of angular-dependent transmission efficiency of a slanted grating is fitted by the RCWA (considering the glass plate as an input region and the Mylar layer as an output region) in conjunction with Fresnel reflection losses (resulting from air-glass and Mylar-air interfaces). Then, the dependence

of the transmission efficiency on the incident angle of the reading beam, θ_{inc} , is used in order to determine the shrinkage factor, δ_s , and the refractive-index modulation, Δn_1 .

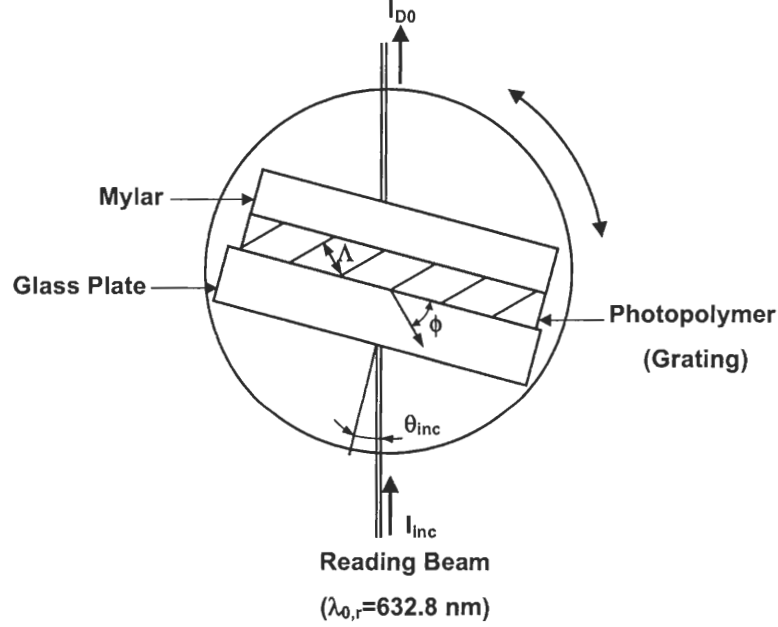


Figure 4.15: Experimental setup for the angular-selectivity measurement of a recorded sample to determine the shrinkage factor, the refractive-index modulation, and the shift of the Bragg angle.

4.4.3 Optimization of Rigorous Coupled-Wave Analysis Fittings to Angular-Dependent Transmission Efficiencies

In order to optimize the fittings of the theoretical results to the experimental data of angular-dependent transmission efficiencies (for determining the shrinkage factor, δ_s , and the refractive-index modulation, Δn_1 , after holographic recording), an error function is defined and minimized. The error function g_{error} is defined as

$$g_{error}(\delta_s, n_{g,r}, \Delta n_1, \theta_{inc,i}, \lambda_{0,r}) = \sum_{\theta_{inc,i}} [DE_{0,RCWA}(\delta_s, n_{g,r}, \Delta n_1, \theta_{inc,i}, \lambda_{0,r}) - DE_{0,exp}(\theta_{inc,i})]^2, \quad (4.37)$$

where $DE_{0,RCWA}$ and $DE_{0,exp}$ are the transmission efficiencies obtained from the RCWA in conjunction with Fresnel reflection losses and the experimental measurements, respectively, at incident angle $\theta_{inc,i}$ (where $i = 1, 2, \dots, M$ and M is the total number of measurements). The number of diffracted orders retained in the RCWA is assumed to be seven [134] (since this number of orders guaranteed convergence of the diffraction efficiencies). In addition, depending on the exposure intensity and the grating period, the nonlinearity parameter of the second harmonic $\chi_{p,2}^s$ (as seen in Fig. 4.5) of the polymer concentration at steady state (corresponding to the ratio of the second harmonic to the first harmonic of dielectric constant in the grating) for the DuPont OmniDex613 photopolymer varies from $\chi_{p,2}^s \sim 0.1$ to $\chi_{p,2}^s \sim 0.2$. As a result, the errors of transmission efficiencies, DE_0 , without considering the second harmonic of the dielectric constant in the grating for the RCWA (i.e. only the first harmonic of the dielectric constant is retained in the RCWA) vary from 0.0008 to 0.0016 and from 0.0022 to 0.0045 for small and large slant-angle gratings respectively as the first-order Bragg condition is satisfied. Therefore, a sinusoidally varying dielectric constant in the grating is assumed. I.e. the second and higher harmonics of the dielectric constant are neglected in the RCWA model since they are a lot smaller than the first harmonic and they do not affect the diffraction efficiencies of interest.

To minimize the error function [shown in Eq. (4.37)], a quasi-Newton method [134, 138] incorporating simple bounds of variables is applied. In this research, ranges of δ_s and Δn_1 are chosen as $0.0\% \leq \delta_s \leq 6.0\%$ and $0.00 \leq \Delta n_1 \leq 0.02$ respectively [70, 75, 124–129, 134]. Furthermore, the refractive index of grating and the free-space wavelength of reading beam are assumed to be $n_{g,r} = 1.50$ and $\lambda_{0,r} = 632.8 \text{ nm}$ respectively. As a result, the new Bragg angle, $\theta_{new,B}$, corresponding to the minimum value of $DE_{0,RCWA}$ can be obtained. The deviation from the Bragg angle, $\Delta\theta_B$, is defined as

$$\Delta\theta_B = \theta_{new,B} - \theta_B, \quad (4.38)$$

where θ_B is the designed Bragg angle. The designed Bragg angles are $\theta_B = 17.01^\circ$ and

$\theta_B = -30.93^\circ$ for both small and large slant-angle gratings respectively (as described in Section 4.4.1).

4.4.4 Recording Shrinkage of DuPont OmniDex613 Photopolymers

In this research, two grating samples with the same grating period and different slant angles are fabricated and tested. The first sample is a small slant-angle grating with $\Lambda = 0.5 \mu m$ and $\phi = 13.71^\circ$, and the second sample is a large slant-angle grating with $\Lambda = 0.5 \mu m$ and $\phi = 45.0^\circ$. The small slant-angle grating is fabricated by use of four different exposure intensities I_0 ($I_0 = 0.043, 0.110, 0.240, 0.368 mW/cm^2$). However, for the fabrication of a large slant-angle grating, the power ratio of the objective beam to the reference beam is $P_o/P_r = 1.96$. In addition, the projection areas of the objective beam and the reference beam are $1.86 cm^2$ and $0.96 cm^2$ respectively. Therefore, in order to obtain the exposure intensity with $I_0 = 0.368 mW/cm^2$, the required powers of the objective beam and the reference beam are $P_o = 0.344 mW$ and $P_r = 0.176 mW$ respectively and thus the total power is $0.52 mW$, which is higher than the maximum available power of the UV laser ($0.5 mW$). In addition, our laser is unstable in the vicinity of $0.5 mW$ output power. As a result, the large slant-angle grating is fabricated only by use of three different exposure intensities with $I_0 = 0.043, 0.110$, and $0.240 mW/cm^2$. After the holographic recordings and the uniform UV exposure for polymerizing the residual free-monomer, both small and large slant-angle gratings are completed, the samples are mounted on a rotational stage (as seen in Fig. 4.15) and the incident angles, θ_{inc} , are scanned from 0.0° to 35.0° (for small slant-angle gratings) and from -40.0° to -20.0° (for large slant-angle gratings) to study the angular-dependent transmission efficiencies. Finally, the quasi-Newton method is applied to optimize the theoretical fittings of RCWA to the curves of angular-dependent transmission efficiencies to determine the shrinkage factors (after recording), the refractive-index modulations, and the deviations of Bragg angles (as described in Section 4.4.3).

A. Small Slant-Angle Gratings

Figure 4.16 shows the experimental results and the RCWA fittings of angular-dependent transmission efficiencies of small slant-angle gratings ($\Lambda = 0.5 \mu m, \phi = 13.71^\circ$), which are fabricated by four different exposure intensities I_0 ($I_0 = 0.043, 0.110, 0.240, 0.368 \text{ mW/cm}^2$). As seen in Fig. 4.16, comparing the experimental curves to the RCWA fittings, the oscillations of experimental curves can be observed, especially as the incident angles (θ_{inc}) of the reading beam are away from the designed Bragg angle ($\theta_B = 17.01^\circ$). These oscillations of experimental curves result from the multi-reflection effects of Mylar and/or glass layers. The multiple interference effects of the Mylar and/or glass layers were also observed in the RCWA results when the two layers were incorporated in the model as finite-width optically-flat layers. However, the large number of oscillations made the accurate determination of the Bragg angle very difficult and thus it was decided to include these layers in the model as semi-infinite regions and correct the diffraction efficiencies with the Fresnel power reflection factors. The above simplification is also justified by the partial optical flatness of the glass and Mylar layers. Based on the RCWA fittings (represented by solid lines in Fig. 4.16), the Bragg angles shift from the designed value ($\theta_B = 17.01^\circ$) to the small ones ($\theta_{new,B} = 16.34^\circ, 16.32^\circ, 16.16^\circ$, and 16.15° for $I_0 = 0.043, 0.110, 0.240$, and 0.368 mW/cm^2 respectively), implying that the DuPont OmniDex613 photopolymer is shrank after recording. The corresponding shrinkage factors estimated by the RCWA fittings are $\delta_s = 3.38\%, 3.85\%, 4.18\%$, and 4.20% for $I_0 = 0.043, 0.110, 0.240$, and 0.368 mW/cm^2 respectively. In addition, the refractive-index modulations are $\Delta n_1 = 0.015, 0.015, 0.014$, and 0.014 for $I_0 = 0.043, 0.110, 0.240$, and 0.368 mW/cm^2 respectively.

B. Large Slant-Angle Gratings

On the other hand, the experimental results and the RCWA fittings of angular-dependent transmission efficiencies of large slant-angle gratings ($\Lambda = 0.5 \mu m, \phi = 45.0^\circ$), which are

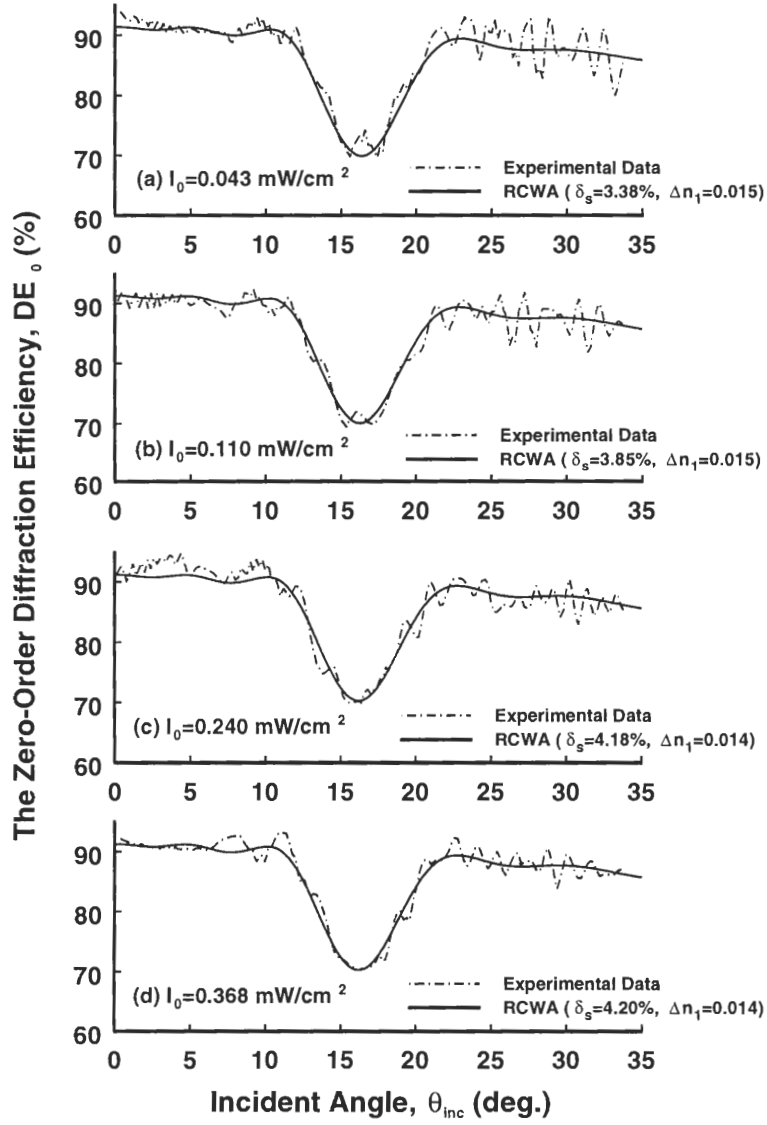


Figure 4.16: Angular selectivity of small slant-angle gratings with $\Lambda = 0.5 \mu\text{m}$ and $\phi = 13.71^\circ$ recorded by four different exposure intensities (a) $I_0 = 0.043 \text{ mW/cm}^2$, (b) 0.110 mW/cm^2 , (c) 0.240 mW/cm^2 , and (d) 0.368 mW/cm^2 . The solid lines represent the RCWA fittings, and the dash lines represent the experimental measurements.

fabricated with three different exposure intensities I_0 ($I_0 = 0.043, 0.110, 0.240 \text{ mW/cm}^2$), are represented in Fig. 4.17. Similarly, the oscillations of experimental curves (with respect to the RCWA fittings) resulting from the multi-reflection effects of Mylar and/or glass layers can be observed. As seen in Fig. 4.17, the Bragg angles shift from the designed value ($\theta_B = -30.93^\circ$) to the small values ($\theta_{new,B} = -31.97^\circ, -32.00^\circ$, and -32.00° for $I_0 = 0.043, 0.110$, and 0.240 mW/cm^2 respectively). The corresponding shrinkage factors and the refractive-

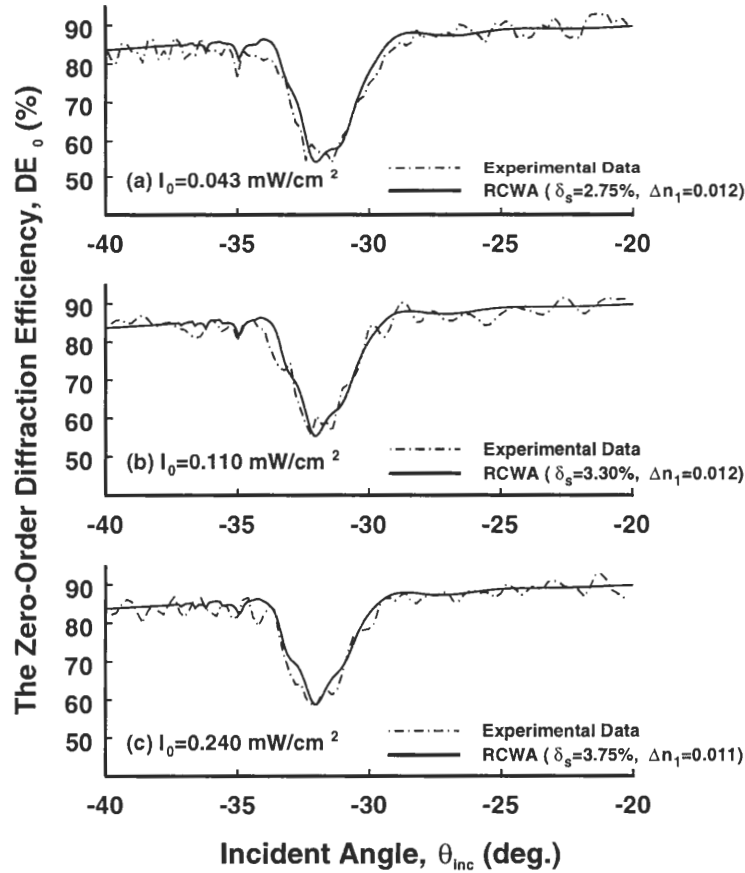


Figure 4.17: Angular selectivity of large slant-angle gratings with $\Lambda = 0.5 \mu\text{m}$ and $\phi = 45.0^\circ$ recorded by three different exposure intensities (a) $I_0 = 0.043 \text{ mW/cm}^2$, (b) 0.110 mW/cm^2 , and (c) 0.240 mW/cm^2 . The solid lines represent the RCWA fittings, and the dash lines represent the experimental measurements.

index modulations estimated by the RCWA fittings are $\delta_s = 2.75\%$, 3.30% , and 3.75% and $\Delta n_1 = 0.012, 0.012$, and 0.011 for $I_0 = 0.043, 0.110$, and 0.240 mW/cm^2 respectively.

4.4.5 Effects of Post-Baking Processing

A. Small Slant-Angle Gratings

Figure 4.18(a) shows the results of refractive-index modulations for small slant-angle gratings ($\Lambda = 0.5 \mu\text{m}, \phi = 13.71^\circ$) as a function of baking time for various baking temperatures ($T_b = 90, 120, 150^\circ\text{C}$) and exposure intensities ($I_0 = 0.043, 0.110, 0.240$, and 0.368 mW/cm^2). The corresponding optimum baking conditions of small slant-angle gratings for refractive-index modulations are summarized in Table 4.2. In general, the optimum baking conditions are $T_b = 120^\circ\text{C}$ and $t_b = 1.5 \text{ h}$, and the refractive-index modulation can increase from $\Delta n_1 \sim 0.013$ to $\Delta n_1 \sim 0.028$.

Moreover, Fig. 4.18(b) shows the deviations of Bragg angles for small slant-angle gratings as a function of baking time for various baking temperatures ($T_b = 90, 120, 150^\circ\text{C}$) and exposure intensities ($I_0 = 0.043, 0.110, 0.240$, and 0.368 mW/cm^2). Before post bak-

Table 4.2: Optimum baking conditions for slanted holographic gratings based on DuPont OmniDex613 photopolymers for exposure to $\lambda_{0,w} = 363.8 \text{ nm}$ UV light.

Small Slant-Angle Gratings ($\Lambda = 0.5 \mu\text{m}, \phi = 13.71^\circ$)				
Exposure Irradiance	Optimum Temperature	Optimum Time	$\Delta n_1 (\times 10^{-2})$	
$I_0 (\text{mW/cm}^2)$	$T_b (^\circ\text{C})$	$t_b (\text{h})$	Before Baking	After Baking
0.043	120	1.5	1.31	2.59
0.110	120	2.0	1.29	2.96
0.240	120	1.5	1.26	2.87
0.368	120	1.5	1.24	2.80
Large Slant-Angle Gratings ($\Lambda = 0.5 \mu\text{m}, \phi = 45.0^\circ$)				
Exposure Irradiance	Optimum Temperature	Optimum Time	$\Delta n_1 (\times 10^{-2})$	
$I_0 (\text{mW/cm}^2)$	$T_b (^\circ\text{C})$	$t_b (\text{h})$	Before Baking	After Baking
0.043	120	2.0	1.20	2.01
0.110	120	1.5	1.13	2.12
0.240	120	1.5	1.12	2.33

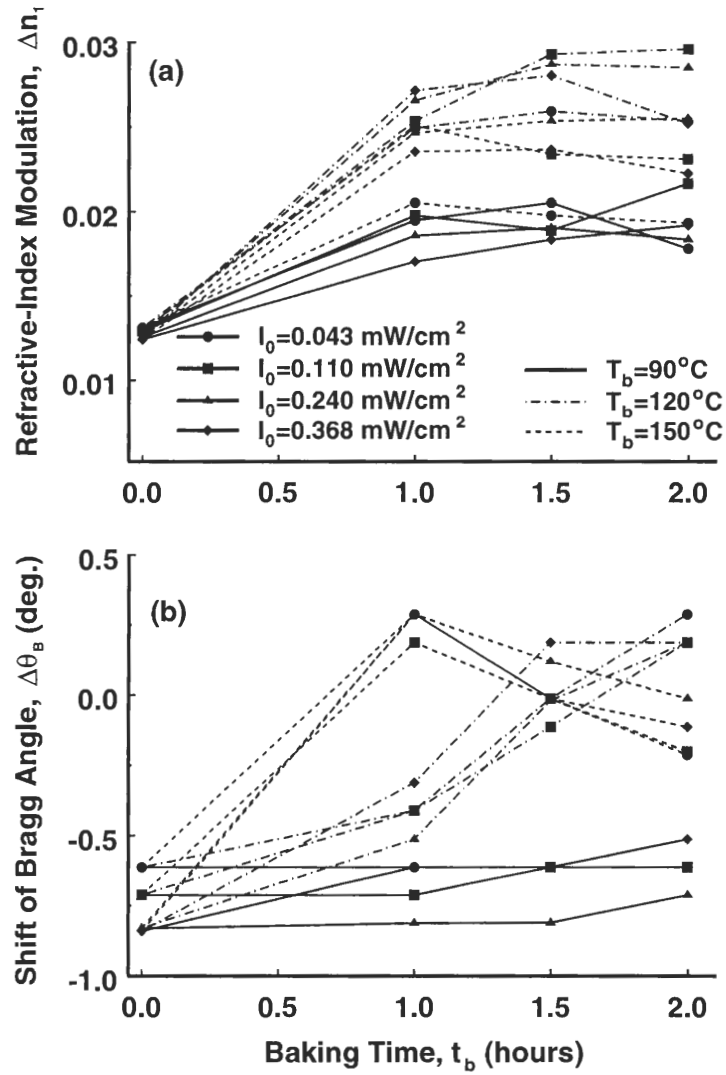


Figure 4.18: Effects of post-baking processing for small slant-angle gratings with $\Lambda = 0.5 \mu\text{m}$ and $\phi = 13.71^\circ$ (recorded by various exposure intensities I_0) on (a) the refractive-index modulations and (b) the shifts of Bragg angles.

ing, the shifts of Bragg angles are $\Delta\theta_B = -0.67^\circ, -0.69^\circ, -0.85^\circ$, and -0.86° for $I_0 = 0.043, 0.110, 0.240$, and 0.368 mW/cm^2 respectively. The negative values of $\Delta\theta_B$ correspond to the shrinkage of photopolymer during holographic recording. As seen in Fig. 4.18(b), for lower baking temperature ($T_b = 90^\circ\text{C}$), the shifts of Bragg angles ($\Delta\theta_B$) before and after baking are almost the same. The reason for this interesting phenomenon is that the material expansion resulting from thermal processing at lower baking temperature ($T_b = 90^\circ\text{C}$) is reversible. Therefore, the grating periods and slant angles do not change a lot after the grating samples (baked at $T_b = 90^\circ\text{C}$) are cooled down to room temperature. As a result, the shifts of Bragg angles are almost the same. However, as the baking temperature is increased to $T_b = 120^\circ\text{C}$, the shifts of Bragg angles ($\Delta\theta_B$) increase as the baking time increases. For example, for exposure intensity with $I_0 = 0.240 \text{ mW/cm}^2$, the deviations of Bragg angles are $\Delta\theta_B = -0.85^\circ, -0.51^\circ, -0.02^\circ$, and 0.19° for no post-baking, $t_b = 1.0, 1.5$, and 2.0 h respectively. The monotonical increase of $\Delta\theta_B$ for this baking temperature ($T_b = 120^\circ\text{C}$) results from the irreversible expansion and the decrease of the average refractive index ($n_{g,r} = 1.495$ instead of 1.50) after post-baking processing of the recording material, and thus, introduce a positive shift of Bragg angle. Furthermore, if the baking temperature is increased to $T_b = 150^\circ\text{C}$, the value of $\Delta\theta_B$ [as seen in Fig. 4.18(b)] increases as baking time increases from $t_b = 0.0 \text{ h}$ to $t_b = 1.0 \text{ h}$ because of the irreversible expansion and the decrease of the average refractive index during heating processing. However, as the baking time increases further (from $t_b = 1.0 \text{ h}$ to $t_b = 2.0 \text{ h}$), in addition to the irreversible expansion and the decrease of the average refractive index (resulting in a positive shift of Bragg angle), volatile components are lost during heating and result in the shrinkage, and therefore, a negative shift of Bragg angle. Therefore, $\Delta\theta_B$ start to decrease as the baking time increases further (from $t_b = 1.0 \text{ h}$ to $t_b = 2.0 \text{ h}$) at higher baking temperature ($T_b = 150^\circ\text{C}$). In general, the deviation of Bragg angle is strongly dependent on the baking temperature and the baking time.

Figure 4.19 shows an example of the curves of angular-dependent transmission

efficiencies for small slant-angle gratings ($\Lambda = 0.5 \mu\text{m}$, $\phi = 13.71^\circ$), recorded at $I_0 = 0.240 \text{ mW/cm}^2$, before and after baking at three different temperatures ($T_b = 90, 120$, and 150°C) for $t_b = 1.5 \text{ h}$. As shown in Fig. 4.19, after baking, the minimum values of transmission efficiencies decrease from $DE_0 = 69.87\%$ (no post-baking) to $DE_0 = 35.40\%$, 20.05% , and 20.38% for $T_b = 90, 120$, and 150°C with $t_b = 1.5 \text{ h}$ respectively. The decrease of DE_0 corresponds to the increase of the refractive-index modulation after post-baking, which is consistent with the result shown in Fig. 4.18(a). In addition, the new Bragg angles (relating to the incident angles for the minimum values of DE_0) determined by the RCWA shift from $\theta_{\text{new},B} = 16.16^\circ$ to $\theta_{\text{new},B} = 16.20^\circ, 16.99^\circ$, and 17.15° for $T_b = 90, 120$, and 150°C with $t_b = 1.5 \text{ h}$ respectively. It is noted that the new Bragg angle for the grating baked at $T_b = 120^\circ\text{C}$ for 1.5 h is $\theta_{\text{new},B} = 16.99^\circ$, which is very close to the designed value ($\theta_B = 17.01^\circ$). Therefore, the shrinkage resulting from the holographic recording can be compensated by the post-baking processing, especially for the baking conditions with

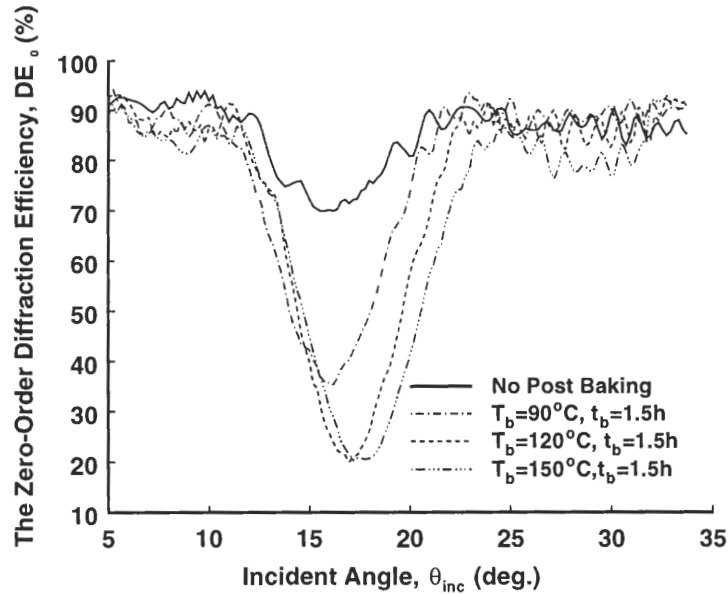


Figure 4.19: Angular-dependent transmission efficiencies of small slant-angle gratings ($\Lambda = 0.5 \mu\text{m}$ and $\phi = 13.71^\circ$) recorded by $I_0 = 0.240 \text{ mW/cm}^2$ before and after baking at three various temperatures ($T_b = 90, 120$ and 150°C) for $t_b = 1.5 \text{ h}$.

$T_b = 120^\circ C$ and $t_b = 1.5 h$.

B. Large Slant-Angle Gratings

For large slant-angle gratings with grating periods $\Lambda = 0.5 \mu m$ and slant angles $\phi = 45.0^\circ$, the results of both refractive-index modulations as a function of baking time for various baking temperatures ($T_b = 90, 120, 150^\circ C$) and exposure intensities ($I_0 = 0.043, 0.110$, and $0.240 mW/cm^2$) are summarized in Fig. 4.20(a). Similarly, the corresponding optimum baking conditions of large slant-angle gratings for refractive-index modulations are summarized in Table 4.2. In general, the refractive-index modulation can increase from $\Delta n_1 \sim 0.011$ to $\Delta n_1 \sim 0.022$ based on the optimum baking conditions with $T_b = 150^\circ C$ and $t_b = 1.5 h$.

Furthermore, Fig. 4.20(b) represents the shifts of Bragg angles for larger slanted gratings as a function of baking time for various baking temperatures ($T_b = 90, 120, 150^\circ C$) and exposure intensities ($I_0 = 0.043, 0.110$, and $0.240 mW/cm^2$). The trends of shifts of Bragg angles for large slant-angle gratings with respect to the baking temperature and the baking time are similar to the cases for small slant-angle gratings [as seen in Fig. 4.18(b)]. For the lower baking temperature ($T_b = 90^\circ C$), the post-baking processing does not compensate the negative shifts of Bragg angles resulting from holographic recording (i.e. the shifts of Bragg angles before and after baking are almost the same) because of the reversible thermal-expansion. However, for the baking temperature with $T_b = 120^\circ C$, the shifts of Bragg angles ($\Delta\theta_B$) increase monotonically as the baking time increases because of the irreversible expansion and the decrease of the average refractive index of gratings during heating processing. For example, for exposure intensity with $I_0 = 0.240 mW/cm^2$, the deviations of Bragg angles are $\Delta\theta_B = -1.07^\circ, -0.37^\circ, 0.03^\circ$, and 0.33° for no post-baking, $t_b = 1.0, 1.5$, and $2.0 h$ respectively. Therefore, the shift of Bragg angle caused by recording can be compensated by post-baking processing with $T_b = 120^\circ C$ and $t_b = 1.5 h$. In addition, as the baking temperature is increased to $T_b = 150^\circ C$, the values of $\Delta\theta_B$ increases as baking time increases from $t_b = 0.0 h$ to $t_b = 1.0 h$ because the irreversible expansion and

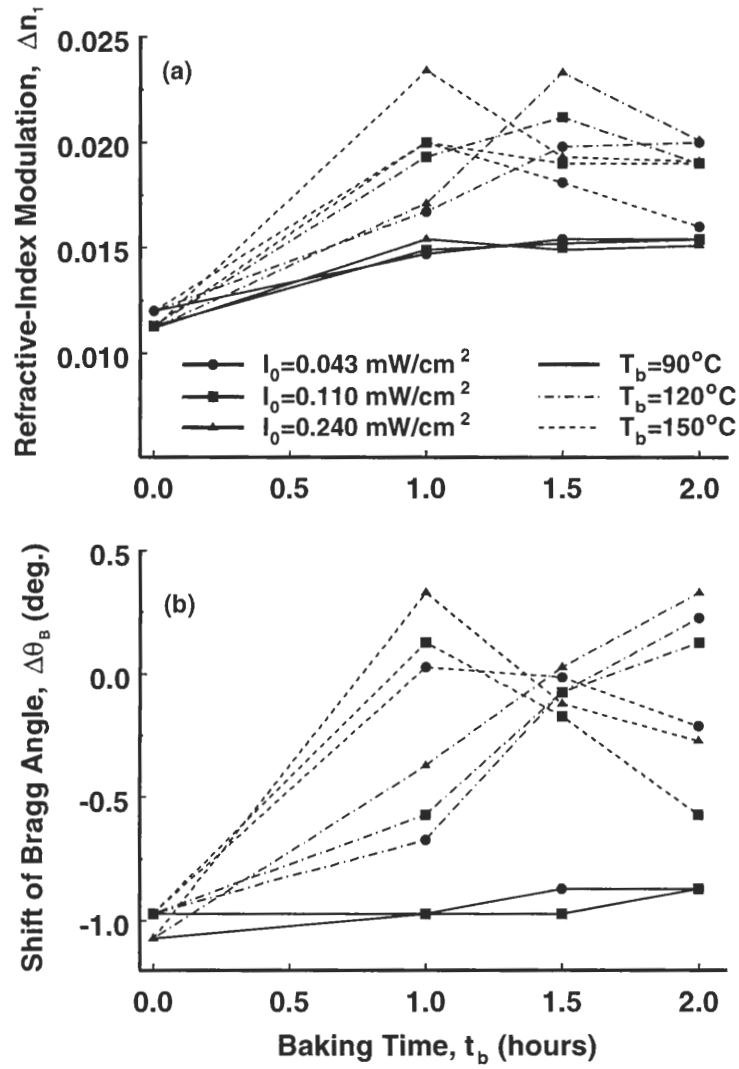


Figure 4.20: Effects of post-baking processing for large slant-angle gratings with $\Lambda = 0.5 \mu\text{m}$ and $\phi = 45.0^\circ$ (recorded by various exposure intensities I_0) on (a) the refractive-index modulations and (b) the shifts of Bragg angles.

the decrease of the average refractive index during heating processing are dominant as the baking time is less than one hour. However, as the baking time increases from $t_b = 1.0\text{ h}$ to $t_b = 2.0\text{ h}$, the shift of Bragg angle starts to decrease because the loss of volatile components during baking processing becomes more important and results in the negative shift of Bragg angle, and therefore, the decrease of the shift of Bragg angle.

Figure 4.21 shows an example of the curves of angular-dependent transmission efficiencies for large slant-angle gratings ($\Lambda = 0.5\text{ }\mu\text{m}$, $\phi = 45.0^\circ$), recorded at the exposure intensity of $I_0 = 0.240\text{ mW/cm}^2$, before and after baking at three different temperatures ($T_b = 90, 120$, and 150°C) for $t_b = 1.5\text{ h}$. As shown in Fig. 4.21, after baking, the minimum values of transmission efficiencies decrease from $DE_0 = 58.69\%$ (no post-baking) to $DE_0 = 39.44\%$, 11.24% , and 11.76% for $T_b = 90, 120$, and 150°C with $t_b = 1.5\text{ h}$ respectively. The decrease of DE_0 correspond to the increase of the refractive-index modulation after post-baking. In addition, the new Bragg angles (corresponding to the incident angles

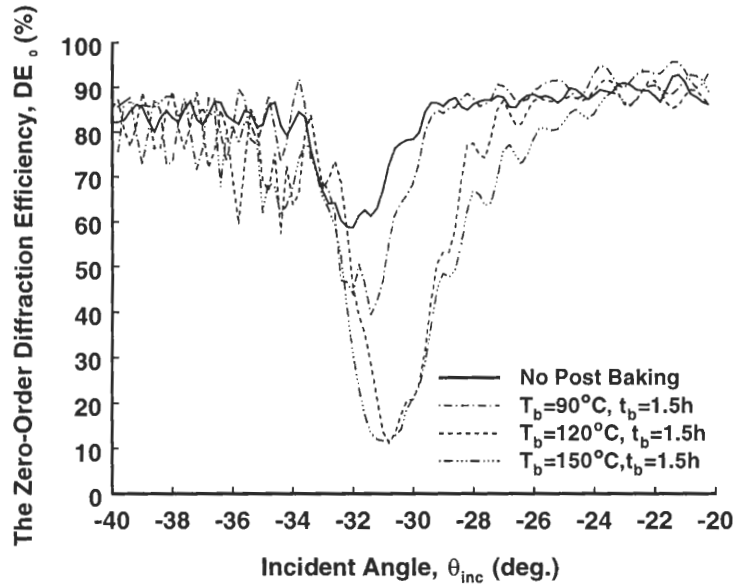


Figure 4.21: Angular-dependent transmission efficiencies of large slant-angle gratings ($\Lambda = 0.5\text{ }\mu\text{m}$ and $\phi = 45.0^\circ$) recorded by $I_0 = 0.240\text{ mW/cm}^2$ before and after baking at three various temperatures ($T_b = 90, 120$ and 150°C) for $t_b = 1.5\text{ h}$.

of the minimum values of DE_0) estimated by the RCWA shift from $\theta_{new,B} = -32.00^\circ$ to $\theta_{new,B} = -31.92^\circ, -30.90^\circ$, and -31.05° for $T_b = 90, 120$, and $150^\circ C$ with $t_b = 1.5 h$ respectively. It is noted that the new Bragg angle for the grating baked at $T_b = 120^\circ C$ for $1.5h$ is $\theta_{new,B} = -30.90^\circ$, which is very close to the designed value ($\theta_B = -30.93^\circ$). Therefore, the shrinkage resulting from the holographic recording can be compensated by the post-baking processing with $T_b = 120^\circ C$ and $t_b = 1.5 h$.

4.4.6 Characteristic Parameters of Holographic Photopolymers

Similarly, in order to study the dynamics of slanted grating formations in photopolymers, the real-time diffraction-monitoring technique in conjunction with the RCWA is applied to obtain the dynamic diffraction efficiencies, and thus, the growth curves of refractive-index modulations during hologram recording. For each exposure intensity, nine samples were prepared and exposed. Furthermore, in order to determine the characteristics parameters of DuPont OmniDex613 for slanted-grating fabrications, a quasi-Newton method incorporating with an error function [134] is used to optimize the fittings of theoretical results to the experimental data of refractive-index modulations. The detail optimization for the theoretical fittings to the experimental data can be found in Section 4.3.4. Figure 4.22 shows theoretical fittings to the experimental data of refractive-index modulations for both small and large slant-angle gratings. The solid lines represent the theoretical fittings based on the RCWA analysis as well as the characteristic parameters summarized in Table 4.3. The error bars represent the average, the maximum, and the minimum values of refractive-index modulations of these nine recorded samples at each specific exposure intensity. As shown in Fig. 4.22, the theoretical predictions are very good.

Table 4.3 summarizes the characteristic parameters of both small and large slant-angle gratings. As seen in Table 4.3, for the lower exposure intensity ($I_0 = 0.043 mW/cm^2$), the diffusion coefficient of a slanted grating is $D_0 \sim 0.6 \times 10^{-12} cm^2/sec$, which is smaller than that of an unslanted grating with $D_0 \sim 1.0 \times 10^{-12} cm^2/sec$ (as shown in Table 4.1).

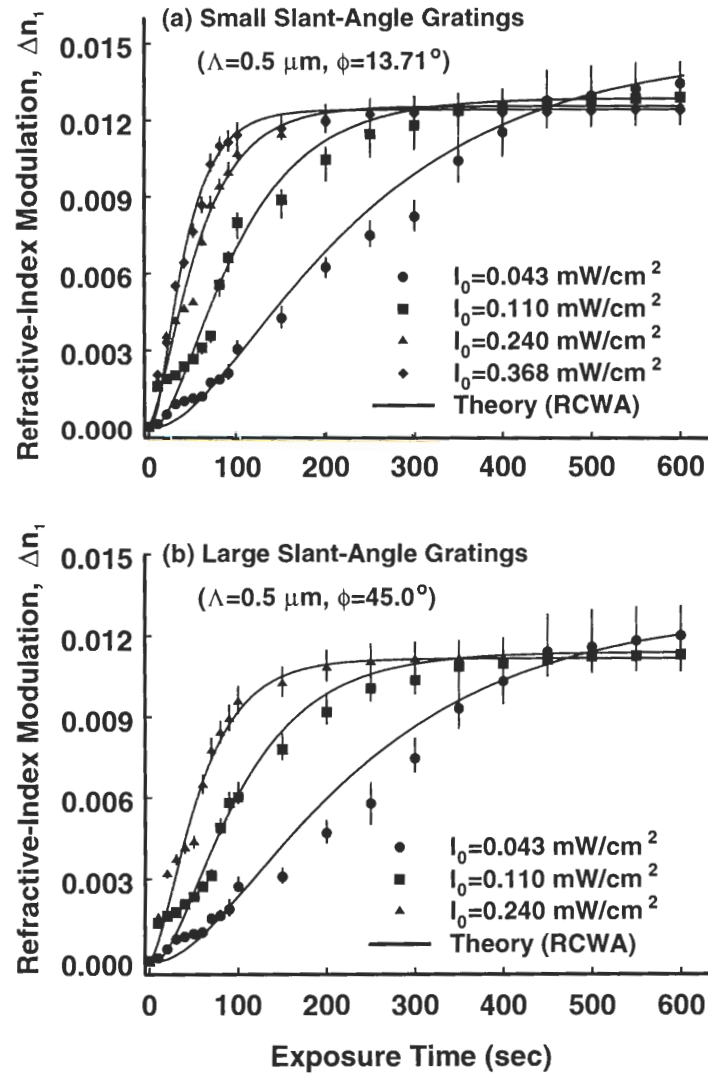


Figure 4.22: Comparisons between theoretical models and experimentally obtained refractive-index modulations for (a) small slant-angle gratings ($\Lambda = 0.5 \mu\text{m}$ and $\phi = 13.71^\circ$) and (b) large slant-angle gratings ($\Lambda = 0.5 \mu\text{m}$ and $\phi = 45.0^\circ$) recorded by various exposure intensities I_0 . The solid lines represent the theoretical results based on the RCWA and on characteristic parameters listed in Table 4.3.

Since the lower exposure intensity corresponds to the lower polymerization rate, the free monomer has longer diffusion distance. As a result, both the photopolymer-Mylar and the photopolymer-glass boundaries will affect the diffusion mechanism of free monomers, and thus, a smaller diffusion coefficient is obtained. However, for the higher exposure intensity ($I_0 = 0.240 \text{ mW/cm}^2$), since the free monomers are polymerized quickly, they cannot “sense” the existences of both the photopolymer-Mylar and the photopolymer-glass boundaries. In the other words, the diffusion mechanism of a slanted grating with a higher exposure intensity is the same as that of an unslanted one. Therefore, the diffusion coefficient of a slanted grating recorded by a higher intensity ($I_0 = 0.240 \text{ mW/cm}^2$) is $D_0 \sim 1.0 \times 10^{-12} \text{ cm}^2/\text{sec}$, which is very close to the corresponding value of an unslanted one (as seen in Table 4.1). Moreover, the average nonlocal response lengths for both small and large slant-angle gratings are $\sqrt{\sigma} = 50.61 \text{ nm}$ and 53.68 nm , which is close to the value of an unslanted grating ($\sqrt{\sigma} = 59.27 \text{ nm}$) [134].

Table 4.3: Characteristic parameters of slanted holographic grating formations based on the DuPont OmniDex613 photopolymers for exposure to $\lambda_{0,w} = 363.8 \text{ nm}$ UV light

Small Slant-Angle Gratings ($\Lambda = 0.5 \mu\text{m}, \phi = 13.71^\circ$)							
Exposure Irradiance $I_0(\text{mW/cm}^2)$	κ $\text{cm}/\sqrt{\text{mWsec}}$	R_D	σ_D	C_p cm^3/mole	C_m cm^3/mole	D_0 cm^2/sec	$\sqrt{\sigma}$ nm
0.043	0.032	1.40	0.49	3.8×10^{-4}	4.0×10^{-4}	0.588×10^{-12}	55.68
0.110	0.059	0.69	0.44	4.1×10^{-4}	4.3×10^{-4}	0.854×10^{-12}	52.77
0.240	0.072	0.49	0.39	4.6×10^{-4}	4.2×10^{-4}	1.094×10^{-12}	49.68
0.368	0.096	0.33	0.31	5.5×10^{-4}	5.6×10^{-4}	1.216×10^{-12}	44.29
Average	0.0648		0.41	4.5×10^{-4}	4.53×10^{-4}	0.938×10^{-12}	50.61
Large Slant-Angle Gratings ($\Lambda = 0.5 \mu\text{m}, \phi = 45.0^\circ$)							
Exposure Irradiance $I_0(\text{mW/cm}^2)$	κ $\text{cm}/\sqrt{\text{mWsec}}$	R_D	σ_D	C_p cm^3/mole	C_m cm^3/mole	D_0 cm^2/sec	$\sqrt{\sigma}$ nm
0.043	0.032	1.36	0.51	3.4×10^{-4}	3.6×10^{-4}	0.571×10^{-12}	56.81
0.110	0.058	0.68	0.47	3.7×10^{-4}	3.9×10^{-4}	0.828×10^{-12}	54.54
0.240	0.073	0.49	0.39	4.1×10^{-4}	3.9×10^{-4}	1.109×10^{-12}	49.68
Average	0.0543		0.46	3.73×10^{-4}	3.8×10^{-4}	0.836×10^{-12}	53.68

4.5 Summary and Discussion

The one-dimensional nonlocal diffusion equation governing the holographic grating formation in the DuPont photopolymer was rewritten in the dimensionless form and rigorously solved by use of the FDTD method. The behavior of hologram recording was studied with respect to dimensionless variables including dimensionless reaction rate R_D , dimensionless nonlocal variance parameters σ_D , and dimensionless time t_D . The preceding numerical analysis has shown that these dimensionless variables play an important roles on the monomer-concentration profile and the polymer-concentration profile and thus the refractive-index modulation.

For the larger dimensionless reaction rate ($R_D > 1.0$), the diffusion coefficient is larger than the polymerization rate, so the free monomers have enough time to propagate from the dark regions to the bright regions. Therefore, the polymer-concentration profile at the steady state resembles more a sinusoidal variation. However, for the smaller dimensionless reaction rate ($R_D < 1.0$), the polymerization occurs faster than diffusion, and results in two peaks of the polymer-concentration profile near the dark regions. In general the larger R_D , corresponding to smaller grating period, higher diffusion coefficient, or lower exposure irradiance, creates a higher refractive-index-modulation holographic grating. Besides the dimensionless reaction rate, the dimensionless nonlocal variance parameter σ_D is another important factor for the holographic recording. For a given R_D , the larger σ_D , more resembles a sinusoidal polymer-concentration profile, but the lower the visibility of the profile. Therefore, increasing σ_D , that is decreasing grating period or increasing nonlocal response length, results in a weaker first-order holographic grating.

In addition the numerical results of the FDTD method were compared to those of the four-harmonic-component approximation [84] to quantify the accuracy of the low-harmonic-component approximation. In general the accuracy of the four-harmonic-component approximation increases as R_D increases and σ_D increases. The error of four-harmonic-component

approximation was larger than 10% for $R_D < 1.0$ and for all value of σ_D . Thus, for smaller R_D ($R_D < 1.0$) the four-harmonic-component approximation is not a very precise numerical method for the analysis of holographic grating formations.

In this research the both unslanted and slanted holographic gratings were fabricated based on the DuPont OmniDex613 photopolymer using UV light of $\lambda_{0,w} = 363.8 \text{ nm}$. The dynamic behaviors of holographic grating formations were studied by use of real-time diffraction-monitoring technology. For unslanted holographic grating with the lower exposure irradiance (corresponding to the lower polymerization rate) the diffraction-efficiency growth curve rose monotonically with a slow rate. In this case more exposure time was needed to reach the steady state. As the exposure irradiance increased, the saturation level of refractive-index modulation increased because the polymerization rate was comparable to the diffusion rate. As a result, the grating profiles resembled more the illuminating fringe pattern. However, as the exposure irradiance increased furthermore, the diffraction-efficiency growth curve rose more quickly but reached a smaller saturation level because R_D became smaller resulting in more nonlinearity of the polymer-concentration profile. Moreover, instead of Kogelnik's theory we applied RCWA to convert the diffraction-efficiency growth curves to the corresponding index-modulation growth curves. Comparing to the RCWA, the error of refractive-index modulation predicted by Kogelnik's theory was $\sim 30\%$. We have also shown that post baking processing could enhance the refractive-index modulation by two times. According to experimental results the optimal baking temperature was $T_b = 120^\circ\text{C}$, and the optimal baking time was $t_b = 1.5 \text{ h}$. The characteristic parameters of holographic recording for unslanted gratings were estimated by fitting the theoretical model to the experimental data. In this research, the estimated diffusion coefficient and the nonlocal response length of the DuPont OmniDex613 photopolymer for unslanted gratings were $D_0 = 1.0 \times 10^{-12} \text{ cm}^2/\text{sec}$ and $\sqrt{\sigma} = 59.27 \text{ nm}$ respectively for a recording wavelength of 363.8 nm .

On the other hand, for the slanted holographic gratings, the dynamic behaviors

of slanted holographic grating formations are similar to those of unslanted holographic gratings. Applying the angular-selectivity experiment in conjunction with the RCWA fitting, the recording-shrinkage factor of the DuPont OmniDex613 photopolymer varies from $\delta_s \sim 2.75\%$ to $\delta_s \sim 4.20\%$, which is very close to the corresponding results found in literature [70, 75, 126–129]. For example, the shrinkage factor of a DuPont HRF600 photopolymer recorded at $\lambda_{0,w} = 514.5 \text{ nm}$ varies from $\delta_s \sim 2.8\%$ to $\delta_s \sim 3.5\%$ (depending on the exposure intensity) [126, 127]. However, for a DuPont HRF-600X001 photopolymer recorded at $\lambda_{0,w} = 514.6 \text{ nm}$, the shrinkage factor is $\delta_s \sim 5.25\%$ [128]. In addition, the effects of post-baking conditions on the refractive-index modulations and the shifts of Bragg angle of slanted holographic gratings are also investigated systematically. According to our experimental results, the post-baking processing can not only double the refractive-index modulations of slanted holographic gratings, which is consistent with those of unslanted gratings [134], but also compensate the recording shrinkage due to the irreversible thermal expansion, the decrease of the average refractive index, and the loss of volatile components of recording material during post-baking processing. It is noted that the first two effects (i.e. the irreversible thermal expansion and the decrease of the average refractive index) result in a positive shift of Bragg angle, and the third effect (i.e. the loss of volatile components) results in a negative shift of Bragg angle. In general, the optimal baking temperature and baking time are $T_b = 120^\circ\text{C}$ and $t_b = 1.5 \text{ h}$ respectively.

Finally, the characteristic parameters of DuPont OmniDex613 photopolymers for slanted holographic gratings are determined by fitting the theoretical model to the experimental data. In contrast to unslanted gratings that the diffusion coefficient is constant ($D_0 \sim 1.0 \times 10^{-12} \text{ cm}^2/\text{sec}$) for all exposure intensities, the diffusion coefficients for both small and large slant-angle gratings are dependent on exposure intensities. For the smaller exposure intensity ($I_0 = 0.043 \text{ mW/cm}^2$), the diffusion coefficient of a slanted grating is $D_0 \sim 0.6 \times 10^{-12} \text{ cm}^2/\text{sec}$ that is smaller than that of an unslanted grating because free monomers have longer diffusion distance, and therefore, both the photopolymer-Mylar and

the photopolymer-glass boundaries affect the diffusion process. However, as the exposure intensity increases, the diffusion coefficient increases and approaches to the value of an unslanted grating because the higher exposure intensity corresponds to higher polymerization rate, and as a result, the diffusion process of a slanted grating with a higher exposure intensity ($I_0 = 0.240 \text{ mW/cm}^2$) resembles that of an unslanted grating. Furthermore, the average nonlocal response lengths for both smaller and larger slanted gratings are $\sqrt{\sigma} = 50.61 \text{ nm}$ and 53.68 nm .

CHAPTER 5

OUTPUT VOLUME HOLOGRAPHIC GRATING COUPLERS

Output grating couplers have been proposed to provide a means of coupling an incident guided mode out of a waveguide for use in a variety of integrated optics applications [13–16]. However, for practical applications the preferential-order coupling is usually necessary to achieve a high coupling efficiency and a low optical cross-talk of the system. In literature, researchers have fabricated preferential-order surface-relief grating couplers for output coupling by using a variety of methods, such as gratings with reflective layers embedded in the substrate [25, 26, 42–45], blazed gratings [47, 48], and gratings comprised of parallelogramic surface profiles [49, 50]. However, these methods add complexity to the fabrication process because of complicated deposition, very precise electron-beam lithography, or chemically assisted ion-beam etching process.

On the other hand, volume holographic grating couplers (VHGCs), first proposed by Kogelnik and Sosnowski [52], provide high coupling efficiency and high preferential-order coupling in integrated optics [12, 20–22, 66]. Of course, VHGCs have limitations in both grating period and slant angle due to the limited recording wavelengths and the interference patterns available in the holographic recording. Fortunately, for practical applications, especially for couplers with high preferential-order coupling [20–22], the grating period is about from $0.3\mu m$ to $0.7\mu m$ (depending on the operation wavelength) and the slant angle is about 45 degrees, which can be fabricated by UV in conjunction with high-index

prisms [22, 66]. Furthermore, the use of photopolymers eliminates all of the chemical and etching steps, therefore reducing the fabrication complexity.

Because of the diverse applications of output grating couplers, many researchers have proposed various numerical methods to study their characteristics. Peng *et al.* [87, 88] first used modal analysis in conjunction with the leaky-mode approach to analyze rigorously the output surface-relief grating coupler for both TE and TM polarizations. Moreover, Tamir and Peng [89] studied the leakage parameters (relating to coupling efficiencies) of output surface-relief gratings with respect to grating duty cycle, grating refractive indices, grating height, grating period, and grating profile on the basis of perturbation theory. Izhaky and Hardy [90, 91] proposed the unified coupled-mode formalism to study the problems of parallel waveguides with or without surface-relief gratings. Specifically, they studied the effects of grating parameters including groove depths, duty cycles, operation wavelengths, and refractive indices on the grating coupler performance. Viewing the surface-relief grating as a sequence of two alternating types of waveguide sections connected by means of step discontinuities, Borsboom and Frankena [92, 93] used the modal representation of the fields in the waveguide sections with scattering matrices of step discontinuities to study the two-dimensional uniform and focusing (chirped) surface-relief grating couplers with finite lengths for output coupling. In addition, Dinesen and Hesthaven [94, 95] proposed a boundary variation method (BVM) for the analysis of both infinite periodic and finite aperiodic (chirped) output surface-relief grating couplers in two- and three-dimensional structures. Recently, Lalanne *et al.* [96–98] applied the Fourier-modal method to analyze the waveguide and the surface-relief grating diffraction problems with the introduction of a virtual periodicity along the transverse direction in conjunction with artificial absorbers at the boundaries of the elementary cells of the periodic structure.

For the analysis of output VHGCs, Harris *et al.* [99] applied the modified Born approximation, the WKB approach, and the reciprocity theory, to analyze VHGCs without solving rigorously Maxwell’s equations in the grating region. Peng *et al.* [88] applied modal

analysis in conjunction with the leaky-mode approach to analyze an output VHGC with a sinusoidal permittivity variation. Wang and Dilauro [100] applied the thin grating decomposition method in conjunction with conventional waveguide analysis to analyze an output VHGC embedded in a waveguide. Jones *et al.* [101] also analyzed an output VHGC embedded in a waveguide using the modal theory and Svidzinskii's theory. In addition, Schultz *et al.* [20] exploited the RCWA in conjunction with the leaky-mode (RCWA/LM) approach to analyze, design, and fabricate output VHGCs. However, the leaky-mode approach does not take into account the effects of the modal reflection and the additional mode excitation resulting from the discontinuity between the waveguide and the holographic grating coupler and generally is not an accurate representation of the radiated (diffracted) field.

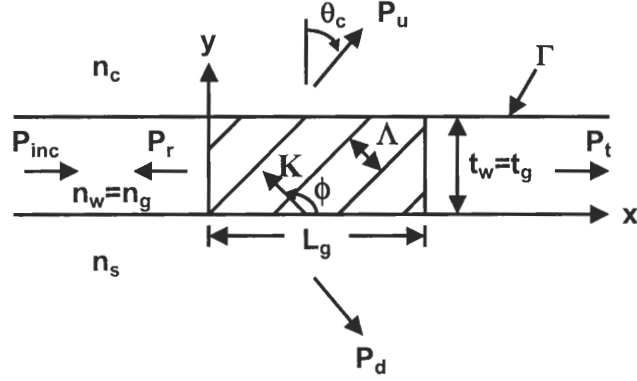
Although different numerical methods have been applied to study the output-coupling characteristics for both surface-relief grating couplers and VHGCs, there has been no rigorous analysis for output VHGCs taking into account discontinuity effects as well as multimode excitation and interference. In this chapter, FDFD method is applied to analyze rigorously an output VHGC [139] and compares to the RCWA/LM approach with respect to coupling efficiencies, branching ratios, and leakage parameters. Two basic configurations of waveguide output-couplers comprised of a VHGC in the waveguide film region and in the waveguide cover region are analyzed. Both normal (zero-degree) and off-normal (45-degree) output coupling are investigated. Moreover, Both TE and TM polarizations are considered. Furthermore, far-field distributions obtained from FDFD-calculated near-field distributions using rigorous diffraction integrals [17] are also presented. The diffraction integral for the far-field calculation can be found in Appendix C.

5.1 Output Volume Holographic Grating Coupler Configurations

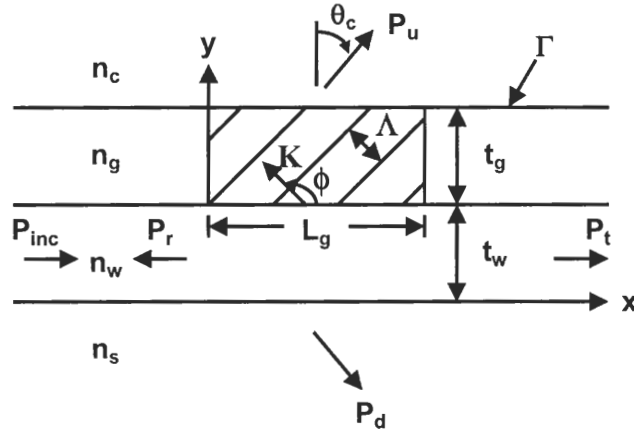
In this research, an output VHGC in the waveguide film region as well as in the waveguide cover region [shown in Figs. 5.1(a) and 5.1(b) respectively] are analyzed by use of the FDFD method [55] in conjunction with the uniaxial perfectly matched layer (UPML) [55, 117]. For both configurations, the waveguide consists of a glass substrate with refractive index n_s , a waveguide film layer with refractive index n_w and thickness t_w , and a cover layer with refractive index n_c . In addition, the waveguide mode is incident from the left onto the grating coupler. The average refractive index, the thickness, and the length of the holographic grating are n_g , t_g , and L_g respectively. In addition, the grating vector \mathbf{K} is defined as $\mathbf{K} = |\mathbf{K}|(\hat{x} \cos \phi + \hat{y} \sin \phi)$ where $|\mathbf{K}| = 2\pi/\Lambda$, Λ is the grating period, ϕ is the slant angle of the grating, and \hat{x} , \hat{y} are the unit vectors along the x and y directions respectively. The permittivity in the grating region can be represented by Eq. 2.1.

As shown in Fig. 5.1, a guided mode of power P_{inc} is incident on the output VHGC. The output VHGC is designed to couple out the guided mode into the cover region with a pre-specified propagation direction θ_c . After using the FDFD method to calculate the scattered fields (\mathbf{E}_z or \mathbf{H}_z components for TE or TM polarization respectively), the fast Fourier transform (FFT) (as seen in Section 2.4) is applied to calculate the corresponding Fourier (angular) spectrums F of the upward and the downward fields, and therefore, the diffracted powers coupled into the cover (upward direction), P_u , and into the substrate (downward direction), P_d . In addition, the modal decomposition of guided fields is used to calculate both the transmitted power, P_t , and the reflected power, P_r . The modal decomposition of the power calculations of waveguide modes can be found in Appendix D. In order to quantify the performance of an output VHGC, the coupling efficiency CE_i is defined (in percent) as

$$CE_i = \frac{P_i}{P_{inc}} \times 100, \quad (5.1)$$



(a)



(b)

Figure 5.1: Two basic configurations of waveguide output-couplers comprised of a VHGC (a) in the waveguide film region and (b) in the waveguide cover region. The waveguide consists of a cover region with refractive index n_c , a film region with refractive index n_w , and a substrate region with refractive index n_s . The thickness of the waveguide film region is t_w . The volume holographic grating has a grating vector $|\mathbf{K}| = 2\pi/\Lambda$ (Λ is the grating period), a slant angle ϕ , a length L_g , and a thickness t_g . The average refractive index in the grating region is n_g . The designed out-coupling angle in the cover region is θ_c . The power of the incident beam is P_{inc} . P_u , P_d , P_t , and P_r denote the upward-coupling power, the downward-coupling power, the transmitted power, and the reflected power, respectively.

where P_{inc} is the incident power, and P_i ($i = u, d, r, t$) is the diffracted power in the specific coupling direction. The branching ratio BR , relating to the preferential-order coupling, is defined (in percent) as

$$BR = \frac{P_u}{P_u + P_d} \times 100. \quad (5.2)$$

Furthermore, the leakage parameter α_l , corresponding to the coupling efficiency, is defined as [22]

$$\alpha_l = -\frac{1}{2L_g} \ln \frac{P_t}{P_{inc}}. \quad (5.3)$$

In order to calculate the far-field distribution, the diffraction integral [17], relating the far field at an arbitrary point in space to the near-field profile along a boundary Γ (defined as the interface between the grating layer and the cover region), is applied in this research.

5.2 Output Volume Holographic Grating Couplers in the Waveguide Film Region

The output VHGC analyzed in this research is comprised of a fused-silica glass substrate of refractive index $n_s = 1.4567$, and of air as the cover region of refractive index $n_c = 1.0$. For an output VHGC in the waveguide film region [as shown in Fig. 5.1(a)], the waveguide material is assumed to be the DuPont's OmniDex613 photopolymer with refractive index $n_w = 1.5$. The thicknesses of the waveguide and the grating are $t_w = t_g = 1.8 \mu m$. The thickness t_w is designed to support a single TE mode and a single TM mode in this waveguide. The propagation constants for both TE₀ mode and TM₀ mode in this waveguide are $\beta_{TE_0} = 9.335 \mu m^{-1}$ and $\beta_{TM_0} = 9.327 \mu m^{-1}$, respectively. In addition, the grating material is DuPont's OmniDex613 photopolymer with average dielectric constant $\epsilon_0 = 2.25$ ($n_g = 1.5$) and modulation $\epsilon_1^c = 0.06$ ($\Delta n_1 \simeq 0.02$) [134]. The grating period Λ and the slant angle ϕ of the VHGCs for both zero-degree ($\theta_c = 0^\circ$) and 45-degree ($\theta_c = 45^\circ$) output coupling are designed using the phase-matching conditions for the first diffracted order [22],

which will be discussed in Section 7.1. Based on the phase-matching conditions for the first diffracted order, the design parameters of an output VHGC in the waveguide film region for both zero- and 45-degree output coupling are summarized in Table 5.1. VHGCs of two different lengths ($L_g = 100, 250 \mu m$) are considered. Furthermore, the incident waveguide mode used in this analysis is TE_0 or TM_0 for TE or TM polarization respectively. The freespace wavelength of the incident light is assumed to be $\lambda_0 = 1.0 \mu m$.

Table 5.1: Design parameters of output volume holographic grating couplers

Output VHGCs in the Waveguide Film Region				
	TE Polarization		TM Polarization	
Coupling Angle θ_c (deg.)	Λ (nm)	ϕ (deg.)	Λ (nm)	ϕ (deg.)
0	473.7	-45.28	473.9	-45.30
45	651.5	-59.52	651.7	-59.56
Output VHGCs in the Waveguide Cover Region				
	TE Polarization		TM Polarization	
Coupling Angle θ_c (deg.)	Λ (nm)	ϕ (deg.)	Λ (nm)	ϕ (deg.)
0	470.6	-44.91	470.9	-44.94
45	647.3	-58.91	647.7	-58.96

5.2.1 Output Coupling Efficiencies

Figure 5.2 shows the numerical results of the transverse field profiles at $x = 0 \mu m$ and $x = 100 \mu m$ of an output VHGC in the waveguide film region. Both TE and TM polarizations with zero- and 45-degree output coupling are presented. As seen in Figs. 5.2(a) and 5.2(c), the electric fields of TE polarization for both zero- and 45-degree output coupling are coupled into the substrate as well as into the cover region. On the other hand, for TM polarization with zero-degree output coupling [as shown in Fig. 5.2(b)] the magnetic field is weakly coupled out of the waveguide. However, comparing Figs. 5.2(b) and 5.2(d), the magnetic field coupled into the cover region of 45-degree output coupling is stronger than that of the zero-degree output coupling for TM polarization. Therefore, the characteristics

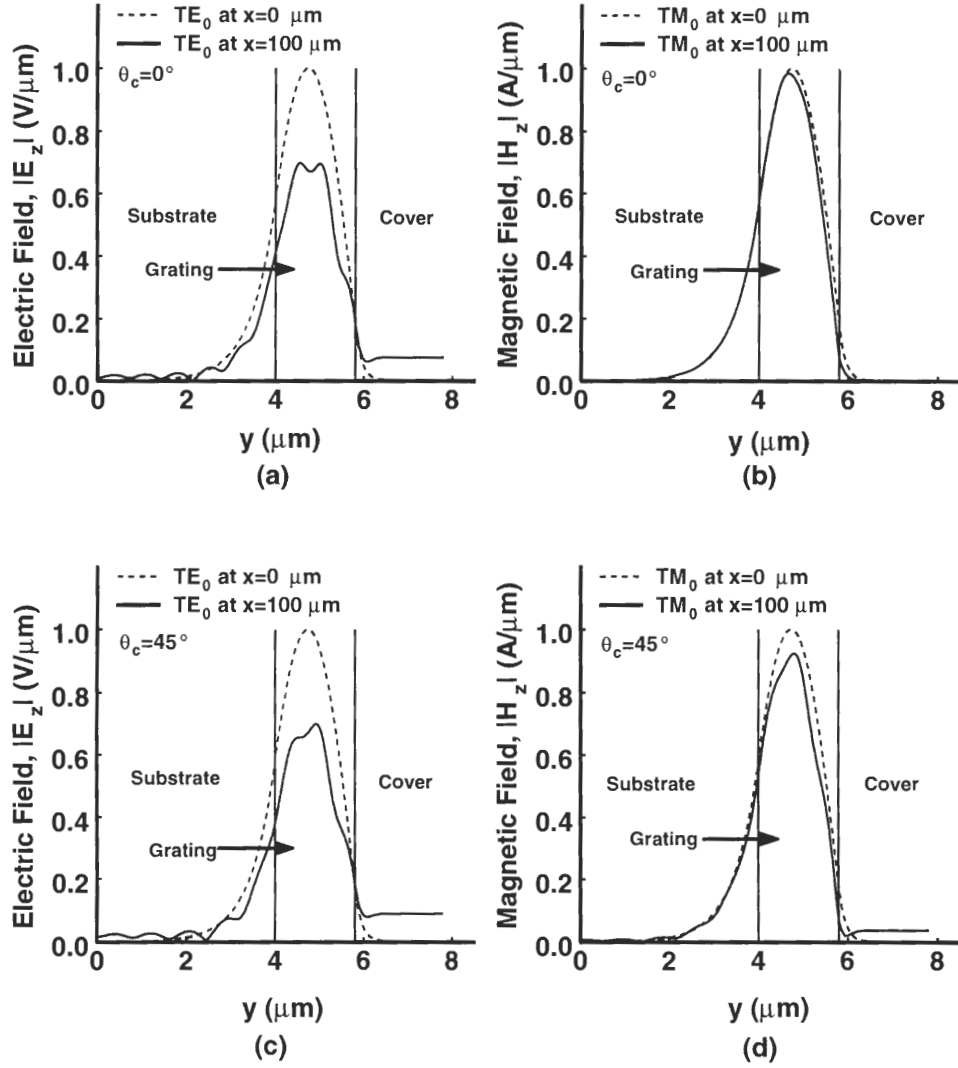


Figure 5.2: The transverse field profiles of a VHGC in the waveguide film region for (a) TE polarization with zero-degree output coupling, (b) TM polarization with zero-degree output coupling, (c) TE polarization with 45-degree output coupling, and (d) TM polarization with 45-degree output coupling. The dash lines and the solid lines represent the field profiles at $x = 0$ μm (i.e. incident waveguide mode) and at $x = 100$ μm respectively.

of VHGCs are strongly dependent on the incident polarization and the output-coupling angle. In order to quantify the performances of output VHGCs for both TE and TM polarizations, the coupling efficiencies CE , branching ratios BR , and leakage parameters α_l of VHGCs for both zero- and 45-degree output coupling are summarized in Table 5.2. The numerical results of the FDFD method are also compared to those of the RCWA/LM approach.

As seen in Table 5.2, the upward coupling efficiencies CE_u of TE polarization calculated using the FDFD method are much higher than those of TM polarization for zero-degree output coupling, which are in agreement with Figs. 5.2(a) and 5.2(b). For example, as the holographic grating length is $L_g = 250 \mu m$, the upward coupling efficiency of TE polarization is $CE_u = 76.38\%$; in contrast, the upward coupling efficiency of TM polarization is only $CE_u = 0.29\%$. In addition, the average leakage parameters predicted by the FDFD method for both TE and TM polarizations are $\alpha_l = 0.33 \times 10^{-2} \mu m^{-1}$ and $\alpha_l = 0.74 \times 10^{-5} \mu m^{-1}$, respectively. On the other hand, for 45-degree output coupling, the upward coupling efficiencies CE_u of TM polarization calculated using the FDFD method are comparable to those of TE polarization. For example, as the holographic grating length is $L_g = 250 \mu m$, the upward coupling efficiency of TE polarization is $CE_u = 77.20\%$; however, the upward coupling efficiency of TM polarization is $CE_u = 29.79\%$. In addition, the average leakage parameters predicted by the FDFD method for both TE and TM polarizations are $\alpha_l = 0.37 \times 10^{-2} \mu m^{-1}$ and $\alpha_l = 0.73 \times 10^{-3} \mu m^{-1}$, respectively. Moreover, with respect to the cases of zero-degree output coupling for TE polarization, the average branching ratio BR of 45-degree output coupling is 92.27%, which is smaller than that of zero-degree output coupling (95.16%).

By comparing the FDFD method to the RCWA/LM approach for an output VHGC in the waveguide film region (as seen in Table 5.2), the branching ratios estimated using the FDFD method for both TE and TM polarizations and for both zero- and 45-degree output coupling are generally smaller than the RCWA/LM predicted values. The reason of

higher branching ratio predicted by use of the RCWA/LM approach is that the RCWA/LM approach does not consider the modal reflection and the scattering into radiation resulting from the discontinuity between the waveguide and the grating. In addition, the leaky-mode approach is only an approximation of the radiation field. In other words RCWA/LM approach only provides relative quantities of upward and downward coupling efficiencies. However, the FDFD method rigorously solves the output VHGC without neglecting the effect of discontinuity. As a result, the FDFD method calculates absolute quantities instead

Table 5.2: Performance of an output VHGC in the waveguide film region and comparison with the RCWA/leaky-mode (RCWA/LM) approach for zero- and 45-degree output coupling

Outcoupling Angle, $\theta_c = 0^\circ$							
TE Polarization ($\Lambda = 473.7 \text{ nm}$, $\phi = -45.28^\circ$)							
Numerical Method	$L_g(\mu m)$	$CE_u(\%)$	$CE_d(\%)$	$CE_t(\%)$	$CE_r(\%)$	$BR(\%)$	$\alpha_l(1/\mu m)$
FDFD	100	46.72	2.33	50.92	0.03	95.25	0.34×10^{-2}
	250	76.38	3.96	19.64	0.02	95.07	0.33×10^{-2}
RCWA/LM	100	45.60	0.02	54.38	0.00	99.96	0.31×10^{-2}
	250	78.16	0.03	21.81	0.00	99.96	0.31×10^{-2}
TM Polarization ($\Lambda = 473.9 \text{ nm}$, $\phi = -45.30^\circ$)							
Numerical Method	$L_g(\mu m)$	$CE_u(\%)$	$CE_d(\%)$	$CE_t(\%)$	$CE_r(\%)$	$BR(\%)$	$\alpha_l(1/\mu m)$
FDFD	100	0.13	0.03	99.84	0.00	81.25	0.80×10^{-5}
	250	0.29	0.05	99.66	0.00	85.29	0.68×10^{-5}
RCWA/LM	100	0.09	0.00	99.91	0.00	97.67	0.44×10^{-5}
	250	0.22	0.00	99.78	0.00	97.67	0.44×10^{-5}
Outcoupling Angle, $\theta_c = 45^\circ$							
TE Polarization ($\Lambda = 651.5 \text{ nm}$, $\phi = -59.52^\circ$)							
Numerical Method	$L_g(\mu m)$	$CE_u(\%)$	$CE_d(\%)$	$CE_t(\%)$	$CE_r(\%)$	$BR(\%)$	$\alpha_l(1/\mu m)$
FDFD	100	48.68	4.07	47.25	0.00	92.28	0.38×10^{-2}
	250	77.20	6.48	16.32	0.00	92.26	0.36×10^{-2}
RCWA/LM	100	45.74	3.84	50.42	0.00	92.26	0.34×10^{-2}
	250	75.61	6.34	18.05	0.00	92.26	0.34×10^{-2}
TM Polarization ($\Lambda = 651.7 \text{ nm}$, $\phi = -59.56^\circ$)							
Numerical Method	$L_g(\mu m)$	$CE_u(\%)$	$CE_d(\%)$	$CE_t(\%)$	$CE_r(\%)$	$BR(\%)$	$\alpha_l(1/\mu m)$
FDFD	100	13.25	0.32	86.43	0.00	97.64	0.73×10^{-3}
	250	29.79	0.68	69.53	0.00	97.77	0.73×10^{-3}
RCWA/LM	100	13.55	0.26	86.19	0.00	98.14	0.74×10^{-3}
	250	30.45	0.58	68.97	0.00	98.14	0.74×10^{-3}

of relative quantities of coupling efficiencies for output VHGCs.

5.2.2 Electric and Magnetic Fields

In order to gain a better physical understanding of the behavior of an output VHGC in the waveguide film region, it is useful to represent the amplitude (corresponding to the coupling efficiency) and the phase (corresponding to the direction of wave propagation) patterns of total field, which includes both the incident and the diffracted fields calculated by the FDFD method. Figure 5.3 shows the total field patterns of an output VHGC with $L_g = 100 \mu m$ in the waveguide film region illuminated by both TE_0 and TM_0 modes for both zero- and 45-degree output coupling. The waveguide layer is located between $y = 4.0 \mu m$ and $y = 5.8 \mu m$, and the volume holographic grating is located between $x = 0.5 \mu m$ and $x = 100.5 \mu m$. Dark areas indicate regions of low values (of field or phase), and lighter areas indicate regions of higher values.

As seen in Fig. 5.3(a), the amplitude of the electric field $|E_z|$ in the waveguide for TE polarization with zero-degree output coupling decreases as x increases because more power is coupled out of the waveguide along the propagation direction. In this case, the upward coupling efficiency is 46.72% (as seen in Table 5.2). However, for the TM polarization with zero-degree output coupling [as shown in Fig. 5.3(b)], the amplitude of the magnetic field $|H_z|$ remains almost constant because the upward coupling efficiency is very small ($CE_u = 0.13\%$). Therefore, the grating coupler is polarization-dependent for zero-degree output coupling. The results are in agreement with Figs. 5.2(a) and 5.2(b). On the other hand, as seen in the phase patterns of zero-degree output coupling for both TE and TM polarizations, the phase fronts in the cover region are parallel to the surface of the waveguide. In other words the directions of wave propagation in the cover region for both TE and TM polarizations are perpendicular to the surface of the waveguide (i.e. $\theta_c = 0^\circ$), which are in agreement with the design of zero-degree output coupling. In addition, the radiation fields due to scattering into radiation modes resulting from the discontinuity between the

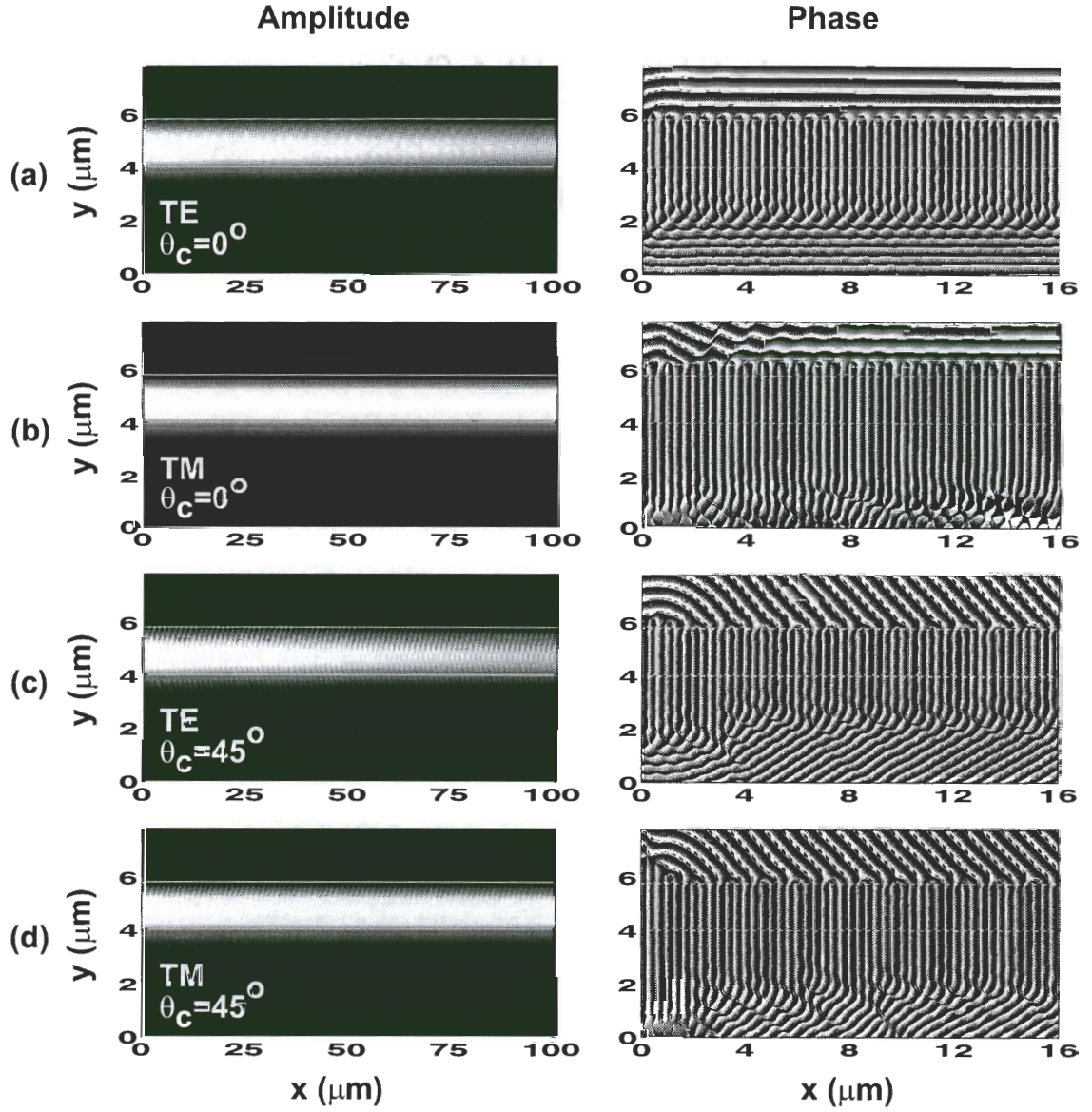


Figure 5.3: Two-dimensional field-amplitude and field-phase patterns of an output VHGC with $L_g = 100 \mu m$ and $t_g = t_w = 1.8 \mu m$ in the waveguide film region for (a) TE polarization with zero-degree output coupling, (b) TM polarization with zero-degree output coupling, (c) TE polarization with 45-degree output coupling, and (d) TM polarization with 45-degree output coupling.

waveguide and the grating can be observed at $x < 2.0 \mu m$ in the cover as well as in the substrate for both TE and TM polarizations.

In the case of the 45-degree output coupling [as seen in Figs. 5.3(c) and 5.3(d)], the field amplitudes in the waveguide decrease along the propagation direction for both TE and TM polarizations. In contrast to zero-degree output coupling, the grating coupler is nearly polarization-independent for 45-degree output coupling. From the phase patterns, it can be seen that the directions of wave propagation in the cover are 45 degrees. Similarly, the radiation fields due to scattering into radiation modes can also be observed near the discontinuity between the waveguide and the grating. Moreover, as seen in the phase patterns of Fig. 5.3, the incident waveguide mode interacts with the whole grating and propagates along the x direction without any mode conversion.

The corresponding intensities of Fourier spectrums of the upward field profiles (E_z or H_z for TE or TM polarization) at $y = 7.8 \mu m$ of output VHGCs with $L_g = 100 \mu m$ in the waveguide film region for both zero- and 45-degree output coupling are shown in Fig. 5.4. As seen in Figs. 5.4(a) and 5.4(b) (corresponding to the design of zero-degree output coupling), the intensities of the Fourier spectrums for both TE and TM polarizations are centered at $\theta_c = 0.34^\circ$ and at $\theta_c = 0.28^\circ$, respectively. In contrast, the Fourier-spectrum intensities of 45-degree output coupling are centered at $\theta_c = 45.50^\circ$ for TE polarization [as seen in Fig. 5.4(c)] and at $\theta_c = 45.46^\circ$ for TM polarization [as seen in Fig. 5.4(d)]. The reason of the difference between the calculated value of θ_c and the designed value of θ_c is that the grating period and the slant angle are designed based on the propagation constant of a waveguide without the grating modulation being considered (i.e. the grating is considered homogeneous with an average refractive index). The presence of the modulation affects slightly the real part of the propagation constant which results in the small difference of the diffracted angle θ_c from their designed values.

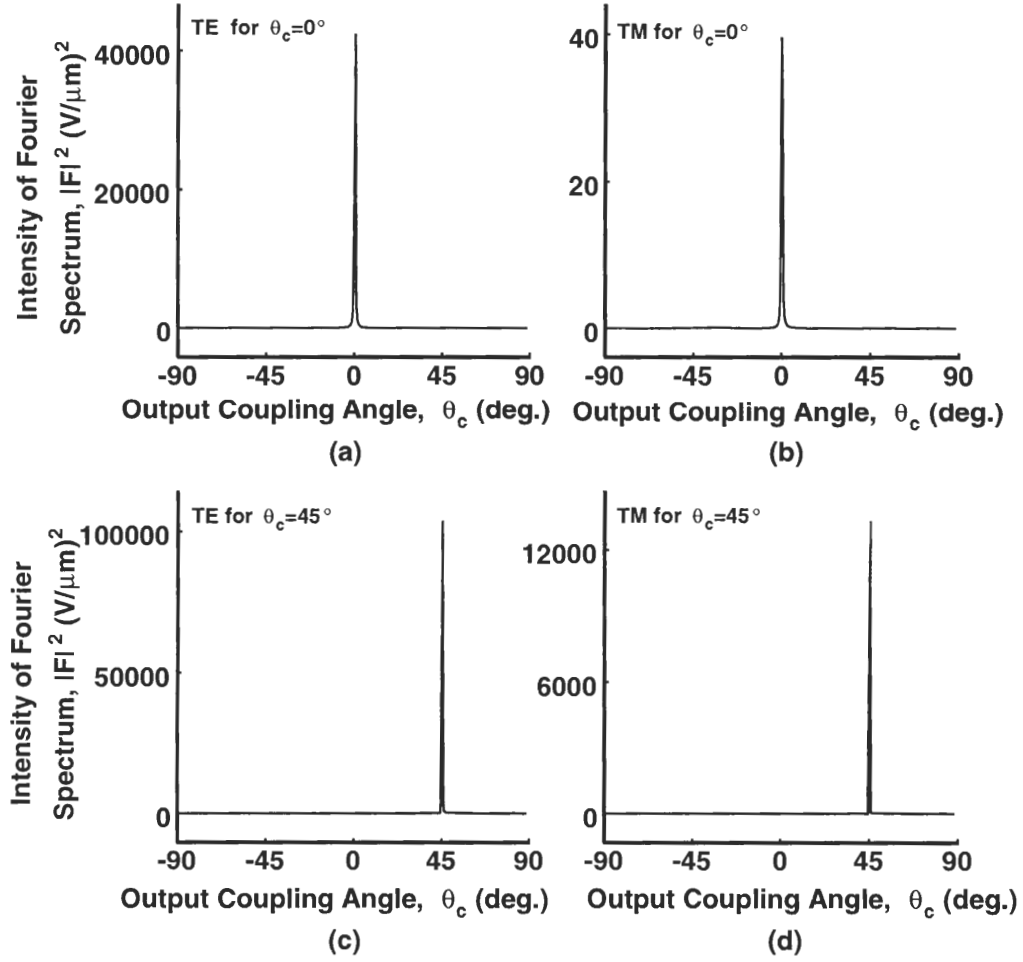


Figure 5.4: Corresponding intensities of Fourier spectrums of the upward field profiles at $y = 7.8 \mu m$ of an output VHGC with $L_g = 100 \mu m$ in the waveguide film region for (a) TE polarization with zero-degree output coupling, (b) TM polarization with zero-degree output coupling, (c) TE polarization with 45-degree output coupling, and (d) TM polarization with 45-degree output coupling.

5.2.3 Near and Far Fields

Figure 5.5 shows the normalized electric field intensities at the top surface of the waveguide film layer for the case of an output VHGC in the waveguide film region with zero-degree output coupling for TE polarization. As seen in Fig. 5.5, since the RCWA/LM approach does not take into account the effect of the incident mode, the normalized electric field intensity of the RCWA/LM approach is only an exponential decay along the x direction. This exponential decay is due to the leaky mode that is coupled through the grating. However, for the FDFD method, the normalized electric field intensity is not only an exponential decay but also contains an oscillatory term because the FDFD method provides a rigorous analysis by including the incident mode in the calculation. The oscillation with a period of $2\pi/\beta_{TE_0} = 0.672 \mu m$ results from the interference between the TE_0 waveguide mode and the radiation field. In order to interpret the oscillatory term, it is useful to represent the

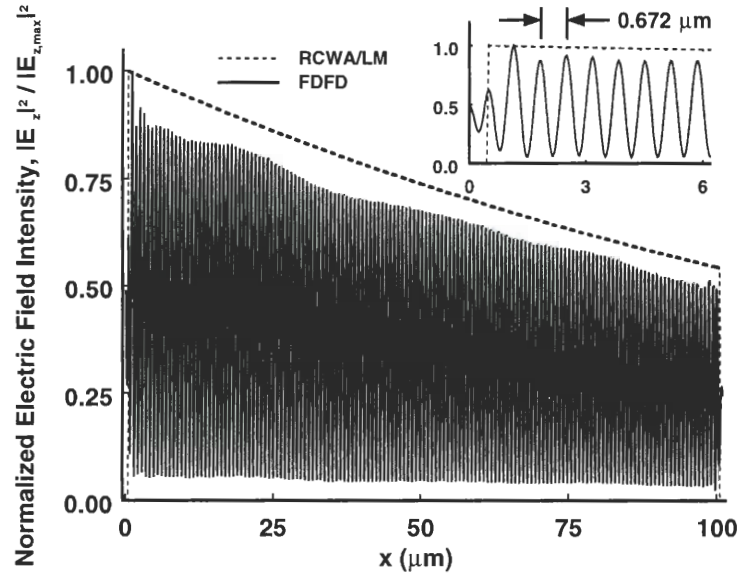


Figure 5.5: Normalized field intensity at the top surface of the waveguide film layer (i.e. at $y = 5.8 \mu m$) of an output VHGC with $L_g = 100 \mu m$ in the waveguide film region for TE polarization with zero-degree output coupling. The dash lines and the solid lines represent the results of the RCWA/LM approach and the FDFD method respectively.

total field in the waveguide film region. Since the reflection is less than 0.1% (as seen in Table 5.2), the reflected field can be neglected. As a result, the total field in the waveguide film region and along the film-cover boundary can be represented as

$$E_{z,tot} = [1 + C_0 \exp(-j\beta_{TE_0}x)] \exp(-\alpha_l x), \quad (5.4)$$

where $\exp(-\alpha_l x)$ corresponds to the field component of the diffracted field, $\exp(-j\beta_{TE_0}x)$ corresponds to the field component of the leaky TE_0 mode in the waveguide, and $C_0 = |C_0| \exp(j\psi_0)$ is a complex constant that represents the waveguide mode at the film-cover interface. Therefore, the electric field intensity can be written as

$$I_{z,tot} = |E_{z,tot}|^2 = \exp(-2\alpha_l x) [1 + |C_0|^2 + 2|C_0| \cos(\beta_{TE_0}x - \psi_0)]. \quad (5.5)$$

From Eq. (5.5), we can see the electric field intensity is an exponential decay with decay rate $2\alpha_l$ [from the term of $\exp(-2\alpha_l x)$] and it has an oscillatory term with a period of $2\pi/\beta_{TE_0}$ [from the term of $\cos(\beta_{TE_0}x - \psi_0)$]. As seen in Fig. 5.5, the decay rate is about $2\alpha_l = 0.61 \times 10^{-2} \mu m^{-1}$, and the period of the oscillation is $0.672 \mu m$, which is in close agreement to the value of $2\pi/\beta_{TE_0}$ ($\beta_{TE_0} = 9.335 \mu m^{-1}$ in this case).

Furthermore, using the diffraction integral (as described in Appendix C), the corresponding normalized electric field intensities of an output VHGC in the waveguide film region with zero-degree output coupling for TE polarization at three different distances y_o ($y_o = 2 \mu m, 100 \mu m$, and $1 mm$) measured from the surface of the grating are shown in Fig. 5.6. The numerical results of both the RCWA/LM approach and the FDFD method are represented. As seen in Fig. 5.6(a), the result of the FDFD method is very close to that of the RCWA/LM approach when $y_o = 2 \mu m$. The agreement between the FDFD method and the RCWA/LM approach away from the film-cover boundary is due to the exponential decay of the waveguide mode along the y -direction, i.e. C_0 in Eq. (5.5) decays exponentially as a function of y . In this case, the output-coupled field intensity decreases along the propagation direction. However, as the observation distances increase [as seen

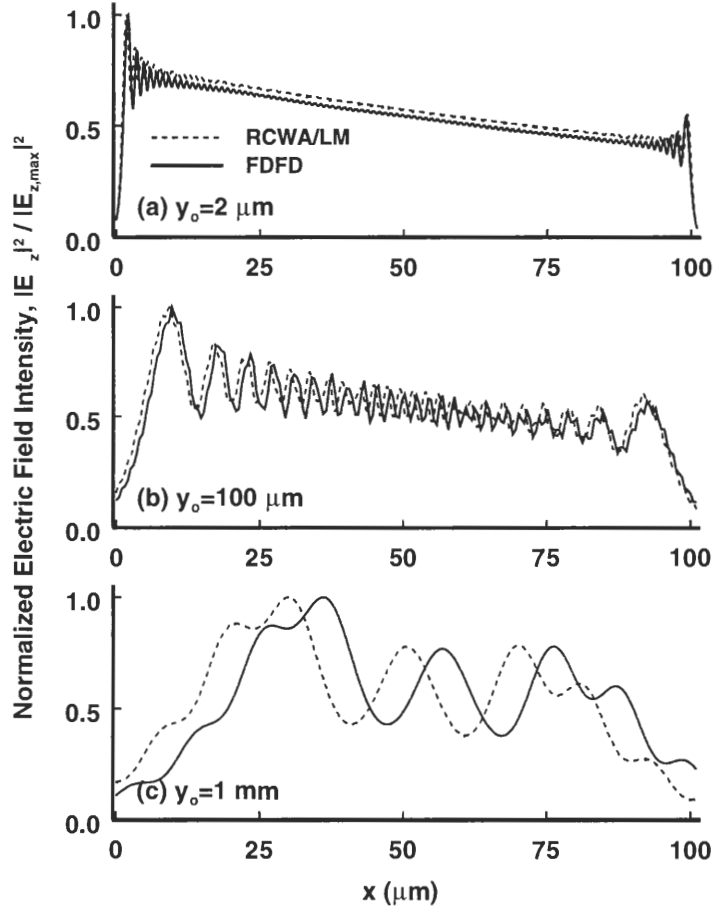


Figure 5.6: Normalized intensity of far-field distribution at (a) $y_o = 2 \mu\text{m}$, (b) $y_o = 100 \mu\text{m}$, and (c) $y_o = 1 \text{ mm}$ of an output VHGC with $L_g = 100 \mu\text{m}$ in the waveguide film region for TE polarization with zero-degree output coupling. The dash lines and the solid lines represent the results of the RCWA/LM approach and the FDFD method respectively.

in Figs. 5.6(b) and 5.6(c)], the results of the FDFD method are shifted from those of the RCWA/LM approach. The reason of this shift is that the output coupling angle in this case is $\theta_c = 0.34^\circ$ instead of $\theta_c = 0^\circ$ that the RCWA/LM approach assumes. For example, based on the output coupling angle $\theta_c = 0.34^\circ$ and the propagation distance $y_o = 1\text{ mm}$, the shift of the FDFD method from the RCWA/LM approach is $5.9\text{ }\mu\text{m}$, which is in agreement with the result shown in Fig. 5.6(c).

5.3 Output Volume Holographic Grating Couplers in the Waveguide Cover Region

For the configuration of an output VHGC in the waveguide cover region [as shown in Fig. 5.1(b)], the thicknesses of the waveguide film and the grating are $t_w = 0.4\text{ }\mu\text{m}$ and $t_g = 6.0\text{ }\mu\text{m}$ (DuPont's OmniDex613 photopolymer in laminate sheet), respectively. In addition, the waveguide material is assumed to be a polyimide (Ultradel 9020D) with refractive index $n_w = 1.56$. Based on this waveguide structure, there are five TE modes and five TM modes for the film-grating structure. The propagation constants of the first two TE modes are $\beta_{TE_0} = 9.456\text{ }\mu\text{m}^{-1}$ (confined in the film region) and $\beta_{TE_1} = 9.407\text{ }\mu\text{m}^{-1}$ (confined in the film-grating region). On the other hand, the propagation constants of the first two TM modes are $\beta_{TM_0} = 9.445\text{ }\mu\text{m}^{-1}$ and $\beta_{TM_1} = 9.405\text{ }\mu\text{m}^{-1}$. Similarly, applying the phase-matching conditions, the design parameters of an output VHGC in the waveguide cover region are summarized in Table 5.1.

5.3.1 Output Coupling Efficiencies

Figure 5.7 shows the numerical results of the transverse field profiles at $x = 0\text{ }\mu\text{m}$ and $x = 100\text{ }\mu\text{m}$ of an output VHGC in the waveguide cover region. In addition, the coupling efficiencies CE , branching ratios BR , and leakage parameters α_l of output VHGCs in the waveguide cover region are summarized in Table 5.3. As seen in Fig. 5.7 and Table 5.3,

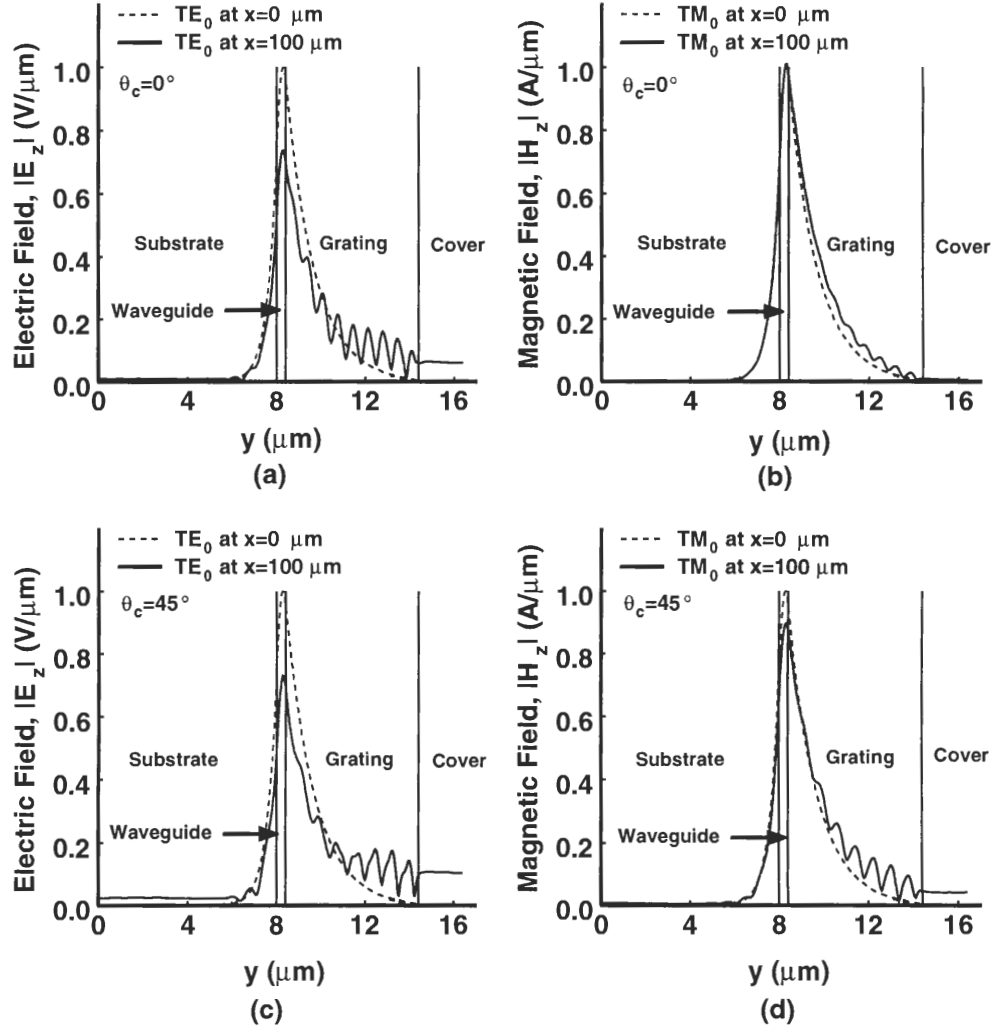


Figure 5.7: The transverse field profiles of an output VHGC in the waveguide cover region for (a) TE polarization with zero-degree output coupling, (b) TM polarization with zero-degree output coupling, (c) TE polarization with 45-degree output coupling, and (d) TM polarization with 45-degree output coupling. The dash lines and the solid lines represent the field profiles at $x = 0$ μm (i.e. incident waveguide mode) and at $x = 100$ μm respectively.

the characteristics of an output VHGC in the waveguide cover region is similar to those of an output VHGC in the waveguide film (as seen in Fig. 5.2 and Table 5.2). For zero-degree output coupling, the output-coupling efficiency of TE polarization ($CE_u = 72.88\%$ for $L_g = 250\mu m$) is much larger than that of TM polarization ($CE_u = 0.86\%$ for $L_g = 250\mu m$), and thus, a polarization-dependent coupler is obtained. However, for 45-degree output coupling, the output coupling efficiency of TM polarization ($CE_u = 33.69\%$ for $L_g = 250\mu m$) become larger and comparable to that of TE polarization ($CE_u = 73.42\%$

Table 5.3: Performance of an output VHGC in the waveguide cover region and comparison with the RCWA/leaky-mode (RCWA/LM) approach for zero- and 45-degree output coupling

Outcoupling Angle, $\theta_c = 0^\circ$							
TE Polarization ($\Lambda = 470.6 nm$, $\phi = -44.91^\circ$)							
Numerical Method	$L_g(\mu m)$	$CE_u(\%)$	$CE_d(\%)$	$CE_t(\%)$	$CE_r(\%)$	$BR(\%)$	$\alpha_l(1/\mu m)$
FDFD	100	41.37	1.19	57.37	0.70	97.20	0.28×10^{-2}
	250	72.88	3.03	23.71	0.38	96.01	0.29×10^{-2}
RCWA/LM	100	42.34	0.09	57.57	0.00	99.78	0.28×10^{-2}
	250	74.68	0.17	25.15	0.00	99.78	0.28×10^{-2}
TM Polarization ($\Lambda = 470.9 nm$, $\phi = -44.94^\circ$)							
Numerical Method	$L_g(\mu m)$	$CE_u(\%)$	$CE_d(\%)$	$CE_t(\%)$	$CE_r(\%)$	$BR(\%)$	$\alpha_l(1/\mu m)$
FDFD	100	0.35	0.02	99.62	0.01	94.59	0.19×10^{-4}
	250	0.86	0.05	99.08	0.01	94.51	0.19×10^{-4}
RCWA/LM	100	0.33	0.02	99.65	0.00	95.45	0.18×10^{-4}
	250	0.84	0.04	99.12	0.00	95.45	0.18×10^{-4}
Outcoupling Angle, $\theta_c = 45^\circ$							
TE Polarization ($\Lambda = 647.3 nm$, $\phi = -58.91^\circ$)							
Numerical Method	$L_g(\mu m)$	$CE_u(\%)$	$CE_d(\%)$	$CE_t(\%)$	$CE_r(\%)$	$BR(\%)$	$\alpha_l(1/\mu m)$
FDFD	100	42.35	4.08	53.57	0.00	91.21	0.31×10^{-2}
	250	73.42	7.29	19.29	0.00	90.99	0.33×10^{-2}
RCWA/LM	100	42.94	4.11	52.95	0.00	91.27	0.32×10^{-2}
	250	72.65	6.95	20.40	0.00	91.27	0.32×10^{-2}
TM Polarization ($\Lambda = 647.7 nm$, $\phi = -58.96^\circ$)							
Numerical Method	$L_g(\mu m)$	$CE_u(\%)$	$CE_d(\%)$	$CE_t(\%)$	$CE_r(\%)$	$BR(\%)$	$\alpha_l(1/\mu m)$
FDFD	100	14.53	0.30	85.17	0.00	97.98	0.80×10^{-3}
	250	33.69	0.70	65.61	0.00	97.96	0.84×10^{-3}
RCWA/LM	100	17.27	0.22	82.51	0.00	98.72	0.96×10^{-3}
	250	37.68	0.49	61.83	0.00	98.72	0.96×10^{-3}

for $L_g = 250 \mu m$). Moreover, the branching ratios estimated using the FDFD method for both TE and TM polarizations with zero- and 45-degree output coupling are smaller than the RCWA/LM predicted values. The reason of the higher branching ratios predicted by the RCWA/LM approach are the same as in the case of an output VHGC in the waveguide film region (discussed in Section 5.2.1).

5.3.2 Electric and Magnetic Fields

The amplitude and the phase patterns of the total field of an output VHGC with $L_g = 100 \mu m$ in the waveguide cover region are shown in Fig. 5.8. As seen in Fig. 5.8, the characteristics of field amplitudes along the propagation direction, the phase patterns both in the cover and in the substrate, and the radiation fields due to scattering into radiation modes resulting from the discontinuity between the waveguide and the grating are similar to those of an output VHGC in the waveguide film.

Another interesting phenomenon of the configuration of an output VHGC in the waveguide cover region is the modal conversion and the modal interference between the incident waveguide mode and the modes in the grating layer. For example, as seen in the phase pattern of Fig. 5.8(c), the incident waveguide mode only interacts with the lower region of the grating and converts into the leaky mode as $x < 15 \mu m$ in the grating layer. These effects can not be predicted by the RCWA/LM approach. From the phase fronts, it can be seen that the direction of the wave propagation in the upper region of the grating layer is about 28.13° (measured from the y axis), which corresponds to $\theta_c = 45^\circ$ in air (cover). However, when the propagation distance increases further ($x > 15 \mu m$), the diffracted field propagating in the upper-grating region starts to convert back to the waveguide leaky mode through the grating. As a result, it can be seen that the phase fronts at about $x = 30 \mu m$ are similar to the phase fronts of the incident mode, i.e. the wave fronts are perpendicular to the x axis. The similar phenomenon can also be observed for TE polarization with zero-degree output coupling and for TM polarization with 45-degree output coupling [as shown

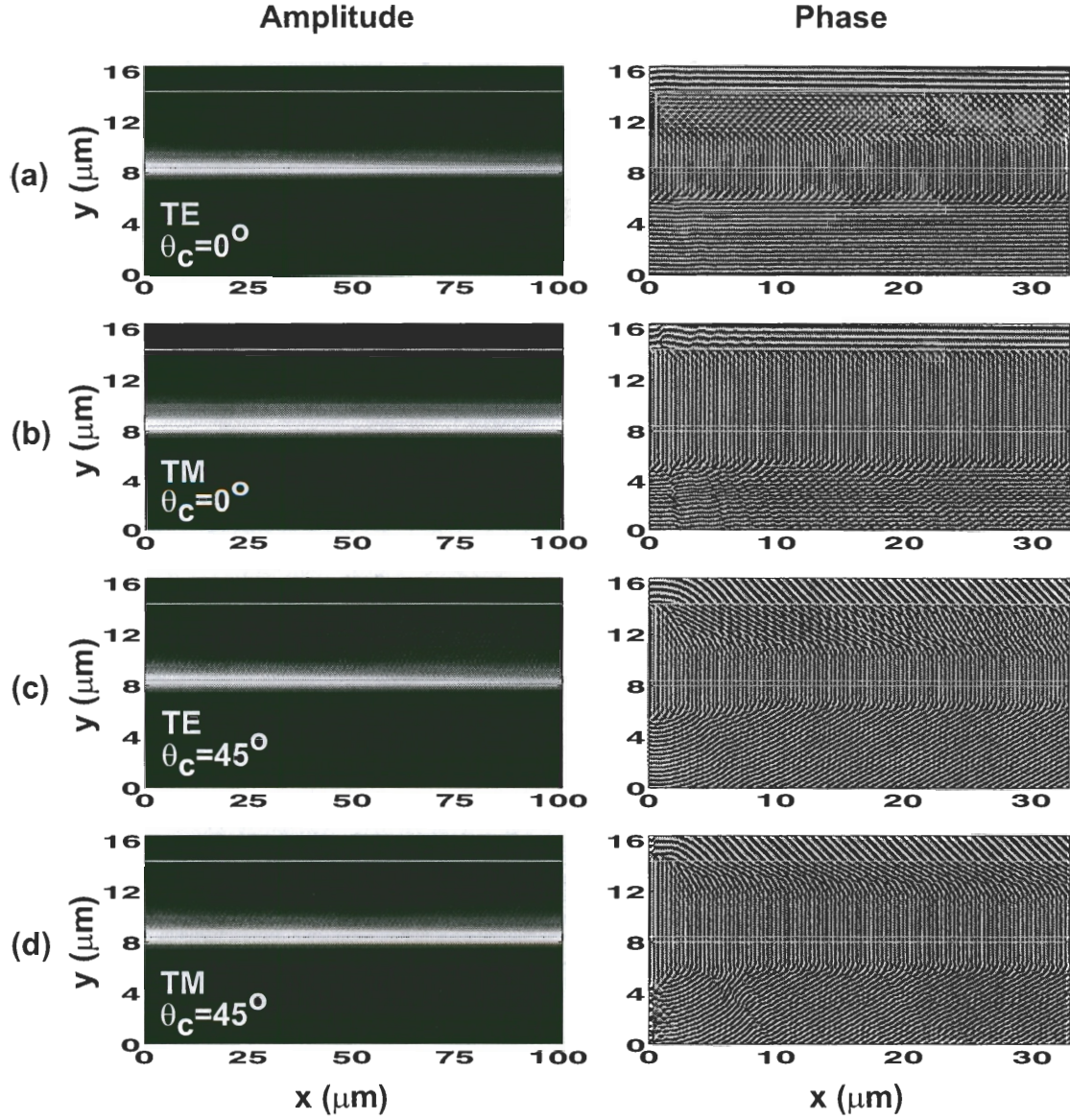


Figure 5.8: Two-dimensional field-amplitude and field-phase patterns of an output VHGC with $L_g = 100 \mu\text{m}$ and $t_g = 6.0 \mu\text{m}$ in the waveguide cover region for (a) TE polarization with zero-degree output coupling, (b) TM polarization with zero-degree output coupling, (c) TE polarization with 45-degree output coupling, and (d) TM polarization with 45-degree output coupling.

in Figs. 5.8(a) and 5.8(d)]. In conclusion, the output VHGC in this case overmodulates the waveguide mode. In order to verify this overmodulation phenomenon of an output VHGC, a new waveguide structure with a thinner grating ($t_g = 1.8 \mu m$ instead of $t_g = 6.0 \mu m$) is analyzed by using the FDFD method. Figure 5.9 shows the amplitude and the phase patterns of the total field of an output VHGC with $t_g = 1.8 \mu m$ and $L_g = 100 \mu m$ in the waveguide cover region. From the phase pattern of the total field [as seen in Fig. 5.9(b)], there is no overmodulation in this case, and, therefore, the diffracted mode does not convert back to the incident mode.

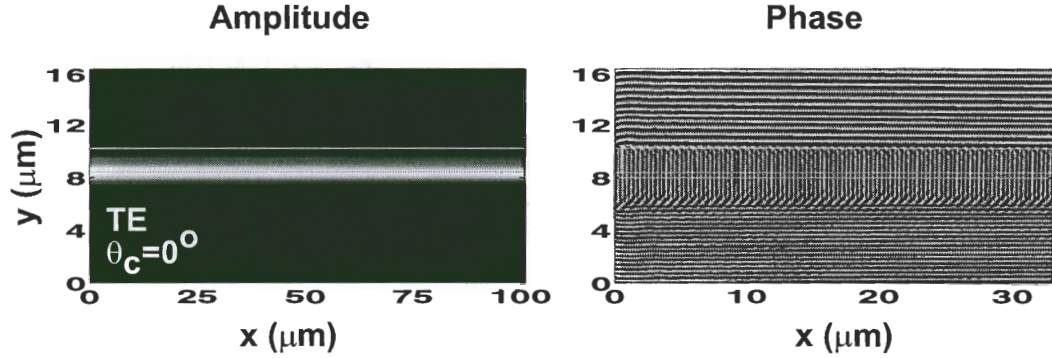


Figure 5.9: Two-dimensional field-amplitude and field-phase patterns of an output VHGC with $L_g = 100 \mu m$ and $t_g = 1.8 \mu m$ in the waveguide cover region for TE polarization with zero-degree output coupling.

Furthermore, the corresponding intensities of Fourier spectrums of the upward field profiles (E_z or H_z for TE or TM polarization) at $y = 16.4 \mu m$ of output VHGCs with $L_g = 100 \mu m$ and $t_g = 6.0 \mu m$ in the waveguide cover region for both zero- and 45-degree output coupling are shown in Fig. 5.10. As can be determined from Figs. 5.10(a) and 5.10(b), the intensities of Fourier spectrums for both zero-degree output coupling are centered at $\theta_c = 0.38^\circ$ for TE polarization and at $\theta_c = 0.35^\circ$ for TM polarization. On the other hand, the Fourier-spectrum intensities of 45-degree output coupling are centered at $\theta_c = 45.53^\circ$ and at $\theta_c = 45.47^\circ$ for both TE and TM polarizations, respectively [as seen in Figs. 5.10(c) and 5.10(d)]. Similar to the case of an output VHGC in the waveguide film region, the

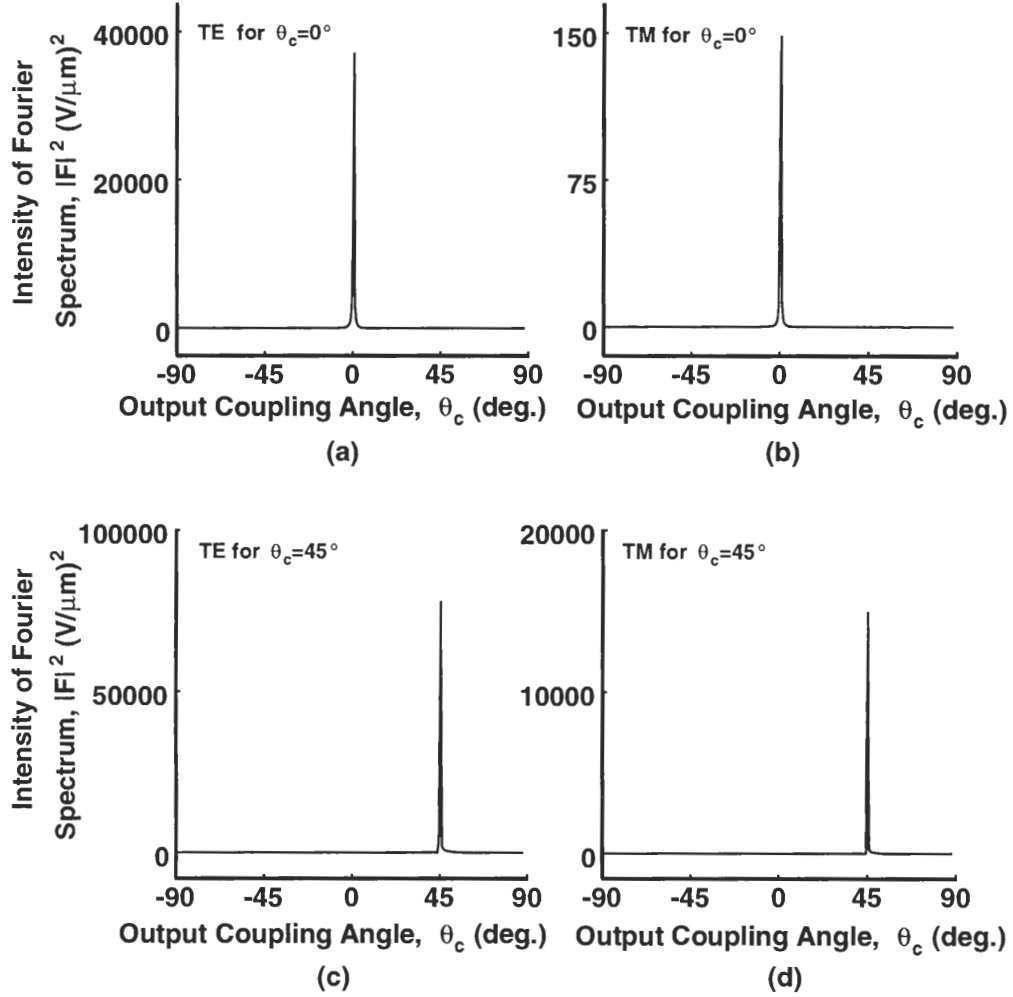


Figure 5.10: Corresponding intensities of Fourier spectrums of the upward field profiles at $y = 16.4 \mu\text{m}$ of an output VHGC with $L_g = 100 \mu\text{m}$ and $t_g = 6.0 \mu\text{m}$ in the waveguide cover region for (a) TE polarization with zero-degree output coupling, (b) TM polarization with zero-degree output coupling, (c) TE polarization with 45-degree output coupling, and (d) TM polarization with 45-degree output coupling.

difference between the calculated value of θ_c and the designed value of θ_c results from the design of the grating period and the slanted angle using the unperturbed by the grating propagation constant of the incident mode.

5.3.3 Near and Far Fields

Figure 5.11 shows the normalized electric field intensities at the top surface of the waveguide film layer for the case of an output VHGC in the waveguide cover region with zero-degree output coupling for TE polarization. As seen in Fig. 5.11, the normalized electric field intensity of the RCWA/LM approach is an exponential decay with the decay rate of $2\alpha_l = 0.552 \times 10^{-2} \mu m^{-1}$ along the propagation direction because of the leaky mode coupling. However, for the FDFD method, the normalized electric field intensity is not only an exponential decay but also has an oscillatory component along the x direction. In contrast to the case of an output VHGC in the waveguide film region (as seen in Fig. 5.5), there are two different oscillation periods (as seen in Fig. 5.11). Similarly, in order to explain this oscillation phenomenon, it is useful to represent the total field in the waveguide film region and at the film-grating interface. Neglecting the reflected field and taking into account of the additional TE_1 mode excitation, the total field can be represented as

$$E_{z,tot} = [1 + C_0 \exp(-j\beta_{TE_0}x) + C_1 \exp(-j\beta_{TE_1}x)] \exp(-\alpha_l x), \quad (5.6)$$

where $C_0 = |C_0| \exp(j\psi_0)$ and $C_1 = |C_1| \exp(j\psi_1)$ are complex constants at the grating-cover interface. Thus, the electric field intensity can be written as

$$I_{z,tot} = |E_{z,tot}|^2 = \exp(-2\alpha_l x) \{1 + |C_0|^2 + |C_1|^2 + 2|C_0| \cos(\beta_{TE_0}x - \psi_0) + 2|C_1| \cos(\beta_{TE_1}x - \psi_1) + 2|C_0||C_1| \cos[(\beta_{TE_0} - \beta_{TE_1})x - (\psi_0 - \psi_1)]\}. \quad (5.7)$$

From Eq. (5.7), it can be seen that the electric field intensity is an exponential decay with a decay rate $2\alpha_l$ and contains oscillations of three different periods. The first two oscillation periods are $2\pi/\beta_{TE_0}$ [from the term of $\cos(\beta_{TE_0}x - \psi_0)$] and $2\pi/\beta_{TE_1}$ [from the term of

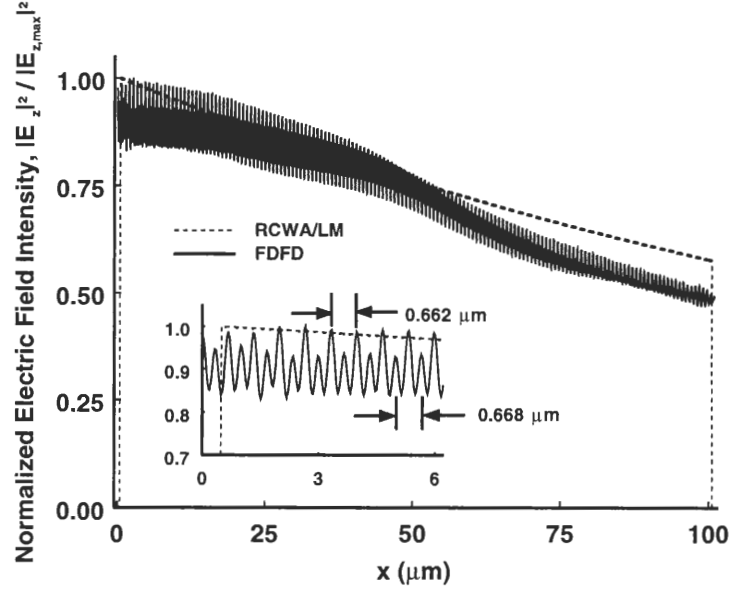


Figure 5.11: Normalized field intensity at the top surface of the waveguide film layer (i.e. at $y = 8.4 \mu m$) of an output VHGC with $L_g = 100 \mu m$ and $t_g = 6.0 \mu m$ in the waveguide cover region for TE polarization with zero-degree output coupling. The dash lines and the solid lines represent the results of the RCWA/LM approach and the FDFD method respectively.

$\cos(\beta_{TE_1} x - \psi_1)]$, which correspond to the incident TE_0 mode and the additional TE_1 mode excitation (at the waveguide discontinuity), respectively. As seen in Fig. 5.11, these two oscillation periods are $0.662 \mu m$, which is close to the value of $2\pi/\beta_{TE_0}$ ($\beta_{TE_0} = 9.456 \mu m^{-1}$ in this case), and $0.668 \mu m$, which is close to the value of $2\pi/\beta_{TE_1}$ ($\beta_{TE_1} = 9.407 \mu m^{-1}$ in this case). In conclusion, an additional mode (TE_1 mode) is excited for the configuration of an output VHGC in the waveguide cover region. Furthermore, from the term of $\cos[(\beta_{TE_0} - \beta_{TE_1})x - (\psi_0 - \psi_1)]$, the third oscillation period is $2\pi/(\beta_{TE_0} - \beta_{TE_1})$ (also known as the beat length) resulting from the mode interference between the TE_0 mode and the TE_1 mode. The beat length resulting from the mode interference will be discussed in the Section 5.3.4.

Applying the diffraction integral (as described in Appendix C) the normalized electric field intensities of an output VHGC in the waveguide cover region with zero-degree output coupling for TE polarization at three different distances y_o ($y_o = 2 \mu m$, $100 \mu m$, and $1 mm$)

away from the grating-cover boundary are shown in Fig. 5.12. The numerical results of both the RCWA/LM approach and the FDFD method are represented. Similar to the case of an output VHGC in the waveguide film region, the results of the FDFD method are shifted from those of the RCWA/LM approach as the observation distances increase because the output coupling angle in this case is $\theta_c = 0.38^\circ$ instead of $\theta_c = 0^\circ$ [as seen in Fig. 5.10(a)].

As seen in Fig. 5.12(a), for the case of an output VHGC in the waveguide cover region, the field intensity at $y_o = 2\ \mu m$ initially decreases along the propagation direction. However, as the propagation distance increases furthermore, the field intensity starts to increase. In contrast to this case, the output-coupled field intensity along the propagation direction for the case an output VHGC in the waveguide film region is monotonically decreased [as seen in Fig. 5.6(a)]. The reason of this difference between these two configurations is that there is an additional TE_1 mode excitation and interference with the fundamental TE_0 mode in the grating layer for the case of an output VHGC in the waveguide cover region. This mode excitation and mode interference can be found in the phase pattern of the total field [as shown in Fig. 5.8(a)]. Because of the interference between the TE_0 mode and the TE_1 mode, the beat length (discussed in Section 5.3.4) can be observed in the electric-field-intensity profile near the grating-cover boundary.

5.3.4 Beat Lengths

As has been mentioned in Section 5.3.3, there is an additional TE_1 mode excitation and interference with the fundamental TE_0 mode for the case of an output VHGC in the waveguide cover region. According to Eq. (5.7), the mode interference between the TE_0 mode and the TE_1 mode can be characterized by the beat length $L_b = 2\pi/(\beta_{TE_0} - \beta_{TE_1})$. In order to study the characteristics of the beat length resulting from the mode interference, two output VHGCs with different thicknesses (one is $t_g = 6.0\ \mu m$ and the other is $t_g = 1.8\ \mu m$) in the waveguide cover region for TE polarization with zero-degree output coupling are analyzed by use of the FDFD method. For the case of $t_g = 6.0\ \mu m$, there are five TE modes in the

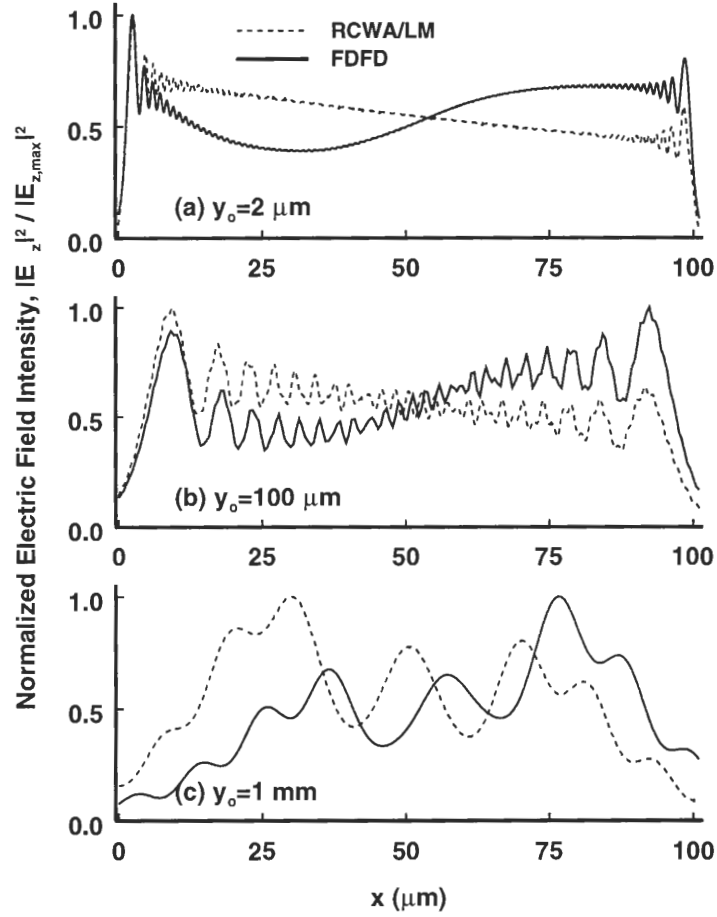


Figure 5.12: Normalized intensity of far-field distribution at (a) $y_o = 2 \mu m$, (b) $y_o = 100 \mu m$, and (c) $y_o = 1 mm$ of an output VHGC with $L_g = 100 \mu m$ and $t_g = 6.0 \mu m$ in the waveguide cover region for TE polarization with zero-degree output coupling. The dash lines and the solid lines represent the results of the RCWA/LM approach and the FDFD method respectively.

waveguide structure (confined in the film-grating region). The corresponding propagation constants of the first two TE modes are $\beta_{TE_0} = 9.456 \mu m^{-1}$ and $\beta_{TE_1} = 9.407 \mu m^{-1}$. However, for the case of $t_g = 1.8 \mu m$, there are only two TE modes with propagation constants $\beta_{TE_0} = 9.452 \mu m^{-1}$ and $\beta_{TE_1} = 9.246 \mu m^{-1}$ in this waveguide.

As seen in Fig. 5.13(a) (for the case of $t_g = 6.0 \mu m$ and $L_g = 250 \mu m$), the normalized electric field intensity at $y_o = 2 \mu m$ is non-monotonically decreased along the x direction with $L_b = 127.78 \mu m$, which is close to the value of $2\pi/(\beta_{TE_0} - \beta_{TE_1})$ ($\beta_{TE_0} = 9.456 \mu m^{-1}$ and $\beta_{TE_1} = 9.407 \mu m^{-1}$ in this case). On the other hand, for the case of $t_g = 1.8 \mu m$ and $L_g = 100 \mu m$ [as seen in Fig. 5.13(b)], the normalized electric field intensity at $y_o = 2 \mu m$

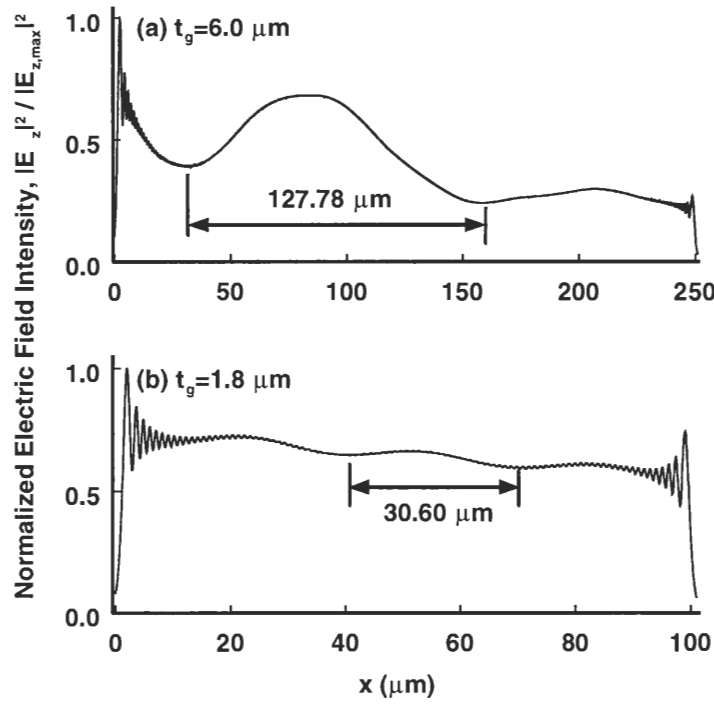


Figure 5.13: Non-monotonical decrease of the normalized intensity of electric field distribution at $y_o = 2 \mu m$ for the configuration of an output VHGC with (a) $t_g = 6.0 \mu m$ and (b) $t_g = 1.8 \mu m$ in the waveguide cover region for TE polarization with zero-degree output coupling. The numerical results are calculated by use of the FDFD method.

is non-monotonically decreased along the x direction with $L_b = 30.60 \mu m$, which is close to the value of $2\pi/(\beta_{TE_0} - \beta_{TE_1})$ ($\beta_{TE_0} = 9.452 \mu m^{-1}$ and $\beta_{TE_1} = 9.246 \mu m^{-1}$ in this case). Furthermore, comparing Figs. 5.13(a) to 5.13(b), we can see the non-monotonical decrease variation of the case of $t_g = 6.0 \mu m$ is more obvious than that of the case of $t_g = 1.8 \mu m$. The reason of this interesting result is that the propagation constant of the TE_1 mode (β_{TE_1}) is closer than that of the TE_0 mode (β_{TE_0}) for the case of $t_g = 6.0 \mu m$ (with respect to the case of $t_g = 1.8 \mu m$). Therefore, the additional TE_1 mode is more easily excited. In addition, the thicker grating has higher overmodulation effect and results in stronger interference between the TE_0 mode and the TE_1 mode, and larger electric-field-intensity variation. The actual periodicities are close to the predicted values but can not be exactly predicted since the propagation constants are the unperturbed by the modulation ones.

5.4 Summary and Discussion

Two configurations of volume holographic grating couplers (VHGCs) for output coupling in integrated optics are rigorously analyzed using the finite-difference frequency-domain (FDFD) method. Both TE and TM polarizations with zero- and 45-degree output coupling are analyzed with the FDFD method and compared with the rigorous coupled-wave analysis in conjunction with the leaky-mode (RCWA/LM) approach. For both configurations, the upward coupling efficiency of TE polarization is much higher than that of TM polarization for zero-degree output coupling, and thus polarization-dependent couplers can be obtained. On the other hand, the upward coupling efficiency of TM polarization is comparable to that of TE polarization for 45-degree output coupling. Therefore, the grating coupler could be polarization-independent if the grating is designed for 45-degree output coupling.

Comparing the results of the FDFD method and the RCWA/LM approach, the FDFD method shows that the normalized electric field intensity is not only an exponential decay, which the RCWA/LM approach assumes, but also has oscillatory components along

the propagation direction because the FDFD method takes into account the interference between all modes (excited in the waveguide film-grating region) and the radiation fields. In addition, the FDFD results shows that there is a higher-order waveguide mode excitation and interference with the fundamental waveguide mode in the case of an output VHGC in the waveguide cover region. Because of this additional mode excitation and mode interference, the intensity of the output-coupled field could decrease non-monotonically along the propagation direction. The period of this non-monotonical decrease corresponds to the beat length resulting from the interference between the fundamental waveguide mode and the higher-order waveguide mode. Furthermore, a thicker grating has stronger non-monotonical decrease variation along the propagation direction as compared to a thinner grating. Moreover, a thicker grating has stronger overmodulation effect and results in stronger interference between the fundamental waveguide mode and the higher-order waveguide mode.

CHAPTER 6

INPUT VOLUME HOLOGRAPHIC GRATING COUPLERS

In contrast to the output grating coupler, the input grating coupler is used to convert an incident light beam into guided modes of a waveguide. As has been mentioned in Section 1.2.4, a variety of numerical methods including the perturbation theory [102, 107, 108, 114], the modified Born approximation and the reciprocity theory [106], the rigorous electromagnetic formalism developed by Neviere *et al.* [103–105, 109–112], and three-layer waveguide model [115] have been applied to analyze an infinite surface-relief grating illuminated by a plane wave or a Gaussian beam. In addition, the perturbation theory [116] has been also applied to analyze both unslanted and slanted input VHGCs with infinite lengths illuminated by a plane wave with TE polarization. However, for practical applications for high-data rate interconnections, the input VHGC should have finite length, and the incident beam is a finite beam such as a Gaussian beam. Therefore, the grating length and the beam size could significantly affect the input coupling efficiency for an input VHGC. In addition, as the incident beam is coupled into a guided mode by a grating coupler, this guided mode will propagate in the waveguide and will be coupled out of the waveguide by the same grating. As a result, the input coupling efficiency will also depend on the incident-beam position on the grating coupler. For these reasons, the effects of grating lengths, beam sizes, and incident-beam positions on the input coupling efficiencies of input VHGCs will be investigated in this chapter to determine the optimum coupling conditions.

6.1 Input Volume Holographic Grating Coupler Configurations

Similarly to the configurations of output VHGCs (as seen in Section 5.1), two basic configurations of an input VHGC with finite length, L_g , placed in the waveguide film region [as shown in Fig. 6.1(a)] as well as in the waveguide cover region [as shown in Fig. 6.1(b)] are analyzed by use of the FDFD method [55, 139]. For both configurations, the waveguide

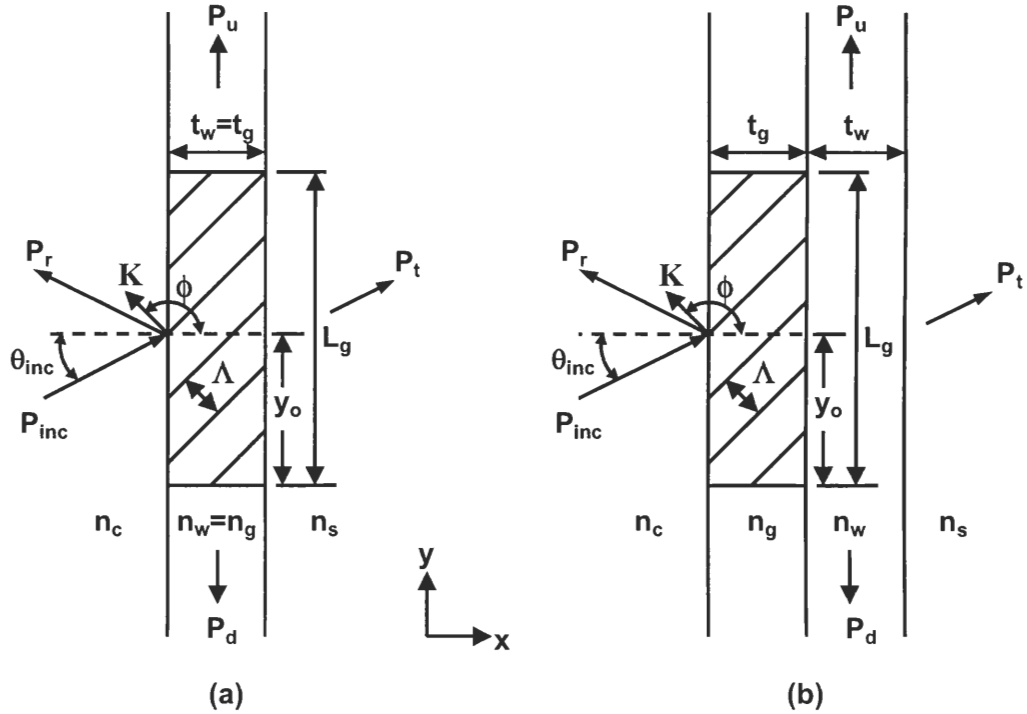


Figure 6.1: Two basic configurations of waveguide input-couplers comprised of a VHGC (a) in the waveguide film region and (b) in the waveguide cover region. The waveguide consists of a cover region with refractive index n_c , a film region with refractive index n_w , and a substrate region with refractive index n_s . The thickness of the waveguide film region is t_w . The volume holographic grating has a grating vector \mathbf{K} , a slant angle ϕ , a length L_g , and a thickness t_g . The average refractive index in the grating region is n_g . The incident beam with incident angle θ_{inc} and incident position y_o is incident on the grating. The power of the incident beam is P_{inc} . P_u , P_d , P_t , and P_r denote the upward-coupling power, the downward-coupling power, the transmitted power, and the reflected power, respectively.

consists of a glass substrate with refractive index n_s , a waveguide film layer with refractive index n_w and thickness t_w , and a cover layer with refractive index n_c . The average refractive index, the thickness, the grating period, and the slant angle of the holographic grating are n_g , t_g , Λ , and ϕ respectively. The period and the slant angle of input VHGCs are designed to couple the incident beam into the TE_0 mode. In addition, the permittivity in the grating region can be represented by Eq. (2.1).

On the other hand, in order to study the effects of incident-beam positions on the coupling efficiencies of input VHGC, a finite beam with incident angle θ_{inc} and incident position y_o is incident on the grating from the cover region with refractive index n_c (as seen in Fig.6.1). Furthermore, in order to study the effects of beam sizes and beam profiles on the coupling efficiencies of input VHGCs, a Gaussian beam with beam waist W , a flat cosine-squared beam (i.e. a quasi plane wave) with flat width W , and an exponential-decay beam with decay width W are introduced in this research. The window functions, $g(y')$, for these three incident beams can be represented as

$$g(y') = \exp \left[\left(\frac{-y'}{W/2} \right)^2 \right], \quad (6.1)$$

for the Gaussian beam,

$$g(y') = \begin{cases} 1 & 0 \leq |y'| \leq \frac{W}{2} \\ \cos^2 \left[\frac{|y'| - \frac{W}{2}}{2(D-W)} \pi \right] & \frac{W}{2} \leq |y'| \leq D - \frac{W}{2}, \\ 0 & D - \frac{W}{2} \leq |y'| \leq \infty \end{cases} \quad (6.2)$$

for the flat cosine-squared beam, and

$$g(y') = \begin{cases} \exp \left[-\alpha_l \left(y' - \frac{W}{2} \right) \right] & 0 \leq |y'| \leq \frac{W}{2} \\ \cos^2 \left[\frac{|y'| - \frac{W}{2}}{2(D-W)} \pi \right] & \frac{W}{2} \leq |y'| \leq D - \frac{W}{2}, \\ 0 & D - \frac{W}{2} \leq |y'| \leq \infty \end{cases} \quad (6.3)$$

for the exponential-decay beam. α_l is the leakage parameter of a VHGC, which can be determined by use of the leaky-mode approach. Substituting Eqs. (6.1), (6.2), and (6.3) into

Eq. (2.3), the resulting incident Gaussian, flat cosine-squared, and exponential-decay beams for TE/TM polarization can be obtained. The corresponding configurations of incident beams with finite widths are summarized in Fig. 6.2.

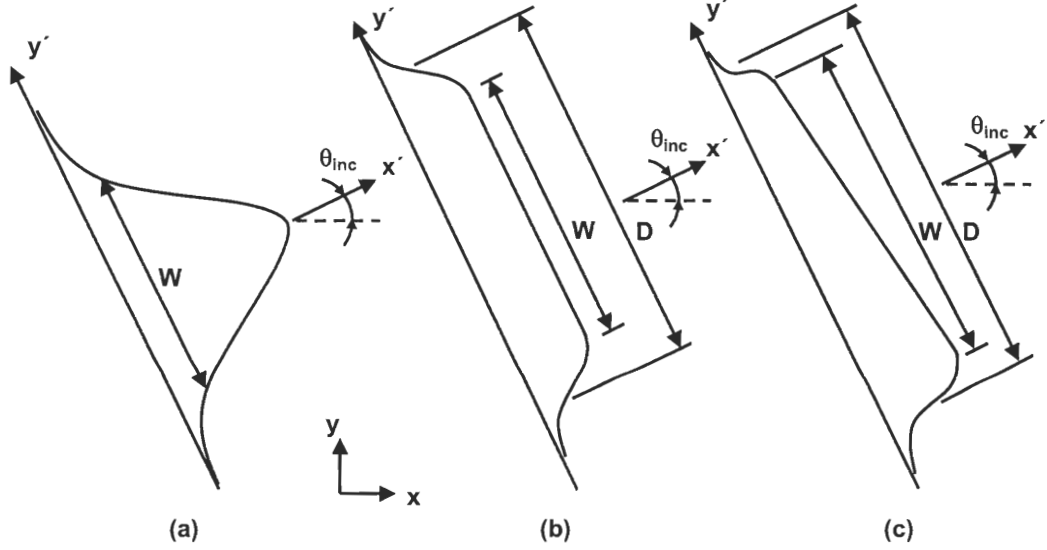


Figure 6.2: Three finite-width incident beams of (a) a Gaussian beam with beam waist W , (b) a flat cosine-squared beam (i.e. a quasi plane wave) with flat width W , and (c) an exponential-decay beam with decay width W . θ_{inc} is the incident angle of the incident beam.

Similar to the analysis of output VHGCs (as seen in Chapter 5), the FDFD method in conjunction with UPMLs is applied to calculate the scattered fields of the input VHGC, and the modal decomposition of guided fields (as described in Appendix D) is used to calculate the corresponding power coupled into the TE_m mode of the waveguide both in the upward direction, P_{u,TE_m} , and in the downward direction, P_{d,TE_m} . In order to quantify the performance of an input VHGC, the input coupling efficiency of TE_m mode CE_{i,TE_m} is defined (in percent) as

$$CE_{i,TE_m} = \frac{P_i}{P_{inc}} \times 100, \quad (6.4)$$

where P_{inc} is the incident power, and P_i ($i = u, d$) is the diffracted power coupling in the upward direction or in the downward direction.

In this chapter, an input VHGC with finite length $L_g = 50 \mu m$ in the waveguide film region as well as in the waveguide cover region illuminated by a Gaussian beam, a flat cosine-squared beam, and an exponential-decay beam is analyzed. For all cases treated in this chapter, normally incident beams (i.e. $\theta_{inc} = 0^\circ$) of TE polarization from the cover region are considered. The incident position y_o of the finite incident beam are varied between $0.3L_g$ to $0.9L_g$ (i.e. $y_o = 0.3L_g, 0.4L_g, 0.5L_g, 0.6L_g, 0.7L_g, 0.8L_g$, and $0.9L_g$). In addition, three different beam sizes of $W = L_g, 0.5L_g$, and $0.25L_g$ for the Gaussian, flat cosine-squared, and exponential-decay beams are investigated. The freespace wavelength of the incident beam is assumed to be $\lambda_0 = 1.0 \mu m$.

6.2 Input Volume Holographic Grating Couplers in the Waveguide Film Region

For an input VHGC in the waveguide film region [as shown in Fig. 6.1(a)], the waveguide material is assumed to be the DuPont's OmniDex613 photopolymer with refractive index $n_w = 1.5$. The thicknesses of the waveguide and the grating are $t_w = t_g = 1.8 \mu m$. The thickness t_w is designed to support a single TE mode in this waveguide. The propagation constants for TE₀ mode in this waveguide is $\beta_{TE_0} = 9.335 \mu m^{-1}$. In addition, the grating material is DuPont's OmniDex613 photopolymer with average dielectric constant $\epsilon_0 = 2.25$ ($n_g = 1.5$) and modulation $\epsilon_1^c = 0.06$ ($\Delta n_1 \simeq 0.02$) [134]. The grating period and the slant angle of the input VHGC are designed to couple the normally incident beam (as a plane wave) into TE₀ mode of the waveguide. Applying the phase-matching conditions (as seen in Section 7.1), the grating period and the slant angle of the input VHGC in the waveguide film region are $\Lambda = 473.7 nm$ and $\phi = 135.28^\circ$ respectively.

6.2.1 Electric Fields

Figure 6.3 shows the amplitude patterns of the total electric-field of a finite VHGC with $L_g = 50 \mu\text{m}$ in the waveguide film region illuminated by a Gaussian beam with beam waist $W = 0.5L_g$ at three different incident positions ($y_o = 0.3L_g, 0.6L_g$, and $0.9L_g$). The waveguide layer is located between $x = 2.0 \mu\text{m}$ and $x = 3.8 \mu\text{m}$, and the finite volume holographic grating is located between $y = 10 \mu\text{m}$ and $y = 60 \mu\text{m}$. Dark areas indicate regions of lower field amplitude, and the lighter areas indicate regions of higher field amplitude. In addition, both transmitted fields at $x = 8 \mu\text{m}$ and waveguide-coupled fields at $y = 80 \mu\text{m}$ corresponding to Fig. 6.3 are also represented in Fig. 6.4.

As seen in Fig. 6.3(a) with the incident position $y_o = 0.3L_g$, the Gaussian beam normally incident from the cover region is coupled into the TE_0 mode propagating in

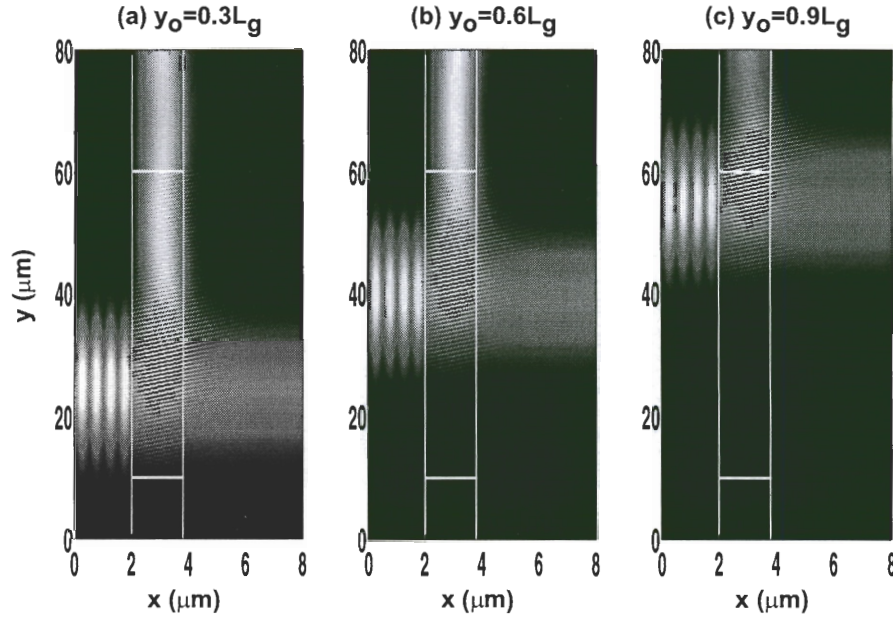


Figure 6.3: Two-dimensional field-amplitude patterns of a finite input VHGC with $L_g = 50 \mu\text{m}$ in the waveguide film region illuminated by a TE-polarized Gaussian beam with beam waist $W = 0.5L_g$ at the incident position of (a) $y_o = 0.3L_g$, (b) $y_o = 0.6L_g$, and (c) $y_o = 0.9L_g$.

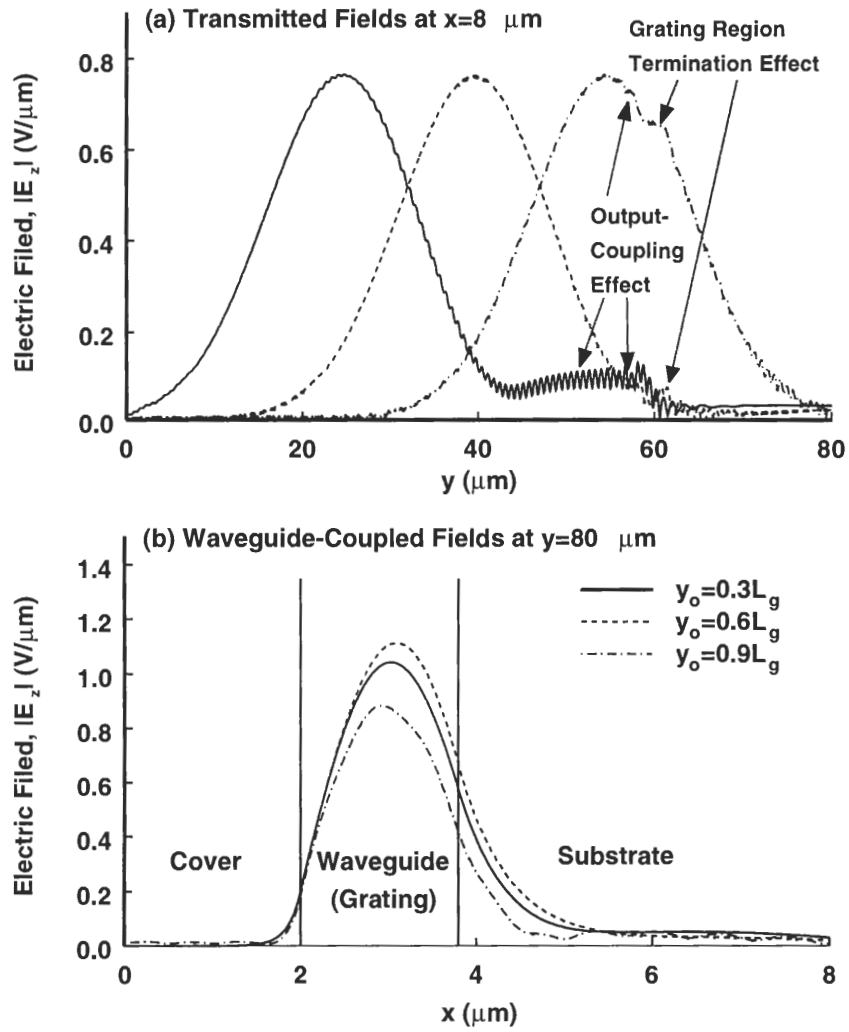


Figure 6.4: Field profiles corresponding to Fig. 6.3 for (a) the transmitted field at $x = 8 \mu\text{m}$ and (b) the waveguide-coupled field at $y = 80 \mu\text{m}$.

the waveguide and then this guided mode is coupled out of the waveguide by the same VHGC from $y = 40 \mu m$ to $y = 60 \mu m$ [as seen in Fig. 6.4(a)]. This output-coupling effect will result in the leakage of guided mode from the waveguide and therefore deteriorate the performance of input VHGC. However, as the incident-beam position is increased to $y_o = 0.6L_g$, the output-coupling effect is small [as seen in Figs. 6.3(b) and 6.4(a)] because the larger value of y_o corresponds to a shorter output-coupling length (i.e. less power of the guided mode will be coupled out of the waveguide for the larger y_o), and consequently, more power of the guided mode remains in the waveguide. Therefore, as seen in Fig. 6.4(b), the amplitude of the waveguide-coupled field of $y_o = 0.6L_g$ is higher than that of $y_o = 0.3L_g$. In other words, the input coupling efficiency increases as the incident-beam position increases from $y_o = 0.3L_g$ to $y_o = 0.6L_g$. As the incident-beam position increases further, for example $y_o = 0.9L_g$, although the output-coupling effect of $y_o = 0.9L_g$ is much smaller than those of $y_o = 0.3L_g$ and $y_o = 0.6L_g$ [as seen in Fig. 6.4(a)], some of the incident beam initially falls outside the VHGC and transmits through the waveguide without getting diffracted [as seen in Fig. 6.3(c)]. This grating region termination effect can be seen in Fig. 6.4(a). Therefore, the amplitude of the waveguide-coupled field decreases as the incident-beam position increases to $y_o = 0.9L_g$ [as seen in Fig. 6.4(b)]. In summary, for a finite input VHGC in the waveguide film region, there is an optimum incident-position for a finite incident-beam to obtain the maximum coupling efficiency. The optimization of an input VHGC in the waveguide film region will be discussed in Section 6.2.2.

6.2.2 Optimization of Input Coupling Efficiencies

Figure 6.5 shows the numerical results of input coupling efficiencies of TE_0 mode in the upward direction (CE_{u,TE_0}) as a function of normalized incident-beam positions with various incident-beam widths and different incident-beam profiles for a VHGC in the waveguide film region. As seen in Fig. 6.5(a), the optimum incident-positions, $y_{o,opt}$, and the corresponding input coupling efficiencies, CE_{u,TE_0} , of Gaussian beams with beam waists $W = L_g, 0.5L_g$,

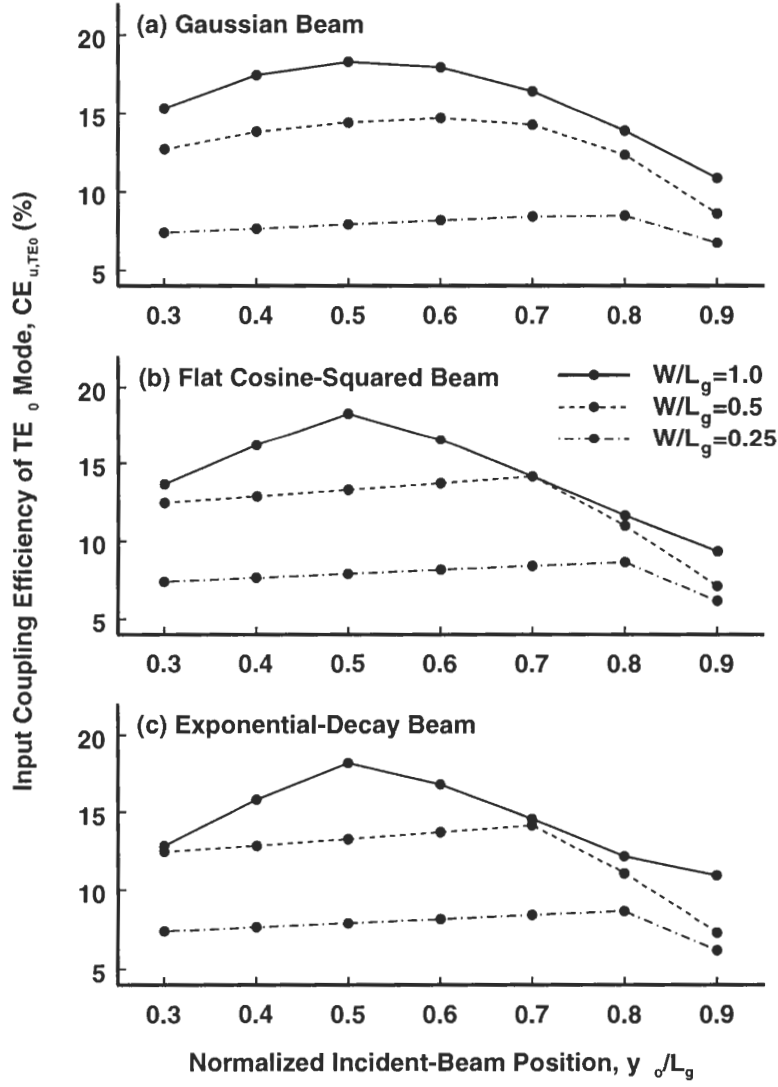


Figure 6.5: Input coupling efficiencies of TE_0 mode in the upward direction as functions of y_0/L_g and W/L_g for a finite input VHGC with $L_g = 50 \mu m$ in the waveguide film region illuminated by (a) a Gaussian beam, (b) a flat cosine-squared beam, and (c) an exponential-decay beam.

and $0.25L_g$ are $y_{o,opt} = 0.5L_g, 0.6L_g$, and $0.8L_g$ and $CE_{u,TE_0} = 18.29\%, 14.71\%$, and 8.46% respectively. As has been discussed in Section 6.2.1, for $y_o < y_{o,opt}$, the input coupling efficiency increases as the incident-beam position increases because the output-coupling effect decreases. On the other hand, for $y_o > y_{o,opt}$, the input coupling efficiency decreases as the incident-beam position increases because the grating region termination effect increases (i.e. more of the incident beams initially falls outside the VHGC). Furthermore, the input coupling efficiency (at the optimum coupling condition) decreases as the incident-beam width decreases because narrower beams are more spread in the wave-vector space, resulting in significant deviations from the Bragg condition, and thus, less coupling efficiencies. The characteristics of input coupling efficiencies with respect to the incident-beam position (y_o/L_g) and the incident-beam width (W/L_g) for a finite input VHGC illuminated by a flat cosine-squared beam [as seen in Fig. 6.5(b)] and by an exponential-decay beam [as seen in Fig. 6.5(c)] are similar to that of a finite input VHGC illuminated by a Gaussian beam. Comparing Figs. 6.5(a), 6.5(b), and 6.5(c), the beam profiles do not significantly affect the performance of a finite input VHGC.

The optimum incident-positions and the corresponding coupling efficiencies in the upward direction (CE_{u,TE_0}) of a finite input VHGC in the waveguide film region illuminated by various incident-beam profiles with different incident-beam widths are summarized in Table 6.1. As seen in Table 6.1, as the incident-beam widths decrease from $W = L_g$ to $W = 0.5L_g$, the optimum incident-positions increase from $y_{o,opt} = 0.5L_g$ to $y_{o,opt} = 0.6L_g$ for the Gaussian beam and to $y_{o,opt} = 0.7L_g$ for both the flat cosine-squared beam and the exponential-decay beam. However, as the incident-beam width decreases further (i.e. $W = 0.25L_g$), the optimum incident-beam positions for all beam profiles increase to $y_{o,opt} = 0.8L_g$. Consequently, for a given beam profile, the optimum incident-position $y_{o,opt}$ shifts to the end of the VHGC as the incident-beam width decreases. However, the optimization of a finite input VHGC is weakly dependent on the beam profiles. Finally, it is worth mentioning that the input coupling efficiencies of TE_0 mode in the downward direction (CE_{d,TE_0}) for

all cases treated in this section are less than 0.02%.

Table 6.1: Optimization of a finite input VHGC with length $L_g = 50 \mu m$ in a waveguide film region illuminated by various incident-beam profiles.

Beam Profiles	Optimization for Coupling into TE ₀ Mode		
	Beam Width W/L_g	Optimum Incident-Position $y_{o,opt}/L_g$	Input Coupling Efficiency $CE_{u,TE_0}(\%)$
Gaussian	1.0	0.5	18.29
	0.5	0.6	14.71
	0.25	0.8	8.46
Flat Cosine-Squared	1.0	0.5	18.30
	0.5	0.7	14.15
	0.25	0.8	8.65
Exponential-Decay	1.0	0.5	18.19
	0.5	0.7	14.13
	0.25	0.8	8.65

6.3 Input Volume Holographic Grating Couplers in the Waveguide Cover Region

For the configuration of an input VHGC in the waveguide cover region [as shown in Fig. 6.1(b)], the thicknesses of the waveguide film and the grating are $t_w = 0.4 \mu m$ and $t_g = 6.0 \mu m$ (DuPont's OmniDex613 photopolymer in laminate sheet), respectively. Moreover, the waveguide material is assumed to be a polyimide (Ultradel 9020D) with refractive index $n_w = 1.56$. Based on this waveguide structure, there are five TE modes for the film-grating structure. The propagation constants of the first two TE modes are $\beta_{TE_0} = 9.456 \mu m^{-1}$ (confined in the film region) and $\beta_{TE_1} = 9.407 \mu m^{-1}$ (confined in the film-grating region). Designing the input VHGC to couple the normally incident beam (as a plane wave) into TE₀ mode of the waveguide by applying the phase-matching conditions, the period and the slant angle of the input VHGC in the waveguide cover region are $\Lambda = 470.6 nm$ and $\phi = 134.91^\circ$ respectively.

6.3.1 Electric Fields

The amplitude patterns of the total electric-field of a finite VHGC with $L_g = 50 \mu m$ in the waveguide cover region illuminated by a Gaussian beam with beam waist $W = 0.5L_g$ at three different incident positions ($y_o = 0.3L_g, 0.6L_g$, and $0.9L_g$) are shown in Fig. 6.6. In this case, the grating is located between $x = 2.0 \mu m$ and $x = 8.0 \mu m$ and between $y = 10 \mu m$ and $y = 60 \mu m$. In addition, the waveguide layer is from $x = 8.0 \mu m$ to $x = 8.4 \mu m$. Again, dark areas indicate regions of lower field amplitude, and the lighter areas indicate regions of higher field amplitude. In addition, both transmitted fields at $x = 16 \mu m$ and waveguide-coupled fields at $y = 80 \mu m$ corresponding to Fig. 6.6 are also represented in Fig. 6.7.

As seen in Figs. 6.6 and 6.7(a), the characteristics of a finite input VHGC in the waveguide cover region are similar to those of a finite input VHGC in the waveguide film

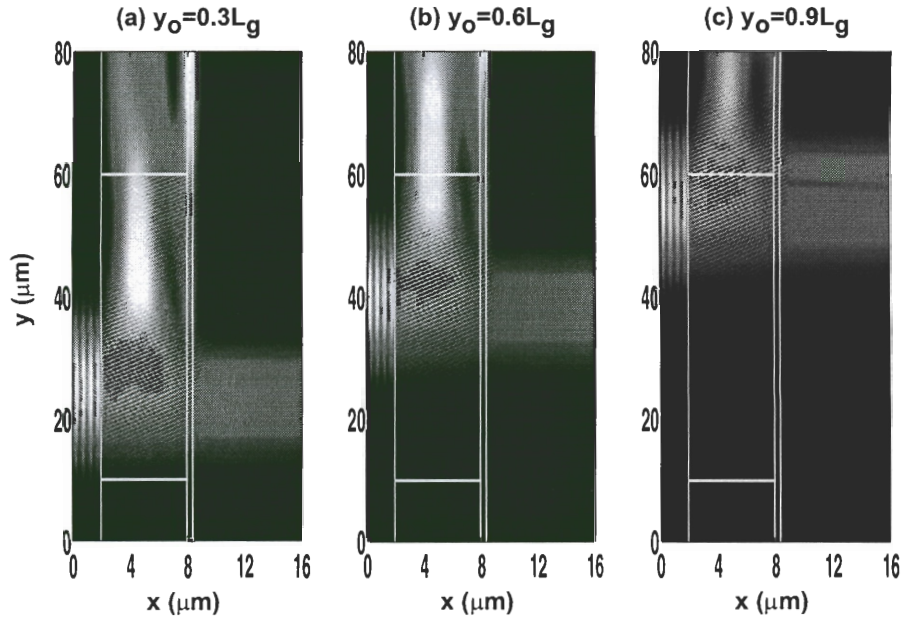


Figure 6.6: Two-dimensional field-amplitude patterns of a finite input VHGC with $L_g = 50 \mu m$ in the waveguide cover region illuminated by a TE-polarized Gaussian beam with beam waist $W = 0.5L_g$ at the incident position of (a) $y_o = 0.3L_g$, (b) $y_o = 0.6L_g$, and (c) $y_o = 0.9L_g$.

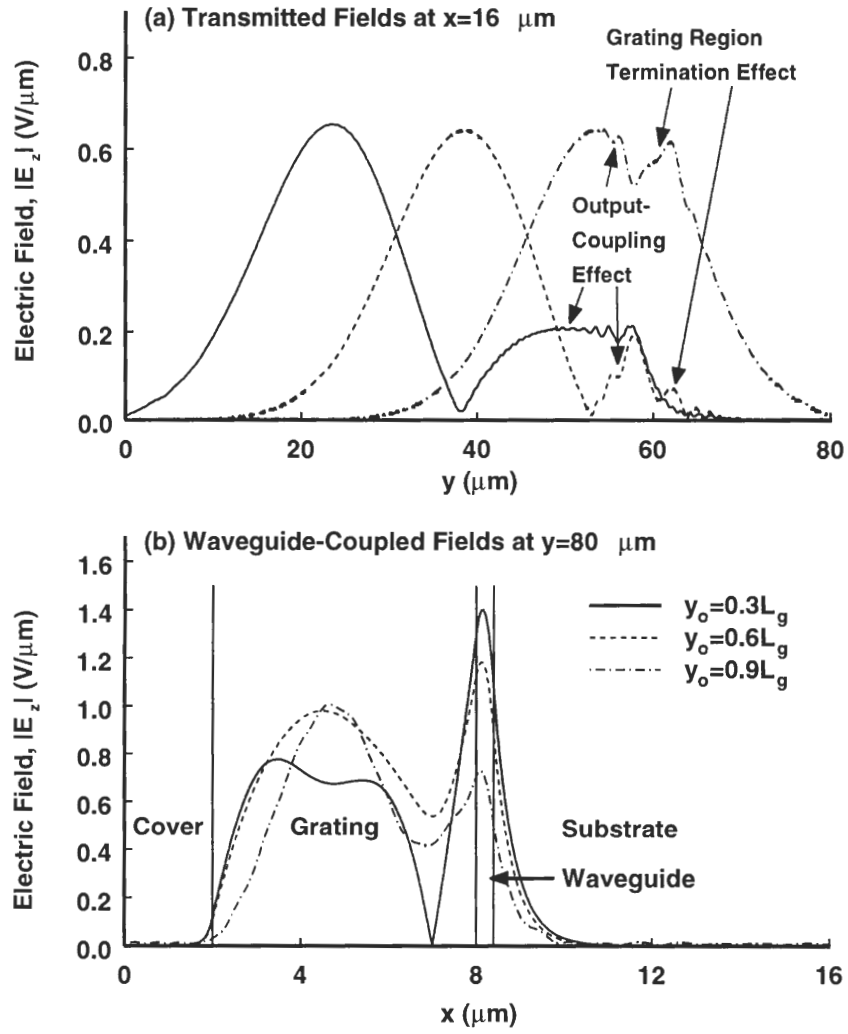


Figure 6.7: Field profiles corresponding to Fig. 6.6 for (a) the transmitted field at $x = 16 \mu\text{m}$ and (b) the waveguide-coupled field at $y = 80 \mu\text{m}$.

region. The output-coupling effect, resulting in the leakages of guided modes from the waveguide and therefore deteriorating the performance of a finite input VHGC, decreases as the incident-beam position increases. On the other hand, the grating region termination effect, causing an incomplete interaction between the finite beam and the finite VHGC and thus worsening the input coupling efficiency, increases as the incident-beam position increases. As a result, there is an optimum incident-position for a finite incident-beam for a finite input VHGC in the waveguide cover region. The optimization of an input VHGC in the waveguide cover region will be discussed in Section 6.3.2. Furthermore, in contrast to the configuration of a finite input VHGC in the waveguide film region [as seen in Figs. 6.3 and 6.4(b)], another interesting phenomenon for the case of a finite input VHGC in the waveguide cover region is an additional TE_1 mode excitation. As seen in Figs. 6.6 and 6.7(b), besides the fundamental TE_0 mode (confined in the film layer), an additional TE_1 mode (confined in the grating-film layer) are excited by the input VHGC.

6.3.2 Optimization of Input Coupling Efficiencies

The numerical results of input coupling efficiencies (in the upward direction) of TE_0 mode (CE_{u,TE_0}) and TE_1 mode (CE_{u,TE_1}) as a function of normalized incident-beam positions with various incident-beam widths and different incident-beam profiles for a VHGC in the waveguide cover region are represented in Figs. 6.8 and 6.9 respectively. It is noted that for all cases treated in this section, the input coupling efficiencies (in the upward direction) of TE_2 mode (CE_{u,TE_2}), TE_3 mode (CE_{u,TE_3}), and TE_4 mode (CE_{u,TE_4}) are less than 1.0%, 2.0% and 0.005% respectively. On the other hand, the input coupling efficiencies for all guided modes in the downward direction are less than 0.06%. In addition, the optimum incident-positions ($y_{o,opt}$) and the corresponding coupling efficiencies (in the upward direction) for both TE_0 and TE_1 modes of a finite input VHGC in the waveguide cover region illuminated by various incident-beam profiles with different incident-beam widths are summarized in Table 6.2.

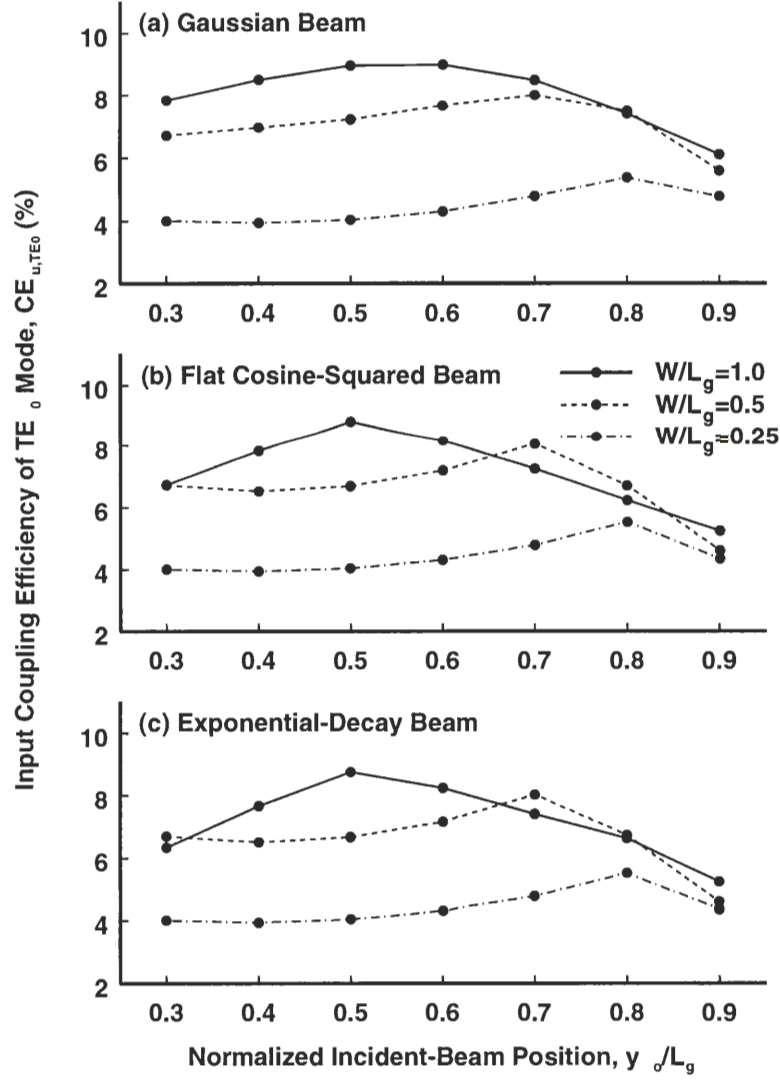


Figure 6.8: Input coupling efficiencies of TE_0 mode in the upward direction as functions of y_0/L_g and W/L_g for a finite input VHGC with $L_g = 50 \mu m$ in the waveguide cover region illuminated by (a) a Gaussian beam, (b) a flat cosine-squared beam, and (c) an exponential-decay beam.

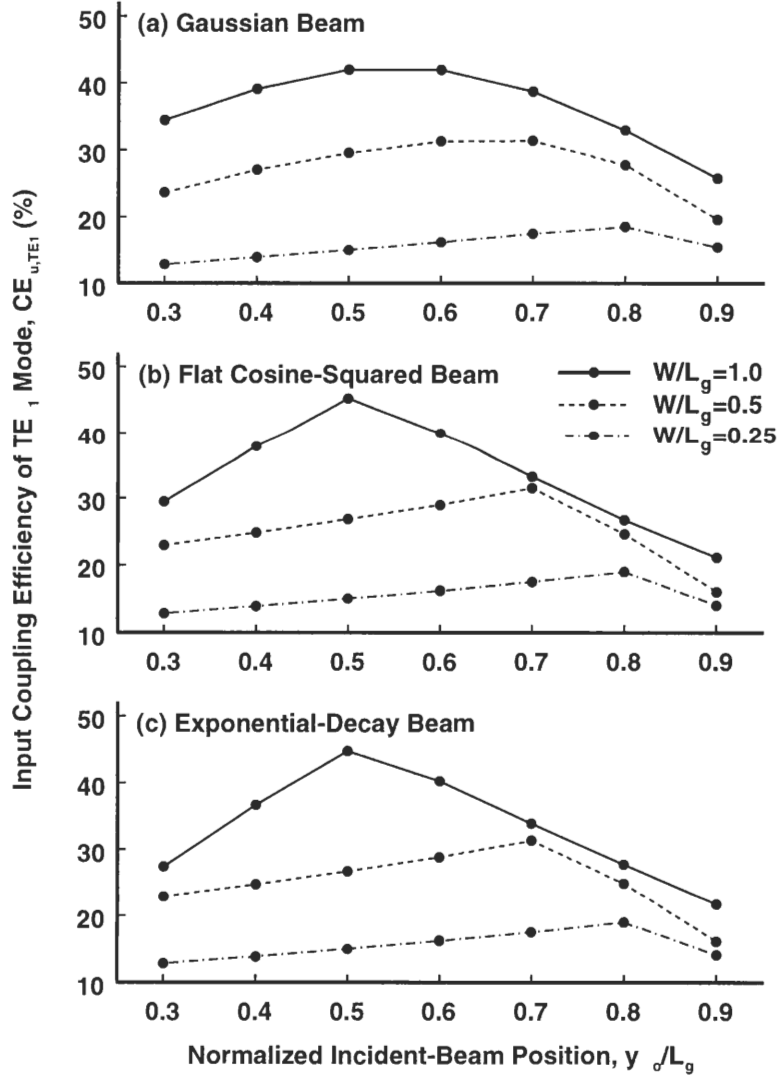


Figure 6.9: Input coupling efficiencies of TE₁ mode in the upward direction as functions of y_0/L_g and W/L_g for a finite input VHGC with $L_g = 50 \mu m$ in the waveguide cover region illuminated by (a) a Gaussian beam, (b) a flat cosine-squared beam, and (c) an exponential-decay beam.

As seen in Figs. 6.8 and 6.9, similar to the case of a finite input VHGC in the waveguide film region (shown in Fig. 6.5), the input coupling efficiency is strongly dependent on the incident-beam width as well as on the incident-beam position, but is weakly dependent on the incident-beam profile. On the other hand, as seen in Table 6.2, the optimum incident-positions of $y_{o,opt}$ for both TE_0 and TE_1 modes shift to the end of the VHGC as the incident-beam width decreases. Furthermore, the corresponding input coupling efficiencies for both TE_0 and TE_1 modes (at the optimum coupling condition) decrease as the incident-beam width decreases. However, the incident-beam profile does not significantly affect the

Table 6.2: Optimization of a finite input VHGC with length $L_g = 50 \mu m$ in a waveguide cover region illuminated by various incident-beam profiles.

Optimization for Coupling into TE_0 Mode			
Beam Profiles	Beam Width W/L_g	Optimum Incident-Position $y_{o,opt}/L_g$	Input Coupling Efficiency $CE_{u,TE_0}(\%)$
Gaussian	1.0	0.6	8.98
	0.5	0.7	8.00
	0.25	0.8	5.37
Flat Cosine-Squared	1.0	0.5	8.83
	0.5	0.7	8.07
	0.25	0.8	5.53
Exponential-Decay	1.0	0.5	8.76
	0.5	0.7	8.03
	0.25	0.8	5.52
Optimization for Coupling into TE_1 Mode			
Beam Profiles	Beam Width W/L_g	Optimum Incident-Position $y_{o,opt}/L_g$	Input Coupling Efficiency $CE_{u,TE_1}(\%)$
Gaussian	1.0	0.5	42.02
	0.5	0.7	31.38
	0.25	0.8	18.57
Flat Cosine-Squared	1.0	0.5	45.27
	0.5	0.7	31.43
	0.25	0.8	19.02
Exponential-Decay	1.0	0.5	44.78
	0.5	0.7	31.33
	0.25	0.8	19.01

optimization of a finite input VHGC in the waveguide cover region.

Comparing Figs. 6.8 and 6.9, although the input VHGC is designed to couple the normally incident beam into the TE_0 mode of the waveguide based on the phase-matching condition for the first diffracted order, the input coupling efficiencies of the TE_1 mode are much higher than those of the TE_0 mode. For example, for a VHGC in the waveguide cover region illuminated by a Gaussian beam with $W = 0.5L_g$ at the optimum incident-position of $y_o = 0.7L_g$, the input coupling efficiencies of TE_0 mode and TE_1 mode are $CE_{u,TE_0} = 8.00\%$ and $CE_{u,TE_1} = 31.38\%$. In order to explain this interesting phenomenon, let us apply this VHGC in the waveguide cover region as an output grating coupler to couple the TE_0 mode normally out of the waveguide (i.e. the output coupling angle in the cover region is $\theta_c = 0^\circ$). As discussed in detail in Section 5.3.2, the output coupling angle is $\theta_c = 0.38^\circ$ instead of the designed value of $\theta_c = 0^\circ$ because the grating period and the slant angle are designed based on the propagation constant of a waveguide without the grating modulation being considered (i.e. the grating is considered homogeneous with an average refractive index). As a result, the effective tangential-component of the grating vector (i.e. the component of the grating vector along the propagation direction of the guided mode) is $K_{y,eff} = 9.414 \mu m^{-1}$, which is away from the expected value $K_y = 9.456 \mu m^{-1}$ (i.e. the propagation constant of TE_0 mode), but is closer to the propagation constant of TE_1 mode. On the other hand, if this VHGC is used to couple the normally incident beam into the waveguide, more incident light will be coupled into the TE_1 mode than into the TE_0 mode.

6.4 Summary and Discussion

The effects of the incident-beam width, the incident-beam position, and the incident-beam profile on the input coupling efficiency of a finite input VHGC are investigated for TE incident polarization by use of the FDFD rigorous electromagnetic method. Two configurations of an input VHGC embedded in the waveguide film region as well as an input VHGC placed

in the waveguide cover region are examined.

For both configurations, the preceding numerical analysis has shown that the incident-beam width as well as the incident-beam position can dramatically affect the input coupling efficiency. In general, for a given VHGC, the input coupling efficiency decreases as the incident-beam width decreases because a narrower beam corresponds to a broader spectrum of spatial frequencies, resulting in a significant deviation from the Bragg condition, and thus, a smaller coupling efficiency. On the other hand, for the incident-position effect, depending on both the output-coupling effect and the grating region termination effect, an optimum incident-position $y_{o,opt}$, which is strongly dependent on the incident-beam width, for a given beam can be obtained. For example, the optimum incident-positions of a VHGC in the waveguide film region illuminated by a Gaussian beam are $y_{o,opt} = 0.5L_g, 0.6L_g$ and $0.8L_g$ as the incident-beam widths are $W = L_g, 0.5L_g$, and $W = 0.25L_g$ respectively. The similar results for the optimization of a flat cosine-squared beam and an exponential-decay beam can also be observed. In summary, the optimum incident-beam position shifts to the end of a VHGC as the incident beam width decreases. However, the beam profile does not dramatically affect the input coupling efficiency as well as the optimization of input coupling.

In addition, the FDFD results show that there is a higher-order waveguide mode excitation in the configuration of an input VHGC in the waveguide cover region. A rather interesting observation is that the input coupling efficiency of TE_1 mode is much higher than that of TE_0 mode, even though the input VHGC is designed to couple the normally incident beam into the TE_0 mode of the waveguide. The reason of this interesting result is that the effective tangential-component of the grating vector corresponding to the tangential component of the first diffracted order is closer to the propagation constant of TE_1 mode than to that of TE_0 mode.

CHAPTER 7

DESIGN, FABRICATION, AND PERFORMANCE OF A VOLUME HOLOGRAPHIC GRATING COUPLER

In this research, a VHGC in the waveguide cover region with output coupling angle $\theta_c = 0^\circ$ [as seen in Fig. 5.1(b)] will be designed, fabricated, and tested. For ease of testing this device, the operation wavelength (i.e the reading beam) at freespace is $\lambda_{0,r} = 632.8 \text{ nm}$. The waveguide material is the Avatrel 2000P polymer (fabricated by Promerus, LLC) with refractive index $n_{w,r} = 1.518$ at $\lambda_{0,r} = 632.8 \text{ nm}$. The thickness of the waveguide is designed as $t_w = 0.5 \mu\text{m}$. In order to fabricate a holographic grating, a commercial argon-ion laser (Spectra-Physics BeamLok 2065-S) with freespace wavelength $\lambda_{0,w} = 363.8 \text{ nm}$ is used to create the desired interference pattern. The grating material is DuPont's OmniDex613 photopolymer with refractive index $n_{g,r} = 1.50$ and $n_{g,w} = 1.535$ at $\lambda_{0,r} = 632.8 \text{ nm}$ and $\lambda_{0,w} = 363.8 \text{ nm}$ respectively. The refractive-index modulation and the thickness of this grating are $\Delta n_1 \sim 0.02$ and $t_g = 6.0 \mu\text{m}$ respectively. In addition, the substrate is fused silica with refractive index $n_s = 1.4567$ and the cover is air ($n_c = 1.0$). As a result, the waveguide grating coupler supports a single waveguide mode with propagation constant $\beta_{TE_0} = 14.897 \mu\text{m}^{-1}$ and seven photopolymer modes with corresponding propagation constants $\beta_{TE_1} = 14.879 \mu\text{m}^{-1}$, $\beta_{TE_2} = 14.848 \mu\text{m}^{-1}$, $\beta_{TE_3} = 14.800 \mu\text{m}^{-1}$, $\beta_{TE_4} = 14.738 \mu\text{m}^{-1}$, $\beta_{TE_5} = 14.659 \mu\text{m}^{-1}$, $\beta_{TE_6} = 14.567 \mu\text{m}^{-1}$, and $\beta_{TE_7} = 14.466 \mu\text{m}^{-1}$.

7.1 Design of a Volume Holographic Grating Coupler

In order to design a VHGC (operated at $\lambda_{0,r} = 632.8 \text{ nm}$) to couple out the guided mode into the cover region with a pre-specified output coupling angle θ_c (as seen in Fig. 5.1), the standard phase-matching condition between the incident guided mode and desired diffracted wave is applied. Figure 7.1 shows the corresponding wavevector diagram for the case of a VHGC in the waveguide cover region. In this case, the waveguide is comprised of a substrate with refractive index n_s , a grating layer with refractive index $n_{g,r}$, a waveguide film region with refractive index $n_{w,r}$, and a cover region with refractive index n_c . β is the propagation constant of a guided mode of this waveguide without the grating modulation being considered.

As seen in Fig. 7.1, the x -component of the grating vector K_x is determined by using the phase matching condition to achieve the pre-specified output coupling angle θ_c ,

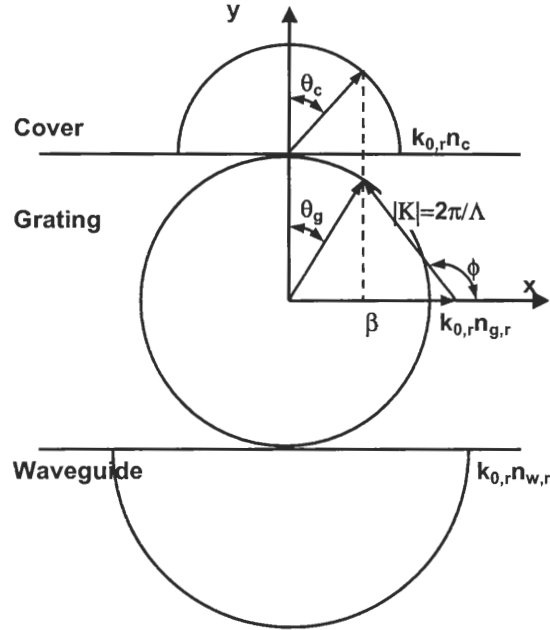


Figure 7.1: Corresponding wavevector diagram for the design of a VHGC in the waveguide cover region with output coupling angle θ_c .

and the y -component of the grating vector K_y is determined by using the Bragg condition. Therefore, the grating vector can be represented as

$$\mathbf{K} = K_x \hat{x} + K_y \hat{y} = (k_{0,r} n_c \sin \theta_c - \beta) \hat{x} + k_{0,r} n_{g,r} \cos \theta_g \hat{y}, \quad (7.1)$$

where $k_{0,r} = 2\pi/\lambda_{0,r}$ is the freespace wave number, and θ_g is the output coupling angle in the grating layer. In addition, since $n_{g,r} \sin \theta_g = n_c \sin \theta_c$, the slant angle of the grating can be written as

$$\phi = \tan^{-1} \frac{K_y}{K_x} = \tan^{-1} \frac{\sqrt{n_{g,r}^2 - n_c^2 \sin^2 \theta_c}}{n_c \sin \theta_c - n_{eff}}, \quad (7.2)$$

where $n_{eff} = \beta/k_{0,r}$ is the effective index of this waveguide. Furthermore, according to the wavevector diagram, the grating period can be represented as

$$\Lambda = \frac{2\pi}{|\mathbf{K}|} = \frac{2\pi}{\beta - k_{0,r} n_c \sin \theta_c} \cos \phi. \quad (7.3)$$

Although Eqs. (7.2) and (7.3) are derived for a VHGC in the waveguide cover region, they could be applied for a VHGC in the waveguide film and/or cover region for both output coupling and input coupling.

7.2 Design of a Holographic Recording Configuration

7.2.1 Arrangement of Interferometric Recording

In order to fabricate a VHGC in the waveguide cover region, the interferometric recording configuration shown in Fig. 7.2 is applied. As shown in Fig. 7.2 recording light from an argon-ion TE-polarized laser with freespace wavelength $\lambda_{0,w} = 363.8 \text{ nm}$ is focused and smoothed by a spatial filter and then collimated by a lens with a focal length of $f = 1000 \text{ mm}$ to obtain a uniform phase-front. Then, the recording beam is redirected by use of a fixed mirror to a polarizing beamsplitter. The polarizing beamsplitter consisting of a rotatable half-wave plate, followed by a beamsplitter cube and a fixed half-wave plate, is used to split the recording beam into two incident beams (referred to the objective beam and the

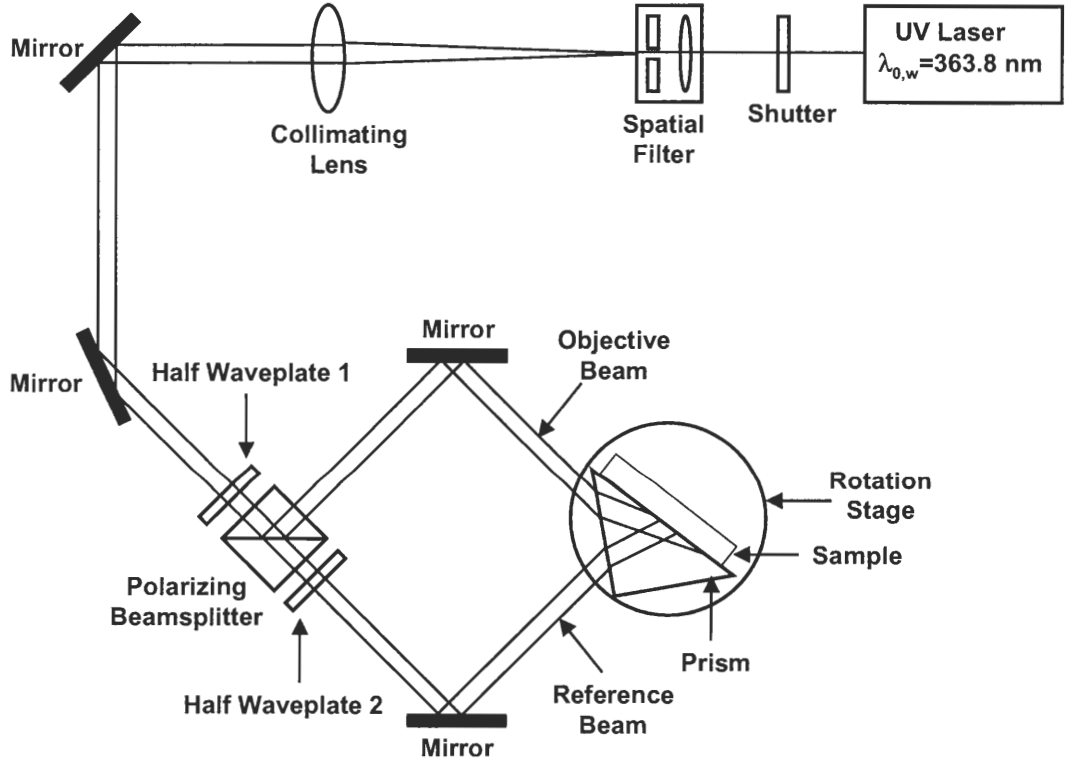


Figure 7.2: Configuration of volume holographic grating recording.

reference beam). The power ratio of the objective beam and the reference beam P_o/P_r can be adjusted by the rotation of the first half-wave plate. Then, both the objective beam and the reference beam are redirected by two gimbaled mirrors toward the recording sample. The sample is prepared by laminating a DuPont OmniDex613 photopolymer on an Avatrel waveguide. The fabrication processing will be discussed in Section 7.3. Similar to the configuration for the fabrication of a large slant-angle holographic grating (as seen in Fig. 4.14), a fused silica $45^\circ - 45^\circ - 90^\circ$ prism with refractive index $n_{p,w} = 1.47$ is inserted between the prepared sample and air to obtain the desired interference pattern, especially for the grating with large slant-angle $\phi = 20.32^\circ$. The outside surfaces of the prism are

AR coated to reduce reflections. The configuration of the prism system is represented in Fig. 7.3.

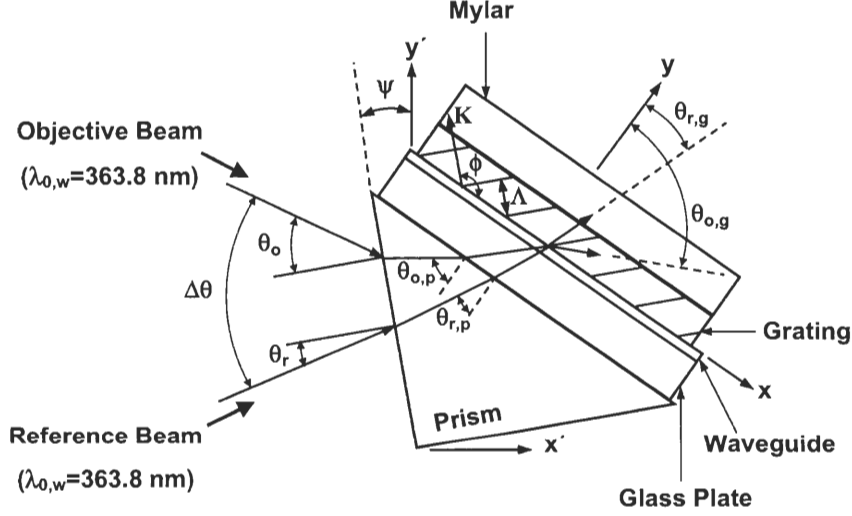


Figure 7.3: Configuration of a prism system for the fabrication of volume holographic gratings. An argon-ion laser with free-space wavelength $\lambda_{0,w} = 363.8 \text{ nm}$ is used as a writing beam to create the fringe interference. The coordinate systems used for the grating and the prism are $x - y$ and $x' - y'$ respectively. The angle between the objective beam and the reference beam are $\Delta\theta$, and the rotation angle of the prism (in counterclockwise) is ψ . The corresponding angle of the incident angles of the objective beam and the reference beam are $\theta_o = \Delta\theta/2 + \psi$ and $\theta_r = \Delta\theta/2 - \psi$ respectively.

7.2.2 Interference Pattern

The configuration of the prism system to create the desired interference pattern is shown in Fig. 7.3. As shown in Fig. 7.3, the angle between the objective beam and the reference beam is $\Delta\theta$, and the rotation angle (in counterclockwise direction) of the prism is ψ . Therefore, the incident angles of the objective beam (θ_o) and the reference beam (θ_r) can be written as

$$\theta_o = \frac{\Delta\theta}{2} + \psi, \quad (7.4)$$

$$\theta_r = \frac{\Delta\theta}{2} - \psi. \quad (7.5)$$

From the Snell's law and the geometry of the prism, the incident angles of the objective beam both in the prism ($\theta_{o,p}$) and in the grating ($\theta_{o,g}$) and the incident angles of the reference beam both in the prism ($\theta_{r,p}$) and in the grating ($\theta_{r,g}$) can be represented as

$$\theta_{o,p} = 45^\circ + \sin^{-1} \left(\frac{\sin \theta_o}{n_{p,w}} \right), \quad (7.6)$$

$$\theta_{o,g} = \sin^{-1} \left(\frac{n_{p,w}}{n_{g,w}} \sin \theta_{o,p} \right), \quad (7.7)$$

$$\theta_{r,p} = 45^\circ - \sin^{-1} \left(\frac{\sin \theta_r}{n_{p,w}} \right), \quad (7.8)$$

$$\theta_{r,g} = \sin^{-1} \left(\frac{n_{p,w}}{n_{g,w}} \sin \theta_{r,p} \right). \quad (7.9)$$

As a result, the recorded grating vector $\mathbf{K} = K_x \hat{x} + K_y \hat{y}$ are

$$K_x = k_{0,w} n_{g,w} (\sin \theta_{r,g} - \sin \theta_{o,g}), \quad (7.10)$$

$$K_y = k_{0,w} n_{g,w} (\cos \theta_{r,g} - \cos \theta_{o,g}), \quad (7.11)$$

where $k_{0,w} = 2\pi/\lambda_{0,w}$ is the freespace wavevector of the writing (recording) beam. Finally, the slant angle, ϕ , and the grating period, Λ , can be represented as

$$\phi = \tan^{-1} \left(\frac{K_y}{K_x} \right), \quad (7.12)$$

$$\Lambda = \frac{2\pi}{\sqrt{K_x^2 + K_y^2}}. \quad (7.13)$$

However, as has been discussed previously, the holographic recording introduces material shrinkage of the DuPont OmniDex613 photopolymer, and therefore, changes the grating period and the slant angle. Figure 7.4 shows the effect of the material shrinkage on the grating vector. From the geometry of the grating (as seen in Fig. 7.4), the new slant angle, ϕ_s , and the new grating period, Λ_s , resulting from recording shrinkage are

$$\phi_s = \tan^{-1} \left(\frac{\tan \phi}{1 - \delta_s} \right), \quad (7.14)$$

$$\Lambda_s = \Lambda \frac{\cos \phi_s}{\cos \phi}, \quad (7.15)$$

where δ_s is the shrinkage factor. Therefore, the new grating vector $\mathbf{K}_s = K_{x,s} \hat{x} + K_{y,s} \hat{y}$ can

be written as

$$K_{x,s} = K_x, \quad (7.16)$$

$$K_{y,s} = \frac{K_y}{1 - \delta_s}. \quad (7.17)$$

It is noted that the recording shrinkage does not change the x -component of the grating vector. Depending on the exposure intensity, the shrinkage factor of a DuPont OmniDex613 photopolymer varies from $\delta_s \sim 2.75\%$ to $\delta_s \sim 4.20\%$ (discussed in Chapter 4).

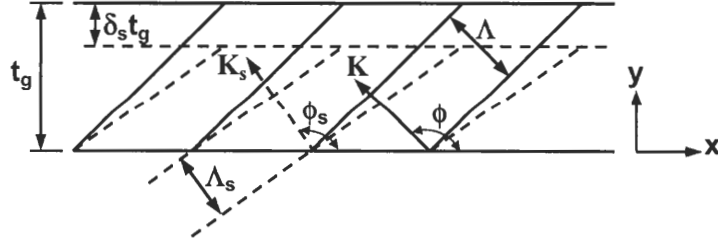


Figure 7.4: Effects of material shrinkage on a photopolymer after holographic recording. The solid lines represent the grating configuration (with period Λ , slant angle ϕ , and grating vector \mathbf{K}) without material shrinkage, and the dash lines represent the grating configuration (with period Λ_s , slant angle ϕ_s , and grating vector \mathbf{K}_s) after recording shrinkage. The original thickness and the shrinkage factor of the photopolymer are t_g and δ_s respectively.

In addition, in order to obtain a high-contrast interference pattern, the intensities of the objective beam and the reference beam have to be adjusted to be equal (i.e. the fringe visibility $V = 1.0$ inside the photopolymer). Considering the Fresnel reflection losses and different projection areas of the objective beam and the reference beam, the power ratio between the objective beam and the reference beam for $V = 1.0$ can be easily derived as

$$\frac{P_o}{P_r} = \frac{(1 - R_{f,r})(1 - R'_{f,r}) \cos \theta_r \cos \theta_{r,p} \cos(\theta_{o,p} - 45^\circ)}{(1 - R_{f,o})(1 - R'_{f,o}) \cos \theta_o \cos \theta_{o,p} \cos(\theta_{r,p} - 45^\circ)}, \quad (7.18)$$

where $R_{f,i}$ and $R'_{f,i}$ ($i = o, r$) are the Fresnel reflection losses of the i beam at the prism-glass interface and at the glass-grating interface respectively.

Figure 7.5 shows an example for the design of the grating period (Λ), the slant angle (ϕ), the output coupling angle (θ_c), and the power ratio of the objective beam and the reference beam (P_o/P_r) of a VHGC in the waveguide cover region based on the prism system (as seen in Fig. 7.3) as functions of the angle between the objective beam and the reference beam ($\Delta\theta$) as well as the rotation angle of the prism (ψ). The solid lines and the dash lines represent the cases of shrinkage factors with $\delta_s = 0.0\%$ and $\delta_s = 3.0\%$ respectively. As seen in Figs. 7.5 (a) and (b), as the shrinkage factor increases, the grating period decreases and the slant angle increases. However, the recording shrinkage does not change the output coupling angle θ_c [as seen in Fig. 7.5 (c)] because the x -component of the grating vector is the same before and after recording (i.e. $K_x = K_{x,s}$). Although the recording shrinkage does not affect the output coupling angle, it introduces a deviation of the y -component of the grating vector increases ($K_{y,s} = K_y/1 - \delta_s$). However, as has been discussed in Chapter 4, this shift of the y -component of the grating vector can be compensated by using post-baking processing. As seen in Fig. 7.5, in order to obtain the zero-degree output coupling angle ($\theta_c = 0^\circ$), the angle between the objective beam and the reference beam and the rotation angle (in counterclockwise) of the prism are $\Delta\theta = 83.58^\circ$ and $\psi = 7.70^\circ$ respectively for $\delta_s = 0.0\%$. As a result, the corresponding grating period and the slant angle are $\Lambda = 298.27\text{ nm}$ and the slant angle $\phi = -44.99^\circ$ respectively. In addition, the power ratio of the objective beam and the reference beam is $P_o/P_r = 4.81$ for the fringe visibility $V = 1.0$ inside the photopolymer.

7.3 Fabrication of a Volume Holographic Grating Coupler

7.3.1 Sample Preparation

In this research, the waveguides are fabricated by using a 15% (by weight) solution of Avatrel 2000P. Before fabricating waveguides, the fused-silica substrates (with thickness $\sim 1.0\text{ mm}$) are first rinsed using TCE, acetone, methanol, and isopropanol. Then, the

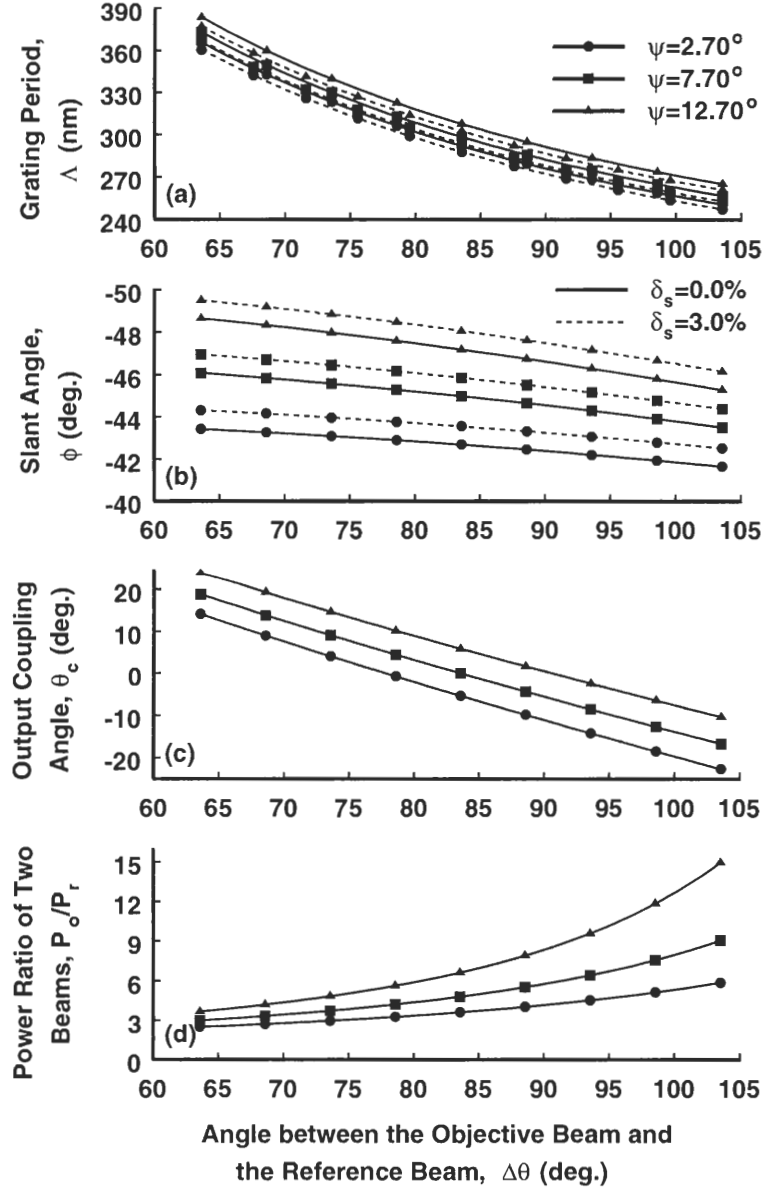


Figure 7.5: Design of (a) the grating period (Λ), (b) the slant angle (ϕ), (c) the output coupling angle (θ_c), and (d) the power ratio of the objective beam and the reference beam (P_o/P_r) of a VHGC in the waveguide cover region based on the prism system for holographic recording (as seen in Fig. 7.3) as functions of the angle between the objective beam and the reference beam ($\Delta\theta$) as well as the rotation angle of the prism (ψ). The solid lines and the dash lines represent the cases of shrinkage factors with $\delta_s = 0.0\%$ and $\delta_s = 3.0\%$ respectively. In addition, the operation wavelength and the effective index of the waveguide are assumed to be $\lambda_{0,r} = 632.8 \text{ nm}$ and $n_{eff} = 1.5003$ respectively.

substrates are dried at 100°C by a hot plate for 2 minutes to drive off excess moisture. Next, the AP3000 adhesion promoter is spun on the substrate at 3000 rpm with increasing rate 1000 rpm/sec for 30 seconds. Then, a 15% (by weight) solution of Avatrel 2000P is spun on the on the sample at 6000 rpm with increasing rate 1000 rpm/sec for 120 seconds. After the spinning processing is finished, the waveguide sample is placed on a hot plate at 100°C for 10 minutes. As a result, the thickness of the Avatrel waveguide is $t_w = 0.5\text{ }\mu\text{m}$.

The recording material for the grating fabrication is the DuPont OmniDex613 photopolymer. A photopolymer piece with a width of $1 - 2\text{ cm}$ cutting from a photopolymer sheet is prepared by removing one of the Mylar cover sheets. Then, the photopolymer piece is laminated on the Avatrel waveguide. Next, the sample (consisting of a fused-silica substrate, a $0.5\text{ }\mu\text{m}$ -thick Avatrel waveguide, a photopolymer piece, and a Mylar layer) is placed in the prism system (as seen in Figs. 7.2 and 7.3) for the grating fabrication. It is noted that mineral oil is used between the sample and the prism for the index match.

7.3.2 Grating Recording

A VHGC with zero-degree output coupling ($\theta_c = 0^{\circ}$) is fabricated in this research. Based on the desired operation freespace wavelength ($\lambda_{0,r} = 632.8\text{ nm}$) and the waveguide structure consisting of a substrate with refractive index $n_s = 1.4567$, a $0.5\text{ }\mu\text{m}$ -thick Avatrel waveguide with refractive index $n_{w,r} = 1.518$, a $6.0\text{ }\mu\text{m}$ -thick grating with refractive index $n_{g,r} = 1.50$, and air as a cover ($n_c = 1.0$), the propagation constant and the effective index of TE_0 mode are $\beta_{\text{TE}_0} = 14.897\text{ }\mu\text{m}^{-1}$ and $n_{eff} = 1.5003$ respectively. Substituting $\beta_{\text{TE}_0} = 14.897\text{ }\mu\text{m}^{-1}$ (as β) and $n_{eff} = 1.5003$ into Eqs. 7.2 and 7.3, the slant angle and the grating period for zero-degree output coupling ($\theta_c = 0^{\circ}$) are $\phi = -44.99^{\circ}$ and $\Lambda = 298.27\text{ nm}$ respectively. Although the grating period and the slant angle are designed without considering the shrinkage effect, which results in the changes of the grating period and the slant angle, and thus, the deviation of Bragg angle, the shift of Bragg angle due to holographic recording can be compensated by applying the post-baking processing. In

addition, the post-baking processing can also improve the refractive-index modulation, and thus, the coupling efficiency.

Following the procedure for the design of a holographic recording configuration (described in Section 7.2.2), in order to fabricate a slanted grating with the period $\Lambda = 298.27 \text{ nm}$ and the slant angle $\phi = -44.99^\circ$ the angle between the objective beam and the reference beam and the rotation angle (in counterclockwise direction) of the prism are set as $\Delta\theta = 83.58^\circ$ and $\psi = 7.70^\circ$ respectively (as seen in Fig. 7.3). Furthermore, the power ratio of the objective beam and the reference beam are selected as $P_o/P_r = 4.81$ to obtain the equal intensities of these two beams (i.e. the fringe visibility $V = 1.0$ inside the photopolymer). Then, the sample placed in the prism system is exposed at intensity $I_0 = 0.110 \text{ mW/cm}^2$ for 10 minutes. After recording, the sample is rinsed using isopropanol for removing the mineral oil. Then, the sample is cured by a uniform UV light with wavelength $\lambda_0 = 365.0 \text{ nm}$ and exposure irradiance $I_0 = 2.0 \text{ mW/cm}^2$ for 5 minutes to fix both the Avatrel waveguide and the grating. Next, the sample is baked at temperature $T_b = 120^\circ\text{C}$ for 1.5 hours to improve the refractive-index modulation as well as the coupling efficiency and compensate the shrinkage effect resulting from the holographic recording. After the post-baking, the other Mylar layer can be easily removed from the sample.

7.4 Performance of a Volume Holographic Grating Coupler

In order to determine the performance of a VHGC designed for zero-degree output coupling ($\theta_c = 0^\circ$), an angular-selectivity testing configuration shown in Fig. 4.15 is used. A VHGC sample (fabricated in Section 7.3) is mounted on a rotational stage and is illuminated by a He-Ne TE-polarized laser with free-space wavelength $\lambda_{0,r} = 632.8 \text{ nm}$. Light transmitted through the sample (not diffracted) is measured for a range of incident angles (θ_{inc}) around the designed coupling angle.

Figure 7.6 shows the normalized transmitted power as a function of incident angle

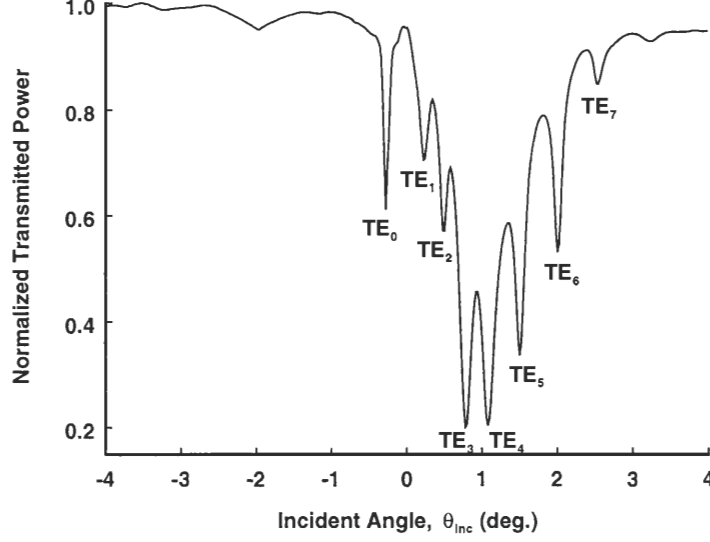


Figure 7.6: The normalized transmitted power as a function of incident angle θ_{inc} for the fabrication of VHGC.

θ_{inc} for the VHGC described in Section 7.3. As seen in Fig. 7.6, there are eight resonances representing the coupling into the fundamental TE_0 mode (confined in the film layer) and the photopolymer modes (confined in the film-grating layer). For the fundamental TE_0 mode, the input coupling angle (i.e. the output coupling angle) of the experimental measurement is $\theta_{c,exp} = -0.28^\circ$ and the transmission efficiency is 61.17% (i.e. the input coupling efficiency of TE_0 mode is $CE_{TE_0} \sim 39.93\%$). It is noted that the measured coupling angle $\theta_{c,exp} = -0.28^\circ$ is slightly off their designed value ($\theta_c = 0^\circ$). The possible reasons for the deviation of the measured coupling angle ($\theta_{c,exp}$) from the designed coupling angle (θ_c) are the fabrication errors resulting from the holographic recording process (determining the period and the slant angle of a grating) and the spin-on process (defining the thickness of a waveguide-film layer). On the other hand, even though a perfect grating and a perfect waveguide are fabricated, the measured and designed values of the coupling angle may be different because the grating period and the slant angle are designed based on the propagation constant of a waveguide without the grating modulation being considered (i.e. the grating is considered

homogeneous with an average refractive index). The presence of the modulation affects slightly the real part of the propagation constant which results in the small difference of the diffracted angle from its designed value (described in Sections 5.2.2 and 5.3.2). In addition, as discussed in Section 6.3.1, the tangential component of an ideal grating (i.e. K_x in Fig. 7.1) is also different from the expected value, and therefore, causes the deviation of the measured coupling angle from its designed value.

Assuming the fabricated grating is perfect (i.e. $K_x = 14.897 \mu m^{-1}$), the incident angle can be replaced with a corresponding effective index, n_{eff} , by applying the relationship

$$n_{eff} = \frac{K_x}{k_{0,r}} - \sin(\theta_{inc}). \quad (7.19)$$

The experimental results of the normalized transmitted power as a function of the corresponding refractive index is shown in Fig. 7.7. In addition, the experimental measurements of the performance of a VHGC in the waveguide cover region with respect to the coupling angles, the corresponding refractive indices, and the coupling efficiencies for all guided modes are summarized in Table 7.1.

Table 7.1: Experimental measurements of the performance of a VHGC in the waveguide cover region with respect to the coupling angle, the effective index, and the coupling efficiency.

Guided Modes	Coupling Angle $\theta_{c,exp}$ (deg.)	Effective Index n_{eff}	Coupling Efficiency $CE(\%)$
TE ₀	-0.28	1.5052	39.93
TE ₁	0.22	1.4965	29.39
TE ₂	0.48	1.4919	42.84
TE ₃	0.78	1.4867	79.85
TE ₄	1.08	1.4815	79.69
TE ₅	1.50	1.4741	66.34
TE ₆	2.00	1.4654	46.85
TE ₇	2.54	1.4560	15.18

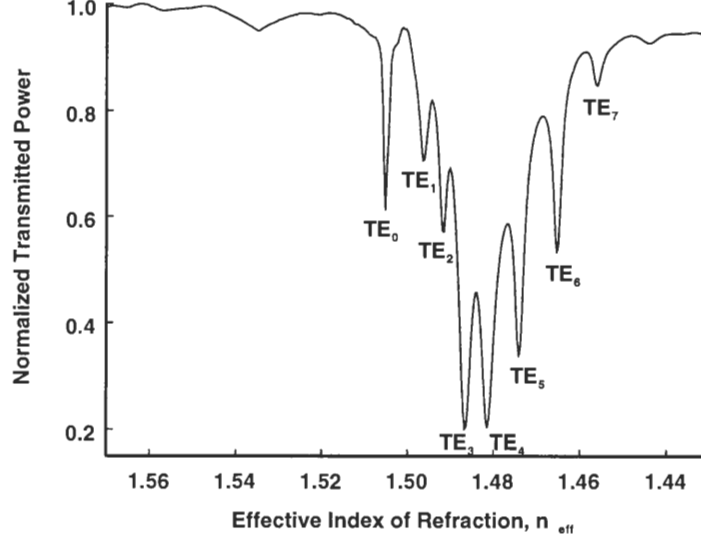


Figure 7.7: The normalized transmitted power as a function of the corresponding refractive index, n_{eff} for the fabrication of VHGC.

7.5 Summary and Discussion

The present chapter discusses the design, fabrication, and testing of a VHGC in the waveguide cover region for zero-degree output and/or input coupling ($\theta_c = 0^\circ$) of TE_0 mode at the operation wavelength of $\lambda_{0,r} = 632.8 \text{ nm}$. The waveguide material is the Avatrel 2000P polymer, and the thickness of the waveguide is designed as $t_w = 0.5 \mu\text{m}$ to support a single mode confined the film layer. On the other hand, the grating coupler is designed by use of the phase-matching condition for the first diffracted order and is fabricated based on the DuPont OmniDex613 photopolymer. In addition, the effect of the recording shrinkage on the grating period and the slant angle are also discussed in Section 7.2.2. As seen in Fig. 7.5, the grating period decreases and the slant angle increases as the shrinkage factor increases. However, the recording shrinkage does not change the tangential component of the grating vector (i.e. K_x does not change after holographic recording) as well as the coupling angle. In order to study the performance of a VHGC fabricated in Section 7.3, an angular-selectivity

measurement is applied. As seen in Fig. 7.6, eight resonances corresponding to coupling into the fundamental TE_0 mode (confined in the film layer) and the photopolymer modes (confined in the film-grating layer) are observed. For coupling into the TE_0 mode, the coupling efficiency is $CE_{TE_0} \sim 39.93\%$, and the coupling angle is $\theta_{c,exp} = -0.28^\circ$, which is very close to the designed value ($\theta_c = 0^\circ$).

CHAPTER 8

CONCLUSIONS

Grating couplers including volume holographic grating couplers (VHGCs) and surface-relief grating couplers have been proposed for use in integrated optics systems because of their compatibility with other optical and electronic devices. In contrast to the surface-relief grating couplers, VHGCs provide attractive advantages including high coupling efficiency, high preferential-order coupling, and dry processing (i.e. no etching) [20–22, 52, 66]. However, for practical applications, the needed VHGCs could have limited spatial apertures and are usually illuminated by finite-width beams (such as a Gaussian beams). As a result, the numerical methods of the rigorous coupled-wave analysis (RCWA) and the leaky-mode (LM) approach that have been commonly applied in the past to analyze grating couplers do not provide rigorous analysis because the RCWA assumes the grating is an infinite grating illuminated by a plane wave and the LM approach does not take into account the effects of the discontinuity between the waveguide and the VHGC and the resulting excitation of other guided or radiation modes. In addition, the dynamic characteristics of holographic grating formations in photopolymers are also important issues for the fabrication of VHGCs.

The research in this thesis dealt with the rigorous analysis, design, and fabrication of VHGCs as well as studied in detail the dynamic behaviors of holographic grating formations in photopolymers. The finite difference frequency-domain (FDFD) method from Chapter 2 and the finite-number-of-periods holographic gratings analysis in Chapter 3 have been presented at a conference [54] and published [55]. Most of the work in Chapter 4 on dynamics of holographic grating formations in photopolymers has been presented at a conference [133],

published [134], and submitted for publication [141]. The results of Chapter 5 for output VHGCs analysis have been accepted for publication [139]. Finally, the research in Chapter 6 of input VHGCs analysis is also being prepared for submission [142].

8.1 Summary of Results

8.1.1 Finite-Difference Frequency-Domain Method

The finite-difference frequency-domain (FDFD) method in conjunction with uniaxial perfectly matched layers (UPMLs) was presented for the first time to rigorously analyze finite gratings illuminated by finite beams. This numerical technique allows rigorous analysis of VHGCs as well as surface-relief grating couplers, which can be placed either in the film or in the cover of a waveguide, for both output and input coupling. In order to verify the FDFD method and the performance of the UPML, the planar interface problems for both TE and TM polarizations were tested. It was found that the performance of the UPML, such as the artificial reflection error from the UPML, is dependent on the characteristics (such as the conductivity, the dielectric constant, and the thickness) of the UPML. In general, the artificial reflection error from the UPML decreases as the conductivity of the UPML increases and finally reaches a saturation value with -90 dB . On the other hand, it was found that the numerical error decreases as the number of grid per wavelength increases (i.e. the mesh size decreases) and the convergence of the TM polarization is slower than that of TE polarization for solving the Helmholtz equations. In general, the numbers of grid per wavelength for both TE and TM polarization are $N_x, N_y \geq 20$ and $N_x, N_y \geq 25$ respectively for the FDFD analysis.

8.1.2 Finite-Number-of-Periods Holographic Gratings

Finite-number-of-periods (FNP) holographic gratings illuminated by finite-width incident beams (for both TE and TM polarizations) have been rigorously analyzed by use of the

FDFD method in conjunction with the UPMLs. Both unslanted and slanted gratings in transmission and reflection configurations were examined. The diffraction efficiencies of various diffracted orders were used as the metric of each grating performance. These diffraction efficiencies were also compared to the ones predicted by the RCWA that is applicable to infinite-number-of-periods (INP) gratings and infinite-width incident beams (plane waves). It was found that the maximum diffraction efficiencies for the FNP holographic gratings never exceeded that of the corresponding INP holographic gratings.

For unslanted gratings with at least 20 grating periods, the diffraction efficiencies estimated by the FDFD method were close to the ones predicted by the RCWA and remained constant as the incident-beam width increases because in this case the width of the incident beam was smaller the grating width, and the resulting diffraction resembled the diffraction by an infinite-width grating. In addition, as the number of periods decreased, the diffraction efficiency also decreased for a constant beam width. On the other hand, for slanted transmission/reflection gratings with at least 20 grating periods, the diffraction efficiencies determined by the FDFD method approached the efficiencies predicted by the RCWA as the incident-beam width increased because the wider the incident beam was, the more it resembled a plane-wave characteristic. However, as the incident-beam widths increased greater than ~ 10 grating periods ($W > 10\Lambda_y$), the diffraction efficiencies slowly converged to the values predicted by the RCWA.

For the comparison of the accuracy of the RCWA for FNP surface-relief gratings and FNP holographic gratings, the errors of the RCWA decrease as the grating width and the incident-beam width increased. In general, the errors of the RCWA for FNP holographic gratings and FNP surface-relief gratings are of the same order revealing that the effects of the FNP on the diffraction performance are equally important but are also case and polarization dependent.

8.1.3 Dynamics of Holographic Grating Formations in Photopolymers

The dynamic characteristics of holographic grating formations in photopolymers were studied by use of both theoretical analysis [a nonlocal diffusion model and the finite-difference time-domain (FDTD) method] and experimental techniques (including a real-time diffraction-monitoring technique and an angular-selectivity measurement). Both unslanted and slanted gratings were recorded at UV wavelength of 363.8 nm based on DuPont OmniDex613 photopolymers and tested. Furthermore, the effects of the post-baking conditions were also investigated.

For the theoretical analysis based on the nonlocal diffusion model rigorously solved by use of the FDTD method, it was found that the behavior of hologram recording was strongly dependent on the dimensionless reaction rate R_D (corresponding to the exposure intensity, the diffusion coefficient of free monomers, and the grating period), the dimensionless nonlocal variance parameters σ_D (relating to the nonlocal response length), and the dimensionless time t_D . For the larger dimensionless reaction rate ($R_D > 1.0$), the diffusion coefficient was larger than the polymerization rate, so the free monomers had enough time to propagate from the dark regions to the bright regions, and therefore, the polymer-concentration profile at the steady state resembled more a sinusoidal variation (i.e. a better first-order holographic grating was obtained). However, for the smaller dimensionless reaction rate ($R_D < 1.0$), the polymerization occurred faster than diffusion, and resulted in two peaks of the polymer-concentration profile near the dark regions. Besides the dimensionless reaction rate, the dimensionless nonlocal variance parameter σ_D (corresponding to the effects of the formation of polymer chains growing away from their initial locations) was another important factor for the holographic recording. For a given R_D , the larger σ_D , more resembled a sinusoidal polymer-concentration profile, but the lower the visibility of the profile. Therefore, increasing σ_D , i.e. decreasing grating period or increasing nonlocal response length, resulted in a weaker first-order holographic grating. In addition the numer-

ical results of the FDTD method were compared to those of the four-harmonic-component approximation [84] to quantify the accuracy of the low-harmonic-component approximation. It was found that the accuracy of the four-harmonic-component approximation increased as R_D increased and σ_D increased. The error of four-harmonic-component approximation was larger than 10% for $R_D < 1.0$ and for all value of σ_D .

Based on the angular-selectivity experiment in conjunction with the RCWA fitting for slanted holographic gratings, the recording-shrinkage factor of the DuPont OmniDex613 photopolymer varied from $\delta_s \sim 2.75\%$ to $\delta_s \sim 4.20\%$. In addition, it was found that the post-baking processing can not only double the refractive-index modulations of holographic gratings but also compensate the recording shrinkage due to the irreversible thermal expansion, the decrease of the average refractive index, and the loss of volatile components of recording material during post-baking processing. It was noted that the first two effects (i.e. the irreversible thermal expansion and the decrease of the average refractive index) resulted in a positive shift of Bragg angle, and the third effect (i.e. the loss of volatile components) resulted in a negative shift of Bragg angle. In general, the optimal baking temperature and baking time are $T_b = 120^\circ C$ and $t_b = 1.5 h$ respectively.

Finally, the characteristic parameters of DuPont OmniDex613 photopolymers for both unslanted and slanted holographic gratings were determined by fitting the theoretical results of the nonlocal diffusion model to the experimental data (based on the real-time diffraction-monitoring measurement). It was found that for unslanted gratings the diffusion coefficient was constant ($D_0 \sim 1.0 \times 10^{-12} cm^2/sec$) for all exposure intensities. However, for slanted gratings, the diffusion coefficient was dependent on exposure intensities. For the smaller exposure intensity ($I_0 = 0.043 mW/cm^2$), the diffusion coefficient of a slanted grating was $D_0 \sim 0.6 \times 10^{-12} cm^2/sec$ that was smaller than that of an unslanted grating because free monomers had longer diffusion distance, and therefore, both the photopolymer-Mylar and the photopolymer-glass boundaries affected the diffusion process. However, as the exposure intensity increased, the diffusion coefficient increased and approached to the

value of an unslanted grating because the higher exposure intensity corresponded to higher polymerization rate, and as a result, the diffusion process of a slanted grating with a higher exposure intensity ($I_0 = 0.240 \text{ mW/cm}^2$) resembled that of an unslanted grating.

8.1.4 Output Volume Holographic Grating Couplers

Output volume holographic grating couplers (VHGCs) placed either in the film or in the cover waveguide region were rigorously analyzed using the FDFD method. Both TE and TM polarizations with zero- and 45-degree output coupling were investigated and compared with the RCWA/LM approach. For both configurations, it was found that the upward coupling efficiency of TE polarization was much higher than that of TM polarization for zero-degree output coupling, and thus polarization-dependent couplers were obtained. On the other hand, the upward coupling efficiency of TM polarization was comparable to that of TE polarization for 45-degree output coupling. Therefore, the grating coupler could be polarization-independent if the grating was designed for 45-degree output coupling.

Comparing the results of the FDFD method and the RCWA/LM approach, it was found that the FDFD method showed that the normalized electric field intensity was not only an exponential decay, which the RCWA/LM approach assumed, but also had oscillatory components along the propagation direction. This oscillatory behavior of the FDFD method resulted from the interference between the incident mode, the higher-order modes (excited in the waveguide film-grating region), and the radiation fields. In addition, the FDFD results showed that there was a higher-order waveguide mode excitation and interference with the fundamental waveguide mode in the case of an output VHGC in the waveguide cover region and resulted in a non-monotonical decrease of the intensity of the output-coupled field along the propagation direction, which could be characterized by the beat length.

8.1.5 Input Volume Holographic Grating Couplers

A finite volume holographic grating coupler (VHGC) normally illuminated by various incident-beam profiles (including a Gaussian beam, a flat cosine-squared beam, and an exponential-decay beam) with finite beam-widths for input coupling was rigorously analyzed by use of the finite-difference frequency-domain (FDFD) method to study the effects of the incident-beam width, the incident-beam position, and the incident-beam profile on the input coupling efficiency, and therefore, to determine the optimum conditions for input coupling. Both a VHGC embedded in the waveguide film region and a VHGC placed in the waveguide cover region were investigated. Only TE polarization was considered.

For both configurations, both the incident-beam and the incident-beam position could dramatically affect the input coupling efficiency. In general, for a given VHGC, the input coupling efficiency decreases as the incident-beam width decreases. On the other hand, for the incident-position effect, depending on both the output-coupling effect and the grating region termination effect, an optimum incident-position $y_{o,opt}$ strongly depending on the incident-beam width for a given beam could be obtained. For example, the optimum incident-positions of a VHGC in the waveguide film region illuminated by a Gaussian beam were $y_{o,opt} = 0.5L_g, 0.6L_g$ and $0.8L_g$ as the incident-beam widths were $W = L_g, 0.5L_g$, and $W = 0.25L_g$ respectively. The similar results for the optimization of a flat cosine-squared beam and an exponential-decay beam could also be observed. In summary, the optimum incident-beam position shifted to the end of a VHGC as the incident beam width decreased. However, the beam profile did not dramatically affect the input coupling efficiency as well as the optimization of input coupling.

In addition, the FDFD results showed that there was a higher-order waveguide mode excitation in the configuration of an input VHGC in the waveguide cover region. A rather interesting observation was that the input coupling efficiency of TE_1 mode was much higher than that of TE_0 mode, even though the input VHGC was designed to couple the normally

incident beam into the TE_0 mode of the waveguide. The reason of this interesting result was that the effective tangential-component of the grating vector corresponding to the tangential component of the first diffracted order was closer to the propagation constant of TE_1 mode than to that of TE_0 mode.

8.1.6 Design, Fabrication, and Performance of a Volume Holographic Grating Coupler

A VHGC in the waveguide cover region for zero-degree output and/or input coupling ($\theta_c = 0^\circ$) of TE_0 mode at the operation wavelength of $\lambda_{0,r} = 632.8\text{ nm}$ was designed, fabricated, and tested. The waveguide and the grating were fabricated based on the Avatrel 2000P polymer and the DuPont OmniDex613 photopolymer respectively, and the thickness of the waveguide is designed as $t_w = 0.5\text{ }\mu\text{m}$ to support a single mode confined the film layer. Furthermore, the grating coupler was designed by use of the appropriate Bragg condition between the incident guided mode and the desired diffracted wave. According to experimental measurements represented in Chapter 7, the VHGC fabricated in this research showed that for coupling TE_0 mode, the coupling efficiency was $CE_{TE_0} \sim 39.93\%$, and the coupling angle was $\theta_{c,exp} = -0.28^\circ$, which was close to the designed value of $\theta_c = 0^\circ$. The difference between the measured value ($\theta_{c,exp} = -0.28^\circ$) and the designed value ($\theta_c = 0^\circ$) may result from both the fabrication errors and the design rule based on the phase-matching condition.

8.2 Future Research

Several interesting topics remain to be investigated in the area of grating couplers for further research. All of the numerical analysis of this thesis is based on the FDFD method to solve rigorously the Helmholtz equation for finite grating couplers illuminated by finite incident beams, and the resulting linear algebraic equations are solved iteratively by use of the conju-

gate gradient method (CGM). Although the FDFD method provides a rigorous solution to the Helmholtz equation, and the CGM provides a monotonical decrease of its residual error at each iteration (i.e. convergence is guaranteed), the method is inherently computationally-intensive. As a result, other iterative methods, such as the bi-conjugate gradient method (BCGM) [140, 143, 144] and the alternating-direction-implicit (ADI) method [135, 144], can be applied to solve more efficiently the large sparse linear systems. However, these two iterative methods generally have the difficulty of the numerical convergence. Therefore, the further development of the BCGM in conjunction with the preconditioning method is needed to improve the convergence of the BCGM.

Recently, another finite-difference method, the finite-difference time-domain (FDTD) method, has been applied to solve rigorously the Maxwell's equations for finite diffractive optical elements, such as surface-relief gratings [145], diffractive lenses [146], and photonic crystals [147]. Similar to the FDFD method, the FDTD method can be used to analyze inhomogeneous and anisotropic materials. However, in contrast to the FDFD method, the FDTD method provides both transient and steady-state solutions to the Maxwell's equations. Therefore, another possible area of research is to develop the FDTD method for the rigorous analysis of finite volume holographic gratings and compare to the FDFD method. In addition, the further development of the finite-difference method for modeling general 3-D geometries is also an interesting topic in the further research.

In addition to VHGCs, the surface-relief grating couplers can also be used to couple light into and out of waveguides. In contrast to VHGCs, the surface-relief grating couplers have discontinuous variations (i.e. non-sinusoidal variations) of the refractive index and higher refractive-index modulations Δn . However, for most coupling applications, the preferential-order coupling is needed, and therefore, slanted gratings are required. As has been discussed in Chapter 5, slanted VHGCs provide high branching ratios ($BR > 90\%$) for both TE and TM polarizations. Therefore, it would be interesting to study the diffraction characteristics of slanted surface-relief grating couplers and compare to those of VHGCs.

Moreover, there is also a need to develop an optimization processing for the design of surface-relief grating couplers.

Furthermore, because of the fabrication errors resulting from the holographic recording process (for the fabrication of volume holographic gratings) and the grating etching process (for the fabrication of surface-relief gratings), both grating periods and slant angles would deviate from their designed values, and therefore, degenerate the performances of grating couplers. As a result, another interesting research project is to investigate the sensitivity of grating periods and slant angles of both output and input grating couplers for optical interconnections. In addition, for input grating couplers, the sensitivity of incident angles is also of great interest for further research.

APPENDIX A

THE CONJUGATE GRADIENT METHOD

In order to solve large sparse linear systems

$$\bar{\bar{\mathbf{A}}}\mathbf{x} = \mathbf{b}, \quad (\text{A.1})$$

the conjugate gradient method (CGM) is one of the best known iterative technique because its residual error decreases monotonically at each iteration. In principle, the CGM yields an exact solution when the number of iterations reaches the number of equation or unknowns, so the CGM is also referred to as the semi-iterative method.

The CGM algorithm can be derived by applying the standard variational principle to construct a functional whose minimum corresponds to the solution of Eq. A.1. Multiplying $\bar{\bar{\mathbf{A}}}^\dagger [\bar{\bar{\mathbf{A}}}^\dagger = (\bar{\bar{\mathbf{A}}}^*)^T$, where the asterisk denotes complex conjugate and T denotes the transpose matrix] on the both sides of Eq. A.1 and applying the Gram-Schmidt process, the algorithm of the CGM with an initial guess \mathbf{x}_0 for the k -th iterative solution \mathbf{x}_k can be written as:

$$\mathbf{r}_0 = \mathbf{b} - \bar{\bar{\mathbf{A}}}\mathbf{x}_0, \quad (\text{A.2})$$

$$\mathbf{P}_0 = \frac{\bar{\bar{\mathbf{A}}}^\dagger \mathbf{r}_0}{\langle \bar{\bar{\mathbf{A}}}^\dagger \mathbf{r}_0, \bar{\bar{\mathbf{A}}}^\dagger \mathbf{r}_0 \rangle}, \quad (\text{A.3})$$

$$\mathbf{x}_k = \mathbf{x}_{k-1} + \alpha_{k-1} \mathbf{P}_{k-1}, \quad (\text{A.4})$$

$$\mathbf{r}_k = \mathbf{r}_{k-1} - \alpha_{k-1} \bar{\bar{\mathbf{A}}}\mathbf{P}_{k-1}, \quad (\text{A.5})$$

$$\mathbf{P}_k = \mathbf{P}_{k-1} + \beta_{k-1} \bar{\bar{\mathbf{A}}}^\dagger \mathbf{r}_k, \quad (\text{A.6})$$

$$\alpha_{k-1} = \frac{1}{\langle \bar{\bar{\mathbf{A}}}\mathbf{P}_{k-1}, \bar{\bar{\mathbf{A}}}\mathbf{P}_{k-1} \rangle}, \quad (\text{A.7})$$

$$\beta_{k-1} = \frac{1}{\langle \bar{\mathbf{A}}^\dagger \mathbf{r}_k, \bar{\mathbf{A}}^\dagger \mathbf{r}_k \rangle}, \quad (\text{A.8})$$

where \mathbf{r}_k is the residual vector at the k -th iteration, and \mathbf{P}_k is the conjugate search vector at the k -th iteration. In addition, $\langle \mathbf{x}, \mathbf{y} \rangle$ denotes the inner product of two vectors, which is defined as $\langle \mathbf{x}, \mathbf{y} \rangle = \mathbf{x}^{*T} \mathbf{y}$. The iteration is continued till a termination condition is satisfied. The form of a termination condition can be written as:

$$\frac{\|\mathbf{r}_k\|}{\|\mathbf{b}\|} < \varepsilon_r, \quad (\text{A.9})$$

where $\|\mathbf{x}\| = \sqrt{\langle \mathbf{x}, \mathbf{x} \rangle}$ is the Euclidean norm of the vector \mathbf{x} , and ε_r denotes a small number, called the tolerance, which specifies the desired accuracy of solution. In general the values of ε_r used in the literature range from 10^{-4} to 10^{-7} [140].

APPENDIX B

CALCULATION OF REFRACTIVE -INDEX MODULATIONS FROM MEASURED DIFFRACTION EFFICIENCIES

In order to convert the experimentally measured diffraction efficiencies to the corresponding refractive-index modulations, both Kogelnik's theory and the RCWA are applied. However, to avoid the effect of the optically thick glass substrate (with non-optically flat and non-parallel sides), both methods have to be modified by a correction factor R_f for the Fresnel reflection power loss of the glass substrate. The configuration for determining the Fresnel factors is shown in Fig. B.1. R_f was calculated based only on the interface between air and glass. In addition, since Kogelnik's theory is valid in the case that the average refractive index in the grating is equal to those in the input and output regions, additional correction factors had to be used. Two cases were considered: (1) neglecting multiple interference effects between photopolymer and Mylar layers and (2) taking into account the multiple interference effects between photopolymer and Mylar layers. In the first case R'_f , R''_f , and R'''_f (shown in Fig. B.1) have to be used to take into account the reflection losses at each interface. R'_f , R''_f , and R'''_f are calculated by using the Fresnel equations for a planar interface between two media. In the second case (with multiple interference effects included) the correction factor R_f^{mi} is used. In this case R_f^{mi} was calculated taking into account the multiple interference between photopolymer/Mylar with glass and air as input and output

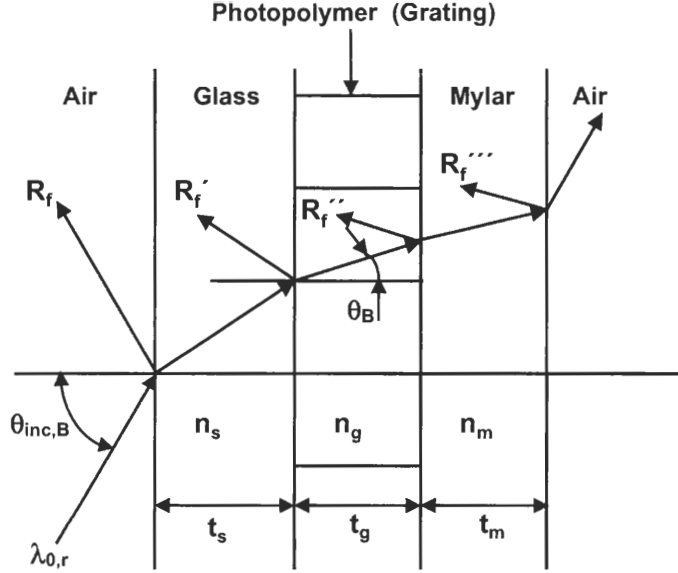


Figure B.1: Configuration for determining correction factors of the Fresnel reflection loss. The sample consists a glass substrate with thickness t_s , a grating with thickness t_g , and a Mylar layer with thickness t_m . The refractive indices of the glass, the grating, and the Mylar layer are n_s , n_g , and n_m , respectively. The incident beam has wavelength $\lambda_{0,r}$ and incident angle $\theta_{b,o}$. R_f indicates the Fresnel reflection coefficient at the interface between air and the glass, and R'_f represents the Fresnel reflection coefficient at the interface between the glass and the grating/Mylar combination.

regions respectively.

As seen in Fig. B.1, the prepared sample consists of a glass substrate with thickness $t_s \simeq 1.0 \text{ mm}$, a photopolymer (grating) with thickness $t_g = 6.0 \mu\text{m}$, and a Mylar layer with thickness $t_m = 57.83 \mu\text{m}$ (that was measured experimentally using a profilometer). The refractive indices of glass, photopolymer (grating), and Mylar layer are $n_s = 1.4567$, $n_g = 1.5$, and $n_m = 1.6$ respectively. The TE-polarized laser beam with freespace wavelength $\lambda_{0,r} = 632.8 \text{ nm}$ is incident from air with an angle $\theta_{inc,B} = 60.42^\circ$ to monitor the diffraction efficiency during exposure. Based on thickness and refractive index of the prepared sample and monitoring condition, correction factors for the Fresnel reflection loss are $R_f = 0.165$,

$R'_f = 5.016 \times 10^{-4}$, $R''_f = 2.220 \times 10^{-3}$, $R'''_f = 0.214$, and $R_f^{mi} = 0.258$. Therefore, the refractive-index modulation estimated by use of modified Kogelnik's theory $\Delta n_{1,Kog}$ can be represented as:

$$Case1: \Delta n_{1,Kog} = \frac{\lambda_{0,r} \sin \theta_B}{\pi t_g} \sin^{-1} \sqrt{\frac{DE_1}{(1 - R_f)(1 - R'_f)(1 - R''_f)(1 - R_f^{mi})}}, \quad (B.1)$$

$$Case2: \Delta n_{1,Kog} = \frac{\lambda_{0,r} \sin \theta_B}{\pi t_g} \sin^{-1} \sqrt{\frac{DE_1}{(1 - R_f)(1 - R_f^{mi})}}, \quad (B.2)$$

where θ_B is the incident angle inside the grating, and DE_1 is the measured diffraction efficiency of the first-diffracted order. For both cases the error of Kogelnik's theory was $\sim 30\%$. A summary of the estimated Δn_1 is shown in Table B.1. Moreover, the refractive-index modulation of the grating is also determined by use of the RCWA by using the equation

$$DE_1^c = \frac{DE_1}{1 - R_f} = f_{RCWA}(\Delta n_1), \quad (B.3)$$

where DE_1^c is the diffraction efficiency calculated using the RCWA and $f_{RCWA}(\ast)$ describes the numerical dependence of the diffraction efficiencies on Δn_1 .

Table B.1: Saturation refractive-index modulations calculated from experimental data using the RCWA or Kogelnik's theory with corrections for Fresnel losses

Exposure Irradiance $I_0(mW/cm^2)$	Refractive-Index Modulations, Δn_1				
	RCWA	Kogelnik ¹	Error(%) ³	Kogelnik ²	Error(%) ³
0.043	0.985×10^{-2}	0.692×10^{-2}	29.75	0.673×10^{-2}	31.68
0.110	1.056×10^{-2}	0.742×10^{-2}	29.73	0.721×10^{-2}	31.72
0.240	1.126×10^{-2}	0.792×10^{-2}	29.66	0.769×10^{-2}	31.71
0.368	1.066×10^{-2}	0.750×10^{-2}	29.64	0.728×10^{-2}	31.71

1: Neglecting multiple interference effects

2: Taking into account photopolymer/Mylar layer multiple interference effects

3: Error calculated using Eq. (4.27)

APPENDIX C

DIFFRACTION INTEGRALS FOR FAR-FIELD CALCULATIONS

In order to calculate the far-field distribution, the diffraction integral [17], relating the far field at an arbitrary point in space to the near-field profile along a boundary Γ , is applied. As shown in Fig. 5.1, the boundary Γ is defined as the interface between the grating layer and the cover region. By applying Green's theorem to Maxwell's equations and incorporating the two-dimensional diffraction condition, the integral expression for the total field at an arbitrary observation point ($\mathbf{r}_o = x_o\hat{x} + y_o\hat{y}$) above the boundary Γ is [17]

$$U(\mathbf{r}_o) = - \int_{\Gamma} U(\mathbf{r}') \left[\frac{k_c}{2j} H_1^{(2)}(k_c |\mathbf{r}_o - \mathbf{r}'|) \frac{y_o}{|\mathbf{r}_o - \mathbf{r}'|} \right] dx', \quad (\text{C.1})$$

where $\mathbf{r}' = x'\hat{x} + y'\hat{y}$ is a source point on the boundary Γ , $|\mathbf{r}_o - \mathbf{r}'| = \sqrt{(x_o - x')^2 + (y_o - y')^2}$ is the distance between the source point on the boundary Γ and the observation point in the cover region, k_c is the wave number in the cover region, and $H_1^{(2)}$ is the first-order Hankel function of the second kind. In addition, the near-field profile $U(\mathbf{r}')$ along the boundary Γ is calculated by using both the RCWA/LM approach and the FDFD method. For the RCWA/LM approach, the normalized near field along the top surface of the waveguide film layer is given by

$$U_{RCWA/LM}(x') = \begin{cases} \exp(-\alpha_l x') & 0 \leq x' \leq L_g \\ 0 & \text{else.} \end{cases} \quad (\text{C.2})$$

For the configuration of the output VHGC in the waveguide film region [as shown in Fig. 5.1(a)], the field along the top surface of the waveguide film layer [as represented

in Eq. (C.2)] is also the field along the boundary Γ . However, for the configuration of the output VHGC in the waveguide cover region [as shown in Fig. 5.1(b)], the field along the boundary Γ is calculated by substituting Eq. (C.2) into Eq. (C.1) with the assumption that the grating is homogeneous with an average refractive index. However, for the FDFD method, the near fields $U_{FDFD}(\mathbf{r}')$ along the boundary Γ for both the output VHGC in the waveguide film region and the output VHGC in the waveguide cover region are obtained rigorously by solving the corresponding linear algebraic equations of the Helmholtz equation.

APPENDIX D

MODAL DECOMPOSITION FOR THE POWER CALCULATIONS OF WAVEGUIDE MODES

A multilayer slab waveguide, shown in Fig. D.1, consists of a stack of N layers with finite thickness bounded on either side by two semi-infinite media, denoted as a substrate with refractive index n_s and a cover with refractive index n_c . The thickness and the refractive index of the i -th layer are t_i and n_i respectively. The slab waveguide is infinite in extent in the xz plane, but finite in the y direction.

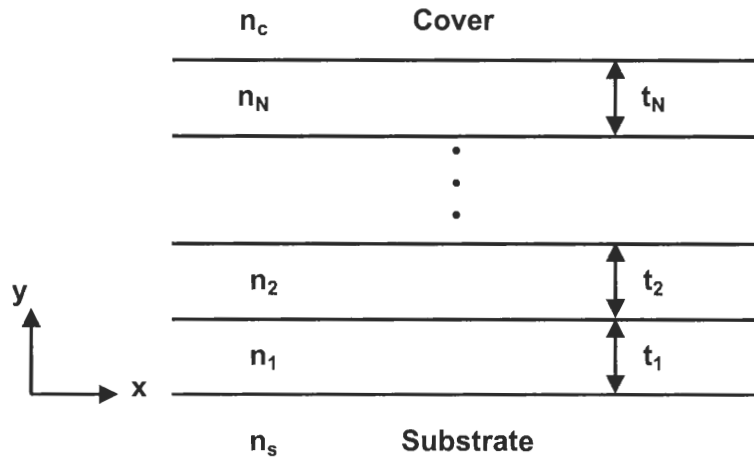


Figure D.1: A configuration of a multilayer slab waveguide consisting of a stack of N layer with finite thickness bounded on either side by two semi-infinite media, denoted as a substrate with refractive index n_s and a cover with refractive index n_c . The thickness and the refractive index of the i -th layer are t_i and n_i respectively.

In order to calculate the power of guided modes supported by the multilayer slab waveguide, the modal decomposition is applied in this research. First, it is assumed that the polarization is TE (electric field along the y -axis). Based on the modal decomposition, any field distribution along the y direction, $\mathcal{E}_z(y)$, of the slab waveguide can be expressed in terms of guided modes and radiation modes as

$$\mathcal{E}_z(y) = \sum_m a_m \mathcal{E}_{mz}(y) + \int_{\beta} q(\beta) \mathcal{E}_z(y, \beta) d\beta, \quad (\text{D.1})$$

where $\mathcal{E}_{mz}(y)$ and $\mathcal{E}_z(y, \beta)$ represent the field profiles of the TE_m guided mode and the radiation mode respectively, and a_m and $q(\beta)$ are unknown coefficients. Therefore, the electric field of the waveguide $E_z(y)$ can be represented as

$$E_z(y) = \sum_m a_m \mathcal{E}_{mz}(y) \exp(-j\beta_m x) + \int_{\beta} q(\beta) \mathcal{E}_z(y, \beta) \exp(-j\beta x) d\beta, \quad (\text{D.2})$$

where β_m and β are the propagation constants of the m -th guided mode and the radiation mode respectively. In addition, it is well known that the modes of the waveguide form a basis and they satisfy the orthogonality conditions of the form

$$\langle \mathcal{E}_{mz}(y), \mathcal{E}_{nz}(y) \rangle = \frac{\beta_m}{2\omega\mu_0} \int_{-\infty}^{\infty} \mathcal{E}_{mz}(y) \mathcal{E}_{nz}^*(y) dy = \mathcal{P}_{TE_m} \delta_{m,n}, \quad (\text{D.3})$$

where ω is the angular frequency, μ_0 is the permeability of freespace, \mathcal{P}_{TE_m} the normalized power of m -th guided mode for TE polarization (per unit length along the z -axis), and $\delta_{m,n}$ is the Kronecker's symbol. It is noted that the orthogonality condition holds for radiation modes as well as between guided modes and radiation modes. Multiplying $\frac{\beta_n}{2\omega\mu_0} \mathcal{E}_{nz}^*(y)$ on the both sides of Eq. D.1 and applying the orthogonality condition, the unknown coefficients of a_m and $q(\beta)$ and be expressed as

$$a_m = \frac{1}{\mathcal{P}_{TE_m}} \langle \mathcal{E}_z(y), \mathcal{E}_{mz}(y) \rangle = \frac{1}{\mathcal{P}_{TE_m}} \frac{\beta_m}{2\omega\mu_0} \int_{-\infty}^{\infty} \mathcal{E}_z(y) \mathcal{E}_{mz}^*(y) dy, \quad (\text{D.4})$$

$$q(\beta) = \frac{1}{\mathcal{P}_{TE_{\beta}}} \langle \mathcal{E}_z(y), \mathcal{E}_z(y, \beta) \rangle = \frac{1}{\mathcal{P}_{TE_{\beta}}} \frac{\beta}{2\omega\mu_0} \int_{-\infty}^{\infty} \mathcal{E}_z(y) \mathcal{E}_z^*(y, \beta) dy. \quad (\text{D.5})$$

As a result, the corresponding power P_{TE} for TE polarization of a slab waveguide can be

expressed as

$$P_{TE} = \sum_m |a_m|^2 \mathcal{P}_{TE_m} + \int_{\beta} |q(\beta)|^2 \mathcal{P}_{TE_{\beta}} d\beta. \quad (\text{D.6})$$

In the other word, the guided power of TE_m mode, P_{TE_m} , can be determined by

$$P_{TE_m} = |a_m|^2 \mathcal{P}_{TE_m}. \quad (\text{D.7})$$

Similarly, for TM polarization, the guided power of TM_m mode, P_{TM_m} , is given by

$$P_{TM_m} = |b_m|^2 \mathcal{P}_{TM_m}, \quad (\text{D.8})$$

where

$$b_m = \frac{1}{\mathcal{P}_{TM_m}} \frac{\beta_m}{2\omega\epsilon_0} \int_{-\infty}^{\infty} \frac{1}{\varepsilon(y)} \mathcal{H}_z(y) \mathcal{H}_{mz}^*(y) dy, \quad (\text{D.9})$$

$$\mathcal{P}_{TM_m} = \frac{\beta_m}{2\omega\epsilon_0} \int_{-\infty}^{\infty} \frac{1}{\varepsilon(y)} |\mathcal{H}_{mz}(y)|^2 dy. \quad (\text{D.10})$$

ϵ_0 is the permittivity of freespace, $\varepsilon(y)$ is the dielectric constant that is function of y , $\mathcal{H}_z(y)$ is an arbitrarily magnetic field profile along the y direction, and $\mathcal{H}_{mz}(y)$ is the magnetic field profile of the TM_m mode.

BIBLIOGRAPHY

- [1] D. A. B. Miller, "Physical reasons for optical interconnection," *Special Issue on Smart Pixels, Int. J. Optoelectron.*, vol. 11, pp. 155–168, May–June 1997.
- [2] D. A. B. Miller, "Rationale and challenges for optical interconnects to electric chips," *Proc. IEEE*, vol. 88, pp. 728–749, June 2000.
- [3] D. A. B. Miller, "Optical interconnects to silicon," *IEEE J. Select. Topics. Quantum. Electron.*, vol. 6, pp. 1312–1317, Nov.–Dec. 2000.
- [4] J.-H. Yeh and R. K. Kostuk, "Substrate-mode holograms used in optical interconnects: design issues," *Appl. Opt.*, vol. 34, pp. 3152–3164, June 1995.
- [5] J.-H. Yeh and R. K. Kostuk, "Free-space holographic optical interconnects for board-to-board and chip-to-chip interconnections," *Opt. Lett.*, vol. 21, pp. 1274–1276, Aug. 1996.
- [6] J.-H. Yeh, R. K. Kostuk, and K.-Y. Tu, "Hybrid free-space optical bus system for board-to-board interconnections," *Appl. Opt.*, vol. 35, pp. 6354–6364, Nov. 1996.
- [7] M. C. Wu, "Micromachining for optical and optoelectronic systems," *Proc. IEEE*, vol. 85, pp. 1833–1856, Nov. 1997.
- [8] S. Sinzinger and J. Janns, "Integrated micro-optical imaging system with a high interconnection capacity fabricated in planar optics," *Appl. Opt.*, vol. 36, pp. 4729–4735, July 1997.
- [9] A. C. Walker, T.-Y. Yang, J. Gourlay, J. A. B. Danes, M. G. Forbes, S. M. Prince, D. A. Baillie, D. T. Neilson, R. Williams, L. C. Wilkinson, G. R. Smith, M. P. Y. Desmulliez, G. S. Buller, M. R. Taghizadeh, A. Waddie, I. Underwood, C. R. Stanley, F. Pottier, B. Vögele, and W. Sibbett, "Optoelectronic systems based on InGaAs-complementary-metal-oxide-semiconductor smart-pixel arrays and free-space optical interconnects," *Appl. Opt.*, vol. 37, pp. 2822–2830, May 1998.
- [10] G. Verschaffelt, R. Buczynski, P. Tuteleers, P. Vynck, V. Baukens, H. Ottevaere, C. Debaes, S. Kufner, M. Kufner, A. Hermanne, J. Genoe, D. Coppée, R. Vounckx, S. Borghs, I. Veretennicoff, and H. Thienpont, "Demonstration of a monolithic multichannel module for multi-Gb/s intra-MCM optical interconnects," *IEEE Photon. Tech. Lett.*, vol. 10, pp. 1629–1631, Nov. 1998.

- [11] D. T. Neilson and E. Schenfeld, "Free-space optical relay for the interconnection of multimode fibers," *Appl. Opt.*, vol. 38, pp. 2291–2296, Apr. 1999.
- [12] F. Lin, E. M. Strzelecki, and T. Jansson, "Optical multiplanar VLSI interconnects based on multiplexed waveguide hologram," *Appl. Opt.*, vol. 29, pp. 1126–1133, Mar. 1990.
- [13] S. H. Song and E. H. Lee, "Focusing-grating-coupler arrays for uniform and efficient signal distribution in a backboard optical interconnect," *Appl. Opt.*, vol. 34, pp. 5913–5919, Sept. 1995.
- [14] Q. Xing, S. Ura, T. Suhara, and H. Nishihara, "Contra-directional coupling between stacked waveguides using grating couplers," *Opt. Commu.*, vol. 144, pp. 180–182, Dec. 1997.
- [15] R. T. Chen, L. Lin, C. Choi, Y. J. Liu, B. Bihari, L. Wu, S. Tang, R. Wickman, B. Picor, M. K. Hibbs-Brenner, J. Bristow, and Y. S. Liu, "Fully embedded board-level guided-wave optoelectronic interconnects," *Proc. IEEE*, vol. 88, pp. 780–793, June 2000.
- [16] T. Tanaka, H. Takahashi, Y. Hibino, T. Hashimoto, A. Himeno, Y. Yamada, and Y. Tohmori, "Hybrid external cavity lasers composed of spot-size converter integrated LDs and UV written Bragg grating in a planar lightwave circuit on Si," *IEICE Trans. Electron.*, vol. E83-C, pp. 875–883, June 2000.
- [17] J. M. Bendickson, E. N. Glytsis, and T. K. Gaylord, "Scalar integral diffraction methods: unification, accuracy, and comparison with a rigorous boundary element method with application to diffractive cylindrical lenses," *J. Opt. Soc. Amer. A*, vol. 15, pp. 1822–1837, July 1998.
- [18] J. M. Bendickson, E. N. Glytsis, and T. K. Gaylord, "Metallic surface-relief on-axis and off-axis focusing diffractive cylindrical mirrors," *J. Opt. Soc. Amer. A*, vol. 16, pp. 113–130, Jan. 1999.
- [19] J. M. Bendickson, E. N. Glytsis, and T. K. Gaylord, "Focusing diffractive cylindrical mirrors: rigorous evaluation of various design methods," *J. Opt. Soc. Amer. A*, vol. 18, pp. 1487–1494, July 2001.
- [20] S. M. Schultz, E. N. Glytsis, and T. K. Gaylord, "Design of a high-efficiency volume grating couplers for line focusing," *Appl. Opt.*, vol. 37, pp. 2278–2287, Apr. 1998.
- [21] S. M. Schultz, E. N. Glytsis, and T. K. Gaylord, "Volume grating preferential-order focusing waveguide coupler," *Opt. Lett.*, vol. 24, pp. 1708–1710, Dec. 1999.

- [22] S. M. Schultz, E. N. Glytsis, and T. K. Gaylord, "Design, fabrication, and performance of preferential-order volume grating waveguide couplers," *Appl. Opt.*, vol. 39, pp. 1223–1232, Mar. 2000.
- [23] T. Suhara, K. Okada, and H. Nishihata, "Focusing grating coupler in AlGaAs optical waveguide," *IEEE Photon. Techn. Lett.*, vol. 4, pp. 903–905, Aug. 1992.
- [24] J. Backlund, J. Bengtsson, C.-F. Carlström, and A. Larsson, "Incoupling waveguide holograms for simultaneous focusing into multiple arbitrary positions," *Appl. Opt.*, vol. 38, pp. 5738–5746, Sept. 1999.
- [25] T. Suhara and H. Hishihara, "Integrated optics components and devices using periodic structures," *IEEE J. Quantum Electron.*, vol. 22, pp. 845–867, June 1986.
- [26] S. Ura, T. Suhara, H. Hishihara, J. Koyama, "An integrated-optic disk pickup device," *J. Lightwave Technol.*, vol. 4, pp. 913–918, July 1986.
- [27] S. Nishiwaki, J. Asada, and S. Uchida, "Optical head employing a concentric-circular focusing grating coupler," *Appl. Opt.*, vol. 33, pp. 1819–1827, Apr. 1994.
- [28] H. Sakata and S. Takeuchi, "Grating-assisted directional coupler filters using Al-GaAs/GaAs MQW waveguide," *IEEE Photon. Tech. Lett.*, vol. 3, pp. 899–901, Oct. 1991.
- [29] Z. M. Chuang and L. A. Coldren, "Enhanced wavelength tuning in grating-assisted codirectional coupler filter," *IEEE Photon. Tech. Lett.*, vol. 5, pp. 1219–1221, Oct. 1993.
- [30] S. Ura, R. Nishida, T. Suhara, and H. Nishihara, "Wavelength-selective coupling among three vertically integrated waveguides by grating couplers," *IEEE Photon. Tech. Lett.*, vol. 13, pp. 133–135, Feb. 2001.
- [31] S. Ura, R. Nishida, T. Suhara, and H. Nishihara, "Wavelength-selective coupling between vertically integrated thin-film waveguides via supermode by a pair of grating couplers," *IEEE Photon. Tech. Lett.*, vol. 13, pp. 678–680, July 2001.
- [32] J. Backlund, J. Bengtsson, C.-F. Carlström, and A. Larsson, "Waveguide input grating couplers for wavelength-division multiplexing and wavelength encoding," *IEEE Photon. Tech. Lett.*, vol. 13, pp. 815–817, Aug. 2001.
- [33] S. Ura, H. Sunagawa, T. Suhara, and H. Nishihara, "Focusing grating couplers for polarization detection," *J. Lightwave Tech.*, vol. 6, pp. 1028–1032, June 1988.
- [34] S. Ura, M. Shinohara, T. Suhara, and H. Nishihara, "Integrated-optic grating-scale-displacement sensors using linearly focusing grating couplers," *IEEE Photon. Tech. Lett.*, vol. 6, pp. 239–241, Feb. 1994.

- [35] J. Dübendorfer and R. E. Kunz, "Compact integrated optical immunosensor using replicated chirped grating coupler sensor chips," *Appl. Opt.*, vol. 37, pp. 1890–1894, Apr. 1998.
- [36] M. Wiki and R. E. Kunz, "Wavelength-interrogated optical sensors for biochemical applications," *Opt. Lett.*, vol. 25, pp. 463–465, Apr. 2000.
- [37] S. Noda, K. Kojima, and K. Kyuma, "Surface-emitting multiple quantum well distributed feedback laser with a broad-area grating coupler," *Electron. Lett.*, vol. 24, pp. 277–278, Mar. 1988.
- [38] T. Rozzi, F. Chiaraluce, and M. Lanari, "A rigorous analysis of DFB lasers with large and aperiodic corrugation," *IEEE J. Quantum Electron.*, vol. 27, pp. 212–223, Feb. 1991.
- [39] H. Haus and Y. Lai, "Narrow-band distributed feedback reflector design," *J. Lightwave Tech.*, vol. 9, pp. 754–760, June 1991.
- [40] G. Sarusi, B. F. Levine, S. J. Pearton, K. M. S. Bandara, R. E. Leibenguth, and J. Y. Andersson, "Optimization of two dimensional gratings for very long wavelength quantum well infrared photodetectors," *J. Appl. Phys.*, vol. 76, pp. 4989–4994, Nov. 1994.
- [41] K. L. Tsai, C. P. Lee, J. S. Tsang, H. R. Chen, and K. H. Chang, "Two-dimensional bi-periodic grating coupled one- and two-color quantum well infrared photodetectors," *IEEE Electron Device Lett.*, vol. 16, pp. 49–51, Feb. 1995.
- [42] D. Mehuys, A. Hardy, D. F. Welch, R. G. Waarts, and R. Parke, "Analysis of detuned second-order grating output couplers with an integrated superlattice reflectors," *IEEE Photon. Tech. Lett.*, vol. 3, pp. 342–344, Apr. 1991.
- [43] M. Oh, S. Ura, T. Suhara, and H. Nishihara, "Integrated-optics focal-spot intensity modulator using electrooptic polymer waveguide," *J. Lightwave Tech.*, vol. 12, pp. 1569–1576, Sept. 1994.
- [44] N. Eriksson, M. Hagberg, and A. Larsson, "Highly efficient grating-coupled surface-emitters with single outcoupling elements," *IEEE Photon. Tech. Lett.*, vol. 7, pp. 1394–1396, Dec. 1995.
- [45] V. A. Sychugov, A. V. Tishchenko, B. A. Usievich, and O. Oarriaux, "Optimization and control of grating coupling to or from a silicon-based optical waveguide," *Opt. Eng.*, vol. 35, pp. 3092–3100, Nov. 1996.
- [46] J. C. Brazas, L. Li, and A. L. Mckeon, "High-efficiency input coupling into optical waveguides using gratings with double-surface corrugation," *Appl. Opt.*, vol. 34, pp. 604–609, Feb. 1995.

- [47] M. Hagberg, T. Kjellberg, N. Eriksson, and A. G. Larsson, "Demonstration of blazing effect in second order gratings under resonant condition," *Electron. Lett.*, vol. 30, pp. 410–412, Mar. 1994.
- [48] M. Hagberg, N. Eriksson, T. Kjellberg, and A. G. Larsson, "Demonstration of blazing effect in detuned second order gratings," *Electron. Lett.*, vol. 30, pp. 570–571, Mar. 1994.
- [49] M. Li and S. Sheard, "Experimental study of waveguide grating couplers with parallelogramic tooth profiles," *Opt. Eng.*, vol. 35, pp. 3101–3106, Nov. 1996.
- [50] T. Liao, S. Sheard, M. Li, J. Zhu, and P. Prewett, "High-efficiency focusing waveguide grating couplers with parallelogramic groove profiles," *J. Lightwave Tech.*, vol. 15, pp. 1142–1148, July 1997.
- [51] Z. Hegedus and R. Netterfield, "Low sideband guided-mode resonant filter," *Appl. Opt.*, vol. 39, pp. 1469–1473, Apr. 2000.
- [52] H. Kogelnik and T. P. Sosnowski, "Holographic thin film couplers," *Bell Syst. Tech. J.*, vol. 49, pp. 1602–1608, Sept. 1970.
- [53] W.-C. Liu and Marek W. Kowarz, "Vector diffraction from subwavelength optical disk structures: two-dimensional modeling of near-field profiles, far-field intensities, and detector signals from a DVD," *Appl. Opt.*, vol. 38, pp. 3787–3797, June 1999.
- [54] S.-D. Wu and E. N. Glytsis, "Finite-number-of-periods holographic gratings: analysis using the finite-difference frequency-domain method," (abstract) Optical Society of America Annual Meeting/ILS-XVII, pg. 56, Oct. 2001.
- [55] S.-D. Wu and E. N. Glytsis, "Finite-number-of-periods holographic gratings with finite -width incident beams: analysis using the finite-difference frequency-domain method," *J. Opt. Soc. Amer. A*, vol. 19, pp. 2018–2029, Oct. 2002.
- [56] T. K. Gaylord and M. G. Moharam, "Analysis and applications of optical diffraction by gratings," *Proc. IEEE*, vol. 73, pp. 894–937, May 1985.
- [57] E. E. Kriezis, P. K. Pandelakis, and A. G. Papagiannakis, "Diffraction of a Gaussian beam from a periodic planar screen," *J. Opt. Soc. Amer. A*, vol. 11, pp. 630–636, Feb. 1994.
- [58] J. M. Bendickson, E. N. Glytsis, and T. K. Gaylord, "Guided-mode resonant sub-wavelength gratings: effects of finite beams and finite gratings," *J. Opt. Soc. Amer. A*, vol. 18, pp. 1912–1928, Aug. 2001.
- [59] Y.-L. Kok, "General solution to the multiple-metallic-grooves scattering problem: the fast-polarization case," *Appl. Opt.*, vol. 32, pp. 2573–2581, May 1993.

- [60] O. Mata-Mendez and J. Sumaya-Martinez, "Scattering of TE-polarized waves by a finite-grating: giant resonant enhancement of the electric field within the grooves," *J. Opt. Soc. Amer. A*, vol. 14, pp. 2203–2211, Sept. 1997.
- [61] G. Pelosi, G. Manara, and G. Toso, "Heuristic diffraction coefficient for plane-wave scattering from edges in periodic planar surfaces," *J. Opt. Soc. Amer. A*, vol. 13, pp. 1689–1697, Aug. 1996.
- [62] K. Hirayama, E. N. Glytsis, and T. K. Gaylord, and D. W. Wilson, "Rigorous electromagnetic analysis of diffractive cylindrical lenses," *J. Opt. Soc. Amer. A*, vol. 13, pp. 2219–2231, Nov. 1996.
- [63] K. Hirayama, E. N. Glytsis, and T. K. Gaylord, "Rigorous electromagnetic analysis of diffraction by finite-number-of-periods gratings," *J. Opt. Soc. Amer. A*, vol. 14, pp. 907–917, Apr. 1997.
- [64] O. Mata-Mendez and F. Chavez-Rivas, "New property in the diffraction of Hermite-Gaussian beams by finite gratings in the scalar diffraction regime: constant-intensity angles in the far field when the beam center is displaced through the grating," *J. Opt. Soc. Amer. A*, vol. 15, pp. 2698–2794, Oct. 1998.
- [65] O. Mata-Mendez and F. Chavez-Rivas, "Diffraction of Gaussian and Hermite-Gaussian beams by finite gratings," *J. Opt. Soc. Amer. A*, vol. 18, pp. 537–545, Mar. 2001.
- [66] Q. Huang and P. R. Ashley, "Holographic Bragg grating input-output couplers for polymer waveguide at an 850-nm wavelength," *Appl. Opt.*, vol. 36, pp. 11198–1203, Feb. 1997.
- [67] H. J. Zhou, V. Morozov, and J. Neff, "Characterization of DuPont photopolymers in infrared light for free-space optical interconnects," *Appl. Opt.*, vol. 34, pp. 7457–7459, Nov. 1995.
- [68] A. Pu and D. Psaltis, "High-density recording in photopolymer-based holographic three-dimensional disks," *Appl. Opt.*, vol. 35, pp. 2389–2398, May 1996.
- [69] G. Zhang, G. Montemezzani, and P. Günter, "Narrow-bandwidth holographic reflection filters with photopolymer films," *Appl. Opt.*, vol. 40, pp. 2423–2427, May 2001.
- [70] U. S. Rhee, H. J. Caulfield, J. Shamir, C. S. Vikram, and M. M. Mirsalehi, "Characteristics of the Du Pont photopolymer for angularly multiplexed page-oriented holographic memories," *Opt. Eng.*, vol. 32, pp. 1839–1847, Aug. 1993.
- [71] S. Piazzolla and B. K. Jenkins, "Holographic grating formation in photopolymers," *Opt. Lett.*, vol. 21, pp. 1075–1077, July 1996.

- [72] S. Piazzolla and B. K. Jenkins, "First-harmonic diffusion model for holographic grating formation in photopolymers," *J. Opt. Soc. Amer. B*, vol. 17, pp. 1147–1157, July 2000.
- [73] J. H. Kwon, H. C. Hwang, and K. C. Woo, "Analysis of temporal behavior of beams diffracted by volume gratings formed in photopolymer," *J. Opt. Soc. Amer. B*, vol. 16, pp. 1651–1657, Oct. 1999.
- [74] S. Calixto, "Dry polymer for holographic recording," *Appl. Opt.*, vol. 26, pp. 3904–3910, Sept. 1987.
- [75] U. S. Rhee, H. J. Caulfield, C. S. Vikram, and J. Shamir, "Dynamics of hologram recording in DuPont photopolymer," *Appl. Opt.*, vol. 34, pp. 846–853, Feb. 1995.
- [76] R. K. Kostuk, "Dynamic hologram recording characteristics in DuPont photopolymers," *Appl. Opt.*, vol. 38, pp. 1357–1363, Mar. 1999.
- [77] G. Zhao and P. Mouroulis, "Diffusion model of holographic formation in dry photopolymer materials," *J. Mod. Opt.*, vol. 41, pp. 1929–1939, Oct. 1994.
- [78] G. Zhao and P. Mouroulis, "Extension of diffusion model of holographic photopolymer," *J. Mod. Opt.*, vol. 42, pp. 2571–2573, Dec. 1995.
- [79] G. Zhao, and P. Mouroulis, "Second order grating formation in dry holographic photopolymers," *Opt. Commu.*, vol. 15, pp. 528–532, Apr. 1995.
- [80] V. L. Colvin, R. G. Larson, A. L. Harris, and M. L. Schilling, "Quantitative model of volume hologram formation in photopolymers," *J. Appl. Phys.*, vol. 81, pp. 5913–5923, May 1997.
- [81] J. T. Sheridan and J. R. Lawrence, "Nonlocal-response diffusion model of holographic recording in photopolymer," *J. Opt. Soc. Amer. A*, vol. 17, pp. 1108–1114, June 2000.
- [82] J. R. Lawrence, F. T. O'Neil, and J. T. Sheridan, "Photopolymer holographic recording material parameter estimation using a nonlocal diffusion based model," *J. Appl. Phys.*, vol. 90, pp. 3142–3148, Oct. 2001.
- [83] F. T. O'Neil, J. R. Lawrence, and J. T. Sheridan, "Comparison of holographic photopolymer materials by use of analytical nonlocal diffusion model," *Appl. Opt.*, vol. 41, pp. 845–852, Feb. 2002.
- [84] J. R. Lawrence, F. T. O'Neil, and J. T. Sheridan, "Adjusted intensity nonlocal diffusion model of photopolymer grating formation," *J. Opt. Soc. Amer. B*, vol. 19, pp. 621–629, Apr. 2002.

- [85] J. T. Sheridan, M. Downey, and F. T. O'Neil, "Diffusion-based model of holographic grating formation in photopolymers: generalized non-local material responses," *J. Opt. A*, vol. 3, pp. 477–488, Oct. 2001.
- [86] H. Kogelnik, "Coupled wave theory for thick holographic gratings," *Bell Syst. Tech. J.*, vol. 48, pp. 2909–2947, 1969.
- [87] S. T. Peng, T. Tamir, and H. L. Bertoni, "Leaky-wave analysis of optical periodic couplers," *Electron. Lett.*, vol. 9, pp. 150–152, June 1973.
- [88] S. T. Peng, T. Tamir, and H. L. Bertoni, "Theory of periodic dielectric waveguides," *IEEE Trans. Microwave Theory Tech.*, vol. 23, pp. 123–133, Jan. 1975.
- [89] T. Tamir and S. T. Peng "Analysis and design of grating couplers," *Appl. Phys.*, vol. 14, pp. 235–254, Mar. 1977.
- [90] N. Izhaky and A. Hardy, "Analysis of grating-assisted backward coupling employing the unified coupled-mode formalism," *J. Opt. Soc. Amer. A*, vol. 16, pp. 1303–1311, June 1999.
- [91] N. Izhaky and A. Hardy, "Characteristics of grating-assisted couplers," *Appl. Opt.*, vol. 38, pp. 6987–6993, Dec. 1999.
- [92] P.-P. Borsboom and H. J. Frankena, "Field analysis of two-dimensional integrated optical gratings," *J. Opt. Soc. Amer. A*, vol. 12, pp. 1134–1141, May 1995.
- [93] P.-P. Borsboom and H. J. Frankena, "Field analysis of two-dimensional focusing grating couplers," *J. Opt. Soc. Amer. A*, vol. 12, pp. 1142–1146, May 1995.
- [94] P. G. Dinesen and J. S. Hesthaven, "Fast and accurate modeling of waveguide grating couplers," *J. Opt. Soc. Amer. A*, vol. 17, pp. 1565–1572, Sept. 2000.
- [95] P. G. Dinesen and J. S. Hesthaven, "Fast and accurate modeling of waveguide grating couplers. II. Three-dimensional vectorial case," *J. Opt. Soc. Amer. A*, vol. 18, pp. 2876–2885, Nov. 2001.
- [96] P. Lalanne and E. Silberstein, "Fourier-modal methods applied to waveguide computational problems," *Opt. Lett.*, vol. 25, pp. 1092–1094, Aug. 2000.
- [97] E. Silberstein, P. Lalanne, J.-P. Hugonin, and Q. Cao, "Use of grating theories in integrated optics," *J. Opt. Soc. Amer. A*, vol. 18, pp. 2865–2875, Nov. 2001.
- [98] Q. Cao, P. Lalanne, and J.-P. Hugonin, "Stable and efficient Bloch-mode computational method for one-dimensional grating waveguides," *J. Opt. Soc. Amer. A*, vol. 19, pp. 335–338, Feb. 2002.

- [99] J. H. Harris, R. K. Winn, and D. G. Dalgoutte, "Theory and design of periodic couplers," *Appl. Opt.*, vol. 11, pp. 2234–2241, Oct. 1972.
- [100] W. Y. Wang and T. J. DiLaura, "Bragg effect waveguide coupler analysis," *Appl. Opt.*, vol. 16, pp. 3230–3236, Dec. 1977.
- [101] M. L. Jones, R. P. Kenna, and C. M. Verber, "Rectangular characteristics gratings for waveguide input and output coupling," *Appl. Opt.*, vol. 34, pp. 4149–4158, July 1995.
- [102] K. Ogawa, W. S. C. Chang, B. L. Sopori, and F. J. Rosenbaum, "A theoretical analysis of etched grating couplers for integrated optics," *IEEE J. Quantum Electron.*, vol. 9, pp. 29–42, Jan. 1973.
- [103] M. Neviere, R. Petit, and M. Cadilhac, "About the theory of optical grating coupler-waveguide system," *Opt. Commun.*, vol. 8, pp. 113–117, Feb. 1973.
- [104] M. Neviere, P. Vincent, R. Petit, and M. Cadilhac, "Systematic study of resonances of holographic thin film couplers," *Opt. Commun.*, vol. 9, pp. 48–53, Sept. 1973.
- [105] M. Neviere, P. Vincent, R. Petit, and M. Cadilhac, "Determination of the coupling coefficient of a holographic thin film coupler," *Opt. Commun.*, vol. 9, pp. 240–245, Nov. 1973.
- [106] D. G. Dalgoutte and C. D. W. Wilkinson, "Thin grating couplers for integrated optics: an experimental and theoretical study," *Appl. Opt.*, vol. 14, pp. 2983–2998, Dec. 1975.
- [107] M. T. Woldarczyk and S. R. Seshadri, "Analysis of grating couplers in planar waveguides for waves at oblique incidence," *J. Opt. Soc. Amer. A*, vol. 2, pp. 171–185, Feb. 1985.
- [108] W. S. Park and S. R. Seshadri, "Analysis of the reflection grating couplers for waves at oblique incidence," *J. Opt. Soc. Amer. A*, vol. 4, pp. 1001–1020, June 1987.
- [109] L. Li and M. C. Gupta, "Effects of beam focusing on the efficiency of planar waveguide grating couplers," *Appl. Opt.*, vol. 29, pp. 5320–5325, Dec. 1990.
- [110] M. C. Gupta and L. Li, "Effect of beam defocus on the efficiency of planar waveguide grating couplers," *Appl. Opt.*, vol. 30, pp. 4402–4405, Oct. 1991.
- [111] D. Pascal, R. Orobitchouk, A. Layadi, A. Koster, and S. Laval, "Optimized coupling of a Gaussian beam into an optical waveguide with a grating coupler: comparison of experimental and theoretical results," *Appl. Opt.*, vol. 36, pp. 2443–2447, Apr. 1997.
- [112] R. Orobitchouk, A. Layadi, H. Gualous, D. Pascal, A. Koster, and S. Laval, "High-efficiency light coupling in a submicrometric silicon-on-insulator waveguide," *Appl. Opt.*, vol. 39, pp. 5773–5777, Nov. 2000.

- [113] J. C. Brazas and L. Li, "Analysis of input-grating couplers having finite lengths," *Appl. Opt.*, vol. 34, pp. 3786–3792, July 1995.
- [114] R. Waldhäusl, B. Schnabel, P. Dannberg, E.-B. Kley, A. Bräuer, and W. Karthe, "Efficient coupling into polymer waveguides by gratings," *Appl. Opt.*, vol. 36, pp. 9383–9390, Dec. 1997.
- [115] C.-K. Kwan and G. W. Taylor, "Optimization of the parallelogrammic gating diffraction efficiency for normally incident wave," *Appl. Opt.*, vol. 37, pp. 7698–7707, Nov. 1998.
- [116] K. Ogawa and W. S. C. Chang, "Analysis of holographic thin film grating coupler," *Appl. Opt.*, vol. 12, pp. 2167–2171, Sept. 1973.
- [117] Z. S. Sacks, D. M. Kingsland, R. Lee, and J.-F. Lee, "A perfectly matched anisotropic absorber for use as an absorbing boundary condition," *IEEE Trans. Antennas. Prop.*, vol. 43, pp. 1460–1463, Dec. 1995.
- [118] S. D. Gedney, "An anisotropic perfectly matched layer-absorbing medium for the truncation of FDTD lattices," *IEEE Trans. Antennas. Prop.*, vol. 44, pp. 1630–1639, Dec. 1996.
- [119] A. Taflove and S. C. Hagness, *Computational Electrodynamics: the finite-difference time-domain method* (Artech House, 2000), Chaps. 6, 7.
- [120] P. P. Silvester, and R. L. Ferrari, *Finite Elements for Electrical Engineers* (Cambridge University Press, 1996).
- [121] J. P. Bérenger, "Perfectly matched layer for the FDTD solution of wave-structure interaction problems," *IEEE Trans. Antennas. Prop.*, vol. 44, pp. 110–117, Jan. 1996.
- [122] J. P. Bérenger, "Improved PML for the FDTD solution of wave-structure interaction problems," *IEEE Trans. Antennas. Prop.*, vol. 45, pp. 466–473, Mar. 1997.
- [123] B. M. Monroe, W. K. Smothers, D. E. Keys, R. R. Kerbs, D. J. Mickish, A. F. Harrington, S. R. Schicker, M. K. Armstrong, D. M. T. Chan, and C. I. Weathers, "Improved photopolymers for holographic grating. I. Imaging properties," *J. Imaging Sci.*, vol. 35, pp. 19–25, 1991.
- [124] W. S. Colburn and K.A. Hanyes, "Volume hologram formation in photopolymer materials," *Appl. Opt.*, vol. 10, pp. 1636–1641, July 1971
- [125] J. E. Boyd, T. J. Trentler, R. K. Wahi, Y. I. Vega-Cantu, and V. L. Colvin, "Effect of film thickness on the performance of photopolymers as holographic recording materials," *Appl. Opt.*, vol. 39, pp. 2353–2358, May 2000.

- [126] V. Moreau, Y. Renotte, and Y. Lion, "Planar-integrated interferometric sensor with holographic gratings," in *Diffraction/Holographic Technologies and Spatial Light Modulators VII*, I. Cindrich, S. H. Lee, R. L. Sutherland, eds., SPIE Proc., vol. 3951, pp. 108–115, 2000.
- [127] V. Moreau, Y. Renotte, and Y. Lion, "Characterization of DuPont photopolymer: determination of kinetic parameters in a diffusion model," *Appl. Opt.*, vol. 41, pp. 3427–3435, June 2002.
- [128] J.-H. Chen, D.-C. Su, and J.-C. Su, "Shrinkage- and refractive-index shift-corrected volume holograms for optical interconnects," *Appl. Phys. Lett.*, vol. 81, pp. 1387–1389, Aug. 2002.
- [129] D. W. Diehl and N. George, "Holographic interference filters for infrared communications," *Appl. Opt.*, vol. 42, pp. 1203–1210, Mar. 2003.
- [130] C. Zhao, J. Liu, Z. Fu, and R. T. Chen, "Shrinkage-corrected volume holograms based on photopolymeric phase media for surface-normal optical interconnects," *Appl. Phys. Lett.*, vol. 71, pp. 1464–1466, Sept. 1997.
- [131] L. Dhar, M. G. Schnoes, T. L. Wysocki, H. Bair, M. Schilling, and C. Boyd, "Temperature-induced changes in photopolymer volume holograms," *Appl. Phys. Lett.*, vol. 73, pp. 1337–1339, Sept. 1998.
- [132] H. J. Eichler, S. Orlic, P. Kuemmel, and B. Schupp, "Multiplexed microholograms for optical data storage," Part of the SPIE Conference on Diffraction and Holographic Technologies, Systems, and Spatial Light Modulators VI, SPIE, vol. 3633, pp. 14–25, 1999.
- [133] S.-D. Wu and E. N. Glytsis, "Holographic grating formation in photopolymers: parameters determination based on a nonlocal diffusion model and the rigorous coupled-wave analysis," (abstract) Optical Society of America Annual Meeting/ILS-XVIII, p. 115, Oct. 2002.
- [134] S.-D. Wu and E. N. Glytsis, "Holographic grating formation in photopolymers: analysis and experimental results based on a nonlocal diffusion model and the rigorous coupled-wave analysis," *J. Opt. Soc. Amer. B.*, vol. 20, pp. 1177–1188, June 2003.
- [135] C. F. Gerald and P. O. Wheatley, *Applied Numerical Analysis* (Addison-Wesley Publishing Company, Reading, MA, 1992), Chap. 8.
- [136] K. T. Weitzel, U. P. Wild, V. N. Mikhailov, and V. N. Krylov, "Hologram recording in DuPont photopolymer films by use of pulse exposure," *Opt. Lett.*, vol. 22, pp. 1899–1901, Dec. 1997.

- [137] J. Yeh, A. Harton, and K. Wyatt, "Reliability study of holographic optical elements made with DuPont photopolymer," *Appl. Opt.*, vol. 26, pp. 6270–7264, Sept. 1998.
- [138] IMSL Inc., "User's manual: math/library, ver. 1.0," pp. 847–858, 1987.
- [139] S.-D. Wu and E. N. Glytsis, "Volume holographic grating couplers: rigorous analysis using the finite-difference frequency-domain method," *Appl. Opt.*, vol. 43, pp. 1009–1023, Feb. 2004.
- [140] M. D. Pocock and S. P. Walker, "The complex bi-conjugate gradient solver applied to large electromagnetic scattering problems, computational costs, and cost scalings," *IEEE Trans. Antennas Propagat.*, vol. 45, pp. 140–146, Jan. 1997.
- [141] S.-D. Wu and E. N. Glytsis, "Characteristics of DuPont photopolymers for slanted holographic grating formations," *J. Opt. Soc. Amer. B.*, vol. 21, 2004 (to be published).
- [142] S.-D. Wu and E. N. Glytsis, "Optimization of finite-length input volume holographic grating couplers illuminated by finite-width incident beams," *Appl. Opt.*, vol. 43, 2004 (in preparation).
- [143] C. F. Smith, A. F. Peterson, and R. Mittra, "The biconjugate gradient method for electromagnetic scattering," *IEEE Trans. Antennas Propagat.*, vol. 38, pp.938–940, June 1990.
- [144] Y. Saad and H. A. van der Vorst, "Iterative solution of linear systems in the 20th century," *J. Comput. Numer. Math.*, vol. 123, pp.1-33, 2000.
- [145] K. H. Dridi and A. Bjarklev, "Optical characteristic vector-field modeling for the accurate analysis of finite diffractive structures of high complexity," *Appl. Opt.*, vol. 38, pp.1668–1676, Mar. 1999.
- [146] S. Shi, X. Tao, L. Yang, and D. W. Prather, "Analysis of diffractive optical elements using a nonuniform finite-difference time-domain method," *Opt. Eng.*, vol. 40, pp. 503–510, Apr. 2001.
- [147] A. Taflov and S. C. Hagness, *Computational Electrodynamics: the finite-difference time-domain method* (Artech House, 2000), Chaps. 16.

VITA

Shun-Der Wu was born on May 6, 1973 in Tainan City, TAIWAN to Ping-Ho Wu and Hsiu-Tuan Wu-Cheng. He received the Bachelor of Science and the Master of Science degrees in Engineering Science from National Cheng-Kung University, Tainan, TAIWAN in 1995 and in 1997 respectively. His master thesis involved the crosstalk analysis for multiple microstrips with discontinuity structures on the printed circuit board by using the moment method. He also worked on both thermal and fluid experiments to study the performance of heat sinks for the electronics packaging systems in his master. He is a member of the Optical Society of America (OSA) and the Institute of Electrical and Electronics Engineers (IEEE).

Permanent Address: 29 Aly30 Ln300 Chunghua S. Rd. Sec.2,
Tainan, 702, TAIWAN

This thesis was typeset with $\text{\LaTeX} 2_{\epsilon}$ ¹ by the author.

¹ $\text{\LaTeX} 2_{\epsilon}$ is an extension of \LaTeX . \LaTeX is a collection of macros for \TeX . \TeX is a trademark of the American Mathematical Society. The macros used in formatting this thesis were written by Dinesh Das, Department of Computer Sciences, The University of Texas at Austin.